

For Reference

NOT TO BE TAKEN FROM THIS ROOM

Ex LIBRIS
UNIVERSITATIS
ALBERTAENSIS





Digitized by the Internet Archive
in 2022 with funding from
University of Alberta Libraries

<https://archive.org/details/Jonys1973>

THE UNIVERSITY OF ALBERTA

RELEASE FORM

NAME OF AUTHOR **Ceslovas K. Jonys**
TITLE OF THESIS **An Experimental Study of Bed-Form**
..... **Mechanics**
.....
DEGREE FOR WHICH THESIS WAS PRESENTED **Ph.D.**
YEAR THIS DEGREE GRANTED **1973**

Permission is hereby granted to THE UNIVERSITY OF
ALBERTA LIBRARY to reproduce single copies of this
thesis and to lend or sell such copies for private,
scholarly or scientific research purposes only.

The author reserves other publication rights, and
neither the thesis nor extensive extracts from it may
be printed or otherwise reproduced without the author's
written permission.

THE UNIVERSITY OF ALBERTA

RELEASE FORM

NAME OF AUTHOR Geoffrey E. Jones

TITLE OF THESIS An Experimental Study of Red-Turn

..... Mechanisms

DEGREE FOR WHICH THESIS WAS PRESENTED Ph.D.

YEAR THIS DEGREE GRANTED 1973

Permission is hereby granted to THE UNIVERSITY OF

ALBERTA LIBRARY to reproduce single copies of this

thesis and to lend or sell such copies for private,

scholarly or scientific research purposes only.

The author reserves other publication rights, and

notifies the thesis not extensive extracts from it may

be printed or otherwise reproduced without the author's

written permission



DATE December 7, 1973

THE UNIVERSITY OF ALBERTA

AN EXPERIMENTAL STUDY OF BED-FORM MECHANICS



BY

GESLOVAS K. JOWYS

A THESIS

SUBMITTED TO THE FACULTY OF GRADUATE STUDIES AND RESEARCH
IN PARTIAL FULFILMENT OF THE REQUIREMENTS FOR THE DEGREE OF
DOCTOR OF PHILOSOPHY

DEPARTMENT OF CIVIL ENGINEERING

EDMONTON, ALBERTA

SPRING, 1973

ABSTRACT

The mechanics of alluvial channel bed-forms were investigated experimentally. Instrumentation to measure flow velocity, pressure distribution and geometry of bed-forms was adapted or devised, and used in obtaining measurements above and within actively translating, light weight sediment bed-forms in a laboratory flume. Velocities were measured with the hydrogen bubble technique. Pressures were sensed at twelve different positions within a bed-form. A series of small diameter stainless steel wires, with a painted scale and installed vertically in the flume were used to measure the geometry and to trace the bed-forms during their passage through the instrumented area.

Preliminary investigations showed that distortion of bed-forms into three-dimensional configuration was caused by side wall effects which retarded the flow and transport of sediments. A manual technique was devised to prevent bed-form distortion and all observations were made with two-dimensional bed-form in the dune phase. Particle movement was in the pure bed-load mode. No suspended materials were

The stability of all bed-forms was analyzed statistically and only those bed-forms which remained constant in length, height, and depth of submergence were analyzed.

Flow shear was estimated from velocity profiles using rigid boundary techniques.

The results showed that the maximum pressure gradient on bed-forms was maximum at locations of maximum bed-form surface slope and, hence, at locations of maximum particle entrainment. The minimum pressure

gradient occurred slightly upstream of the crest and corresponded with the location of zero particle entrainment. From the reattachment point the boundary shear increased in the downstream direction reaching a maximum at approximately $1/4$ of the bed-form wavelength upstream of the crest and decreased to zero at the crest.

The relative contribution by mean boundary shear and mean pressure gradient to particle entrainment showed that the mean pressure gradients exert finite forces upon the stationary particles on the surface of bed-forms. The effects of dilation upon particle concentration and friction in the surface layer were identified as critical in the evaluation of relative contribution to entrainment by different hydrodynamic forces.

Velocity profiles over a section of upstream face of bed-forms were found to be logarithmic. High velocity flow cell and a zone of turbulence were found to extend to the free surface of the flow above the trough region of a bed-form.

ACKNOWLEDGEMENTS

The author wishes to express grateful appreciation to Professor Thomas Blench for his interest, encouragement, guidance and supervision during the investigation and the preparation of this dissertation. Grateful acknowledgement is also expressed to Professors A. W. Peterson and N. Rajaratnam for their valuable advice, suggestions and comments.

Special thanks are due to Mr. A. Charbonneau and his staff in the Hydraulics Laboratory of the University of Alberta for the technical assistance throughout the experimental phase of the investigation.

The investigation was carried out under the University of Alberta Dissertation Fellowship, for which the author is also most grateful.

Last but not least, the author wishes to express thanks to his wife for her encouragement, suggestions, patience and sympathetic understanding throughout the preparation of this work, and the typing of the manuscript.

TABLE OF CONTENTS

CHAPTER	PAGE
Title Page	i
Approval Sheet	ii
Abstract	iii
Acknowledgements	v
Table of Contents	vi
List of Tables	xi
List of Figures	xii
List of Symbols	xv
I. INTRODUCTION	1
Introductory Remarks	
Bed-Waves	
Purpose, Objectives, and Scope	
II. LITERATURE REVIEW	6
General	
Experimental Approaches	
Hydrodynamic Force Systems	
Introductory Remarks	
Boundary Shear Stresses	
Pressure Distribution Effects	
Turbulence Effects	
III. LABORATORY EQUIPMENT AND INSTRUMENTATION	15
Introduction	
Laboratory Equipment	

Flume

Flow System

Characteristics of Sediment

Description

Specific Gravity

Grain Size Analysis

Permeability and Porosity

Angles of Initial Yield and Repose

Experimental Instrumentation

General Considerations

Bed-Form Profile Measurement

Velocity Measurement

Pressure Measurement

Observation Area

IV. BED-FORM DEVELOPMENT EXPERIMENTS 44

Objectives and Methods

Natural Formation of Bed-Forms

Bed-Form Distortion Experiments

Introduction and Classification

Symmetrical Three-Dimensional Bed-Features

Bed-Form Distortion

Analysis of Observations

Bed-Form Control Technique

V. EXPERIMENTAL PROCEDURES 70

Outline

Flume and Sediment Bed Preparation

Levelling of Sediment Bed

Flume Filling Procedure	
Pre-Test Instrument Check and Flow Depth Adjustment	
Verification of Measurement Systems	
Water Level Control	
Bed-Form Development	
Observation and Data Acquisition Procedures	
Outline	
Depth-Wire Observations	
Velocity Observations	
Pressure Measurement	
Integrated Data Acquisition Procedures	
Data Reduction	
VI. EXPERIMENTAL RESULTS	90
Introduction	
Bed-Form Coordinate Systems and Nomenclature	
Flow-Boundary Stability	
Preliminary Observations	
Criteria for Bed-Form Stability	
Statistical Analysis of Bed-Form Equilibrium	
Bed-Form Profile Geometry	
Entrainment and Transport	
General Considerations	
Distribution and Rates of Entrainment	
Sediment Transport	
Hydrogen Bubble - Velocity Measurement Data	
Instantaneous Velocity Profiles	
Flow Discharge Comparison	

Dimensionless Velocity Profiles

Equal Mean Velocity Lines

Flow Turbulence Characteristics

Pressure Measurement

Pressure Data Evaluation

Pressure Distribution Characteristics

VII. ANALYSIS AND DISCUSSION 160

Outline

Analysis of Observations

Bed-Form Geometry

Velocity and Turbulence

Pressure Distribution

Force Requirements for Particle Detachment

Statics of Surface Particles

Concentration and Friction

Minimum Force Requirements for Detachment

Particle Entrainment Forces

Boundary Shear Stresses

Forces Due to Pressure Gradients

Relative Force Contribution

Results

Discussion

VIII. SUMMARY, CONCLUSIONS, AND RECOMMENDATIONS 205

Summary

Conclusions

Recommendations

CHAPTER	PAGE
BIBLIOGRAPHY	210
APPENDIX A: Bed-Material Test Procedures and Test Summaries	214
APPENDIX B: List of Equipment for Hydrogen Bubble Production, Control, and Photography. . .	218
APPENDIX C: Bed-Form Profile Data	220
APPENDIX D: Hydrogen Bubble Mean Dimensionless Velocity and Turbulence Data	224
APPENDIX E: Pressure Measurement Data	228
APPENDIX F: Sample of Raw Experimental Data	230

LIST OF TABLES

TABLE	PAGE
4.1 Observations of Bed-Form Position (x) and Height (h)	
Variation	52
6.1 Basic Bed-Form Geometry Data	98
A.1 Sediment Particle Specific Gravity	215
A.2 Sediment Particle Specific Gravity Distribution	215
A.3 Summary of Grain Size Distribution Tests	215
A.4 Permeability and Volume Concentration Data	216
C.1 Summary of Statistical Bed-Form Stability Test	
Results	221
C.2 Dimensionless Bed-Form Coordinate Data	222
D.1 Mean Dimensionless Velocity $\left(\frac{u}{U_m}\right)$ Profile Data	225
D.2 Mean Dimensionless Turbulence Intensity Data	226
D.3 Mean Dimensionless Velocity $\left(\frac{u}{U_s}\right)$ Profile Data	227
E.1 Dimensionless Mean Pressure Distribution	
$\bar{P} = \frac{P - P_r}{\gamma_c^2 / 2g}$	229

LIST OF FIGURES

FIGURE		PAGE
3.1	Schematic of the Flow System	17
3.2	Photograph of Sediment Particles	18
3.3	Histogram of Specific Gravity Distribution	20
3.4	Grain Size Analysis	21
3.5	Sediment Depth Wire and Hydrogen Bubble Wire Installation	28
3.6	Schematic of Hydrogen Bubble Apparatus	31
3.7	Hydrogen Bubble Electrical Equipment	33
3.8	Photograph of Pulsing Frequency Verification	33
3.9	Pressure Manifolds	38
3.10	Static Pressure Transducer Calibration	40
3.11	Layout of Probes	41
3.12	Photograph of Observation Area	42
4.1 (a) & (b)	Path of Particles	47
4.2	Bed-Form Development Processes	49
4.3	Photograph of Bed-Form Train	53
4.4	Photograph of Intermediate Stage Bed-Form Development	57
4.5	Schematic of Flow Structures	59
4.6	Photograph of Bed-Forms	68
5.1	Typical Hydrogen-Bubble Photograph	86
6.1	Bed-Form Coordinate Systems and Nomenclature	93
6.2 (a) to (g)	Dimensionless Bed-Form Profiles	101

FIGURE		PAGE
6.3	Average Dimensionless Bed-Form Profile	110
6.4	Particle Paths in Stationary Reference Frame	112
6.5	Particle Paths in Moving Reference Frame	112
6.6	Definition Diagram for Entrainment Rate	114
6.7 (a) & (b)	Typical Instantaneous Entrainment Rate Results	115
6.8	Definition Diagram for Entrainment Rate Calculation by Profile Translation Method	118
6.9 (a) to (q)	Particle Entrainment Rate and Transport Distribution	119
6.10	Comparison of Discharge Measurement	138
6.11	Hydrogen Bubble Velocity Profiles $-0.3 < \bar{X} < -0.2$	140
6.12	Mean Dimensionless Velocity Profiles $\left(\frac{u}{U_m}\right)$	142
6.13	Mean Dimensionless Semi-logarithmic Velocity Profiles $\left(\frac{u}{U_s}\right)$	143
6.14	Equal Velocity Lines, $\frac{\bar{L}}{H_r} = 10, \frac{d_{cl}}{H_r} = 2.5$	144
6.15	Illustration of Instantaneous Velocity Profiles, Test 28, Segment $-0.3 < \bar{X} < -0.2$	146
6.16	Distribution of Standard Deviation of Dimensionless Velocity $\frac{u}{U_m}$ Fluctuations	147
6.17	Equal Turbulence Intensity Lines, $\frac{\bar{L}}{H_r} = 10, \frac{d_{cl}}{H_r} = 2.5$	148
6.18	Example of Continuous Pressure Sampling Results	150
6.19	Example of Intermittent Pressure Sampling Results	152
6.20	Typical Pressure Distribution Band	154

FIGURE	PAGE
6.21 Dimensionless Pressure Distribution (a) to (h)	155
7.1 Histograms of Location of Maximum Bed-Form Surface Slope, Pressure Gradient, Pressure, and Minimum Pressure	168
7.2 Statics of Individual Surface Particles	170
7.3 Statics of Surface Particle Layer	170
7.4 Boundary Shear Distribution (a) to (h)	180
7.5 Distribution of Shear Stress due to Pressure Gradient (a) to (f)	187
7.6 Relative Stress Contribution $C = 0.601$, $\Psi'' = 29^\circ$. . (a) to (o)	189
7.7 Relative Contribution of Pressure Gradient Shear Stress with Frictionless Surface Layer Conditions	198
7.8 Comparison of Maximum $\frac{\tau_p}{F}$ v.s. Maximum Entrainment Rate	201

LIST OF SYMBOLS

a	distance from hydrogen bubble wire to a point in the row of hydrogen bubbles
b	regression coefficient
B	constant
C	volume concentration of particles
C'	constant
d	depth of flow
\bar{d}	mean depth of flow above a bed-form
\bar{d}_{c1}	mean depth of flow above crest 1
\bar{d}_{c2}	mean depth of flow above crest 2
D	diameter
D_{50}	characteristic diameter of sediment particle of which 50 per cent is finer by weight
p_m^F	minimum force required to disturb particle equilibrium
p_s^F	minimum force parallel to the local slope of the bed-form required to disturb particle equilibrium
F	force per unit area parallel to the local slope of the bed-form required to disturb the equilibrium of the surface layer of particles
g	gravitational acceleration
g_b	volumetric rate of bed-material entrainment per unit width of bed-form from segment $0.1\bar{L}$ long
G_{bs}	volumetric rate of sediment flux per unit width of flume at the downstream limit of a segment
G_{bc}	volumetric rate of sediment flux per unit width of flume at the crest of a bed-form

h_1	depth wire reading at time t_1
h_1^*	vertical coordinate of bed-form surface at segment limit
h_0	instantaneous vertical coordinate of the origin of the moving reference frame
h_s	instantaneous vertical coordinate of a point on the bed-form surface in the stationary reference frame
h_w	local hydraulic pressure gradient
H	dimensionless vertical coordinate of a point on the bed-form surface in the moving reference frame
\bar{H}	dimensionless vertical coordinate of a point on the mean bed-form profile
\bar{H}_1	mean height of bed-form 1
\bar{H}_2	mean height of bed-form 2
\bar{H}_r	mean reference height of a bed-form
H_s	vertical coordinate of a point on the bed-form surface in the moving reference frame
L	wavelength of bed-form
\bar{L}	mean wavelength of bed-form
m	number of coordinate points in a segment
n_s	number of data points in a segment
n_p	number of full pulse cycles between rows of hydrogen bubbles used in velocity calculations
p	mean observed pressure
p_{cl}	mean reference pressure at the origin of the moving reference frame
P	dimensionless pressure
q_m	mean discharge per one inch width of flume
r	radius of particle

r_s	scale of photograph
R	reaction force
s	specific gravity of particles
t	time
*T	temperature
T	period of one pulse cycle
u	flow velocity in the direction parallel to the free surface
u_*	friction velocity
U_m	mean instantaneous flow velocity
U_s	instantaneous surface flow velocity
\bar{U}_m	mean dimensionless flow velocity $\left(\frac{u}{U_m}\right)$ based on mean instantaneous velocity, all profiles
\bar{U}_s	mean dimensionless flow velocity $\left(\frac{u}{U_s}\right)$ based on instantaneous surface velocity, all profiles
\bar{U}_M	mean velocity based on flow discharge and average depth of flow above bed-form
\bar{V}_b	mean velocity of bed-form translation
\bar{V}_{c2}	mean velocity of flow above the crest of upstream bed-form
V_t	total volume occupied by solid particles and fluid
W	body force due to gravity on all particles contained in a volume one particle diameter deep and one unit in area
W_p	body force on a particle due to gravity
x_o	instantaneous horizontal coordinate of the origin of the moving reference frame
x_p	horizontal position coordinate of a pressure sensor in the stationary reference frame

x_s	instantaneous horizontal coordinate of a point on the bed-form surface in the stationary reference frame
x_v	horizontal coordinate of the hydrogen bubble velocity profile in the fixed reference frame
X	dimensionless horizontal coordinate of a point on the bed-form surface in the moving reference frame
\bar{X}	dimensionless horizontal coordinate of a point in the moving reference frame
\bar{X}_p	horizontal coordinate of pressure sensor in the moving reference frame
X_s	horizontal coordinate of a point on the bed-form surface in the moving reference frame
\bar{X}_v	horizontal dimensionless coordinate of velocity profile in the moving reference frame
y	vertical distance from the sediment bed-surface
Y	dimensionless distance above the bed surface $\frac{y}{d}$
$\alpha = \Psi + \Psi'$	
β	local bed-form surface slope angle to the horizontal
γ	specific weight of water
δ'	viscous sublayer thickness
κ	von Karman's constant
ν	kinematic viscosity
ρ	density of water
ρ	density of sediment particles
σ	standard deviation
τ	shear stress
τ	boundary shear stress due to fluid flow

τ_p	shear stress due to pressure gradient
ϕ_i	angle of initial yield
ϕ_r	angle of repose
Ψ'	angle defining surface particle support geometry
Ψ	surface friction angle between particles
Ψ''	friction angle between particle layers
Ω_g	gradation coefficient
Ω_u	uniformity coefficient

CHAPTER I

INTRODUCTION

1.1 Introductory Remarks

A channel is said to be alluvial if at some stage of flow its non-cohesive boundary materials are entrained, transported, and deposited by the flowing water. The hydraulics of such channels are very complicated because the resulting water-sediment complex constitutes a two phase system which self-adjusts the kinematic characteristics of the flow, establishes the geometry of the channel boundaries, and moves the sediments by different modes of transport. The ability to predict these naturally developed features of an alluvial system often determines the success or failure of a water resources project in terms of economical, environmental, and even sociological considerations.

For nearly one hundred years engineers and geologists have sought to understand the mechanisms of flow in alluvial channels, yet relatively little has been achieved in the analytical formulation of the phenomena. The progress toward a comprehensive solution of the alluvial flow problem, measured by the stage of development within the context of fluid mechanics research has been reviewed by Engel (1969). Using a "knowledge development" progress scale proposed by von Karman in 1934 Engel suggested that the scientific inquiry into this problem has progressed from the initial stage of empirical laws into the intermediate stage of knowledge development. Many variables controlling the phenomena have now been identified

by systematic analysis of the empirical information. Some qualitative and quantitative aspects of the interdependence of various variables have been identified and expressed in functional relationships among different sets of numerics (dimensionless parameters). Some of these relationships may now be used to predict practical flow behaviour within tolerable accuracy limits. In addition entrainment of particles, their transportation along the bed or in suspension, channel boundary stability (bed-wave and meander formation) and channel roughness have been identified and recognized as integral components of the overall problem. The limited progress toward the ultimate goal of establishing a comprehensive alluvial channel flow theory can be partially attributed to the failure on the part of researchers to explore and understand the basic physical features of the phenomenon. In the absence of this information many of the proposed theories have been based on assumptions which most often were incompatible with the natural state of flow. Hence such theories can only be regarded as approximate representations of the natural laws.

It appears, therefore, that the logical research direction toward the establishment of reliable theories for solution of problems of flow in alluvial channels should commence with a systematic experimental exploration of the physical mechanisms responsible for the entrainment, transport, and deposition of solid particles by the flow.

1.2 Bed-Waves

Perhaps the least understood aspect of alluvial flow phenomena concerns the generation and occurrence of trains of periodic bed-forms on the bed of alluvial channels which form from non-cohesive bed materials. The importance of bed-forms from a practical point of view has long been recognized because their presence or absence to a large degree determines

the roughness and hence the flow resistance in the channel. Furthermore, the bed-forms are related to the transportation of material along the bed.

Two general directions of approach, distinguished by the purpose for which the information was sought were employed in the study of bed-forms. Although concerned primarily with engineering design information, the empirical studies recognized at least six distinct bed-form configurations each associated with different conditions (regimes) of flow in the channel. This suggested that different types of bed-forms were generated and maintained by distinct dynamic flow systems and raised the possibility precluding the existence of an universal theory for all bed-forms (Blench, 1969).

The second group of studies, employing physical models, statistical-stochastic techniques or analytical models and aimed toward improvement of understanding of physical laws governing the bed-form processes have been far less successful in reaching their objectives. From the results of these complimentary studies, however, two conclusions were drawn and were used to evolve the present investigation: (1) improvement of understanding of bed-wave mechanics can be expected only from detailed analysis of kinematic and dynamic interaction between the fluid and bed-material in alluvial channels (Kennedy, 1969), and (2) systematic verification of physical facts by experiment should precede analytical formulation of theories (Rivlin, as reported by Davidson et al. 1969).

1.3 Purpose, Objectives, and Scope

The purpose of this study was to investigate experimentally the interaction between the flow and the non-cohesive bed-material particles in alluvial channels. It was intended to extend and improve the understanding of the physical mechanisms responsible for the orderly scour-

transportation-deposition of sedimentary materials in the presence of translating bed-forms.

The investigation was entirely experimental. Unlike in previously reported studies, actively moving alluvial bed-forms were employed for observation of various flow and boundary geometry parameters.

The main objective of this investigation was to verify the general hypothesis that entrainment of stationary bed particles from the surface of active bed-forms in alluvial channels was the result of a combination of hydrodynamic forces which are inherent in the equations of fluid motion. The specific objectives were (1) to develop reliable experimental instrumentation and methodology for studies of moving alluvial bed-forms in a laboratory flume, (2) to obtain experimental data and to establish the characteristics of various flow, sediment response, and bed-form geometry parameters, and (3) to evaluate and correlate the relative magnitudes of the spatial distribution of available forces for the entrainment of bed particles from the surface of bed-forms. Special attention was focused upon the effects of pressure variability upon the sediment particle entrainment by the flow.

A number of limitations were imposed upon the scope of investigation. Since the aims of the present investigation were of fundamental rather than practical significance, to facilitate the experimental inquiry and to simplify analysis, idealized (light weight, spherical shape) bed-material was used and only two-dimensional bed-forms in the tranquil flow regime were studied. Flow velocity measurement technique restricted transport of the sediment to the pure bed-load mode.

No attempt was made to utilize the experimental results for improvement of mathematical models of bed-form mechanisms. The investiga-

tion was intended to demonstrate physical facts about the fluid-sediment interaction phenomena and to establish a precedent for a new type of experimental approach as a guide for future studies.

CHAPTER II

LITERATURE REVIEW

2.1 General

The interest in sedimentary bed-forms can be traced to the last century when Darwin (1883) published the results of experiments of ripple formation in oscillatory flow. Since that time numerous other researchers approached and investigated the problem from different directions. Attempts have been made to explain the bed-form phenomena through classical mechanics concepts, water-sediment interface instability considerations, kinematic wave models, by dimensional analysis considerations and through statistical techniques. And, although considerable insight has been obtained from these studies, none of the above approaches has been entirely successful in explaining the bed-form phenomena.

According to Mercer (1971) three separate but interdependent factors must be considered in the analysis of the bed-form problem:

- (1) The flow of water above the bed-form.
- (2) The geometry of the bed-form.
- (3) The transportation of bed particles over the bed-form.

A bed-form model, therefore, must incorporate three separate relationships:

- (1) The transport of sediment and fluid flow over the bed-form.
- (2) The fluid flow and the geometry of the bed-form profile.
- (3) The transport of sediment and the geometry of the bed-form

profile.

Of the three relationships only the third, concerned with the continuity of sediment motion has been formulated exactly. However, in various analytical models, the other two relationships were based on various simplifying assumptions. As pointed out by Mercer (1971) in the development of the bed-load transport relationships a number of factors, such as pressure gradients, bed-slope and boundary layer developments, which may become important in bed-forms have generally been ignored. Similarly the analytical models generally employed simplified models to represent the flow over the bed-form shapes. For example, Exner (1925) considered a simple one-dimensional flow above the bed and assumed the local flow velocity to be inversely proportional to the local depth of flow. Both Anderson (1953) and Kennedy (1963) assumed potential flow.

Although the various analytical models are found to be highly instructive, they nevertheless have failed to explain satisfactorily the mechanics of bed-forms. The main reason for this failure can be attributed to the fact that the assumptions used in developing the relationships between the flow and the bed-form geometry, and between the flow and the transport of bed-load used in the models did not fully consider the dynamic and kinematic aspects of interaction between the fluid and sediments and were inconsistent with the actual conditions occurring in the two-phase systems.

A review of previously reported experimental investigations related to bed-form mechanics is presented in the subsequent sections.

2.2 Experimental Approaches

The majority of all experimental investigations concerned with

bed-forms and reported in literature have been oriented toward explaining the gross features of the phenomena, especially as it relates to the roughness characteristics of the channel. Only a very small number of investigators have concerned themselves with the flow and sediment response conditions within the macro-environment of individual bed-forms.

Furthermore, literature survey disclosed that, because the problem is very difficult experimentally, no attempts have ever been made to study the phenomena using active bed-forms. This has been recognized by Vanoni and Hwang (1967) who observed that experimental measurements are difficult to make under natural conditions when bed-forms translate and the presence of instruments may modify the sediment surface and bed-form patterns.

Because of these difficulties all previously reported investigations were carried out using stabilized bed-form shapes. The stable bed-form approach, however, only approximately represents the true conditions of flow above the bed-forms. Whether the bed-form shapes are constructed from solid materials or by spraying with adhesives, the natural bulk characteristics of the granular materials are no longer properly represented. In the absence of particle movement the observed velocity profiles, likewise, may not represent the true flow velocity conditions which exist in the presence with sediment transport. Nevertheless, these investigations have provided considerable insight into the flow characteristics which exist above individual bed-forms and offer the only experimental background for a highly complex problem in hydraulics.

2.3 Hydrodynamic Force Systems

2.3.1 Introductory Remarks

The occurrence of bed-forms in alluvial channels is dependent upon an orderly pattern of scour, transport, and deposition of sediment particles. Under equilibrium flow conditions, the flow induced forces which act upon the sediment and the response of the sediment particles to these forces are mutually compatible in that relative to the geometry of the bed-form a steady state of flow, sediment entrainment, transport, and deposition is observed in the mean above the bed-form.

Previous experimental results and general observations of particle entrainment, transport, and deposition above bed-forms have indicated that the forces responsible for the sediment responses vary spatially above the bed-form. Furthermore, there is evidence which suggests that these fluid forces may derive from different origins inherent in the equations of motion. Hence, boundary shear, pressure gradient induced seepage, and turbulence, as well as particle impact and gravity may all contribute to the detachment and transport of sediments.

2.3.2 Boundary Shear Stresses

Traditionally, boundary shear stresses have been considered as the main cause of particle entrainment. This, perhaps may be traced back to the work by Shields (1936), who successfully established incipient motion relation for flow over flat bed with shear as the main parameter. The Shields' criteria, however, although fundamentally sound in the particular context in which they were developed, do not represent the conditions existing above natural bed-forms.

Laursen et al. (1962) investigated flow of air over schematic

triangular shaped bed-forms placed symmetrically at top and bottom of a closed conduit. Boundary shear was evaluated by the Preston technique. The measurements showed that shear increased almost linearly downstream from zero at reattachment point and was maximum at the crest of the bed-forms.

Raudkivi (1963), in a classic paper to-date, measured velocity profiles and evaluated boundary shear due to flow over a bed-form shaped from galvanized sheet metal. His main conclusion was that entrainment and transport of grains were not unique functions of the temporal mean shear or mean velocity. The shear increased from zero at the reattachment point and was maximum at the crest. The critical shear stress for particle entrainment, based on Shields (1936) diagram, was found to be half-way up the upstream slope of the bed-form, which is considerably downstream from the position where actual entrainment of particles took place.

Khanna (1970) also investigated boundary shear of air flow over soft wood bed-form shapes. However, no flow separation occurred at the crest and shear was found to be finite in the downstream direction everywhere above the bed-form.

2.3.3 Pressure Distribution Effects

Pressure and pressure gradients have long been suspect as factors in the erosion and transportation phenomena. Blench (1969) has reported observations of piping failure of antidune slopes. Simons (1962) noted increase in total transport of sand in alluvial channels due to surface water waves. Posey (1963) suggested that when high and low pressure zones exist in the vicinity of bridge piers in porous bed-material the resulting seepage enhances the removal of the surface material.

Pressure distributions over the stabilized triangular bed-forms have been measured by Laursen et al. (1962) who found that a systematic difference existed between the pressure difference for different surface roughness.

The pressure measurements by Raudkivi (1963) established that the maximum pressure occurred at the point of the separation streamline reattachment on the upstream face of the bed-form. This was confirmed by Vanoni and Hwang (1967), and Rifai and Smith (1971).

The position of the minimum pressure intensity on the surface of the bed-forms has not been as well established. On the triangular bed-forms reported by Laursen et al. (1962) the minimum pressure appears to be at the crests of the bed-forms. The minimum pressure from Raudkivi's (1963) measurements occurred slightly upstream of the crests; however, Vanoni and Hwang (1967) and Khanna (1970) found that the minimum pressure was on the lee face of the bed-forms.

Generally, the pressure distribution curves established by measurements over the stabilized bed-forms downstream from the reattachment point were found to be concave downward to approximately half-way between the reattachment and crest positions. The position of pressure distribution curve inflection point, however, has not been specifically identified by any of the authors.

The contribution of pressure gradients established by the flow above granular material bed-forms have not been explored to-date. However, a theory was proposed by Luque (1967) which takes into account the seepage flow through the granular media and the forces which act on the grains near the bed surface. The guiding principle of this theory is the balance of momentum. It connects:

"the rate of change of momentum in the turbulent main flow with the transport of momentum across a turbulent boundary layer towards the bed surface and with the further transmission of stress through the solid and fluid components of the bed."

This theory recognizes that pressure gradient induced seepage may exert considerable drag forces upon the bed surface particles. It indicates that a bed of loose granular sediment is severely eroded at locations where the momentum of the surface flow strongly changes, and attributes ripple occurrence in sand bed channels to strong pressure gradients in the vicinity of stagnation points of standing vortices formed behind discontinuities of the bed surface.

It must be noted that this theory was questioned (Davidson et al. 1969) on the grounds that previously neither Rouse (1940) nor Laursen (1952) found any evidence to indicate that the seepage forces were significant. Yet, a review of these papers disclosed that pressures were not considered by these two investigators.

The effects of seepage force on bed particles comprising the top layer of a stream bed have been investigated experimentally by Martin (1971). These experiments were concerned with seepage normal to the bed and disclosed that seepage force on the top grains was approximately one-half that on grains several layers within the bed.

An extensive review of the effects of seepage into and out of the granular bed has been presented by Watters and Rao (1971). Their main conclusion was that seepage modifies the sublayer and velocity profile characteristics near the sediment bed.

Effluent seepage from the bed was found to decrease the drag upon the particles regardless of their position on the bed. It increased the lift upon a plane bed particle but decreased the lift if the particle

was above the general bed level.

The opposite result was found to hold for influent seepage into the bed.

2.3.4 Turbulence Effects

Turbulence has long been recognized as a potential contributor to the causes of sediment entrainment and transport. The qualitative aspects of turbulent flow upon the detachment of particles have been investigated by Sutherland (1967) who established entrainment hypothesis based upon the concept of turbulent eddies disrupting the viscous sub-layer and impinging directly onto the grain surface. The effects of dynamic turbulent pressure fluctuations upon the bed particles have been recognized also by Konratov et al. (1962).

Turbulence intensity measurements over stabilized bed-forms have been made first by Raudkivi (1966). The results have shown that maximum turbulence energy is reached in the vicinity of the reattachment point and decreases rapidly in magnitude toward the crest. The results presented by Khanna (1970), however, indicate that the highest longitudinal intensity of turbulence occurred in the trough region of the bed-form. These results, however, may have been influenced by the fact that flow did not separate at the crest.

Rifai and Smith (1971) observed turbulence characteristics and found that the macroscale of turbulence is related to the height of the bed-form elements.

More recently, Williams and Kemp (1971) established that close to flat beds the longitudinal velocity distributions had a high positive skewness caused by a number of instantaneous very high velocities.

However, to-date no technique for evaluating the forces upon

sediment particles due to turbulence fluctuations above bed-forms has been evolved for practical applications.

CHAPTER III

LABORATORY EQUIPMENT AND INSTRUMENTATION

3.1 Introduction

Because of the uniqueness of the experimental environment and the absence of a precedent for guidance in selecting apparatus for measurement of flow and bed geometry parameters, part of this investigation was concerned with the development and evaluation of instruments and techniques of measurement. Complete description of laboratory equipment, bed-material, and instrumentation systems are presented and discussed in this chapter.

The discussion related to instrumentation falls into three broad categories. First, the environmental characteristics relevant to the measurement of the various parameters are discussed. Alternative concepts are examined under the restrictions imposed by the test conditions. Next, under separate headings for each of the measured parameters, the respective probe-data acquisition systems are described. Finally, system evaluation study results, to show expected measurement accuracy and compatibility of each system with experimental environment are presented.

3.2 Laboratory Equipment

3.2.1 Flume

The experimental investigation was carried out in a rectangular flume which was located on a special platform 7 feet above the main laboratory floor in the Hydraulics Laboratory of the University of Alberta.

The flume was 119 feet long, 16 inches wide, and 16 inches deep. The sides and the bottom of the flume were of 3/8 inch thick plexiglass panels which were supported by continuous longitudinal two inch aluminum angles. The vertical joints between adjacent panels of the plexiglass walls were at 8 foot centers and were filled with carefully smoothed silicone sealant to eliminate surface roughnesses and make the flume watertight.

The headbox at the upstream end of the flume was 28 inches wide and 19 inches deep. A six inch radius transition at the sides and the bottom guided the flow from the headbox into the flume. At 3 feet from the downstream end, the flume was stepped down to a depth of 15 inches and a gradual transition was provided into a 4 inch diameter pipe.

The flume was supported above the floor by H-frames made of one inch diameter pipes. Lateral and longitudinal cross-bracing was provided by small diameter galvanized steel cables tensioned with turnbuckles.

3.2.2 Flow System

The flow system employed in this investigation was of the re-circulating type in which the discharged water-sediment mixture was pumped back into the headbox of the flume. A schematic of this system is shown in Figure 3.1.

Additional equipment used in the system included the following:

(1) Vertical-centrifugal, five inch diameter pump of the closed impeller type, driven by a constant (1150 rpm) speed, 7.5 horsepower electric motor.

(2) Four inch gate valve for the control of the flow.

(3) An electromagnetic flow meter (rated at 0.01519 millivolts per U.S. gallon per minute) with a recorder for volumetric discharge

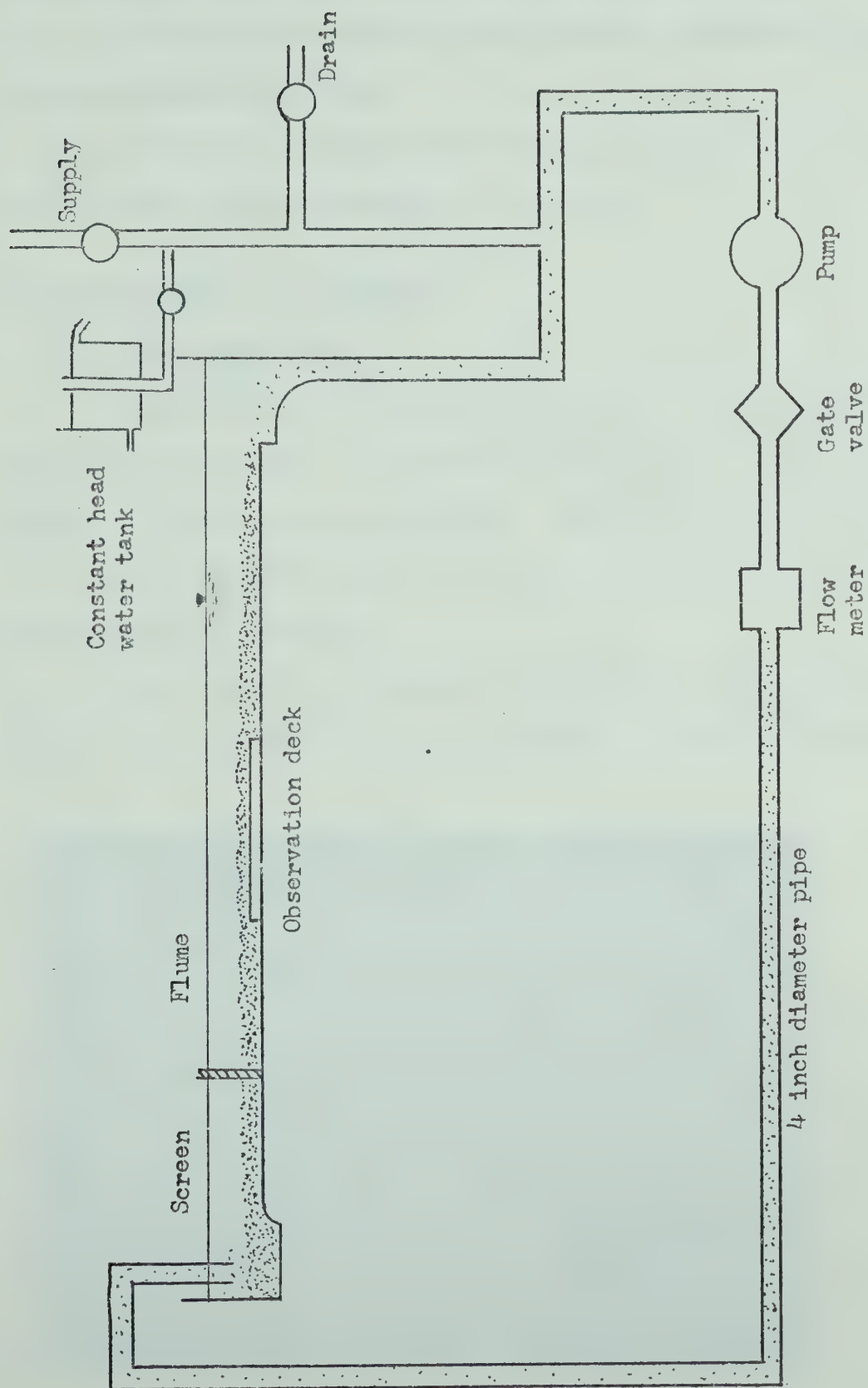


Figure 3.1. Schematic of the flow system

measurement to an accuracy of 0.01 cubic feet per second.

(4) Four inch polythene pipe to convey the flow-sediment mixture to the headbox of the flume.

(5) Plywood plate 24 inches long, 16 inches wide, to suppress surface waves at the upstream end of the flume.

3.3 Characteristics of Sediment

3.3.1 Description

Because this investigation was concerned with fundamental rather than practical aspects of the alluvial flow problem, idealized bed-material was used in the experiments. This simplified the interpretation of results, exaggerated some of the processes, and facilitated some of the experimental procedures.

White spherical polystyrene particles were chosen for the experiments. A macro-photograph of the particles is given in Figure 3.2.

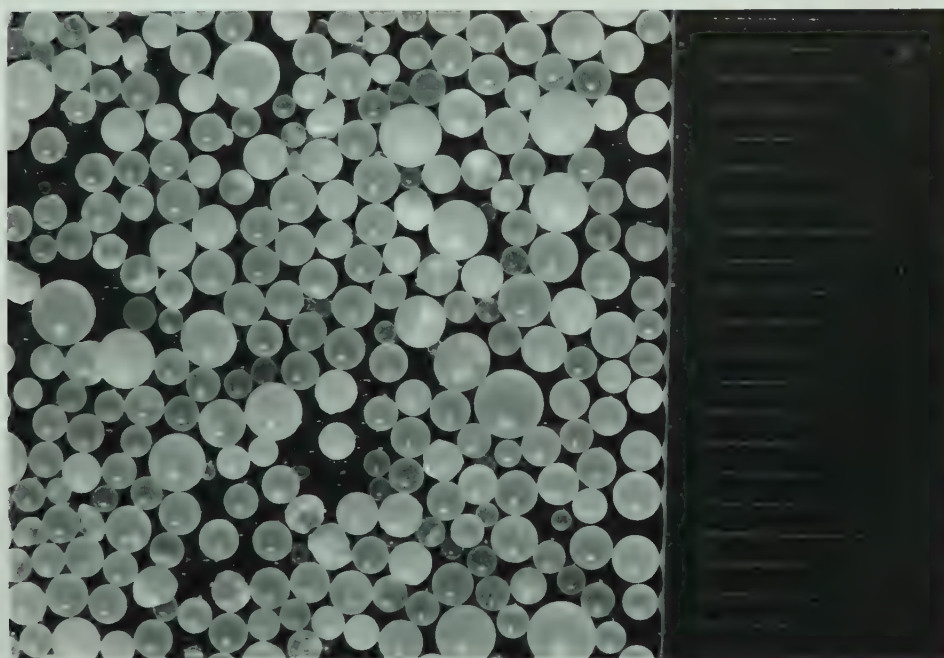


Figure 3.2. Photograph of Sediment Particles

The photograph was taken at the conclusion of the testing program, and the two non-spherical particles seen left of center on the photograph indicate that some grinding of the particles occurred during the movement of the sediment through the pump.

3.3.2 Specific Gravity

The average specific gravity of particles was found to be 1.041. It was determined by general procedures of the American Society for Testing of Materials standard ASTM D854-58 (1965) for soil particle specific gravity. However, it was necessary to reduce the specified particle drying temperature to 30 degrees Celsius because temperatures above 40 degrees Celsius caused discolouration of the polystyrene.

The results of tests to determine variations in the specific gravity of individual particles are summarized by the histogram shown in Figure 3.3. The procedures used to determine the distribution of specific gravities of the sediment and the results of four individual tests are given in Appendix A.

3.3.3 Grain Size Analysis

The grain size distribution of the sediment was determined in accordance with the American Society for Testing of Materials standard ASTM D422-63. The results are summarized in Figure 3.4. Approximately 97% of the particles range in size from one to two millimetres. The median particle diameter D_{50} (the size of sediment of which 50% is finer and 50% is larger by weight) is 1.4 millimetres.

The gradation coefficient

$$\Omega_g = \frac{1}{2} \left[\frac{D_{50}}{D_{16}} + \frac{D_{84}}{D_{50}} \right]$$

is found to be 1.26. The uniformity coefficient

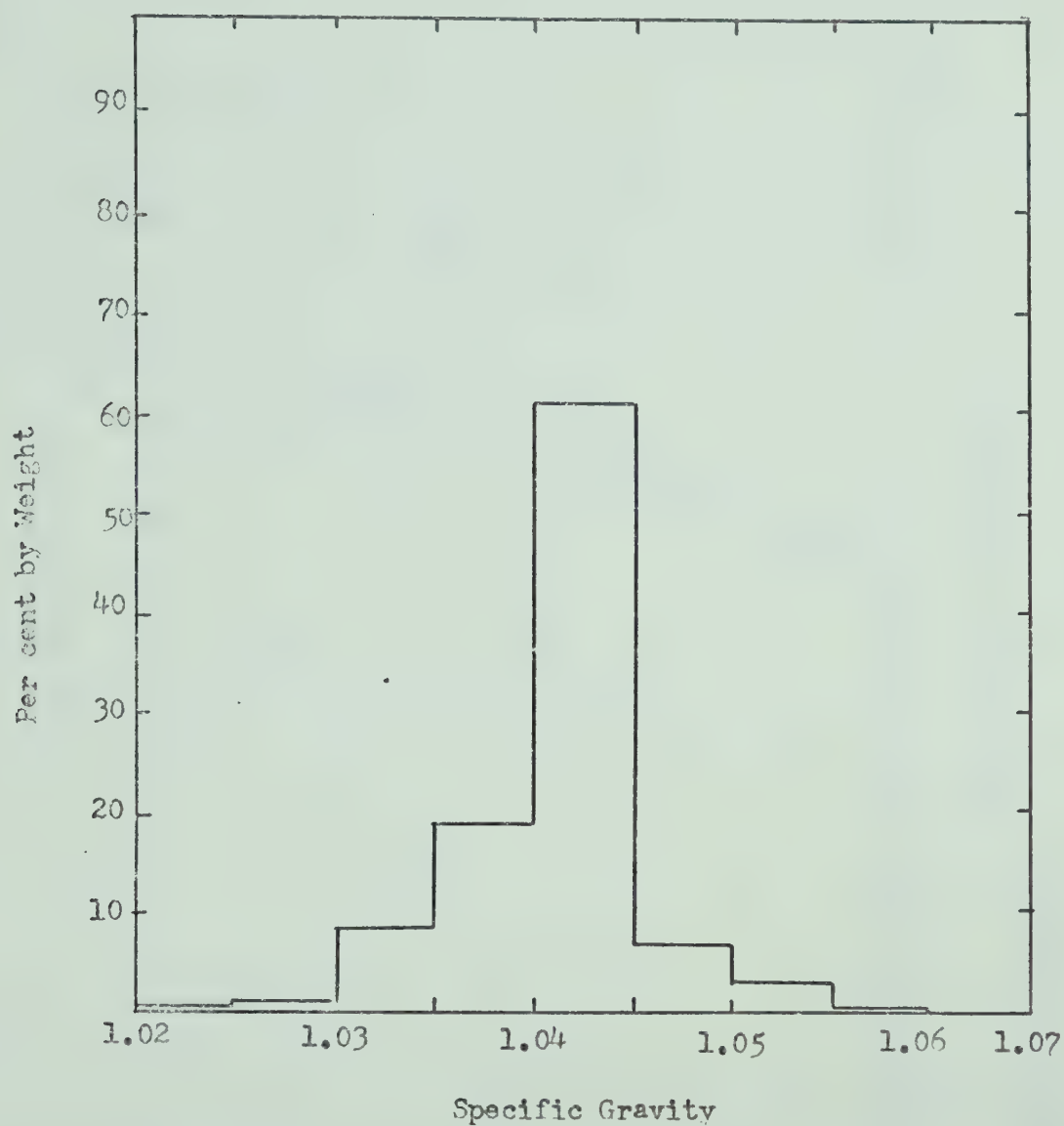


Figure 3.3. Histogram of Specific Gravity Distribution

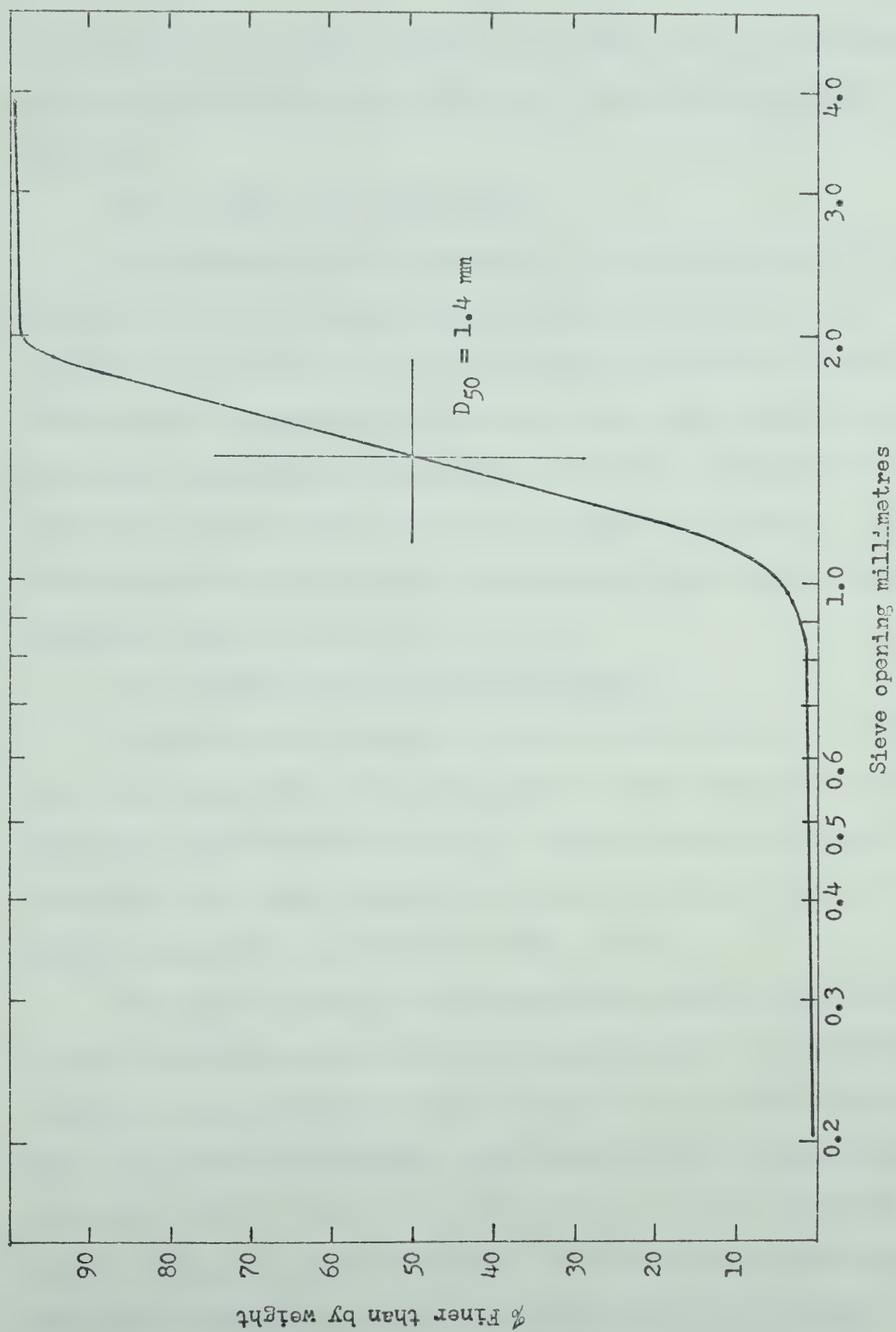


Figure 3.4. Grain size analysis

$$\Omega_u = \frac{D_{50}}{D_{16}}$$

was calculated to be 1.27. According to Junikis (1962), a uniformity coefficient of less than five represents a very uniform grain size distribution.

3.3.4 Permeability and Porosity

The permeability characteristics of the sediment material used in this study were determined using the equipment and procedures described in the American Society for Testing of Materials standard ASTM 2435-65T for permeability of granular soils under constant head. The average coefficient of permeability (at 20°C), determined from five separately prepared samples, was 0.121 centimetres per second. Simultaneously determined sample average porosity and volume concentration values were 0.402 and 0.598 respectively.

3.3.5 Angles of Initial Yield and Repose

A plane surface underlain by loose granular particles can be built up in the gravity field only up to a certain critical slope angle, called the angle of initial yield ϕ_i . When this angle is exceeded, avalanching takes place and the slope assumes a smaller angle ϕ_r commonly called the angle of repose (Allen, 1970a).

The angles ϕ_i and ϕ_r of the polystyrene particles in water used in this investigation were determined experimentally. A closed glass container, approximately one litre in volume, with opposite side walls plane and parallel to each other, was filled half-full with the granular particles. Water was added to the brim of the container which then was closed excluding all air from within. The container was turned on its side, and moved slightly to and fro to establish a flat interface between

the surface of particles and the water above. It was then tilted slowly from one end in one degree increments until a general movement of particles was observed. The angles of tilt of the original surface to the horizontal at the initial movement and the final accumulation of particles, ϕ_1 and ϕ_r respectively were recorded. From ten observations, the averages were found to be $\phi_1 = 31^\circ$ and $\phi_r = 26^\circ$.

It was found, however, that ϕ_1 was affected by the method of the surface particle deposition. If a surface of particles deposited at ϕ_r was tilted in the opposite direction, ϕ_1 was found to be 29 degrees.

3.4 Experimental Instrumentation

3.4.1 General Considerations

Three distinct aspects of the experimental environment pertinent to the development of instrumentation systems for measurement of flow and sediment bed parameters were identified:

- (1) Time dependent (unsteady) nature of the two-phase flow above bed-forms.
- (2) Sensitivity of the natural equilibrium between the flow and the granular bed-material.
- (3) Low absolute magnitudes of velocities and pressures near the sediment bed.

Under established equilibrium conditions a bed-wave retains a constant profile and a steady but varied mean structure of flow above. However, because the bed-wave and its associated flow structure translate, the entire water-sediment system becomes unsteady when viewed from a stationary frame of reference.

To determine experimentally the mean steady state flow characteristics associated with a translating equilibrium bed-wave, measurements

of the various flow parameters at a number of different locations in the flow system are required. To eliminate the unsteadiness factor, which affects the positioning of the sensor probe in relation to the bed-wave, two alternative approaches were considered. In principle, a system of sensor probes installed on an auxiliary vehicle traveling at the speed of the bed-wave would have served the purpose. However, this concept was found to be impractical because measurements were to be made within the mass of bed-wave particles. When a bed-form translates, only a small number of grains on its surface is in actual motion at any time. Movement of sensor probes through the stationary mass of granular particles would have disturbed the stability of boundary materials and consequently the equilibrium of the entire system.

To eliminate the unsteadiness effect all sensor probes were permanently installed in the flume. The instantaneous positions of the probes relative to the moving bed-wave were determined by observing the instantaneous horizontal positions of the bed-wave crest.

The major disadvantage of this method was that observation of a flow parameter could not be repeated at the same, relative to the bed-wave, position with the same sensor probe. On the other hand, a sensor probe with an analog output could provide an uninterrupted picture of the spatial changes of a measured parameter as long as its relative position in the moving reference system was continuously monitored.

It has long been recognized in instrumentation engineering that the introduction of a finite size sensor into a flow modifies the field of the parameter the sensor is to measure. As a result of this phenomena two consequences of direct interest in this investigation were identified; (1) the probe output may not represent the true value of

the measured parameter, and (2) the presence of the probe may destroy the natural equilibrium between the flow and the sediment boundary. The new equilibrium, compatible with the combined flow-sediment-probe interaction system may be totally different from the natural system under investigation.

In most fluid flow measurements, the flow field modification effects upon the sensor may, for practical purposes, be eliminated by calibration of the measurement device in a model environment known to represent the conditions in the prototype. However, because this study was concerned with measurements in an unknown environment, the modelling approach could not be employed.

In principle, at least three alternative approaches may be used to eliminate the flow field modification effects due to sensors on their output and on the boundary stability: (1) reduction of the physical size of the probe elements to zero in the limit, (2) matching of the physical properties of the probe elements to those of the medium in which the measurements are to be made, and (3) employing remote sensing techniques.

None of these alternatives is technically feasible at present. Remote sensing techniques must be perfected by further developments, matching of physical properties of sensor probes to those of the medium is impossible even in single phase flow environments, and sensor probes have not been reduced to zero size. Therefore, the compromise solution was to use sensor probes with minimum physical dimensions.

Simple preliminary tests were carried out to ascertain the maximum permissible size of measurement probes that would not disturb the natural water-sediment boundary equilibrium. In the anticipated range of average flow velocities from approximately 2.5 to 4.5 inches

per second, cylindrical shapes protruding vertically through the sediment boundary into the flow did not disturb the appearance of the sediment bed if the Reynolds number, based on the diameter of the cylinders and average flow velocities did not exceed approximately 350.

The need to measure small absolute values of velocity and pressure may not have been unique in these experiments. Nevertheless this requirement precluded the use of standard laboratory equipment (Pitot tubes and propeller meters) for the measurement of velocities. Similarly it restricted the choice of pressure measurement equipment to the most sensitive, low range commercially available units.

3.4.2 Bed-Wave Profile Measurement

To measure the geometry of the bed-waves, a series of nine 0.012 inch diameter stainless steel wires were employed. Alternate half-inch spaces along the length of each wire were painted red to provide a reference scale. The wires were installed vertically between the bottom of the flume and a support bar above. They were spaced at two or four inch intervals along the longitudinal centre line of the flume. Details of a depth-wire and its support are shown in Figure 3.5 (a). At the bottom the wires were held in position by a threaded brass plug screwed flush with the top of the plate. The wire passed through a hole at the centre of the plug. The wire was prevented from pulling out from the plug by a knot tied on its end.

At the top, each wire was attached to a small tension spring which was held in position by a hook installed on the underside of the supporting bar.

Because the scale divisions on the depth-wires were one half inch the accuracy of bed-wave profile measurement depended upon the observer's ability to interpolate the position of the bed level within

the one half inch division. The precision of the depth-wire technique was ascertained by observations of bed levels on residual bed-forms remaining in the measurement area after the generating flow was stopped. All other conditions such as lighting, observer's position, were maintained identical as in the subsequent experiments where the bed-form geometry was measured.

3.4.3 Velocity Measurement

In view of the considerations in Section 3.4.1 a relatively new method of velocity measurement--the hydrogen bubble technique--was selected for this investigation.

Detailed expositions of the hydrogen bubble techniques have been given by Clutter (1961), Schraub (1965), and Davis and Fox (1967). In the discussion that follows only those aspects of the technique which are pertinent to the present study in the sediment transport research area are considered.

The hydrogen bubble method is primarily a visual method which utilizes the electrolysis of water at a very fine wire to introduce hydrogen gas into the flow. The hydrogen bubbles produced at the wire are swept away by the flowing water and act as tracers which can be made visible by lighting and hence can be photographed. If the electrodes are subjected to pulsating applications of electrical energy, rows of hydrogen bubbles are produced. Since the frequency of pulsations can be controlled and measured, and the distances between adjacent rows of bubbles can be scaled from photographs the velocity at a point in the flow can be calculated by multiplying the true separation distance between two adjacent rows of bubbles by the frequency of pulsation.

The hydrogen bubble method possesses a number of advantages over

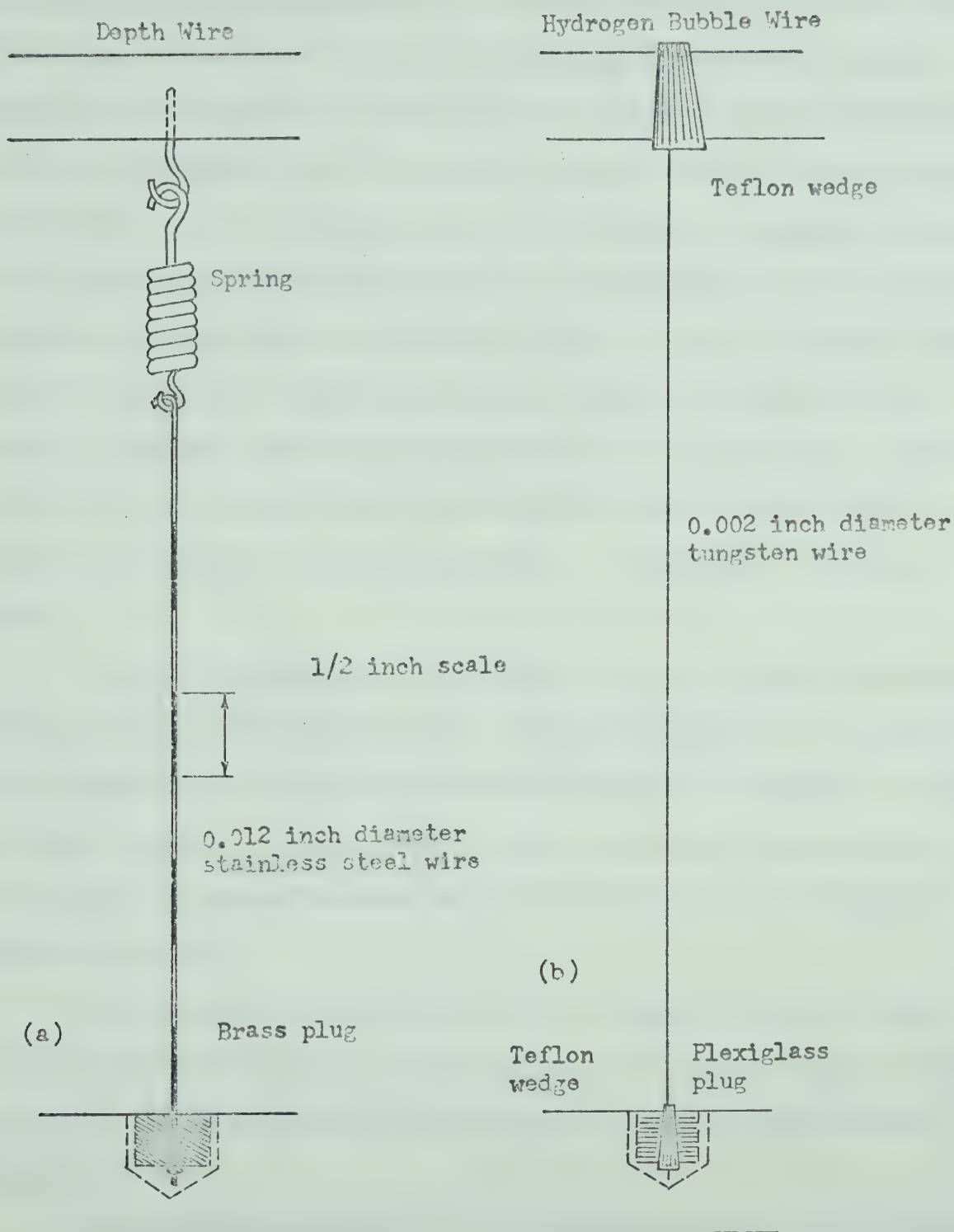


Figure 3.5. Sediment Depth Wire and Hydrogen Bubble Wire Installation

other conventional methods of velocity measurement. First, the electrode wire used to produce hydrogen has a very small diameter which has little effect upon the velocity field in its vicinity. The maximum Reynolds number of the tungsten wire used in these experiments was approximately 5. This was considerably below the Reynolds number values at which the wire wake effects upon the sediment bed become noticeable. Secondly, hydrogen bubble photographs provide information for a simultaneous and continuous measurement of velocity over the entire depth of flow--a condition that cannot be realized by conventional point velocity measurement methods. Third, it provides visual information about the flow structure. Fourth, it can be used to measure very low velocities, with the lower limit determined primarily by the bouyancy effects of the hydrogen bubbles in water.

A major disadvantage of the method is that it yields instantaneous rather than mean velocities of flow. Statistical means can be employed to obtain mean velocity values if sufficient number of instantaneous records are taken, however, the reduction of data is extremely time consuming. Furthermore, transverse movement of water from the plane of photograph cannot be detected.

The apparatus to produce and observe hydrogen bubbles in water consisted of the following: (1) electrodes, (2) electrical apparatus for energizing of the electrodes, (3) illumination, and (4) photographic equipment.

The negative electrodes, at which hydrogen bubbles were generated, were three separate 0.002 inch diameter tungsten wires. They were installed perpendicular to the direction of flow in the vertical plane of the longitudinal centreline of the flume, and were spaced at four inch intervals.

Each wire was held tautly in position by an arrangement shown in Figure 3.5 (b). A slightly tapered hole of small diameter was drilled through the centre of a $1/4$ inch diameter threaded plug. An end of a tungsten wire was passed through the hole and jammed against its side by a matching teflon wedge. The assembly then was screwed into a threaded hole in the bottom plate.

At the top, the wire passed through a slightly tapered $1/4$ inch diameter hole in a $2\frac{1}{2}$ inch wide plexiglass bar. It was tensioned by hand and held against the side of the hole by a matching conical teflon wedge.

A $3/32$ inch diameter aluminum welding rod was used as the positive electrode. It was supported from a plexiglass bar, spanning the sides of the flume, and was located approximately six inches and on the far side from the tungsten wires from the observation window. Depending upon the depth of flow the total submerged length of the anode ranged from 7 to 9 inches. To minimize the disturbance of the flow by the rod, its submerged end was bent into an L-shape and the end leg was positioned parallel to the flow.

The electrical system to produce hydrogen bubbles is shown in a schematic diagram in Figure 3.6. It consists of two groups of components, each serving a different function: (1) power supply for the production of electrolysis, and (2) control and switching equipment for application of the electrical power to the electrodes at preselected frequencies and pulse durations.

The negative terminal of the power supply unit was connected to the tungsten wires through a relay switch and the positive terminal directly to the aluminum anode with the d-c circuit completed through the water. The best results were obtained with a potential of 325 volts across its output terminals.

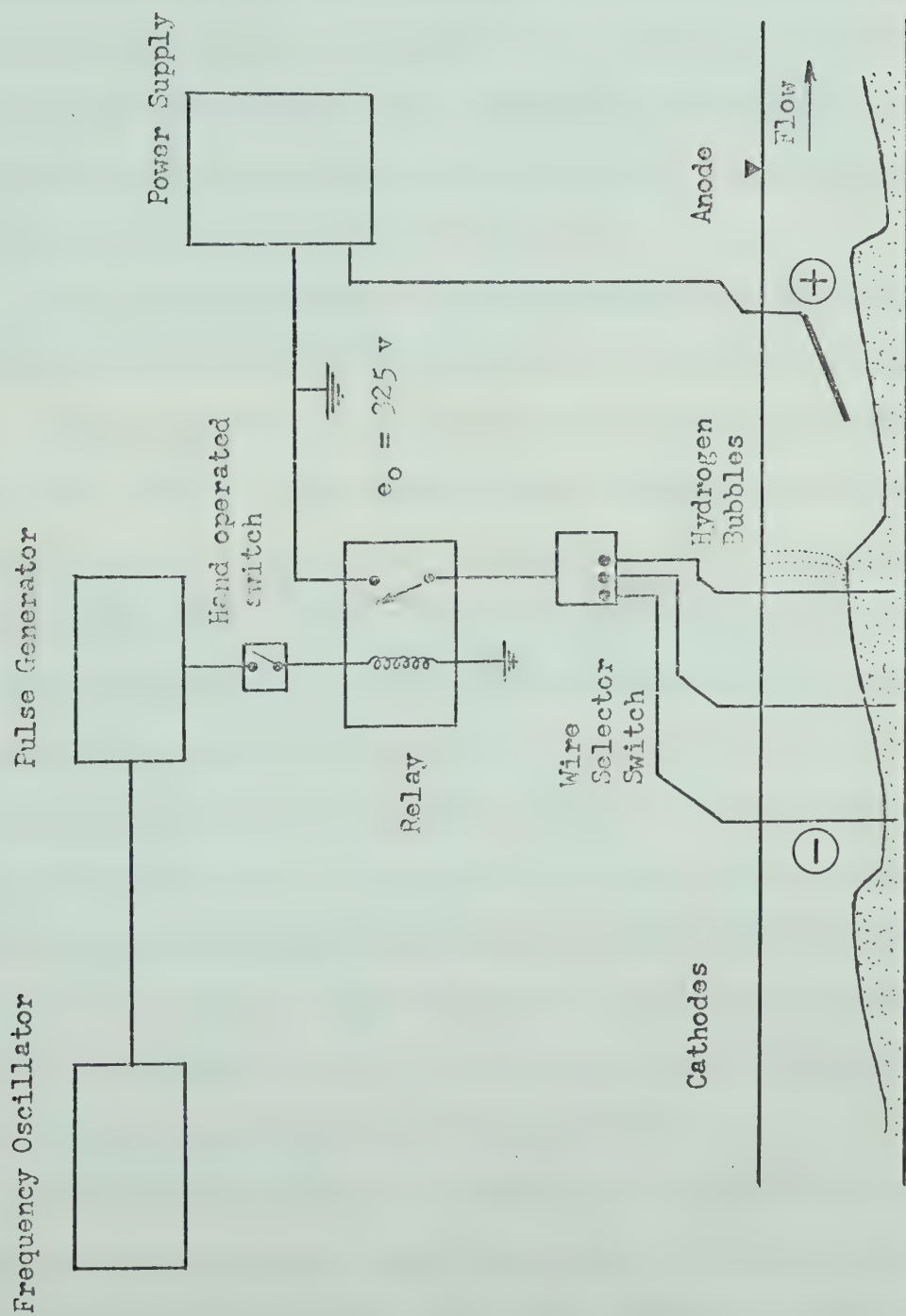


Figure 3.6. Schematic of Hydrogen Bubble Apparatus

The relay switch was activated by a square wave input from the pulse generator at frequencies that were regulated by an ultra-low frequency oscillator.

The operation of the system was controlled manually by a switch installed in the pulsing circuit between the relay and pulse generator. The electrolysis circuit was provided with a selector and polarity reversing switch which allowed any combination of the three tungsten wires to be switched into the circuit simultaneously. A photograph of the electrical equipment is given in Figure 3.7.

For visual observation and photography of the hydrogen bubbles adequate lighting and a dark background were found to be essential.

The illumination of the bubbles was provided by two 650 watt movie lights. The two light filaments were arranged end to end and attached face down to the top of a 12 inch long by 8 inch high by 8 inch wide plywood box. The interior of the box was painted with non-reflecting black paint. A metal partition was installed inside, 4 inches away from and parallel to the bottom of the box. To collimate the light 1/8 inch wide by 9 inches long slits were cut in the partition and the bottom plates of the box. The box was placed on a frame directly above the bar supporting the three tungsten wires and adjusted to direct the curtain of light from the slits through the plexiglass downward into the plane of the hydrogen bubbles. The curtain of light illuminated approximately one half inch wide strip of bed-material.

The hydrogen bubbles were photographed through the observation window with a 35 millimetre camera equipped with a macro-lens.

Throughout this experimental investigation a 10 cycle per second frequency was employed to pulse the wires. The pulse duration that was found to yield best results was approximately 10 milliseconds. To insure

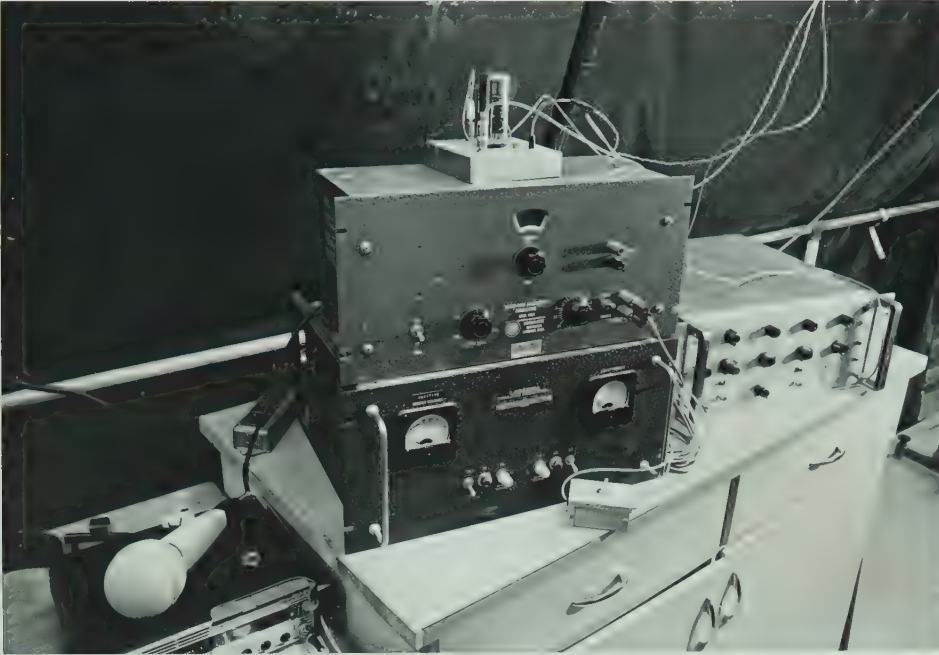


Figure 3.7. Hydrogen Bubble Electrical Equipment

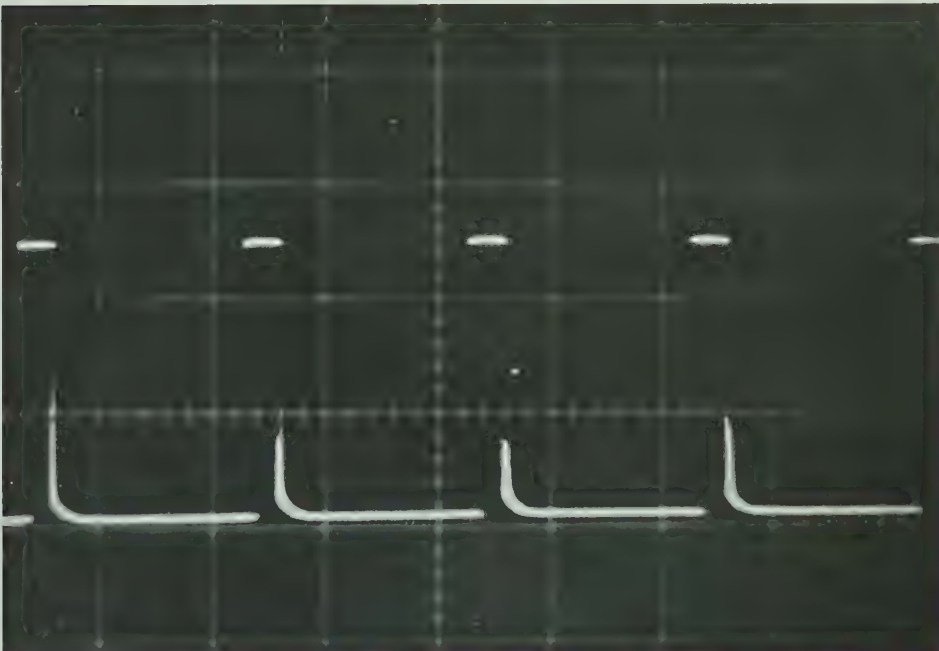


Figure 3.8. Photograph of Pulsing Frequency Verification

that the applied frequency was constant, pulsation frequency checks were made using an oscilloscope. A typical oscilloscope record of pulse duration, its shape and frequency is given in Figure 3.8. This procedure confirmed the ability of the electronic equipment to produce constant voltage pulses at equal time intervals and of equal durations.

The quality of hydrogen bubbles depended very much on the cleanliness of the tungsten wires. Before every experimental run all wires were cleaned using cotton swabs on 6 inch long wooden rods and wetted first in Legroine and then in acetone. Depending on the condition of the water in the flume, cleaning of the wires was often necessary also during test runs. It was found that the wires could be cleaned with the cotton swabs up to one half of an inch from the bed without disturbing the bed during a test run. Improvement in the quality of the bubbles could also be obtained by pulsing the electrodes for short periods of time under reversed polarity conditions.

Often, however, the quality of the bubbles produced by a wire varied for no apparent reason over short periods of time. Such behaviour was noted also by Schraub, et al. (1965) and has never been explained.

The life of the tungsten wires was exceptionally long. Only one set of 3 wires was used through the entire experimental program. It must be noted, however, that no continuous bubble production was ever attempted with these wires.

In the specific application of this technique to study sediment transport phenomena additional problems were encountered. Since the electrode wires were stretched vertically and passed through the full depth of sediment, hydrogen bubbles were produced along the length of the wire within the sediment and could be seen erupting upward along the wire.

To reduce partially the effect of the bubbles generated below the sediment surface upon the bubbles in the flow above the lower portions of each of the wires were coated with a thin layer of insulation. The eruption of the bubbles from below the sediment interface did not occur immediately after the first pulse but was delayed by the time necessary for the bubbles to rise into the flow zone. Generally four or five rows of bubbles could be pulsed and photographed before eruption effects became noted.

A major difficulty was experienced in obtaining satisfactory photographic images of the rows of hydrogen bubbles near the sediment boundary. It was caused by combination of slight bed-wave slope variations in the lateral direction and reflection of light from the white sediment material. On numerous photographs the near-boundary bubbles were photographed against a white background of reflected light and could not be identified in the photographs.

The accuracy of the hydrogen bubble method of velocity measurement has been investigated by Schraub, et al. (1965). Errors in velocity estimation were found to be caused by a number of factors, namely: (1) measurement of displacement between rows of bubbles, (2) averaging effects in changing velocity field, (3) displacement of bubbles out of the plane of the generating wires, (4) bubble response to fluctuations, (5) resolution problems due to finite bubble size and due to finite averaging intervals, (6) bubble rise velocity, and (7) velocity defect behind bubble-generating wire. According to the findings of these investigators, the total uncertainty interval (estimated confidence interval about the expected value of velocity at some specified odds) in estimating the true separation between two adjacent bubbles or bubble rows is controlled by the errors of measurement of the separation dis-

tance, by the averaging uncertainties inherent in evaluating Eulerian velocities by calculation of Lagrangian time-average velocities, and by the displacement of bubbles out of the plane of the generating wire. Other factors were found to introduce only minor uncertainties. In an example cited by Schraub, et al. (1965) an uncertainty of 6.2 per cent was estimated when the single frame method of data reduction was used and bubble displacement was measured 40 diameters downstream from the generating wire.

Although the same single frame method of data reduction was employed in the present experiments, only the relative variations of velocity were of interest. Hence, neither the averaging effects nor the displacement of the bubbles from the plane of the wire were considered to be of sufficient importance and a 5 per cent accuracy in the results of velocity measurements was considered obtainable in the present investigation.

3.4.4 Pressure Measurement

The pressure measurement system consisted of five components:

- (1) pressure sensor devices, (2) manifold, (3) reference pressure source, (4) two pressure transducers, and (5) recording apparatus.

The pressure sensors were made of 0.120 inch outside diameter (0.012 inch wall thickness) stainless steel tubes. To prevent sediment particles from entering and clogging the entire pressure measurement system a fine stainless steel screen (80 mesh) was placed over one end of the tube and was soldered to its outside wall. Five or six 0.75 millimetre holes were punched in the screen to provide adequate size pressure port openings. The other end of the stainless steel tubes was threaded to fit vertically into fittings previously installed in the bottom plate

of the flume. A total of twelve pressure sensing tubes ranging in height from $1/2$ to $3-3/4$ inches were installed in the flume and were connected to a twin manifold system with $1/8$ inch inside diameter flexible tubing.

The purpose of two manifolds was to permit sequential sampling of pressures at six sensor positions with a single pressure transducer. In addition to the six flume pressure source connections, each manifold was equipped also with connecting ports for a pressure transducer, differential reference pressure source, a calibration pressure source or system flushing reservoir, and an interconnecting line to the second manifold. To monitor pressure from any sensor probe, all redundant pressure lines to the manifold were clamped tight with simple laboratory clamps. The manifold assembly is illustrated in Figure 3.9.

A constant pressure source was provided by a free surface water reservoir located behind the flume and attached to the laboratory building wall. The cylindrical reservoir tank, six inches in diameter and eighteen inches high, had five taps each equipped with a valve and a fitting for flexible tubing through which the reference pressure could be imposed on the two transducers or upon the manifold. As initial observations showed that the expected maximum range of pressure variation under experimental conditions would not exceed 0.02 inches of water (differential pressure) variable reluctance differential pressure transducers (PACE Model P90D), rated at plus or minus one inch of water differential, were selected for pressure measurement. A variable reluctance transducer has a magnetically permeable stainless steel diaphragm and two pressure chambers--one on each side of the diaphragm. The diaphragm is clamped between two blocks and deflects when the applied pressures in the chambers are unequal. The deflection of the diaphragm changes the gap of the magnetic flux path on the system of core and coil assemblies

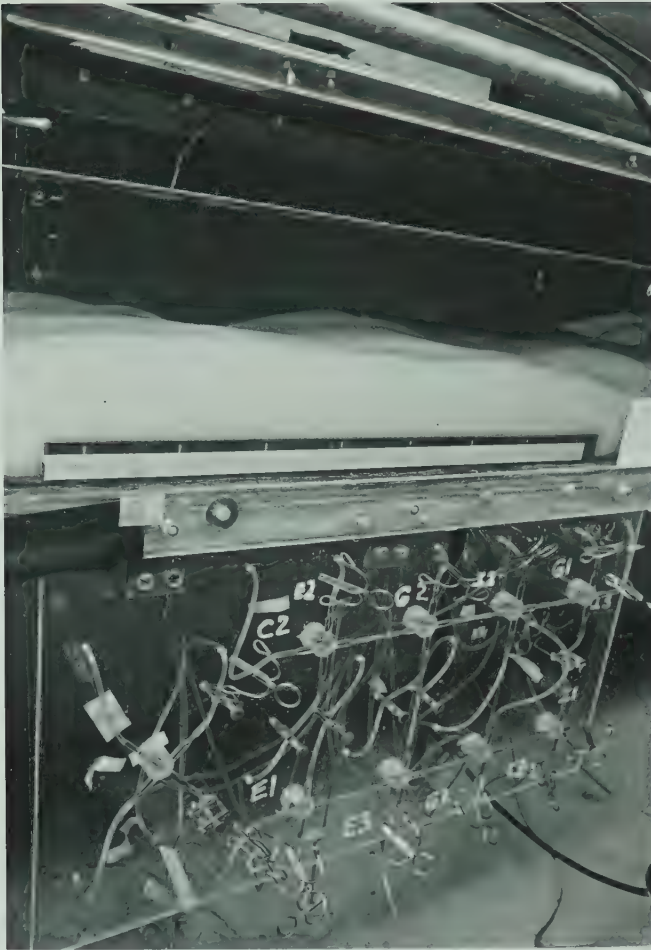


Figure 3.9. Pressure Manifolds

that are embedded in each block. The magnetic reluctance varies with the gap and produces changes in the inductance of the two coils. This change is converted through special circuits of a transducer indicator device into voltage representing pressure differences.

The time variation of the output voltage from the transducer indicators, which represent differential pressures, were recorded by two X-Y pen recorders on charts 10 by 15 inches in size.

Each of the two separate sensor-manifold-transducer-recorder systems was thoroughly evaluated to disclose any system anomalies during experiments which might have rendered the pressure measurements invalid.

As illustrated in Figure 3.10, under static calibration conditions the transducers exhibited completely linear transfer function with hardly a trace of hysteresis. Gage resolution was found to be limited only by the noise in the electrical systems. Using X-Y plotter pen displacement of one inch to represent 0.01 inches of water differential, static differential pressure measurements of 0.001 inches of water were consistently reproduced.

An investigation was carried out also to determine if the ability of a pressure sensor to sense pressures below the water-bed interface was affected by the sediment particles surrounding the pressure ports. The test was made by recording simultaneously the time variations in pressure due to an artificially induced surface wave in the flume and sensed by two probes located at the surface of the sediment bed and buried three inches below. In all tests, the pressure records from the two positions were found to be identical.

3.4.5 Observation Area

All instrument probes were installed in an observation area approximately 50 feet from the upstream end of the flume.

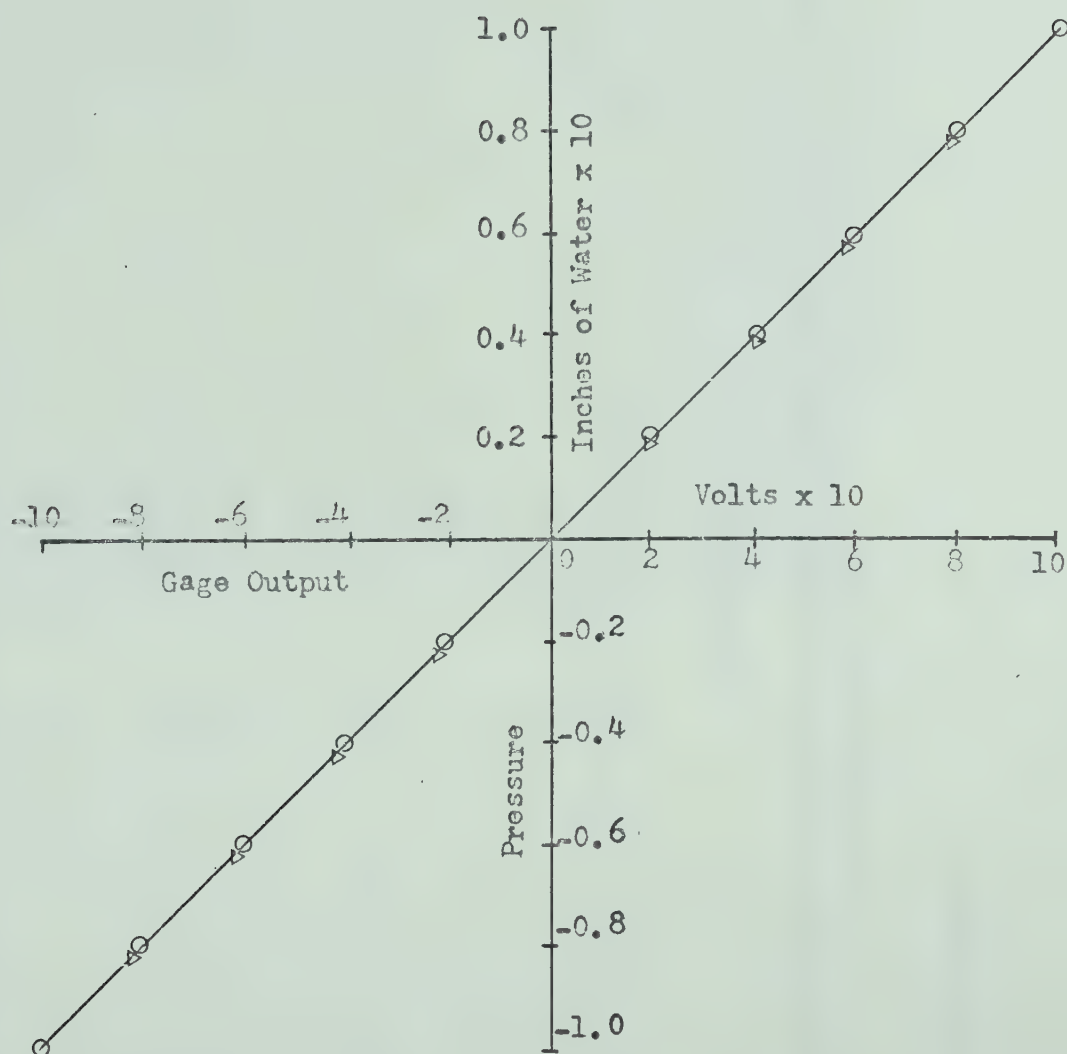


Figure 3.10. Static Pressure Transducer Calibration

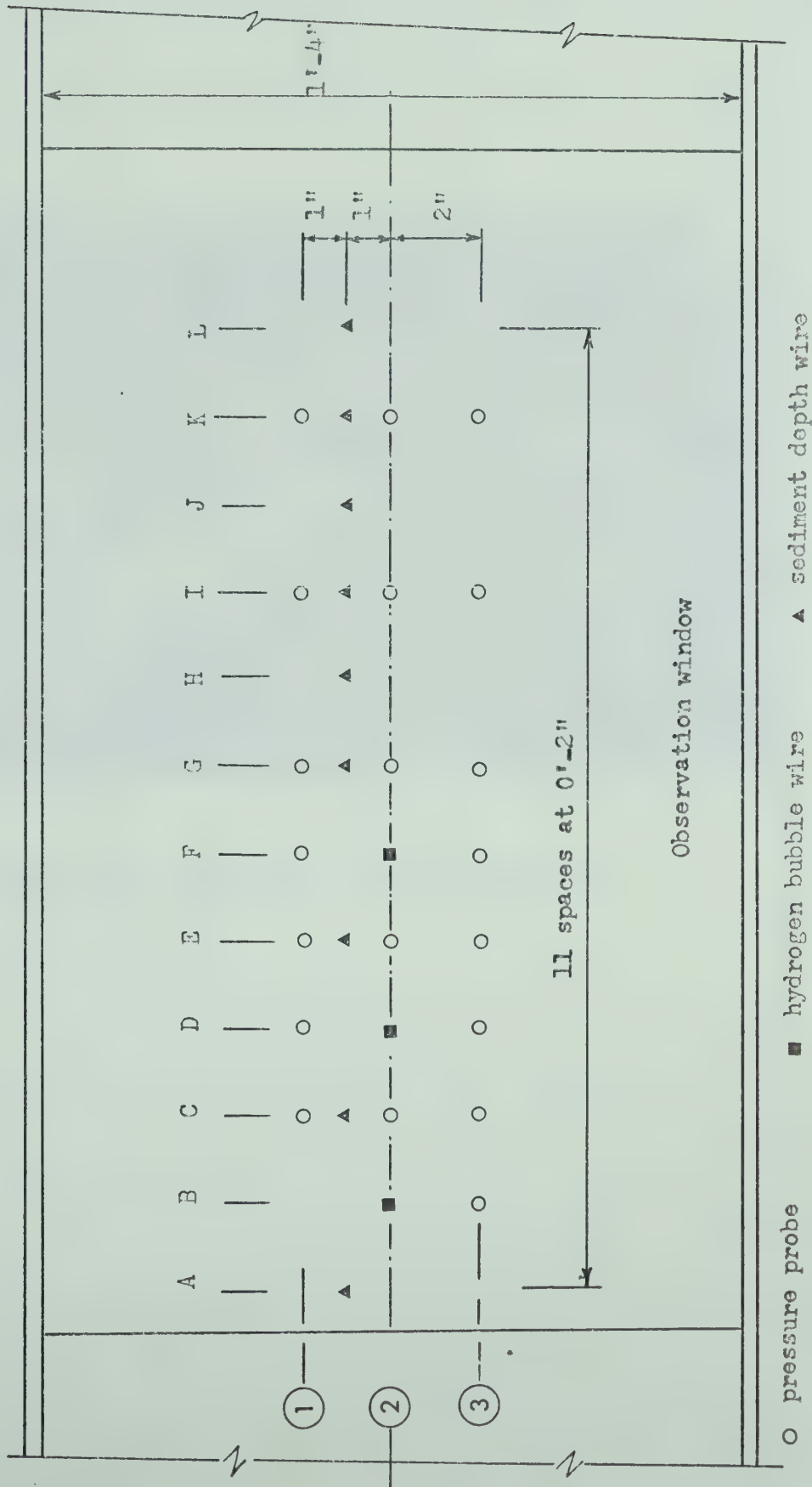


Figure 3.11. Layout of Probes

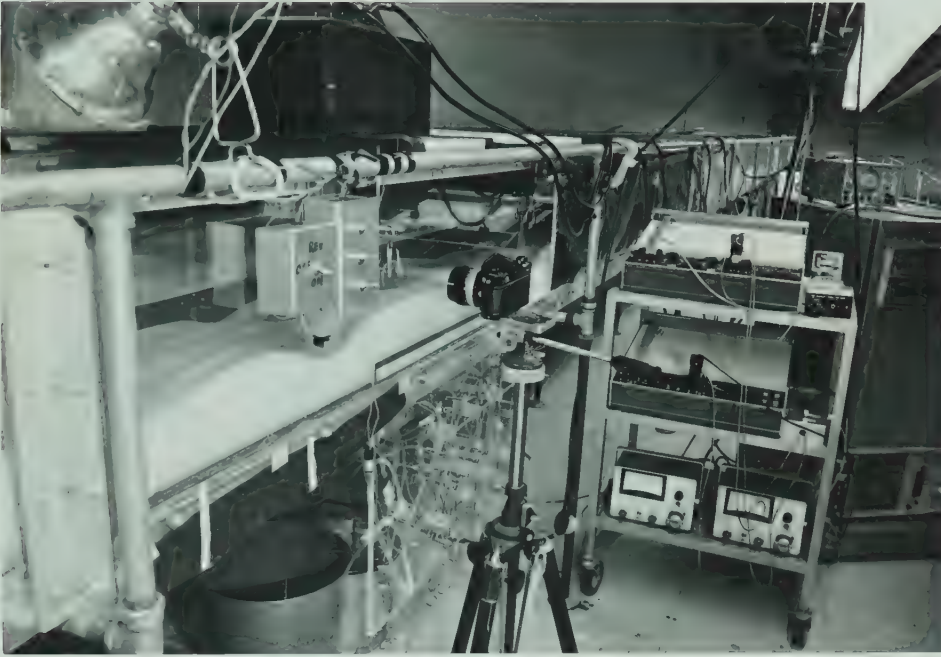


Figure 3.12. Photograph of Observation Area

To improve visual and photographic observations in the flume, a six feet long plexiglass section of the side of the flume was removed and replaced by $3/8$ inch thick glass plate.

All instrument probes were supported by a separate 27 inches long, 16 inches wide, and one half inch thick plate. It was reinforced by a one inch wide and one half inch thick frame, and was installed at the bottom of the flume leaving a space of one half inch between its underside and the flume floor plate.

A system of plexiglass bars was installed at the top of the flume to support depth and hydrogen bubble wires, and hydrogen bubble illumination lights.

The layout of all probes on the instrument plate is shown in Figure 3.11.

To facilitate photography of the hydrogen bubble all stray light and reflections were eliminated from the observation area. Except for a 4 feet long glass observation window, both sides of the flume were covered on the outside with non-reflecting black paper and a black curtain was installed behind the observer's position to eliminate reflection of the laboratory lights from the observation window glass.

The arrangement of equipment, and the working space at the observation window are shown in the photograph given in Figure 3.12.

CHAPTER IV

BED-FORM DEVELOPMENT EXPERIMENTS

4.1 Objectives and Methods

Perhaps the most critical part of this investigation was the development of two-dimensional naturally formed, equilibrium bed-forms for observations and measurements. The difficulties arose because the interaction processes between the flow, sediments, and the side walls of the flume naturally produced irregular, three-dimensional bed-features. Because of this a qualitative study of bed-form initiation, growth and subsequent distortion processes on a level sediment bed was carried out with the following two objectives: (1) to disclose in qualitative terms the basic causes for the appearance of irregular three-dimensional bed-features in the flume, and (2) to develop a method by which trains of two-dimensional bed-forms could be maintained in the flume for measurement purposes.

All observations of bed-form formation and distortion processes were made in the experimental flume. For each set of observations the bed was levelled flat and the flow was established in accordance with procedures described in sections 5.2 and 5.4. The experiments were carried out over a range of flow conditions. Initial (flat bed) average velocities of flow ranged from 2.0 to 3.5 inches per second, and the flow width to depth ratios varied from 4.6 to 14.0.

Observations of boundary geometry characteristics and of flow patterns at different stages of bed-form development were made mostly

visually. Injection of dye with a hypodermic needle was employed to trace the structures of flow above the bed.

Attempts to photograph and to video-record the various processes were only partially successful, primarily because attempts to photograph the initiation process of bed-form development failed. It was found that even extreme side-lighting angles of the bed failed to produce shadows for outlining low bed relief on white coloured sediment material.

4.2 Natural Formation of Bed-Forms

A sequence of three discernible physical processes was identified in the formation of bed-forms on a level bed: (1) initiation, (2) transverse elongation and downstream translation of crests, and (3) bed-form train formation.

After the particle threshold conditions were surpassed, a general but spatially discontinuous movement of groups or "patches" of closely spaced bed particles was observed. The "patches" varied in size from a few particles to several square inches in area, and appeared to be one particle diameter thick. Particles were entrained from seemingly random locations on the bed and were transported along the bed by rolling or sliding in steps of random lengths. On an initially horizontal sediment bed, the transport of particles in "patches" took place in the middle 80 to 85 per cent portion of the flume.

The natural triggering for the start of a bed-form on a flat bed originated from a sudden stoppage on the surface of the bed of one or more particles in the lead of a moving "patch". Repeated visual observations indicated that immediately prior to stopping, these particles broke contact with the bed, and lifted slightly above it. Particle deceleration appeared to commence at the instant their contact with the bed

was broken. Their path, as observed from the side and illustrated in Figure 4.1 (a) shows particle touchdown at a relatively steep angle to the horizontal. It was estimated that the distance between the positions of uplift and deposition was in the order from 5 to 10 particle diameters. No abnormalities on the stationary bed could be detected visually at locations of particle uplift or deposition. The formation of the first bed-form on the level bed commenced immediately after the triggering particles came to rest by a build-up of a single layer of particles above the mean bed. The downstream particles of the layer aligned themselves perpendicularly to the direction of the flow and formed a short length crest.

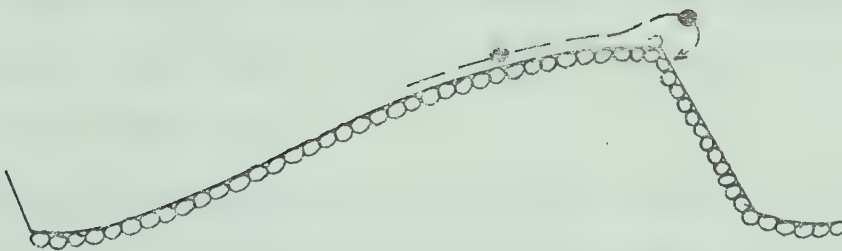
From the instant of initiation the bed-form started moving downstream and, simultaneously began elongating its crest toward both side walls of the flume. Both processes were the result of entrapment of all newly arriving particles from upstream at the crest. Particles deposited in the lee of the crest advanced the crest downstream. Particles trapped near the ends of the crest extended the length of the crest across the flume.

Particles, arriving at the existing crest, were observed to rise slightly and then come to rest in the lee of the crest. As illustrated in Figure 4.1 (b) the paths of particles contributing to crest elongation were observed to be similar to the paths taken by the initial triggering particles.

The supply of material for the initial development of a bed-form was provided from the same "patch" of particles which contributed the triggering particles. However, not all particles of this "patch" contributed to the bed-form development. Some were deposited upstream of the triggering particles, while others, if too distant in the transverse



(a)



(b)

Figure 4.1. Path of Particles

direction of the flume, moved past the triggering particles and were deposited on the bed downstream. This suggested that the momentum of individual particles in a "patch" was unequal, and that the entrainment zone across the flume extended only a limited distance beyond the ends of the crest.

All initially formed crests were straight and elongated toward both walls of the flume at velocities which were estimated to be at least one order of magnitude greater than the downstream velocities of migration of the bed-form.

The formation of a bed-form on a level bed triggered the development of a whole system or of a train of new bed-forms. After the triggering bed-form had developed a short length of crest, a new crest was observed to form at a distance from one to two inches downstream. After a short time delay a similar process was repeated again downstream of the new bed-form and so on until five or six bed-forms appeared on the level surface of the sediment bed.

The process of formation of individual bed-forms in a train differed from the process of formation of the initial crest by the source of sediment material supplied to each crest. The triggering crest was supplied by particles entrained from the level sediment bed from the general area upstream of the crest. In a train all bed-forms derived their material from within the area between two adjacent crests.

The processes of formation and growth of a typical bed-form in a train of bed-forms started with the development of the immediate upstream bed-form, which for convenience is henceforth referred to as bed-form A. These processes are illustrated schematically in Figure 4.2. Initially bed-form A consisted of a single layer of particles above the original level bed. The downstream particles of this layer were aligned

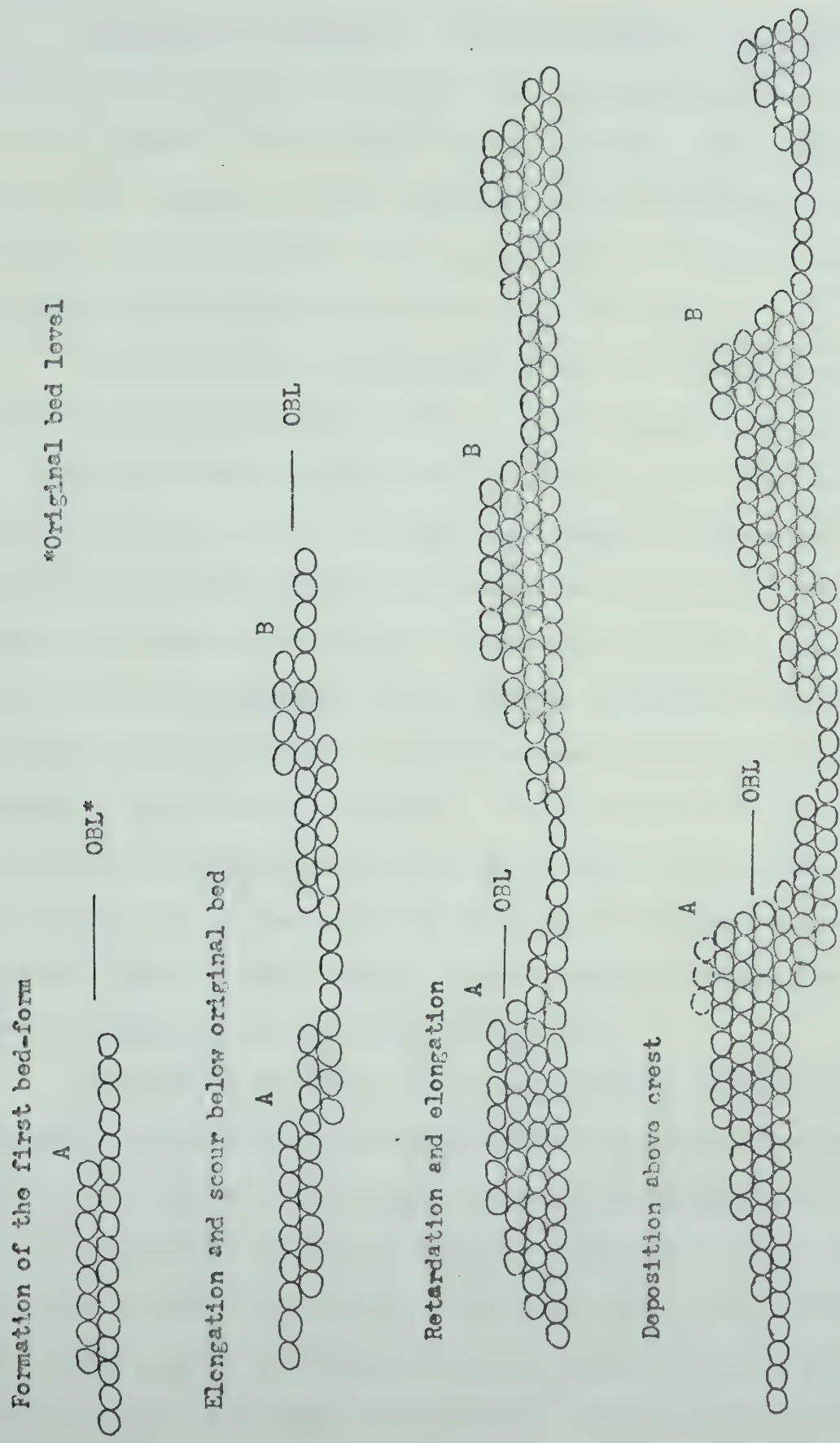


Figure 4.2. Bed-Form Development Processes

across the flume and formed the crest.

Immediately downstream of the crest on the original level bed a zone of quiescence was established from which particles were not entrained. However, further downstream, approximately $3/4$ inches from the crest, there appeared a zone of enhanced particle entrainment from which particles were scoured below the original mean bed elevation and supplied the material for the formation of bed-form B downstream.

The depth of scour of particles below the original mean bed level downstream of bed-form A appeared to be dependent upon two factors: (1) the local intensity of entrainment stresses, and (2) the period of time during which an area of the bed was exposed to entrainment stresses in excess of threshold stresses. Observations suggested that flow separation had occurred at the crest of bed-form A even when the crest was only one particle diameter high and that the intensity of entrainment stresses was increased in the vicinity of reattachment of the separation streamline on the back of bed-form B. The period of time during which a local area on the back of bed-form B was exposed to the enhanced entrainment stresses was controlled by the velocity of downstream migration of bed-form A which in turn depended upon the supply of material to its crest from upstream and the height of the crest.

Observations indicated that during the early stages of bed-form development sufficient momentum was imparted upon all entrained particles for them to reach the crest without intermediate deposition and rest. Since every particle arriving at a crest was trapped in its lee and advanced the crest a distance equal to its diameter, the velocity of a bed-form was maximum immediately after its formation when it was one particle diameter high and migrated on the surface of the original bed.

The time of exposure of an area to the enhanced entrainment stresses downstream of a crest was therefore minimum and the scour of bed-material from the reattachment area in the initial stages of bed-form development, appeared to be limited to a single layer of particles only.

As the bed-form A arrived into an area from which a layer of material had been scoured, its height instantaneously doubled. However, its velocity of migration downstream was reduced by half, because the supply of material to its crest was continuous and independent of the conditions at the crest. The increase in the height of bed-form A shifted the separation streamline reattachment position further downstream. The reduction of its velocity increased the time during which an area in the reattachment zone was exposed to the entrainment stresses. And although it was not possible to determine conclusively the effect of the sudden change in the height of the bed-wave upon the intensity of the entrainment stresses, the combined intensity-exposure effect appeared to enhance the initial scouring action. Additional layers of particles were entrained from below the original bed level and were transported in single steps to the crest of bed-form B. Immediately, the distance between the two adjacent crests started to increase because the velocity of the crest of bed-form B remained unchanged and was higher than the reduced velocity of bed-form A. However, the relatively high intensity of the initial scouring activity, which followed the increase of the height of bed-form A, diminished gradually as the process progressed. Newly entrained particles were not imparted with sufficient momentum to reach the crest of bed-form B in one step and were deposited on the back of the bed-form B. Because the reduction in the initial momentum imparted upon the particles and the increase in the distance between the position of entrainment and the crest of bed-form B were gradual, the deposition of the momentum-deficient

particles above the mean bed level commenced at the crest and progressed in the upstream direction. The growth in height of the bed-forms therefore was a result of scour and deposition of particles below and above the mean bed level respectively.

A train of partially developed bed-forms, photographed 85 minutes after the initiation of the first bed-form, is illustrated in Figure 4.3. Approximate distances (in inches) of individual bed-form crests in this train of bed-forms and their estimated heights (in inches), measured at 40 and 85 minutes after the initiation, are given in Table 4.1. The distances x were measured from the initial position of the first bed-form along the longitudinal centreline of the flume.

TABLE 4.1
OBSERVATIONS OF BED-FORM POSITION (x)
AND HEIGHT (h) VARIATION

Time Minutes	Position (x) or Height (h)	Bed-Waves					
		1	2	3	4	5	6
0	$x =$	*0.0					
	$h =$	*0.1					
40	$x =$	13.5	22.0	27.5	30.5	32.5	
	$h =$	0.7	0.5	0.3	0.15	0.1	
85	$x =$	17.5	32.5	43.5	50.5	55.0	58.0
	$h =$	0.75	0.55	0.3	0.2	0.15	0.1

*In inches

The above photograph and data illustrate the basic aspects of bed-form train formation. During the first 40 minutes after initiation four additional bed-forms developed in the flume. Although in time the heights and wave lengths of individual bed-forms increased, the rates of increase diminished. The velocities of migration of the bed-forms in the downstream



Figure 4.3. Photograph of Bed-Form Train

direction also decreased. The velocity of a bed-form was, however, always greater than the velocity of the adjacent bed-form upstream.

Although the mechanisms previously described relate to the initial stages of bed-form train development they are nevertheless characteristic throughout the entire bed-form train development process. The initial mechanisms, however, exaggerate some of the causes and effects and provide better insight into the entire process.

Considerations of the various processes show that the entire bed-form system tends to asymptotically approach an equilibrium of constant bed-form heights, wave-lengths, and velocity of migration. When a newly formed crest one particle diameter high doubles its height and reduces its velocity by half, entrainment stresses, their location and area exposure time are suddenly and drastically altered in relation to previous conditions downstream of the crest. However, when a bed-form is several particle layers high, and the change in the height is by one particle diameter only, the relative effects upon the particle entrainment parameters and, hence, upon the geometry of the downstream bed-form are much less severe.

4.3 Bed-Form Distortion Experiments

4.3.1 Introduction and Classification

The formation of irregular three-dimensional bed-features on an initially level sediment bed was observed to progress through three stages of development. Each stage was distinguished by a distinctive bed-geometry, namely: (1) two-dimensional bed-forms, (2) symmetrical three-dimensional bed-waves, and (3) irregular three-dimensional bed-features.

In the bed-form distortion experiments, the development of bed-

forms was induced artificially by the wire method described in Section 5.4. No discernible differences were noted between the development of bed-forms downstream from an artificially induced ripple and naturally triggered bed-forms. Up to seven two-dimensional bed-forms were observed to form downstream of the initiating ripple before the appearance of three-dimensional effects.

A simple investigation of flow above a two-dimensional train of bed-forms was carried out in conjunction with the distortion experiments. Coloured dye was injected into the flow at various locations above the bed. It was found that in a $1/4$ to $1/2$ inch wide zone adjacent to the side walls of the flume the flow was laminar. In the remainder of the flow, completely turbulent conditions were indicated by a rapid diffusion of dye into the flow.

4.3.2 Symmetrical Three-Dimensional Bed-Features

The intermediate stage of bed-form development was distinguished by three-dimensional bed features which were symmetrical about the centreline of the flume. Although generally, distortion of bed-forms may be caused by numerous other factors, in these experiments the distortion was caused by side-wall effects.

On a flat bed, the average flux of particles was uniform in the central, 80 to 85 per cent of the flume only, and reduced gradually to zero at the side walls. Because of the reduced particle supply near the walls, the central portion of a bed-form crest translated downstream at a velocity greater than its ends, the crest assumed a flattened U-shape and merged into the flat bed near the walls as its height gradually decreased to zero.

Downstream of a bed-form, entrainment of particles was always

enhanced along the separation streamline reattachment position. From the reattachment area immediately downstream of the curved portions of the crest, sediment particles were transported toward the walls and the centre of the flume and were deposited forming longitudinal ridges with depressions between them. Together with portions of the two adjacent crests, these ridges formed pairs of characteristic "bowl" features.

A typical intermediate stage bed geometry is illustrated in Figure 4.3. The flat bed width to depth ratio was 4.6, and the average velocity, computed from discharge meter reading, was 2.9 inches per second. The photograph, taken 85 minutes after the upstream bed-form was artificially initiated, illustrates symmetrical, three-dimensional bed-features. The crest of the first bed-form is straight and perpendicular to the flow in the central portion of the flume only. It curves backwards from approximately 4-1/2 inches from each wall. Two "bowl" features are seen on the back of the second bed-form and have affected the crest of the downstream ripple. The material, excavated from within the "bowls," and transported to the crest along the inner ridges, has locally advanced the crest and has produced protrusions on each side of the centreline downstream of the crest. The third and all subsequent bed-forms seen in the photograph, have also developed three-dimensional features. Their crests have been retarded near the walls and near the centreline of the flume and the pairs of inner longitudinal ridges, such as are seen on the back of the second bed-form, have joined together and have formed the high ground near the centre of the flume.

The photograph shown in Figure 4.4 illustrates bed-features when the initial width to mean depth ratio in the flume was 9.0 and the average flow velocity was approximately 3.2 inches per second. The "bowls" seen on the back of the second bed-form have been elongated, their inner



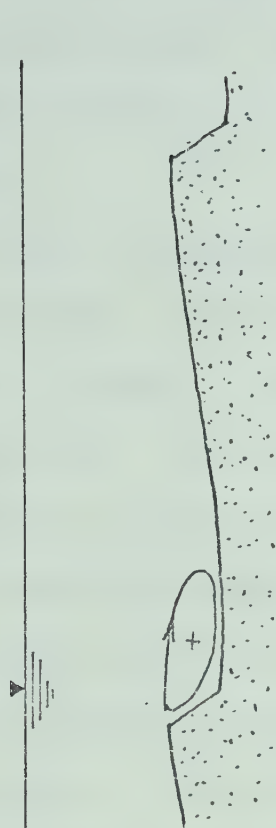
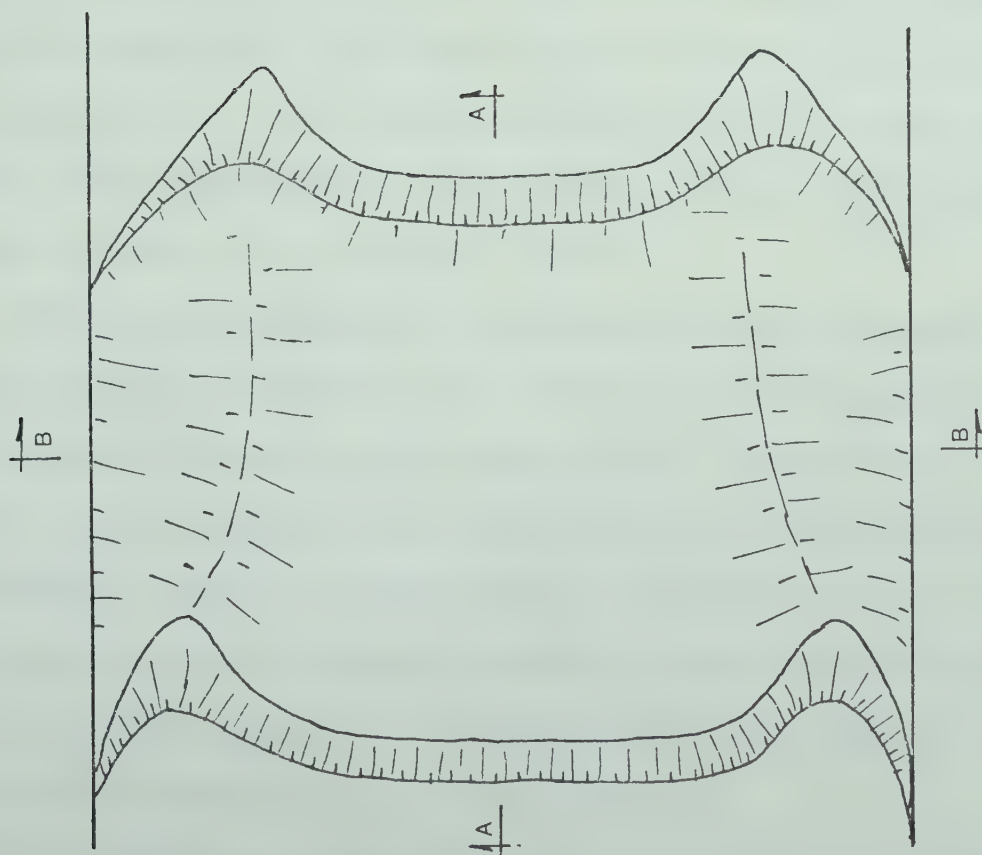
Figure 4.4. Photograph of Intermediate Stage Bed-Form Development

ridges have approached each other, and the crest line, while still symmetrical, has acquired reaches of substantial curvature.

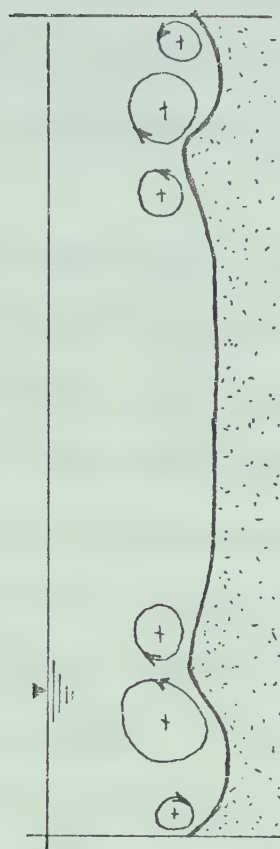
The structures of flow, associated with the intermediate stage of the bed-form distortion processes, were investigated by tracing the movement of dye injected at various locations above the bed, and by observing visually the movement of sediment particles along the bed. Some observations were recorded on video-tape for repeated viewing. The results of these observations are summarized in Figure 4.5.

Excluding the laminar flow conditions which existed near the side walls of the flume, it was found that two distinct zones characterized the flow in the intermediate distortion stage: (1) an upper zone, and (2) a lower zone. The flow in the upper zone was continuous over all bed-features, and was characterized by an absence of macro-scale flow structures. No permanent transverse velocity components in this zone could be identified. The flow in the lower zone was discontinuous and extended downstream from the crest to a position on the back of the downstream bed-form. It was bounded by the upper zone flow above and the sediment bed below. However, its primary distinguishing characteristics were the macro-scale flow structures--the rollers and the spiral flow cells.

The rollers were present in the lee of straight reaches of bed-form crests. Their presence was indicated by a small net displacement of sediment particles in the upstream direction toward the toes of bed-forms. Instantaneous diffusion of injected dye indicated that the intensity of turbulence in the roller was relatively very high. In the area downstream of the curved segment of a crest, close to the sediment bed and near the toe of the bed-form, a permanent drift of fluid toward the centre of the flume was indicated by dye injection. The velocity of



Section A-A



Section B-B

Figure 4.5. Schematic of Flow Structures

this flow was very slow and flow conditions were considerably below particle threshold value. The dye diffused into the main stream only after it moved over the line extending upstream from the inner longitudinal ridge.

The axes of the spiral flow cells were aligned in the general downstream direction. Whenever a pair of "bowl" features had developed on the back of a ripple, a total of six spiral cells, three of each "bowl", could be identified. Two of them occurred within the "bowl", and the third was found to exist outside and adjacent to the inner longitudinal ridge. The spiral cell located within a "bowl" and adjacent to the inner longitudinal ridge was found to be more intense than the other two and could be more easily demonstrated by dye injection. It was designated as the primary spiral. For an observer looking downstream, the directions of rotation of the primary spirals were counterclockwise for the left "bowl" and clockwise for the right "bowl". The direction of rotation of the two secondary cells, associated with each "bowl", were of opposite sense to those of its corresponding primary spirals. The vortex-like features of the flow dispersed gradually into the upper flow zone before reaching the crest of the downstream bed-form.

The general directions of fluid motion in the macro-scale structures strongly suggested that a continuous axis of rotation joins the rollers with the pairs of the spiral cells in the individual "bowls" or in the central portion of the flume downstream of the straight reaches of the crests. Attempts to demonstrate the continuity of the rotation axis, however, were not successful because of rapid diffusion of injected dye due to severe intensity of turbulence in the zones where the curvature of the axis of fluid rotation was most pronounced.

The longitudinal ridges on the bed were built up by particles

delivered by the transverse flow components near the bed. As time progressed, the height of these ridges, particularly the inner ones, increased and eventually appeared to reach a maximum. From that time, all particles delivered by the spiral flow components to the crests of the ridges were immediately swept downstream. The flux of particles was therefore more intense along the ridges, than in adjacent locations and affected the aerial geometry of the downstream bed-form by non-uniform deposition downstream of the crest.

4.3.3 Bed-Form Distortion

The onset of loss of symmetry in the boundary forms signified the appearance of the final stage processes responsible for distortion of the bed-features into random patterns.

The distortion processes usually originated in the vicinity of the third or fourth ripple in a train. Locally, their effects on the bed forms were almost instantaneous, and they progressed downstream affecting established bed-forms as well as the flat bed. The rate at which these effects propagated downstream and established irregular boundary forms on the bed was estimated to be at least one order of magnitude faster than the development of ripples in the initial and intermediate stages.

The triggering mechanisms, which initiated the distortion processes originated generally at locations where a slight asymmetry of boundary features had developed. These were most severe in the vicinity of closely spaced or joined inner ridges, or in the area downstream of large curvature of crests such as existed downstream of crest protrusions.

An investigation of flow structures above the distorted boundary was inconclusive. However, transverse flow velocity components were detected throughout the entire depth of flow, indicating that the two distinct depth zones of flow, associated with the intermediate stage, did not exist.

Visual observations of the movement of particles, suggested also that transport was not uniform across the flume. Some particles were entrained and moved on the backs of the bed waves. Other particles moved in higher concentrations along selected routes between the irregular three-dimensional bed-forms.

In addition to the distortion mechanisms described in previous paragraphs, symmetrical bed-forms were often disturbed by other causes. Typical of these were the V-shaped ripples appearing on the backs of existing bed-forms. They originated at slight depressions on the bed and developed two straight crests which in plan represented the spreading arms of a V. At high velocities of flow this type of disturbance often resulted in a division of the original bed-form into two or more separate bed-features.

4.3.4 Analysis of Observations

The main reasons for the distortion of bed-forms into irregular three-dimensional patterns were traced to the side wall effects upon the flow. When, under generally turbulent flow conditions, the particle threshold was reached throughout most of the bed, the flow boundary layer at the plexiglass walls was laminar and a transition from laminar to turbulent flow was established in a narrow zone adjacent to the wall. In this zone of transition at the bed level the rates of entrainment and of transport of particles per unit area or per unit width perpendicular to the mean flow reduced from a maximum at the fully turbulent edge to zero close to the wall. The variable rate of particle transport contributed to the non-uniform rate of crest movement downstream across the flume, and affected the vertical growth rates of the bed-form. As a result, the crest of a newly developed bed-form was straight and the bed-form was of a uniform height in the central portion of the flume only. Near both

walls, the crest line curved backwards and the height of the bed-form was reduced gradually to zero at or near the wall.

Because of flow separation all along the crest line, the separation streamlines defined a complex, three-dimensional surface in space. The mean intersection line of this surface with the sediment bed surface on the upstream slope of the adjacent bed-form in the central portion of the flume was perpendicular to the mean flow. Near the walls, however, downstream of the curved segments of the crest, the reattachment line was curved and induced flows with transverse components across the flume.

Although it could not be determined if secondary circulation had not been established in the flume prior to the formation of the first bed-form, the appearance of spiral flow cells was directly linked with the establishment of crestline curvature and the associated transverse flow components.

A local net movement of sediment in both directions from the general entrainment area at the reattachment line was produced by the near-boundary flow. From the curved segments of the reattachment line, one portion of the entrained particles was transported toward the nearest wall, and the other toward the middle of the flume. The ability of this flow to sustain particle transport, however, diminished rapidly from the entrainment area.

The initial deposition of particles near the walls appeared to be caused by the upward deflection of the near-boundary flow as it approached the wall. Particles came to rest because the flow could not sustain their movement vertically upward against the gravity. The reasons for the deposition of particles transported toward the centre of the flume are less clear. At least three causes, alone or in combination with each other, may have affected the transporting capacity of this transverse

flow. To maintain the continuity requirement, the near-boundary stream could have been deflected upward by the influence of its counterpart approaching from the opposite side of the flume. It could also have been retarded by the development of an interface with the flow downstream of the straight portion of the crest or by boundary friction.

The development of secondary spiral flow cells and the longitudinal bed-features appeared to be interrelated in a reciprocal fashion. Although the presence of the spiral cells was demonstrated only above bed-features of considerable size, the continuous development of the longitudinal ridges from the outset when curvature of the crest was very large suggested that the secondary cells were also established at that time.

As time progressed, the bed-forms increased in size and the secondary spiral cells increased in diameter. More particles were entrained by the enhanced erosive action along the reattachment lines and were moved toward the ridges by the transverse flow components inherent in the spiral cells. In addition, previously deposited particles were eroded from the sides of the inner longitudinal ridges and the ridges were slowly displaced toward the middle of the flume.

The rotating flow of the primary spiral cell separated from the boundary as it approached the crest of the inner ridge and a counter circulation of lesser intensity (the secondary spiral cell) was developed on the opposite side. The direction of rotation of the fluid suggested a U-shaped vortex tube made up of the secondary spiral at the two inner ridges and the roller in the lee of the straight portion of the crest. An attempt to establish continuity of the axis of this vortex was, however, unsuccessful because of the low intensity of fluid rotation in the roller

and the high intensity of turbulence at the expected junction locations of the roller and the spirals.

During the transitional period of bed-wave development, characterized by the symmetrical pattern of bed-features, the longitudinal extent of the primary and secondary spiral cells appeared to be controlled by the upper flow. Judging from the direction of particle motion in the primary spiral cell area, the near-boundary flow components were nearly perpendicular to the longitudinal axis of the flume near the point of the origin of the spiral and nearly parallel to the axis of the flume where the spiral motion merged with the upper zone flow. The rotating fluid therefore appeared to have been accelerated by shear at its upper boundary and was diffused into the upper zone flow before reaching the crest of the bed-form. The rotational motion features of the secondary spiral cells were similarly affected.

Although the direction of motion of particles approaching the crest of a bed-form was generally downstream across the full width of the flume, zones of particle transport concentration were nevertheless established on the backs of bed-forms with symmetrical bed-features. The zone of maximum concentration occurred along the inner ridges. Particles entrained in areas where transverse boundary currents were present were first delivered to the longitudinal ridges and only then were transported downstream.

The variation of concentration of moving bed particles across the flume affected the crest line of the bed-form at which all particles were deposited. The high concentrations of particles transported along the inner ridges, locally increased the rate of the crest movement downstream. The crest line acquired segments of additional curvature and the separation

streamlines produced a separation surface of even higher complexity.

From the observations it was concluded that during the transitional period a semi-equilibrium state existed between the mutually compatible system of symmetrical bed-features and the secondary flow structures above. Both, the bed-features and the secondary flow cells, retained their individual identities in the total system from the outset of their formation, but continued to increase in physical size and became more sensitive to small disturbances as the processes progressed. The spatial extent and influence of the secondary flow cells was restricted to individual bed-forms and appeared to be governed by the flow above.

The disruption of the symmetrical bed-features and the subsequent development of irregular bed-wave patterns was initiated naturally by small disturbances of the symmetrical geometry of the bed or of the secondary flow structures.

Typical disturbances were generated downstream of a bed-form crest which was subject to locally accelerated rates of particle deposition. Because of the modified crest line curvature, the separation surface intersection with the bed produced local transverse currents that presumably were not compatible with the existing system of secondary flow cells. A different type of disturbance was generated when a pair of inner ridges on the back of a bed-wave approached each other and the associated secondary spiral cells merged together. In all cases the restructuring of the flow produced immediate effects on the bed downstream, disturbing the symmetrical bed-features into irregular shapes.

The observations of the sequence of the events, from the initiation of bed-forms to their subsequent distortion, suggested that the different stages of their development characterized by the symmetrical

and irregular features represented two distinct visible phases (Blench, 1969) of bed-forms that generally corresponded to the ripples and dunes as described by Simons and Richardson (1966). The imposed flow, in all cases, led to the development of dunes. The intermediate stage of symmetrical bed-forms represented a transitional state tending toward an equilibrium in the duned range. The distinguishing characteristics between the two phases, based entirely on simple visual observations may be summarized as follows:

(1) Ripples are associated with small bed-wave heights and small scale secondary flow cells that are bounded by a continuous upper flow zone that extends in both directions, perpendicular and parallel to the flow across the flume. The effects of the secondary flow cells are not transferred across individual bed-wave boundaries, but through shear are dispersed into the upper flow before reaching the crest of the bounding bed-wave.

(2) Dunes are associated with larger bed-form heights, and at least some of the secondary flow cells extend not only the full depth of flow, but extend over a number of adjacent dunes in the direction of flow. The continuous secondary cells tend to oscillate from side to side in the flume, isolating local zones of flow separation from crest of three-dimensional bed-waves. And, sediment transport takes place not only on the backs of the dunes, but along continuous routes of the secondary cells.

4.4 Bed-Form Control Technique

From the findings described in the previous section it was concluded that the distortion of sediment bed-features into three-dimensional shapes was caused by the local retardation of the flow near the side walls of the flume. Local retardation of flow reduced transport of particles

and produced bed-form crest curvature and cells of secondary flow whose stability eventually determined the stability of the total system.

The development of irregular three-dimensional bed-forms was successfully eliminated by preventing the development of excessive crest curvatures near the walls of the flume. A manual technique was employed to maintain a straight crest across the flume. Whenever the central portion of a bed-form had advanced a distance of approximately one inch ahead of the crest at the walls, a 1/16 inch diameter wire was inserted vertically into the sediment, approximately one inch deep, one inch upstream of the crest, and 1/4 inch from the wall. It was then moved slowly downstream dragging adjacent sediment particles forward until a straight crest line was restored. For best results the speed of the wire had to be relatively uniform and slow. The resulting bed-forms are illustrated in Figure 4.6.

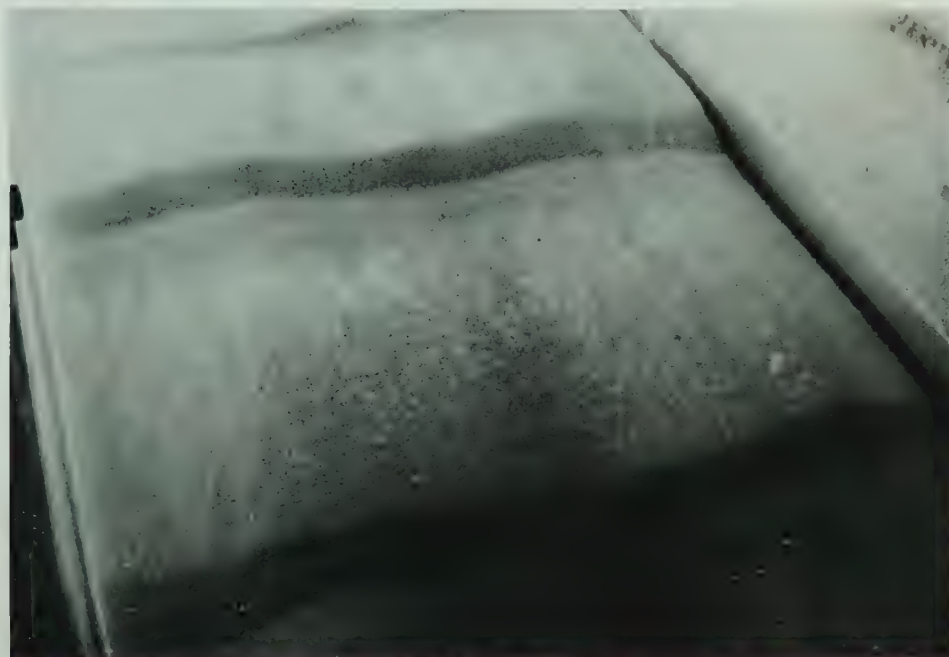


Figure 4.6. Photograph of Bed-Forms

The effects of wire insertion into the sediment bed upon the flow and pressure fields at the instrument probes were investigated separately. Pressures were monitored and transducer output was recorded continuously while bed-form crests were straightened by the wire method. The results showed that, provided the wires were inserted vertically and were moved gently, pressure fields at sensor positions remained unaffected.

CHAPTER V

EXPERIMENTAL PROCEDURES

5.1 Outline

A description of data acquisition procedures is given in this chapter. The presentation is divided into five topics which follow the chronological sequence of procedural steps in a typical test run:

- (1) Flume and sediment bed preparation.
- (2) Preliminary instrumentation check and flow depth adjustment.
- (3) Bed-wave development method.
- (4) Observation and data acquisition procedures.
- (5) Data reduction and handling.

5.2 Flume and Sediment Bed Preparation

5.2.1 Levelling of Sediment Bed

To insure identical initial conditions in the flume in all tests, standard flume and sediment bed preparation procedures were evolved and used throughout this investigation.

One of the preliminary tasks was the preparation of a four inches deep horizontal bed of sediment from the upstream end of the flume near the headbox to approximately twenty feet downstream from the observation area.

The method for levelling the sediment bed was discovered by chance. It was observed that when the water-sediment mixture in the flume was oscillated across the flume at its approximate natural frequency, and then

was allowed to dampen naturally, that the surface of sediment particles tended to assume a horizontal level.

To level the sediment bed, the surface of the water in the flume was initially adjusted to approximately $1/4$ inches above the required horizontal bed surface level. This submerged all granular particles and provided reference plane from which small variations on the bed surface could easily be observed through the sides of the flume.

To level the sediment bed, a $1/32$ inch thick, 18 inches long, and 10 inches wide aluminum plate was used. The 18 inch axis of the plate was aligned horizontally with the longitudinal centreline of the flume, and it was inserted vertically into the water-sediment mixture. The plate was then oscillated by hand with an amplitude of 2 to 3 inches and was gradually advanced along the length of the flume.

To obtain level bed surface this procedure had to be repeated several times. Seldom, if ever, the initial material distribution along the flume was uniform, and after initial levelling it was often necessary to remove or replenish sediment particles from high or low spots.

The effectiveness of this method was investigated by further lowering of the water level in the flume to expose approximately one half of the surface particles. Judging from the accumulations of the granular particles above the water line it was concluded that the areal distribution of high lying particles was not uniform. There was a tendency for the exposed particles to accumulate into areas of irregular shape and size. However, with rare exceptions, the variation in depth between the highest exposed and low submerged surface particles did not exceed two particle diameters. This was determined by filling a few random low spots with wet sediment particles in lifts one particle thick until a common level with

the highest particles was reached.

5.2.2 Flume Filling Procedure

At the conclusion of the levelling process the depth of water above the topmost surface particles was only a small fraction of an inch. To avoid excessive flow velocities capable of disturbing the surface particles during the flume refilling operation, the first one inch of depth above the sediment bed was raised at a very slow rate, usually in about 6 hours. The filling rate could then be increased and the flume was filled with water to a depth of one inch above the anticipated flow depth for the test.

After filling, the water in the flume was left for periods of up to 48 hours to deaerate and to warm to laboratory temperature. The municipal water used in the flume had tap temperatures less than 40 degrees Fahrenheit which was considerably below the normal laboratory temperature. Deaeration was essential because air bubbles in the water produced scatter of light and prevented observation of hydrogen bubbles used in velocity measurements. In addition, there was a tendency for the minute air bubbles in water to cling to individual sediment particles and thus modify their specific gravity.

5.3 Pre-test Instrument Check and Flow Depth Adjustment

5.3.1 Verification of the Measurement Systems

The pre-experiment pressure measurement system verification had a dual purpose. First, it disclosed anomalies in the system, such as the presence of entrapped air bubbles or blocked pressure probe ports. Secondly, it provided a record of a reference pressure for all pressure measurements, essential in evaluating the comparing the experimental pressure data.

The pressure measurement system tests were carried out using the

still surface of water in the flume and an auxiliary free surface reservoir as differential pressure reference. Equipment verification tests were attempted only after all free surface oscillations and surface waves in the flume were completely damped out. Depending upon the severity of the initial disturbances, the time period required for the free surface oscillations to subside ranged up to six hours, during which time no activities were permitted on the experimental floor.

The usual steps in preparing the pressure measurement equipment for an experiment were as follows:

- (1) The electronic equipment was switched on and permitted to warm up for 1-1/2 hours. Preliminary investigations had disclosed that this period of time was necessary to stabilize a very slow, exponentially decreasing electrical drift in one of the two pressure transducer systems.

- (2) Zero differential pressures were imposed on the pressure transducers by interconnecting both pressure chambers of each transducer to the same reference pressure source and transducer output voltages were then adjusted to zero, if necessary.

- (3) The positive pressure chambers of the transducers were connected, through the manifolds, to any two of the twelve pressure probes in the flume, and by using the established zero differential pressure as reference, water level in the auxiliary free surface reservoir was equalized with the water level in the flume.

- (4) Pressure transducer output recorders were started and each of the pressure probes in the flume was then sequentially connected, through a manifold, to a transducer and a one minute sample of its output under the applied zero differential pressure was recorded. In addition an output record was obtained with both chambers of the transducers connected to

the auxiliary free surface tank. This procedure was repeated three times to ascertain the consistency in individual probe outputs.

A differential pressure of 0.002 inches of water above or below the mean output of the six pressure probes used with each of the transducers was arbitrarily selected as the standard indicating no anomalies in the individual probe systems, provided that consistency in this output from repeated measurements was maintained. If the output from any pressure probe was found to be outside of this specified limit, or if variation was detected between repeated measurements, the pressure lines to the probe were flushed with slightly soapy water through the special ports in the manifolds provided for in-place transducer calibration. Usually, the causes of these small anomalies were tiny air bubbles attached to the interior of the pressure lines or at the junctions of the flexible tubing and metal fittings. In most cases the remedial flushing procedure effectively eliminated the problem.

During the initial stages of the experimental program, gage calibrations were checked before each test was run. This pre-test step was omitted as the work progressed in favour of calibration verification between test runs. The pressure measurement systems were observed to maintain constant response characteristics, and the checks served primarily to insure that the proper range settings in the electronic circuits were not accidentally changed.

After the conclusion of pressure system verification, flow was established in the flume by starting the pump motor and slowly opening the flow control valve until a discharge required for the test was attained.

Hydrogen bubble apparatus was switched on, and after a short warm-up period, the wires were pulsed and the production of hydrogen bubbles at each of the three wires separately and in the four different

combinations with each other, was observed visually to insure proper equipment operation.

5.3.2 Water Level Control

Preliminary observations indicated that because of evaporation from the free surface, leakage from the flume and withdrawal of cooling water for pump bearings small amounts of water were lost from the recirculating system. Although these water losses did not exceed 0.25 cubic inches per second the corresponding continuous lowering of the mean water surface from the flume affected all pressure measurements since they were referred to a constant pressure source.

Because the rates of leakage under typical test conditions were found to be constant for periods up to six hours, to maintain a constant mean surface level in the flume an equivalent amount of water was replaced into the system.

To determine the rate at which water had to be replaced, the flume was filled one inch deeper than the required experimental depth and a discharge of water equal to the required experimental discharge was established by adjusting the flow control valve. As the flow in the flume under these conditions was insufficient to entrain or transport sediment particles, and the bed remained level, the piezometric head at any location remained invariant except for the drop in the water surface elevation due to leakage. Before a test was run, therefore, pressure was monitored for 30 minutes at two probe positions in the flume. The corresponding leakage from the flume was calculated from the rate of the recorded pressure drop and replaced back into the flume from a constant head tank located near the upstream end of the flume as indicated in Figure 3.1.

5.4 Bed-Form Development

Initial disturbances of bed particles by surges induced by commencement of flow in the flume were eliminated by establishing a pre-selected experimental discharge at a depth which produced flow velocities and conditions above the bed considerably below particle threshold values. After all possible surging activity in the flume had subsided the water level in the flume was slowly lowered by keeping the system drainage valve open until the flow velocity surpassed particle threshold velocity and movement of bed particles could be observed.

To start the development of bed-forms at any location in the flume a 1/16 inch diameter wire, inserted vertically approximately 1/4 inches into the sediment bed was drawn from one side of the flume to the other. If the depth of the penetration of the wire into the sediment, and the speed with which it was moved were uniform and steady, the particles displaced by the wire and flow in the flume formed a trough-ridge combination of a relatively uniform cross-section across the flume. If this procedure was carried out after particle threshold conditions on the original bed had been surpassed, the wire-formed ridge became the crest of a bed-form and bed-forms then formed downstream of each other in a manner that was identical to the naturally initiated bed-forms.

To eliminate the effects of possible changes in the mean depth of flow in the observation area because of boundary roughness changes during the measurement interval, bed-form development was triggered at four equally spaced locations in the approach channel. This system of bed-forms developed quickly and eventually distorted into an irregular pattern as no attempt was made to control the shape of the bed-forms manually. Once fully developed the irregular bed-forms produced an equilibrium bound-

ary roughness that on the average remained constant over the period of observation, and produced a constant energy gradient.

A more severe difficulty was encountered in the immediate approach channel upstream of the observation deck because bed-forms arriving from upstream were three-dimensional. To facilitate restoration of two-dimensional bed-forms two 1/4 inch opening screens were placed across the flow, approximately six inches from each other, and ten feet upstream of the observation deck. The size of wire of these screens was approximately 1/16 inches, and the restriction was sufficient to suspend temporarily all of the bed particles arriving at the screens. The suspension of bed-material served two functions. It facilitated a more uniform distribution of particles across the flume and reduced secondary circulation effects in the approach channel. Two-dimensional bed-forms were restored using a 1/16 inch diameter wire. However, restored bed-forms were never used for measurement purposes, but served only to maintain a uniform boundary roughness in the channel.

Subsequent evaluation of pressure records indicated that bed-forms developed in the manner described in previous paragraphs produced an average constant depth of flow at the observation area. Provided that the quantity of water in the system remained constant, local pressure variations were therefore attributable to the passage of the bed-wave itself.

To summarize, the procedure of bed-form development for experimental observations consisted of the following steps:

- (1) After the required flow was established, the water level in the flume was gradually lowered by draining, until the chosen flow depth was reached.

(2) Bed-forms were initiated at a location approximately 8 feet upstream of the observation deck and also at four locations in the approach channel upstream of the screens.

(3) The development of bed-forms in the channel area immediately upstream of the observation deck was controlled manually throughout their growth period, and then until the experiment was completed.

(4) Irregular bed-waves arriving from upstream were restored at wavelength intervals corresponding to the naturally developed wavelengths of bed-waves approaching the observation area.

In all experiments the maintenance of the bed-waves in the approach channel was carried out by an assistant observer. The maintenance of bed-waves in the area of observation, because of restricted space, was carried out by the principal observer.

5.5 Observation and Data Acquisition Procedures

5.5.1 Outline

Discussion of experimental procedure are divided into two general parts. In the first, summary outlines of measurement procedures of individual parameters are given separately. Then the sequence of operations and procedures integrating all separate parameter observations is given.

A number of trial experiments were run to determine most efficient procedures to obtain adequate quantity of good quality experimental data. Experimental procedures were evolved from experience gained and observations made in these trial tests.

5.5.2 Depth-Wire Observations

Bed-wave geometry data was obtained by visual observation of the instantaneous position of the surface of sediment at each depth-wire. The observed readings were voice recorded on magnetic tape at the time

of observation.

The method of voice recording of visual observation data was found to be most effective. On the average, it took 25 seconds to scan the positions of the sediment bed at all nine depth-wires. As in most tests, this scan period corresponded to approximately $1/50$ to $1/100$ of the bed-wave period, local depth corrections because of bed-wave migration downstream and relatively small bed surface slopes were minimal and were not required.

A typical sequence of steps for bed-wave profile observation was as follows:

- (1) Depth-wires were illuminated by switching on the hydrogen bubble light.

- (2) The reference position at the upstream depth-wire was determined from the known position of the free surface of flow. This step was necessary because depth-wire scale had no numeric code to indicate the integer number of inches from the reference level to the surface of the sediment.

- (3) Time from the start of experiment was noted and recorded to denote the beginning of the period of depth-wire observation.

- (4) Starting with the upstream wire, sediment level positions were observed at each depth-wire and were voice recorded on magnetic tape. Positions and depths of bed-wave crests or toes occurring between wires were estimated from positions of bed levels at adjacent wires.

- (5) Time on the experimental clock was observed and recorded at the conclusion of the scan of depth-wires.

5.5.3 Velocity Observations

In a typical test, all electronic equipment for the production of hydrogen bubbles was switched on before the test run was started except

for the power unit, which, for safety reasons, was switched on only a short period before the wires were pulsed.

The typical procedure for velocity measurement with the hydrogen bubble technique is outlined as follows:

(1) The power unit and illumination lights were switched on and the selected wires were pulsed to observe visually through the side glass the quality of bubbles. This procedural step indicated if cleaning of the hydrogen bubbles was necessary. This often eliminated a wire cleaning process reducing the possibility of local bed-wave disturbance. It also indicated if any of the wires produced poor quality bubbles that were difficult to observe and would not be recorded on the photographic film.

(2) If wire cleaning was not required, this step was omitted. Otherwise, the dirty wires were first subjected, for 15 to 20 seconds, to reversed polarity pulses, followed by a normal pulsation period of approximately the same duration. Experience showed that the reversal of polarity was most often sufficient to clean the wires and to enhance the quality of the hydrogen bubbles. The reasons for this behaviour, already discussed by Schraub, et al. (1965), have not been explained and remain unknown. If further cleaning was required, it was carried out by the method described previously in Chapter III with the power unit switches off.

(3) The camera position was adjusted to cover the field of the hydrogen bubbles. The lens was focussed on the hydrogen bubble wires. The camera height was adjusted to be at approximately the same elevation as the sediment level. This reduced or eliminated the white background area, due to illumination of the sediment surface by the light from above, against which hydrogen bubbles could not be seen.

(4) The wire or wires were then pulsed by manually operating the

pulsing switch and a photograph of the rows of bubbles was taken by manually depressing the camera shutter before the first row of bubbles produced at a wire had reached the position of the immediate hydrogen bubble wire downstream. This avoided overlapping of the rows of bubbles originating at the two wires.

(5) Time from the beginning of experiment, film frame number, and the wires pulsed were recorded.

5.5.4 Pressure Measurement

As described in Chapter III, the instrumentation for pressure measurement consisted of two differential pressure transducers, each of which could be connected through a manifold to any one of six pressure sensors in the flume. Reference pressure was provided by a constant water level tank which was connected through separate lines directly to the negative sides of the two pressure transducers. Transducer output voltages were recorded in analog form by two X-Y plotters, the X-axis representing time, and Y-axis the transducer output voltage.

Because of very small absolute magnitudes of pressure changes in the light weight sediment bed, adequate resolution of transducer output could be obtained only at high sensitivity settings of the X-Y recorders. This restricted the range of input voltages into the recorders ± 0.02 volts DC, and in effect, restricted the operational differential pressures between the flume and the reference pressure to the near zero range.

Pressure measurements in the sediment bed were obtained in two ways. In the first, which was used in the majority of experiments, the pressures at each sensor position in the flume were sampled for short periods of time in a predetermined or a random sequence. In the second way, either one or both of the transducers were connected to a single sensor probe in the flume for the duration of the experimental run or for a

complete bed-wave passage time period over the sensor.

The pressure data acquisition procedures included also steps to protect the recorders from possible mechanical damage due to excessive input voltages. It was found that removal or replacement of clamps on the pressure lines produced sudden line pressures and consequently transducer output voltages considerably in excess of the available recorder pen travel range under the operating sensitivity settings. To protect the recorders, a switch was installed in their input circuit. The voltage output into the recorders was switched off manually whenever different sensor pressure lines were opened to the manifold.

The pressure recording procedure required manual resetting of the recording pen and restarting of the recording trace every 750 seconds, and the changing of the recording chart every 3000 or 3750 seconds. All pressure data was recorded at a plotter pen speed of $1/50$ inches per second. As the length of the recorder chart was 15 inches, a single sweep lasted 750 seconds. Usually it was possible to record four sweeps on the same chart page by lowering the pen position two inches lower for every sweep.

Although the speed of recorder pen movement in the X-direction of the chart was nominally $1/50$ inches per second, it was found to vary slightly between the two recorders. For a better data control, a low voltage source was connected through a switch to the input terminals of both recorders. Whenever the switch was closed, instantaneous displacement of the recorder pen from the normal pressure trace provided a common time marker on both charts.

The procedural steps discussed in the various paragraphs were interspaced with the actual pressure data acquisition steps. Excluding

these steps the outline of the actual pressure measurement procedure can be summarized as follows:

(1) Immediately prior to the start of a test run, the transducers were connected through the manifold to monitor pressures at any two of the twelve sensor locations in the flume.

(2) The measured differential pressure between the flume and the reference source was observed on the transducer meter dials and was adjusted to zero by raising or lowering the water level in the reference reservoir with a hypodermic needle.

(3) The clamps on the pressure line from the reference reservoir to the manifold were removed. All pressure lines connecting the sensor probes in the flume to the manifolds were clamped tight. This exposed both chambers of the transducers to an identical pressure.

(4) The experimental run was started by activating the test chronometer and by the recording the zero differential pressure output from the pressure transducers. A record of the zero differential pressure was essential as a common reference in data reduction and for correlation of pressures measured by the two independent transducer systems. A continuous output of 30 to 60 seconds in duration was recorded.

(5) Recorder input was interrupted by turning off the protector switch.

(6) Pre-selected sensor pressure line clamps were removed and replaced on lines connecting the manifold to the reference source reservoir.

(7) After a delay of approximately 20 seconds to allow manifold and the transducer chamber pressure to equalize with the pressures at sensor positions in the flume, the protector switches were turned on, and simultaneously the chronometer (time) reading was noted and voice recorded on tape. The identifying numbers of the sensors sampled were also

voice recorded at this time.

(8) When the short period pressure sampling procedure was employed, a pressure record of 50 to 60 seconds in duration was recorded. Otherwise, a continuous recording of pressure from a single sensor was maintained.

(9) At the end of the sampling period the recorder input protector switch was turned off.

(10) Clamps from two other sensor pressure lines were removed and replaced on the lines from the sensors already sampled.

(11) Steps 7 to 10 were repeated until the end of the experiment.

5.5.5 Integrated Data Acquisition Procedures

The different procedures described previously for bed-wave geometry, velocity, and pressure measurements were integrated together in a typical experimental run. Generally, the depth-wire readings and velocity measurements were carried out during the recording periods for the pressure data. Various other observations, bed-wave shape maintenance in the observation area, placement of time markers, etc. were also made during these periods.

All data acquisition tasks, including visual observations and manipulation of equipment were performed by the principal observer who was positioned at the observation window. All equipment was located within reach from this position. The assistant observer, whose duties were to restore two-dimensional bed-forms at the screens and to maintain the shape of the bed-forms in the approach channel, was positioned approximately six feet upstream of the observation area. Both observers maintained their positions with minimum movement throughout a test run to avoid disturbing the flow in the flume.

Considerable experience on the part of the observer in integrating all of the procedural steps and other tasks was required to successfully obtain experimental data. The amount of data obtained was also, to a large degree, restricted by the numerous tasks that the observer had to perform in the available time.

All observations were tied to the time base of each test run. At the beginning of an experiment, a digital chronometer reading in seconds, was activated and all times of all subsequent observations of bed-wave geometry, hydrogen bubble photographs and pressures were noted and recorded. These times provided the common reference through which instantaneous positions of various probes in the flume and consequently the locations of the measured parameters in relation to the bed-wave geometry could be determined.

In addition to the boundary geometry, velocity of flow and pressure data, readings of water temperature, flow discharge and the absolute mean depth of water in the flume were recorded before and after an experimental run.

5.6 Data Reduction

After the conclusion of a test run all data was reduced into digital form.

All observations and data readings contained on the audio tape were transcribed first. Pressure sampling times and sensor identifiers were marked directly on the pressure record charts. Bed-wave profile depth-wire readings and the mean time of scan were recorded in tables. During the initial data transcription only the times, wire data and film frame numbers of the hydrogen bubble photographs taken during the experiment were transcribed.

Depth-wire observation data was transcribed directly from the audio tape into two tables. In the first, the mean time of the scan (from the start of the experiment) and individual wire readings were recorded. In the second table, the measured or estimated positions and elevations of the crests and toes of observed individual bed-waves were entered.

The films of the hydrogen-bubble photographs were developed and prints 3.25 by 4.75 inches in size were made commercially. A typical hydrogen bubble photograph is given in Figure 5.1. Depending upon the size of the hydrogen bubble images on the photograph the digitizing of the visual data was made either directly from the film or from the photographs. It was found that if the images of the hydrogen bubble rows were large the distances between adjacent rows of bubbles could be scaled sufficiently accurately from the photographs. If, however, the



Figure 5.1. Typical Hydrogen-Bubble Photograph

photograph contained rows of bubbles from all three wires, and the images were therefore small, the scaling from the photographs became less accurate because of the small absolute distances between the rows of bubbles and the digitizing was made using a microfilm reader to project the enlarged film image on 0.1 inch square grid.

To digitize the hydrogen bubble information, the scale of the photograph, or of the projected image, was determined first from the mean of the distances between the images of two adjacent hydrogen bubble wires scaled at two different levels below the surface of the flow. As the true distance between these wires in the flume was known, the scale of photograph or the projected image could easily be calculated. In general the two scaled distances at the two levels were identical. However, small differences, up to one per cent of the total distance, were found to exist on some photographs. These errors were attributed to a possible stretching of the film or of the print, or possibly, to the combined optical effects of air, glass and water if the camera lens was slightly tilted from the perpendicular to the glass wall when the exposure was made. Averaging of the measurements, therefore, tended to reduce the error of the true scale of the photograph.

Information to determine the instantaneous velocity profiles above the sediment bed, the location of a velocity profile in relation to a wire, and the flow depth at the wire was extracted from the hydrogen bubble photographs. The horizontal distances between two or more rows of hydrogen bubbles were accurately scaled at different levels between the sediment bed and the free surface. The number of levels at which the spacing between the rows of bubbles was scaled varied from four to ten depending on the apparent uniformity of the velocity profile. The dis-

tance between the wire and the upstream bounding row of bubbles for the determination of the space interval between the rows, was also measured. In addition, the distance from the free surface to the sediment bed at the wire was also scaled.

The transcribed information was summarized for each instantaneous observation of velocity. This summary contained film frame number, time of exposure on the test run time clock, wire pulsation frequency, wire number, data to determine scale of photograph, depth measurement at wire, scaled distances from the wire to the bounding row of bubbles, scaled distances between rows of bubbles and the number of row intervals, and the scaled distances from the free surface to each level at which distances between the rows were measured.

In the reduction of pressure data, the first step was the transcription from the audio tape of all analog trace identification information of their starting times, and special marker times into the pressure data record charts.

Next, a reference pressure common to all sensor probes was established on the original pressure record charts. For this the sensor calibration information obtained in the pre-test instrument check with no flow in the flume was used. The differences in the transducer output voltages between the applied zero differential pressure (both chambers of a transducer connected to the reference reservoir) and the constant hydrostatic head in the flume were determined for each sensor probe. The common reference pressure on the data charts was then established by indicating these differences above or below the zero differential pressure trace for each corresponding sensor. It must be noted that the zero differential pressure reference was used only as a

control to maintain true output relationships between the different sensor probes. For this reason, the level of water in the reference reservoir had to remain constant during the pre-test instrument check and throughout the experimental run. It could, however, be raised or lowered between these steps.

All analog pressure data records exhibited amplitude fluctuations ranging from 0.001 to 0.005 inches of water. As the frequency response of the pressure measurement system precluded meaningful interpretation of the fluctuation pressures, only the mean pressure information was extracted from the records. Upper and lower envelope lines were drawn to include all but the extreme peak pressures recurring at intervals in excess of 30 seconds. The mean pressure line for each sampling interval was then drawn bisecting the distance between the enveloping lines.

The actual digitizing of data was made by measuring the voltage difference between the appropriate sensor reference pressure line and the mean pressure. In converting the analog pressure data into digital form two criteria were considered. If the mean pressure line was constant, only a single pressure value was determined at the mid-interval time of the sampling period. If, however, pressure variation was noted, pressures were determined at the beginning and the end times of the sampling period and between, at intervals depending upon the pressure gradients but not exceeding 50 seconds.

The pressure data were grouped for each sensor probe separately, in tables which identified the probe, its position in relation to the flume (i.e. its horizontal and vertical coordinates) and the times the voltage values of each observation.

CHAPTER VI

EXPERIMENTAL RESULTS

6.1 Introduction

The results of the experimental measurements are presented in this chapter. First, various pertinent terms and reference systems are defined then the descriptions of raw data treatment procedures are given. Criteria for the quality of data are discussed and data sets for final analyses are identified. Final data treatment procedures are described and summaries of results are presented. Included in this chapter are also the results of qualitative observations relevant to the experimental goals.

Exclusive of the preliminary trials a total of 29 individual experiments, under various flow and depth conditions were performed in this investigation.

Because of bed-form deformation, four tests were terminated before completion, and in the remaining 25 experiments, observations and measurements of various parameters were made on 55 individual bed-forms. Because data contained more than 20,000 individual bits of digital information, all preliminary data treatment and plotting were performed by an IBM 360/67 computer and Calcomp plotter.

6.2 Bed-form Coordinate System and Nomenclature

The raw experimental data, transcribed from the audio tape and the analog charts, provided information about the instantaneous absolute

values of the measured parameters at the fixed locations of each probe and at the instant of time of each observation.

To establish the instantaneous positions of the various probes, and consequently the spatial variation of the measured parameters in relation to the geometry of each bed-form, two rectangular coordinate systems--one stationary and one moving--were employed.

The origin of the stationary coordinate system was for convenience placed at the intersection of the first (upstream) depth-wire and the top surface of the instrument plate. The ordinate was aligned vertically along the wire, and the positive direction of the abscissa was pointed downstream along the flume. All observations were made in the stationary reference frame.

The origin of a moving reference frame was placed at the intersection of the vertical line passing through the crest of a moving bed-form and the horizontal line at the mean elevation (in the fixed reference system) of the toe of the bed-form upstream of the reference crest.

The location of the origin of the moving coordinate system for each bed-form was selected because crests and toes were the only clearly recognizable features of a bed-form. The vertical position of the moving origin at the toe, upstream of the reference crest, was chosen because the elevation difference between the toe and the crest downstream served as a convenient reference parameter for non-dimensionalizing of the bed-form profile geometry data. A crest, by definition, was the intersection of the lee slope of a bed-form with the surface of its upstream face. Similarly, a toe was defined by the intersection of the lee slope with the upstream face of the adjacent downstream bed-form.

The coordinate systems and various descriptive terms are

illustrated in Figure 6.1.

Bed-forms in a train were numbered in their sequence of arrival at the observation area. The limits of a bed-wave were considered to extend upstream from the toe of wave (a) to the toe of wave (a + 1).

However, in evaluating bed-form wave lengths a greater variability was found between the wave lengths determined from toe to toe than from crest to crest measurements. This was caused by the cyclic sliding of particles on the lee side of a bed-form which advanced each toe in sudden steps of random length and at random time intervals. To reduce data scatter, particularly in computing parameters that involved the wave length of a bed-form, the adjacent crest to crest distances were adopted as the wave length measures. To differentiate from the bed-form definition, the space between two adjacent crests was called a range. A range was identified by a number corresponding to the number of the upstream bed-form.

6.3 Flow-Boundary Stability

6.3.1 Preliminary Observations

The objectives of the experiments were to obtain measured data from which the characteristics of various flow and sediment transport parameters within the bounds of a two-dimensional bed-form could be reconstructed. To obtain meaningful measurements, the characteristics of the structure of the flow and the response of the sediment particles had to remain essentially unchanged in respect to the geometry of the bed-form during the observation period, when the bed-form traversed across the area containing the stationary instrument probes.

Although all precautions were taken to insure that bed-forms were stable during the observation period, some tests were terminated

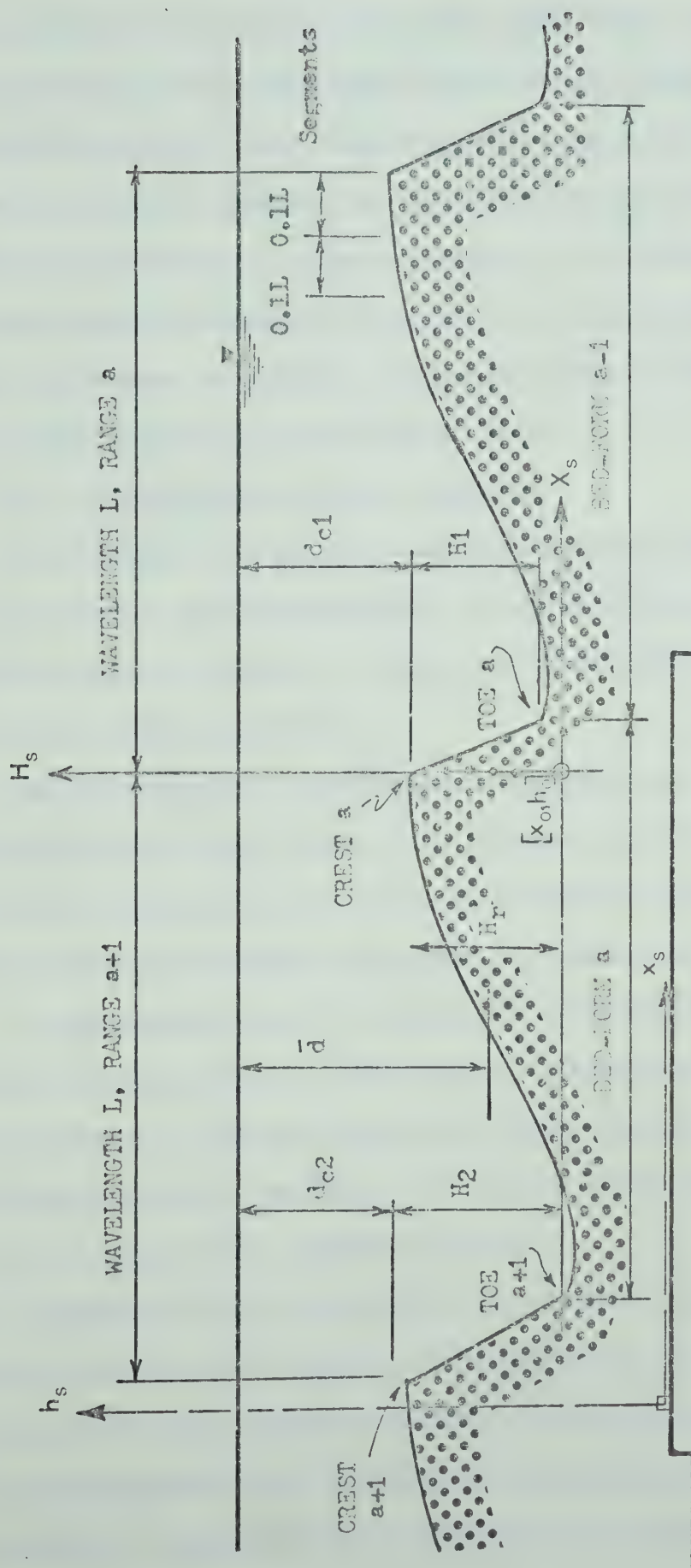


Figure 6.1. Bed-form Coordinate Systems and Nomenclature

before completion when the bed-forms under observation changed their heights or lengths, or in some other way became distorted from the required two-dimensional form. This observation suggested that significant variations in the geometry of bed-form under observation may have been visually undetected in other experiments. As temporal variations of bed-form geometry during the experimental runs could not be monitored, a method was devised to evaluate individual bed-form stability characteristics from experimental bed-form geometry data.

6.3.2 Criteria for Bed-Form Stability

To determine if a bed-form was in equilibrium during the period of its observation, and to insure that the related experimental data were suitable for further analysis, a common set of standards was adopted to all bed-forms in the experiments.

The standards were established on the principle that a bed-form was in equilibrium if the flow and the sediment response characteristics in the space bounded by the upstream and downstream limits of a bed-form remained invariant throughout the period of observation.

It was assumed that the hydrodynamic characteristics of flow were constant during the period of observation if the following parameters remained constant: (1) the mean velocity of flow entering and leaving the spatial element above a bed-form, (2) the wave length of the bed-form, and (3) the height of the upstream bed-form.

Similarly, it was assumed that the sediment response characteristics were constant if the geometry of the bed-wave, as measured by its wave length and height, remained constant during the observation period.

As the imposed flow discharge was constant throughout an experiment, a test for the constancy of elevation of a crest above a reference

provided the test for constancy of flow velocity. The information required for this test was available directly from the observed data.

The information required to test the constancy of bed-form heights was computed from the instantaneous observed elevations of toes and crests.

Finally, the information required to test the constancy of bed-form wave lengths was obtained from the observed data of the instantaneous positions of the two crests in the stationary reference frame in the flume.

6.3.3 Statistical Analysis of Bed-Form Equilibrium

Initially, an attempt was made to evaluate bed-form equilibrium by plotting crest elevations, wave heights, and crest positions on a time base. Because of the limitations of data acquisition techniques and natural effects in the flume, these plots showed considerable data scatter. To avoid inconsistencies in evaluating data by visual means, linear regression techniques were adopted to test stability of experimental bed-forms. In the regression analyses, crest elevations, wave heights, and wave lengths were considered as the dependent variables. The time of each observation was treated as the independent variable, because its measurement incurred less error than measurement of other variables. All computations, including the determination of regression coefficients, were performed by an IBM 360/67 computer using an available library program.

To test if a crest or a toe remained at a constant elevation during an observation period the regression coefficient, representing the slope of the regression line with time as the independent variable, had to equal zero. It was tested at a given significance level under

the null hypothesis $H_0 : \beta = 0$, against the alternative $H : \beta \neq 0$ by the statistic

$$\frac{b - \beta}{\sqrt{\hat{V}[b]}} \quad (6.1)$$

where b is the regression coefficient, and $\hat{V}[b]$ is the variance of its expected value which is distributed as a Student's t -variable with $(n - 2)$ degrees of freedom and where n represents the number of observations (Keeping, 1962).

To determine if the wave length of a bed-form was constant during an observation period, a joint statistical analysis of the regression coefficients b_1 and b_2 of the horizontal positions of two adjacent crests with time as independent variable was carried out. The theoretical background of the statistical test which was used is given by Brownlee (1960). The null hypothesis under a given level of significance was $H_0 : \beta_1 = \beta_2$, against the alternative $H_1 : \beta_1 \neq \beta_2$. The statistic for testing the null hypothesis was

$$\frac{b_1 - b_2}{\sqrt{\hat{V}[b_1 - b_2]}} \quad (6.2)$$

which is distributed as $(n_1 - 2) + (n_2 - 2)$ degrees of freedom where n_1 and n_2 represent the number of observations in data for regression lines 1 and 2 respectively.

The selection of individual bed-form measurement data for further analysis was based on the results of statistical evaluation of the constancy of five bed-form and flow parameters during the observation period, namely: (1) submergence of the upstream bed-form crest, (2) submergence of the bed-form crest, (3) height of the upstream form, (4) height of the

bed-form, and (5) wave length of the bed-form. Significance of all parameters was considered and data were accepted unconditionally if all five parameters were non-significant at the 0.05 level. Otherwise, bed-form test data were accepted if three or less parameters were not significant at .02 level, or two or less parameters were not significant at 0.01 level, or not more than one parameter at 0.005 level. As a result of the above conditions only 17 out of 55 bed-form profiles were accepted for further analysis. A resume of the statistical bed-form equilibrium test results is given in Appendix C.

6.4 Bed-Form Profile Geometry

Stable bed-forms translating downstream with constant velocities reflect the relative equilibrium between the hydrodynamic force and sediment response systems. The geometric characteristics of their profiles may therefore serve in explaining some of the physical aspects of the entrainment and transport of sediment as bed-load along bed-form surfaces.

A summary of the basic bed-form and flow parameters of bed-forms selected for final analysis is presented in Table 6.1.

The mean depth of flow \bar{d} above a bed-form was determined by estimating the area occupied by water between two adjacent crests and dividing it by the mean wave length of the bed-form. The flow area was estimated by the trapezoidal rule method dividing the wave length into ten equal parts.

The mean depth of flow above a crest, \bar{d}_{c1} or \bar{d}_{c2} were determined from the difference between the elevation of the free flow surface and the mean elevation of the crest measured in the stationary reference frame.

The mean height of a bed-form \bar{H}_1 or \bar{H}_2 were determined by subtracting the mean elevation of the toe from the mean elevation of the crest

TABLE 6.1

BASIC BED-FORM GEOMETRY DATA

Test Range	Bed-Form	\bar{q}_m cu in/sec	*T °F	\bar{d} in	\bar{d}_{cl} in	\bar{d}_{o2} in	\bar{K}_1 in	\bar{H}_2 in	\bar{H}_r	\bar{L} in	\bar{v}_b in/sec x100
11 2	1	7.02	77	2.87	1.66	1.96	0.900	1.107	1.403	21.43	0.326
12 2	1	7.78	73	2.92	1.72	2.11	0.880	0.921	1.314	16.59	0.761
17 2	1	11.02	79	3.09	2.31	2.03	0.412	0.833	0.657	16.52	0.739
17 3	2			3.26	2.03	2.53	0.833	0.710	1.159	15.22	0.774
20 2	1	5.62	84	2.14	1.55	1.45	0.567	0.678	0.578	20.68	1.184
20 3	2			2.14	1.45	1.49	0.678	0.650	0.689	13.80	1.247
21 2	1	5.94	85	2.28	1.72	1.71	0.590	0.677	0.666	15.81	0.798
21 3	2			2.26	1.71	1.62	0.677	0.820	0.732	17.23	0.823
22 2	1	9.72	73	3.73	2.31	2.78	1.080	0.914	1.383	12.07	0.674
22 3	2			3.10	2.78	2.28	0.914	0.825	0.321	10.73	0.736
24 2	1	6.05	81	2.43	1.61	1.64	0.795	0.823	0.813	15.93	0.553
24 4	3			2.53	1.75	1.79	0.743	0.858	0.903	15.73	0.353
26 2	1	5.40	71	1.84	1.44	1.42	0.670	0.685	0.720	10.69	0.131
26 3	2				1.42	1.44	0.685	0.671	0.637	12.43	0.117
28 2	1	3.56	81	1.81	1.15	1.18	0.586	0.626	0.655	14.96	0.260
28 3	2			1.86	1.16	1.17	0.626	0.702	0.690	14.80	0.259
28 4	3			1.95	1.17	1.16	0.703	0.750	0.742	16.63	0.257

*Temperature of water

of the bed-form also measured in the stationary reference frame. The mean reference height \bar{H}_x of a bed-form was calculated by subtracting the mean elevation of the origin of the moving reference frame from the mean elevation of the reference crest, measured in the stationary reference frame.

The mean wave length \bar{L} and the mean velocity of translation \bar{V}_b of a bed-form were determined by the joint regression technique described in Section 6.3.3.

The representative profile geometry of an individual bed-form was determined in three steps. First, the bed profile coordinates originally observed in the stationary reference frame were transferred into the moving reference frame. In effect, repeated boundary profile observations at different times of the experiment were superimposed upon each other. Second, all of the observed surface coordinate points were non-dimensionalized and, finally, a mean profile for a bed-form was calculated from the dimensionless coordinate data.

To compute bed-form surface coordinates in a moving reference frame the coordinates of the origin of the moving reference frame x_0 and h_0 for every observation time had to be established. The vertical coordinate h_0 for each bed-form range was determined from the mean elevation of the toe contained in the appropriate bed-form range. The horizontal coordinate x_0 was determined either from observed data or was estimated from regression coefficients relating time and the position of the reference crest in the flume. The application of the regression coefficients was found to be useful in extending the utility of some data points when the governing crest moved outside the observation area.

The horizontal and vertical bed-form surface coordinates X_s and H_s

in the moving reference frame were computed and non-dimensionalized in accordance with the following equations:

$$X_s = x_s - x_0 \quad (6.3)$$

$$H_s = h_s - h_0 \quad (6.4)$$

$$X = \frac{X_s}{\bar{L}} \quad (6.5)$$

$$H = \frac{H_s}{\bar{H}_r} \quad (6.6)$$

where x_s and h_s represent the instantaneous horizontal and vertical coordinate of sediment surface data points in the stationary reference frame.

Finally, the representative profile of an individual bed-form was determined by grouping all available dimensionless bed surface data points into nine segments along the bed-form length, $0.1 \bar{L}$ long each, and computing their mean position in coordinates \bar{X} and \bar{H} in each segment in the dimensionless coordinate system according to

$$\bar{X} = \frac{\sum_{i=1}^m X_i}{m} \quad (6.7)$$

$$\bar{H} = \frac{\sum_{i=1}^m H_i}{m} \quad (6.8)$$

where m is the number of coordinate points in a segment.

The representative mean profiles of bed-forms selected for analysis are presented in Figures 6.2(a) to 6.2(q). Multiplying factors \bar{L} and \bar{H}_r , which may be used to convert a dimensionless profile into natural coordinate system and the relative size of particles D_{50} are also shown for each bed-form. A best fit smooth line was drawn between the weighted

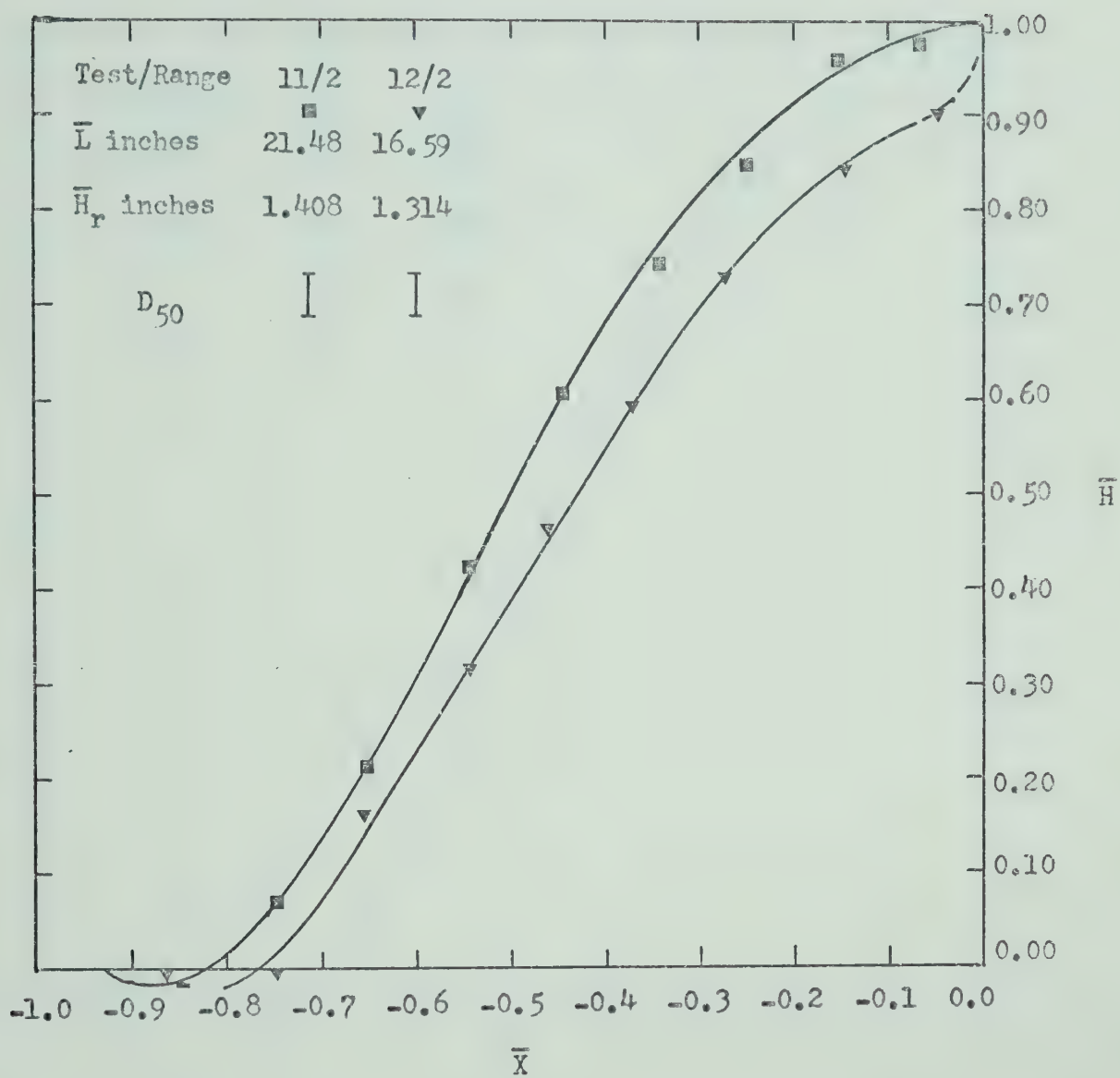


Figure 6.2(a). Mean Dimensionless Bed-Form Profiles,
Test 11, Range 2, and Test 12, Range 2.

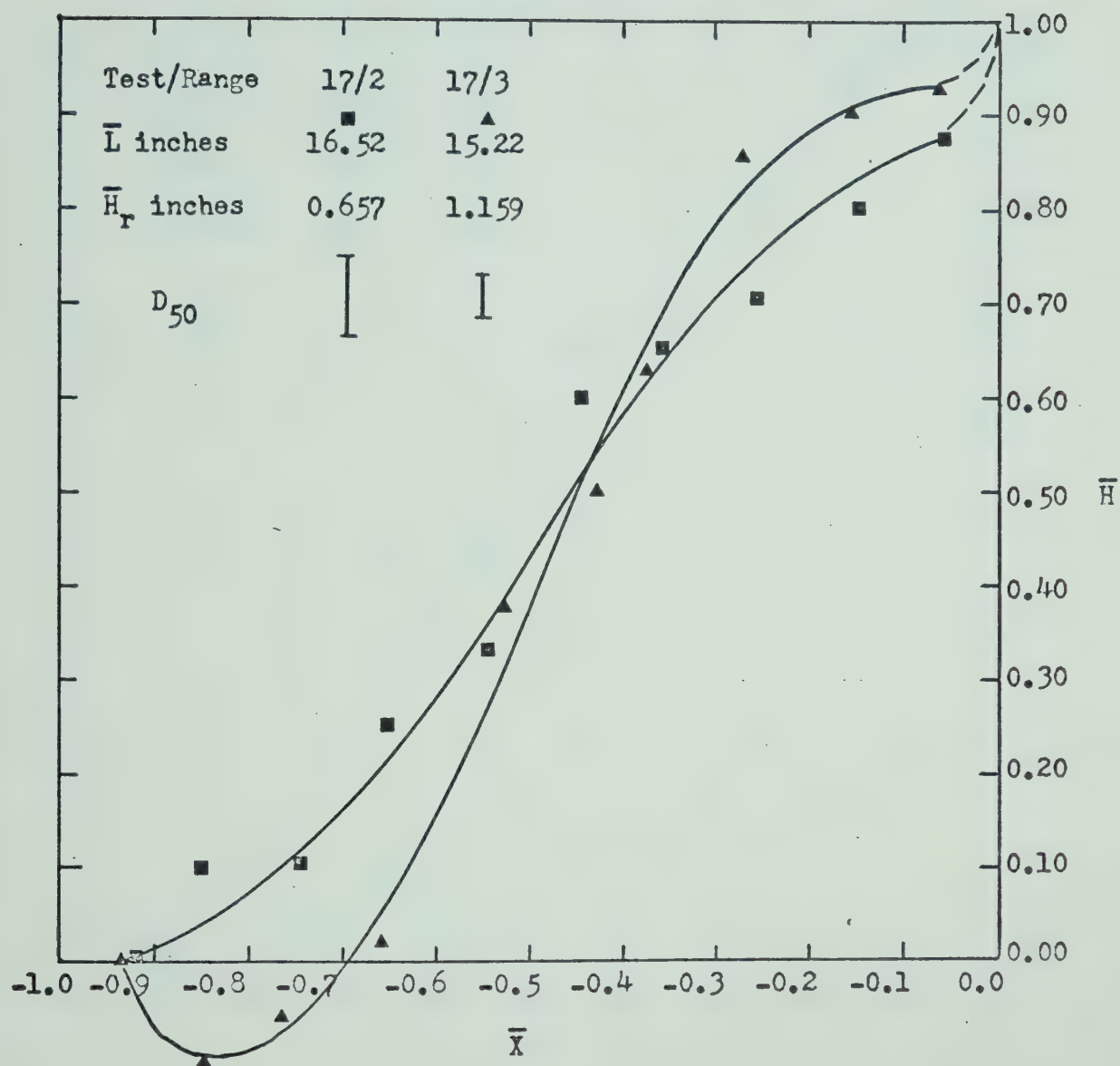


Figure 6.2(b). Mean Dimensionless Bed-Form Profiles,
Test 17, Range 2, and Test 17, Range 3.

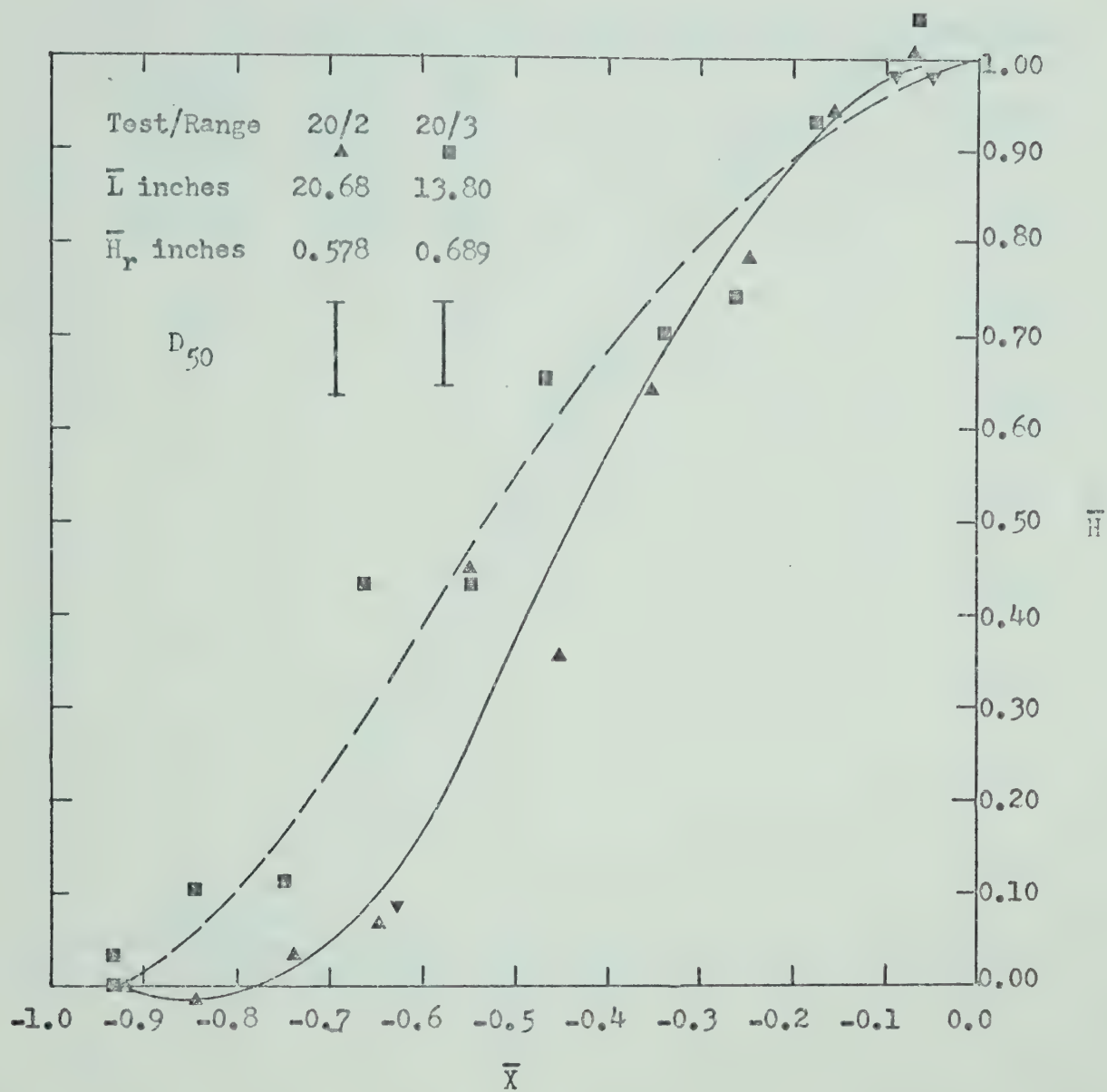


Figure 6.2(c). Mean Dimensionless Bed-Form Profiles, Test 20, Range 2, and Test 20, Range 3.

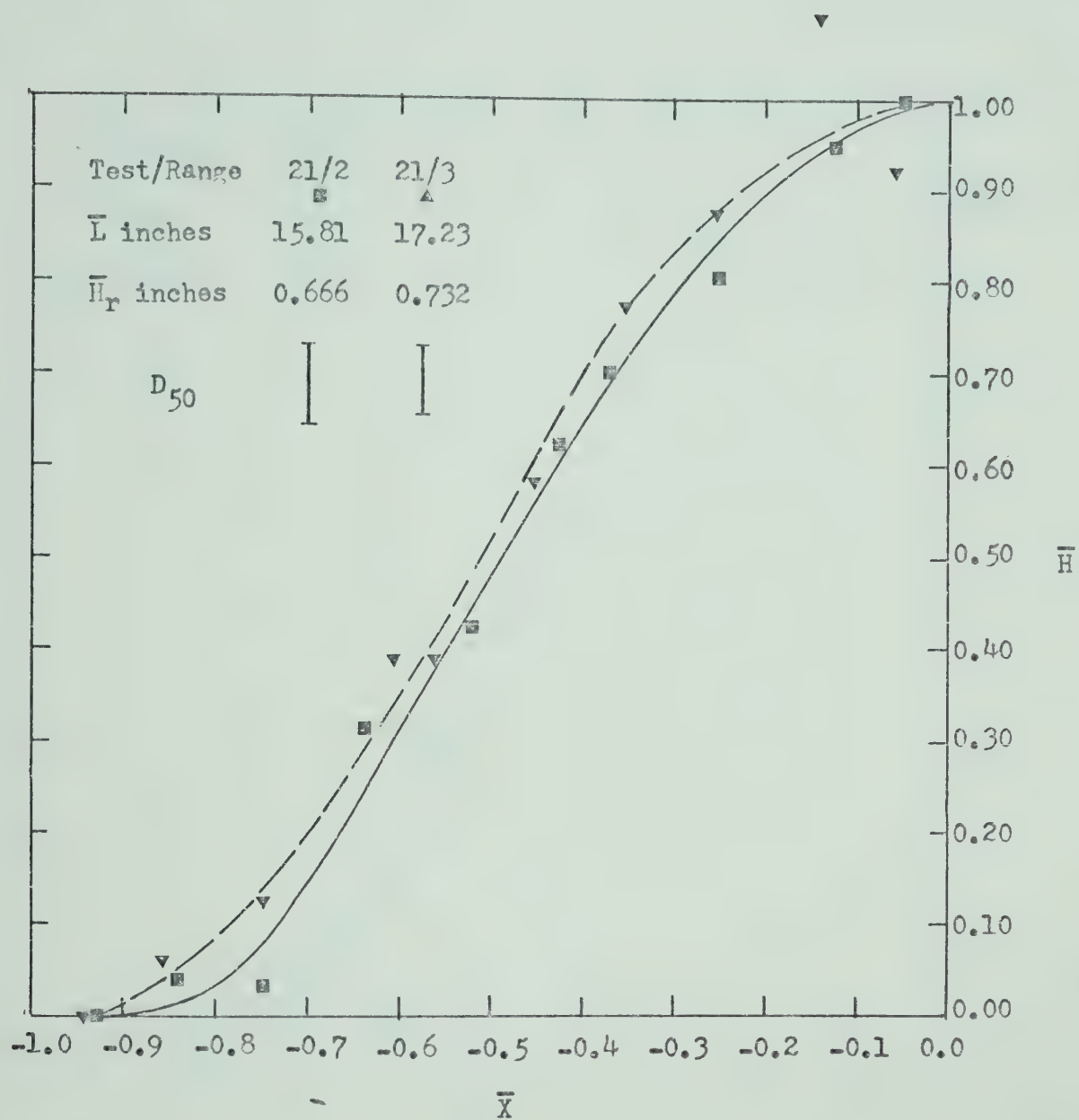


Figure 6.2(d). Mean Dimensionless Bed-Form Profiles,
Test 21, Range 2, and Test 21, Range 3.

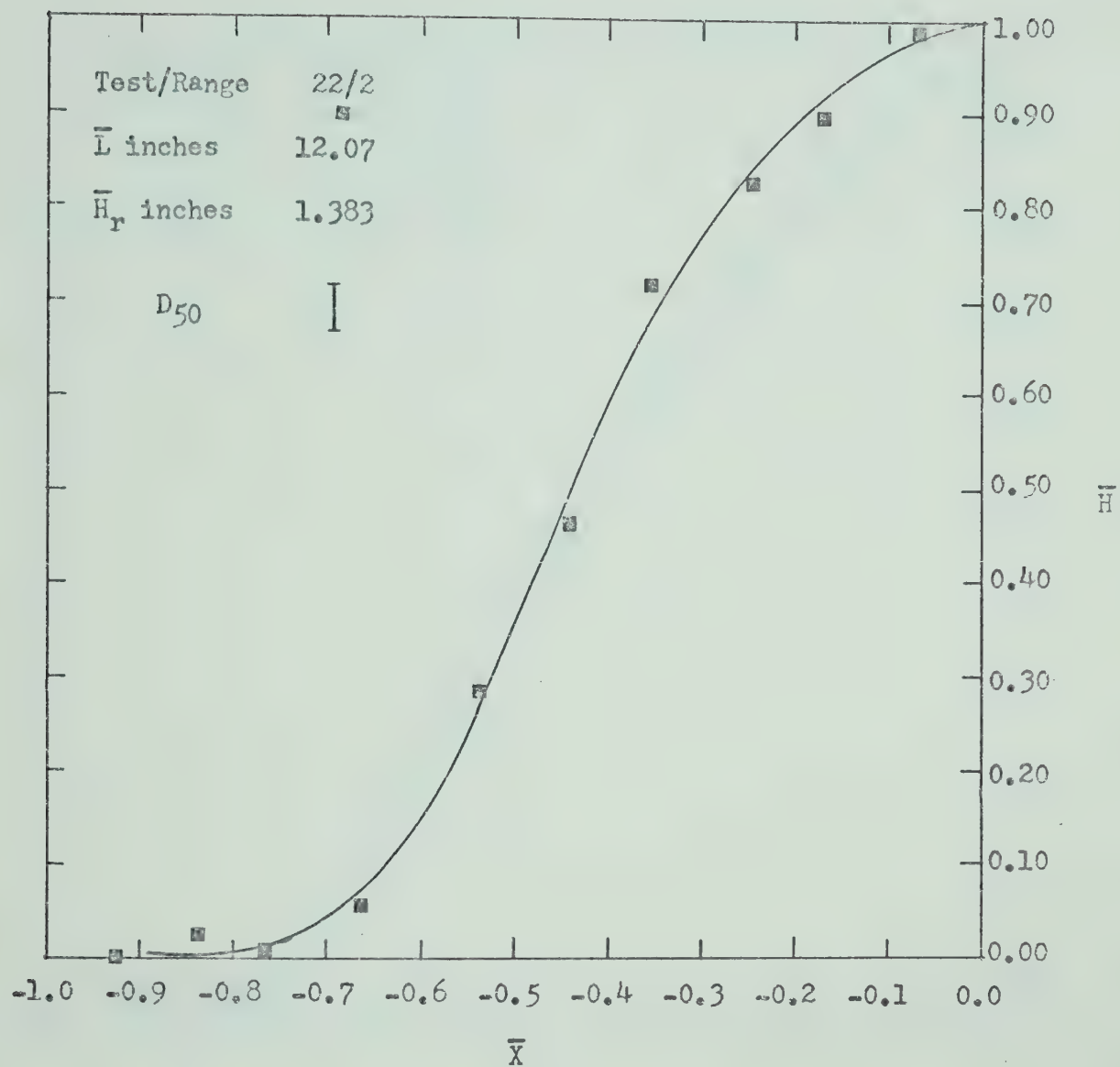


Figure 6.2(e). Mean Dimensionless Bed-Form Profiles,
 Test 22, Range 2.

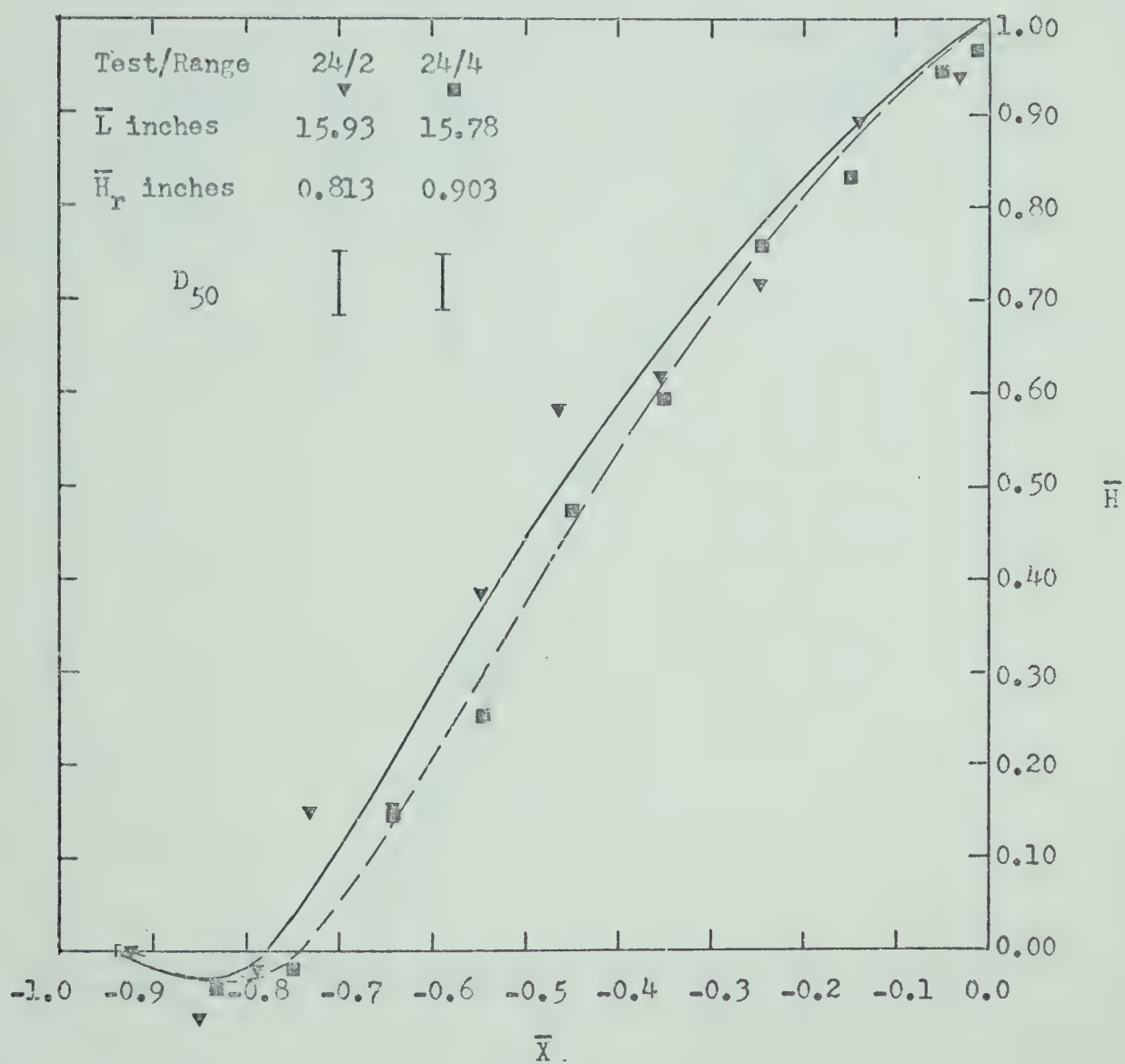


Figure 6.2(f). Mean Dimensionless Bed-Form Profiles,
Test 24, Range 2, and Test 24, Range 4.

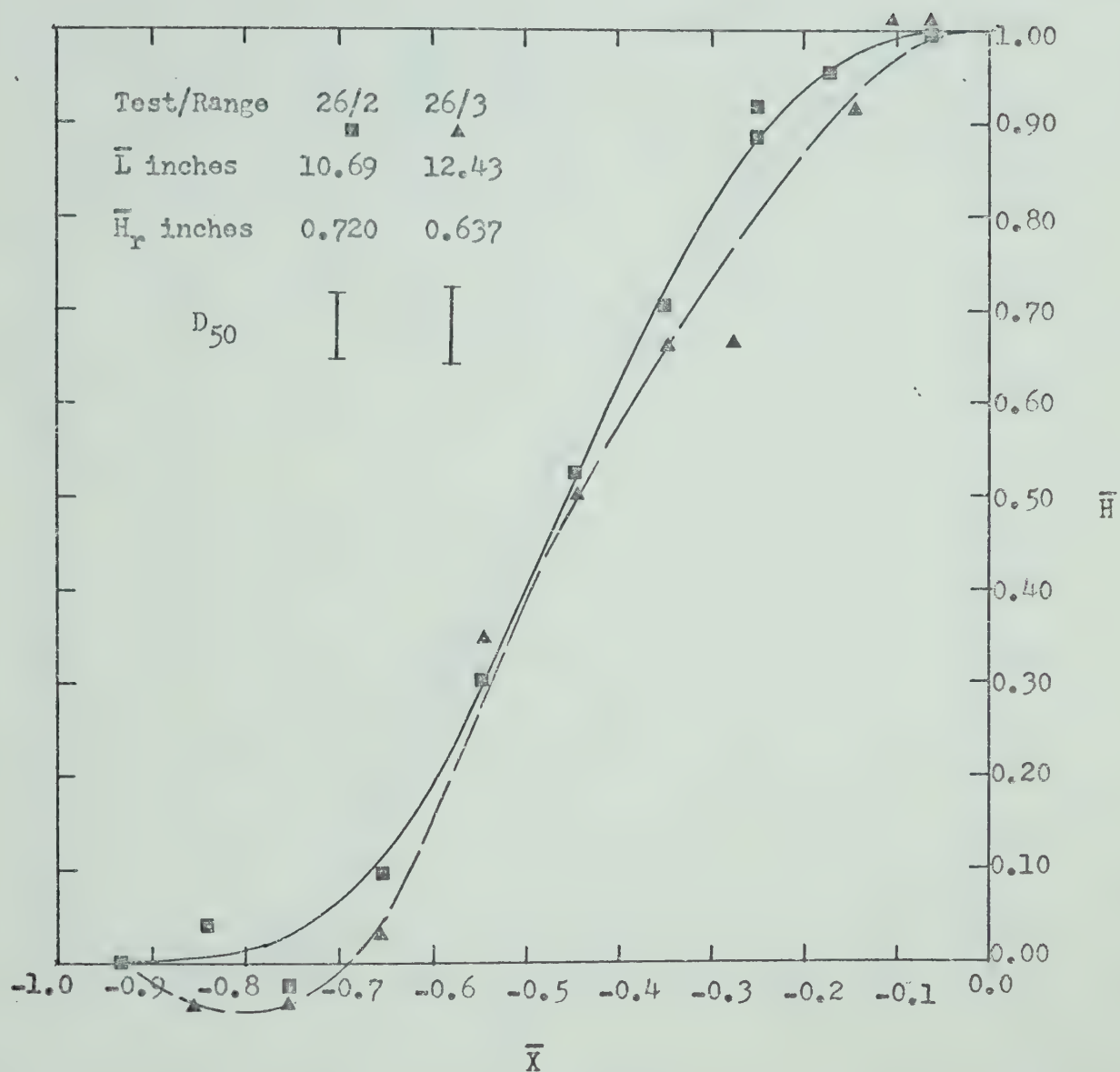


Figure 6.2(g). Mean Dimensionless Bed-Form Profiles,
Test 26, Range 2, and Test 26, Range 3.

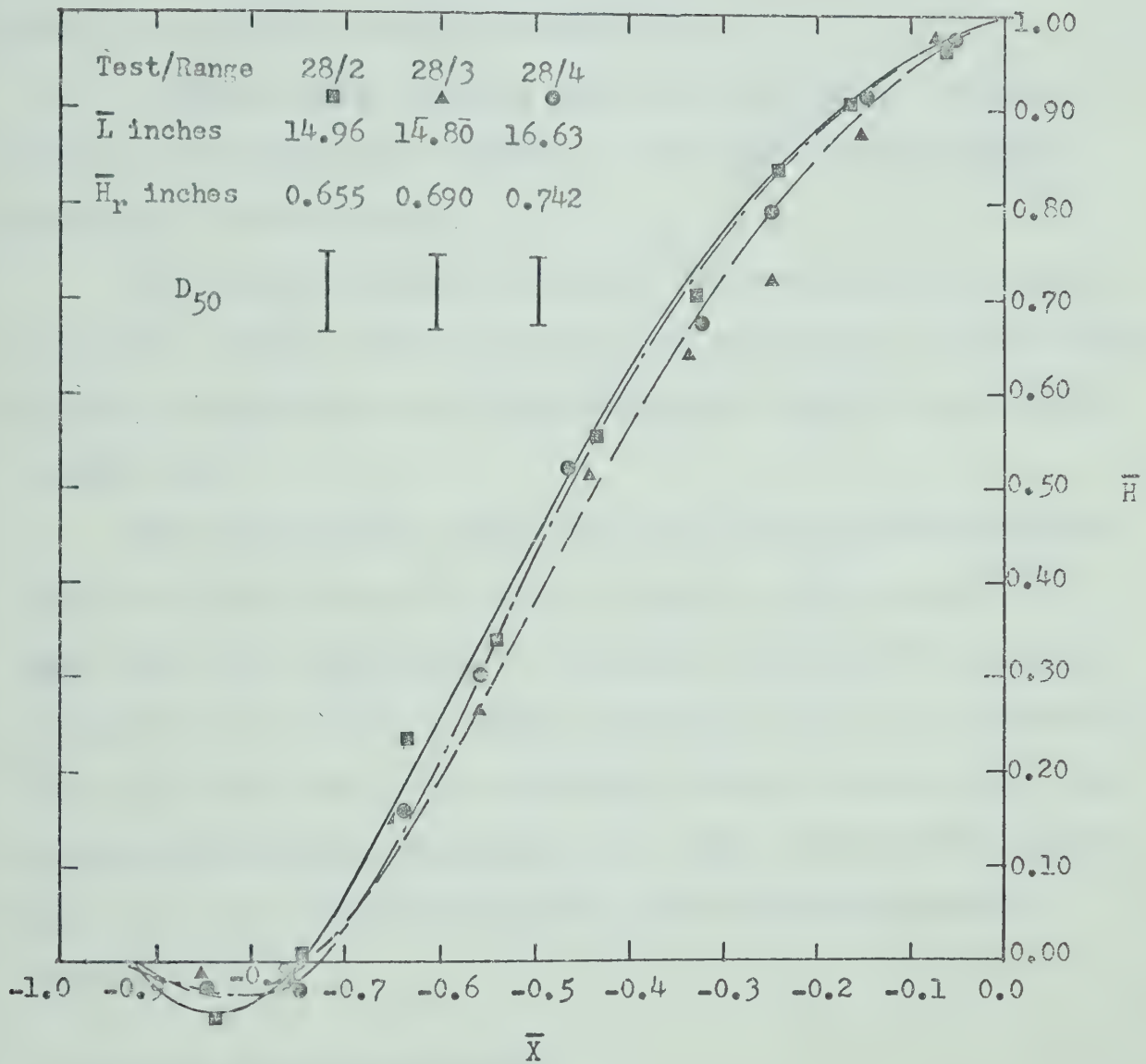


Figure 6.2(h). Mean Dimensionless Bed-Form Profiles,
Test 28, Range 2, Test 28, Range 3, and
Test 28, Range 4.

surface coordinate data points. The relative size of sediment grain shows that in the vertical the surface data points generally fall within one half grain diameter from any estimated surface profile line. This is within the predicted depth-wire reading error.

A common bed-form profile, developed by averaging \bar{H} values at each $0.1 \bar{X}$, is presented in Figure 6.3. Also shown are the limits of scatter of \bar{H} values at each \bar{X} .

The average horizontal position of the bed-form toes was found to be at $\bar{X} = -0.935$. With the exception of one bed-form, the scour below the mean toe elevation in the trough region was less than one particle diameter deep.

The smooth profile of the back of the bed-forms had its maximum slope in the range $-0.60 < \bar{X} < -0.45$. However, on five separate bed-forms (12/2, 17/2, 17/3, 24/2, and 24/4) the smooth profile appears to terminate in the first $0.1 \bar{L}$ segment upstream of the crest, followed by a sharp rise to the crest. This effect was observed visually during some of the experiments when it was noted that often a single particle at the apex of the crest rested slightly above its neighbouring particles upstream.

6.5 Entrainment and Transportation

6.5.1 General Observations

Visual observations indicated that the movement of individual bed particles as bed-load over bed-forms was intermittent. Particles were entrained on the upstream side of the bed-forms, transported along the surface in steps of random lengths and deposited in the lee of the bed-form crests. The particles then remained at rest buried within the bed-form until the continuous entrainment and transport of particles from the

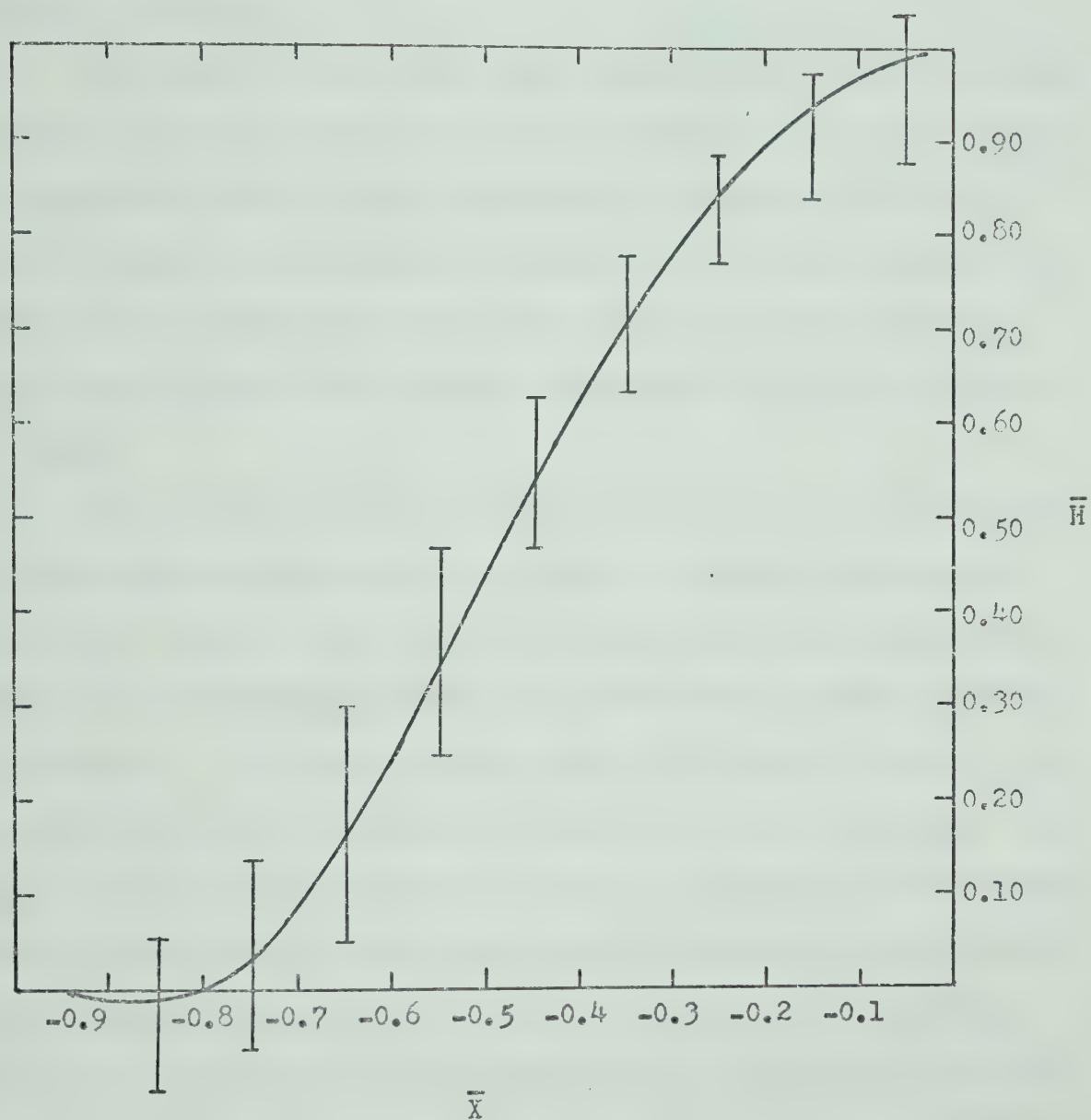


Figure 6.3. Average Dimensionless Bed-Form Profile

upstream side translated the entire bed-form downstream and re-exposed the buried particles for a repeated entrainment, transportation, and deposition sequence.

The period of time during which a particle remained at rest when buried in the bed-form depended upon the position at which the particle was deposited on the lee slope downstream of the crest. The further below the crest it became buried the longer was its time of rest. The distance of its path to the crest after re-exposure and entrainment was similarly longer if the particle was buried near the toe than near the crest.

Viewed from a stationary reference frame an individual particle is transported downstream along an irregular saw-tooth path shown in Figure 6.4. However, when viewed from a reference frame moving at the speed of the translating bed-form, the paths of the particles describe a near triangle. All particles buried within the bed-form recede in the upstream direction at a constant velocity of bed-form translation. When exposed on the upstream side of the bed-form they catch up with the crest with an average velocity much higher than the bed-form velocity itself. If the identity of individual particles is ignored and the bed-form material is considered as a deformable continuum, its motion may be represented by a system of "streamlines" illustrated in Figure 6.5. It suggests that the material in the bed-form rotates about a center located at the crest of the bed-form. Because of the translation of the bed-form, a relatively high angular velocity of rotation of material persists near the crest. The observed paths of particles partially confirm this phenomenon. Particles arriving along the bed were observed to lift slightly above the bed immediately upstream of the crest, and, after

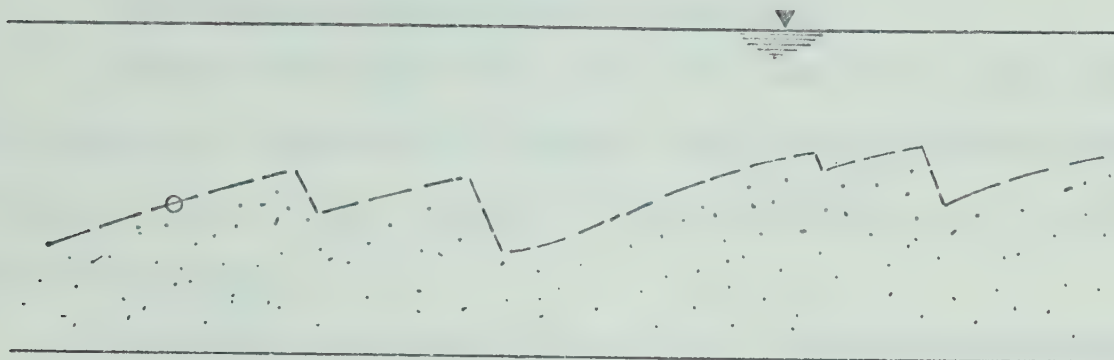


Figure 6.4. Particle Path in Stationary Reference Frame

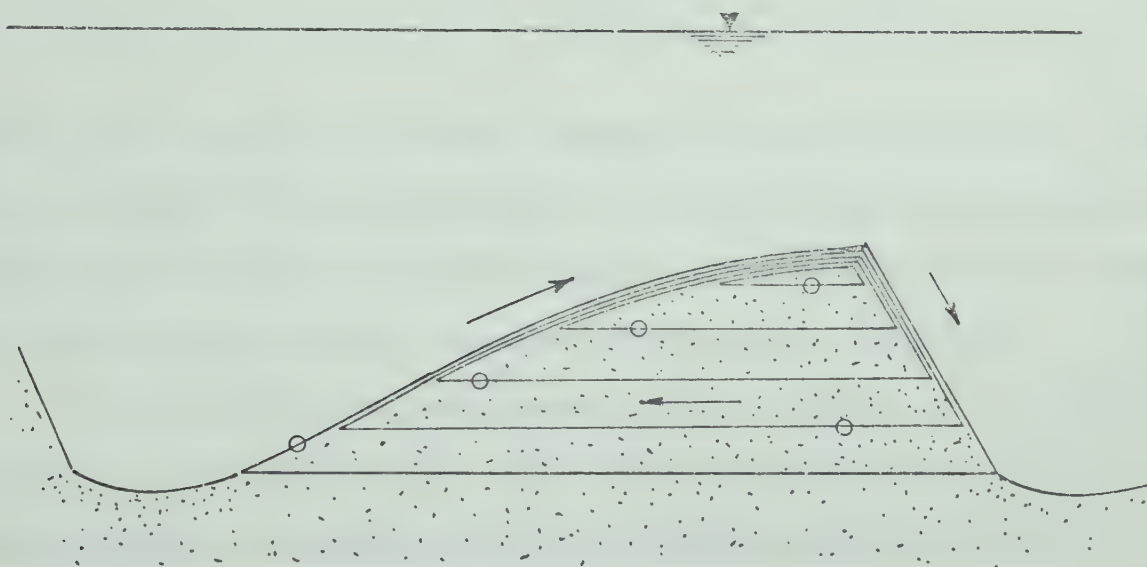


Figure 6.5. Particle Path in Moving Reference Frame

rounding the crest, were deposited near the crest on the lee slope of the bed-form.

6.5.2 Distribution and Rates of Entrainment

Particle entrainment rates (scour) and distribution and, hence, the production of sediment for transport along bed-form surfaces were estimated by two methods, namely: (1) depth-wire method, and (2) profile translation method.

In the depth-wire method, local rates of particle entrainment were calculated from all available depth-wire readings of a bed-form surface profile from the changes of bed elevation at a depth-wire between two subsequent observations using the following formula:

$$h' = \frac{h_1 - h_2}{t_2 - t_1} \quad (6.9)$$

where h_1 and h_2 are the depth-wire readings at observations times t_1 and t_2 respectively. The horizontal position of the computed entrainment rate was considered to be at mid-point between the two positions of the depth-wire in the moving reference frame as illustrated in Figure 6.6.

The distribution of entrainment rates was obtained by grouping the computed local entrainment rate data points into appropriate $0.1 \bar{L}$ segments along the bed-form profile and estimating the mean rate of entrainment from the following formula:

$$\bar{h}' = \frac{\sum_{i=1}^{n_s} h_i}{n_s} \quad (6.10)$$

where n_s is the number of data points in each segment.

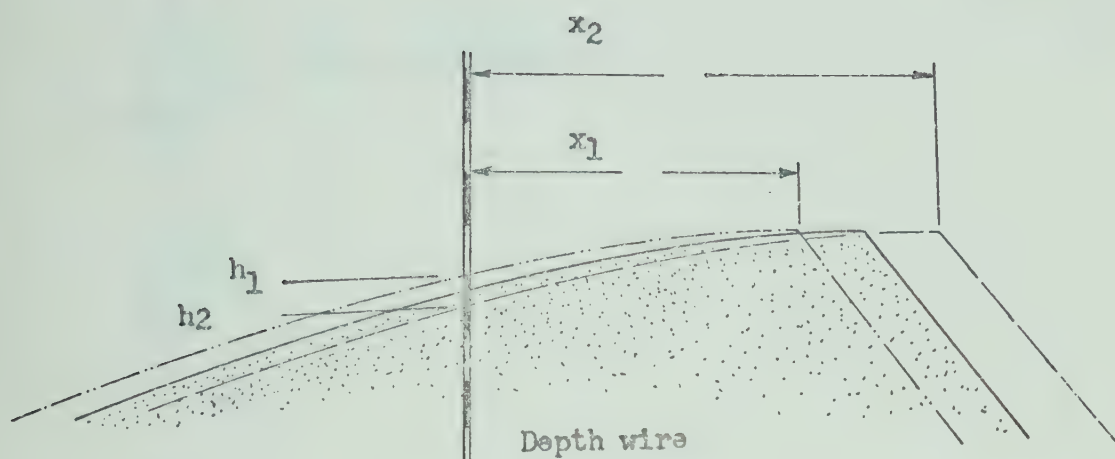


Figure 6.6. Definition Diagram for Entrainment Rate

The volumetric rate of bed-material entrainment g_b per unit width of bed-form from each segment was calculated by the following formula:

$$g_b = 0.1 \bar{L} \bar{h}' \quad (6.11)$$

The distributions of typical entrainment rates h' , calculated from results of tests 28/2 and 28/3 by the above method and rendered dimensionless by multiplying by the ratio of bed-form period to bed-form height, are illustrated in Figures 6.7(a) and 6.7(b). The horizontal position coordinate \bar{X} has been non-dimensionalized in accordance with equation 6.5. The scatter of the data reflects both the error in measure-

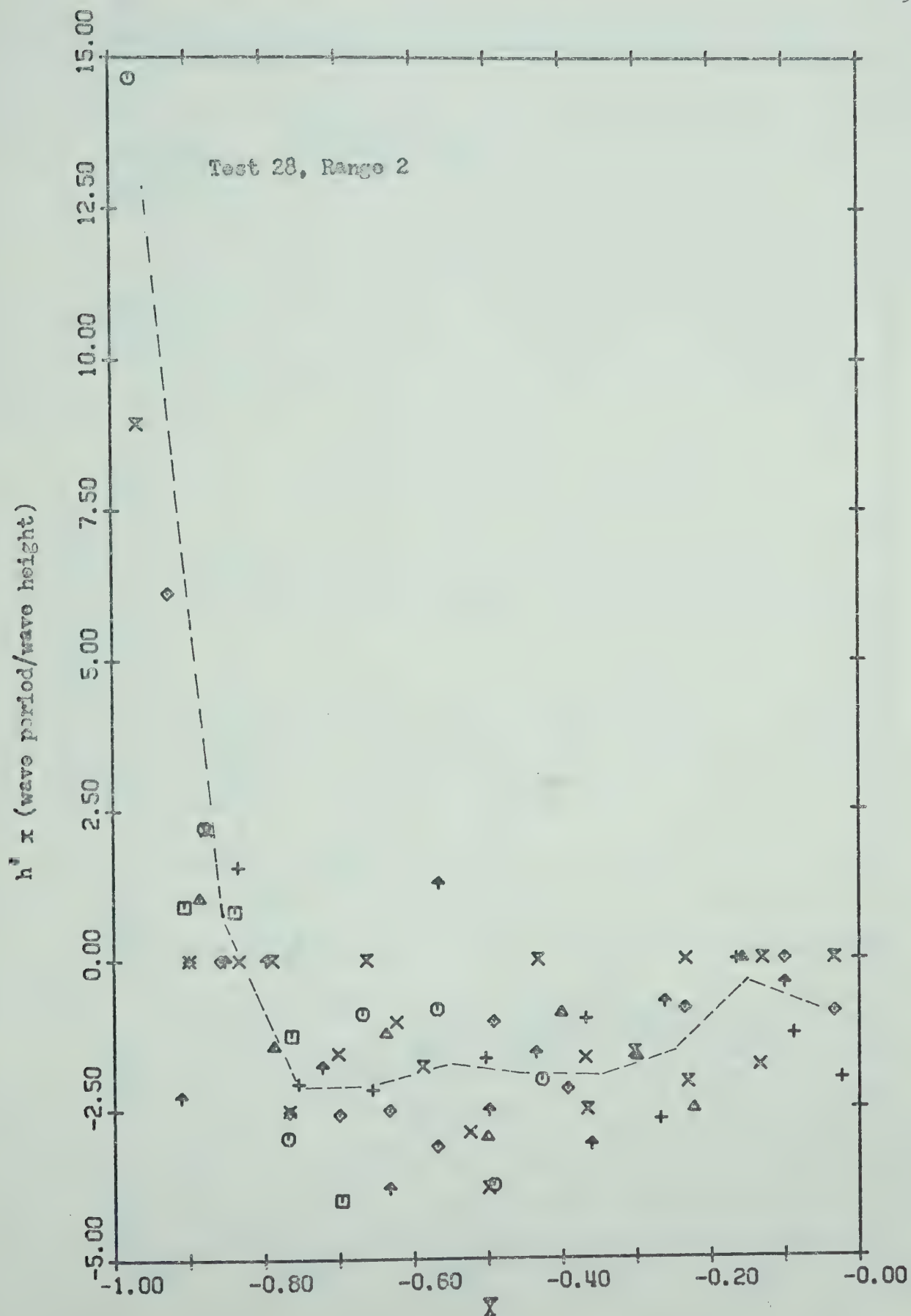


Figure 6.7(a). Typical Instantaneous Entrainment Rate Results

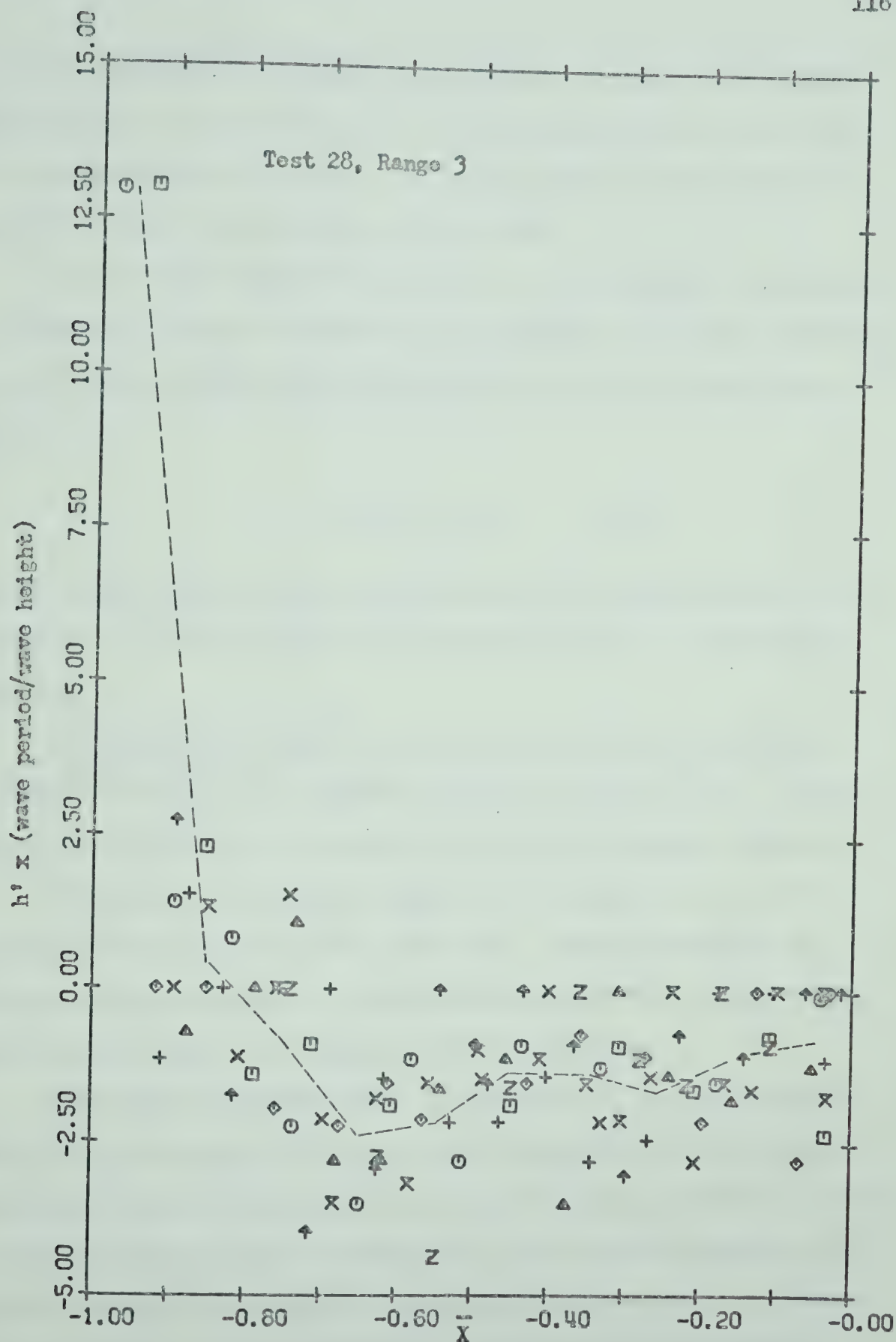


Figure 6.7(b). Typical Instantaneous Entrainment Rate Results

ment and the natural fluctuations of the sediment surface, due to intermittent movement of particles at the same relative position on the bed-form as it translates downstream. The average rates of entrainment \bar{h} distribution along the bed-forms are also shown.

In the second method, the volumetric rates of particle entrainment and distribution from the surface of a bed-form were determined employing the mean bed-form profile data and the velocity of its migration downstream \bar{V}_b from

$$g_b = \bar{V}_b(h_1^* - h_2^*) \quad (6.12)$$

where h_1^* and h_2^* represent the mean elevations of bed-form profile at the upstream and downstream bounds of a segment $0.1 \bar{L}$ long as illustrated in Figure 6.8.

The experimental entrainment rate and distribution results for the seventeen bed-forms are presented in Figures 6.9(a) to (q). The results of both methods of calculation are given for comparison purposes.

Entrainment of particles occurs at all locations of a bed-form where its surface slope is greater than zero. Scouring processes are therefore active downstream of the deepest position of the trough and deposition occurs between the trough and the toe upstream.

The maximum entrainment rate, as estimated by the mean profile method, occurs when $-0.6 < \bar{X} < -0.45$ which corresponds to the location of the maximum slope of bed-form surface. From the maximum position the rate of entrainment drops toward the crest and, in the opposite direction, toward the trough of the bed-form. In general, the same result is obtained by the depth-wire method of calculation but because of the numerical averaging procedure with a limited number of data points in each segment,

the entrainment distribution is not as uniform as the distribution by the profile method.

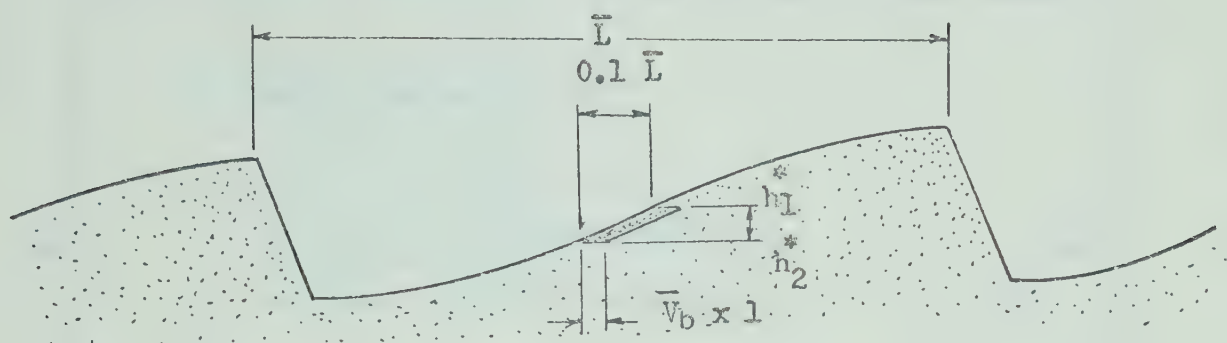


Figure 6.8. Definition Diagram for Entrainment Rate Calculation by Profile Translation Method

6.5.3 Sediment Transport

The distribution of sediment flux per unit width of a bed-form was then calculated by

$$G_{bs} = \sum_{i=1}^s (g_b)_i \quad (6.13)$$

where G_{bs} is the volumetric rate of sediment flux at the downstream limit of segment s as measured by the volume of bed-form scoured.

To determine the distribution of sediment flux on the surface of a bed-form from particle entrainment rates required also the knowledge of the position of zero net transport. In the present calculations this location was assumed to be at the mean position of the maximum pressure as determined from pressure measurements, and was verified by the total rate of sediment flux per unit width of the bed at crest G_{bc} computed from

$$G_{bc} = \bar{H}_l \bar{V}_b \quad (6.14)$$

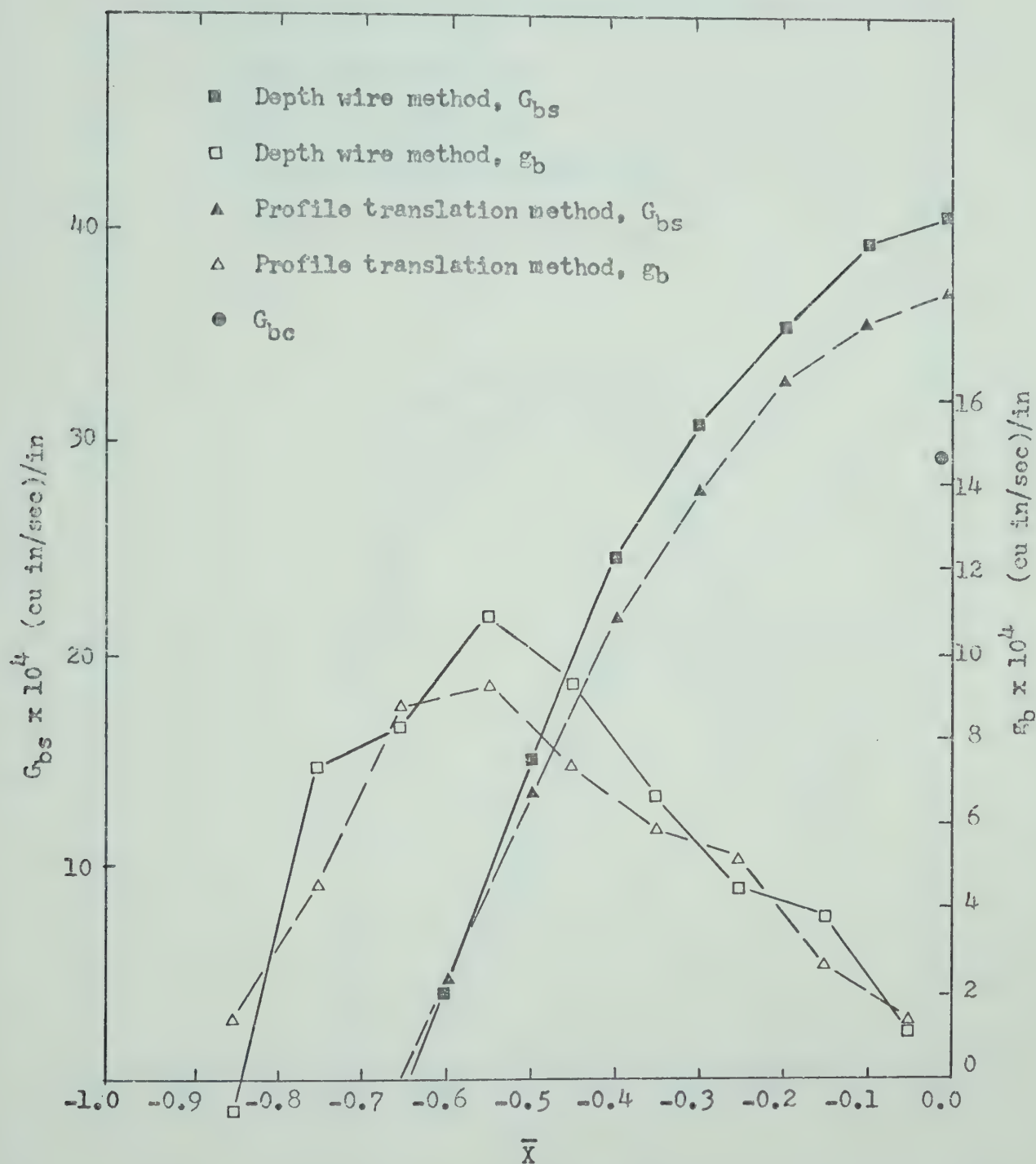


Figure 6.9(a). Distribution of Particle Entrainment and Transport Rates, Test 11, Range 2.

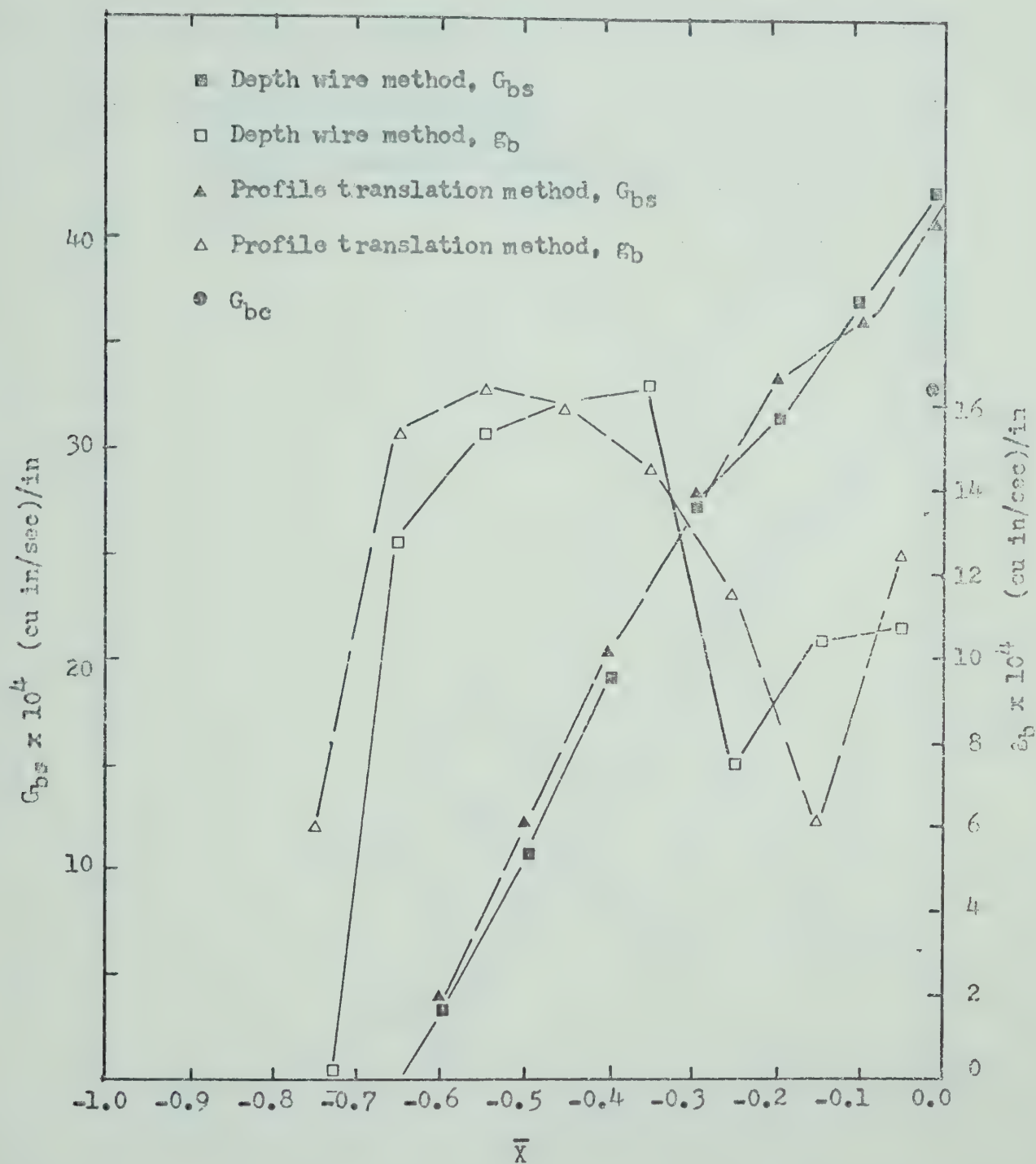


Figure 6.9(b). Distribution of Particle Entrainment and Transport Rates, Test 12 Range 2.

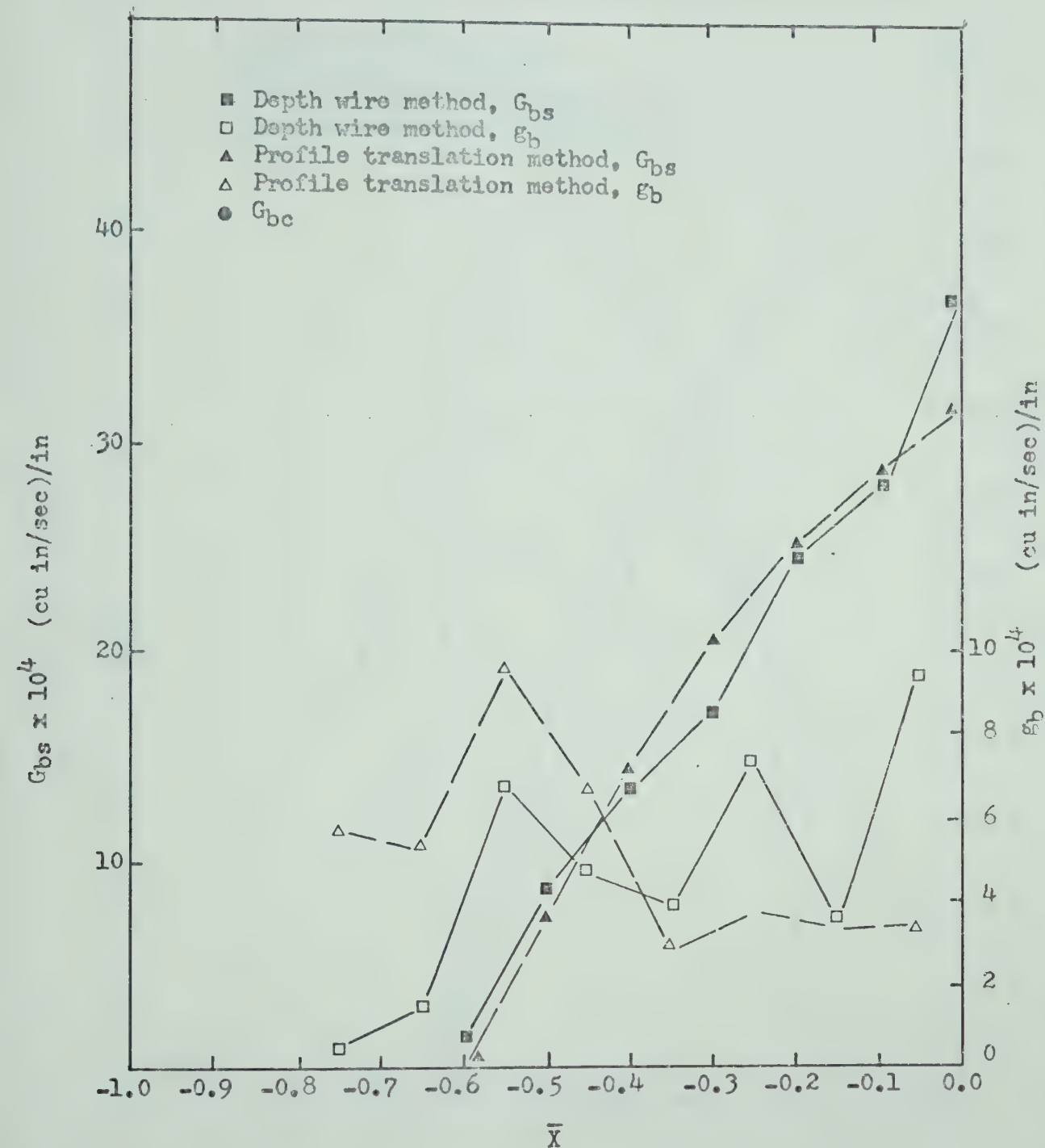


Figure 6.9(c). Distribution of Particle Entrainment and Transport Rates, Test 17, Range 2.

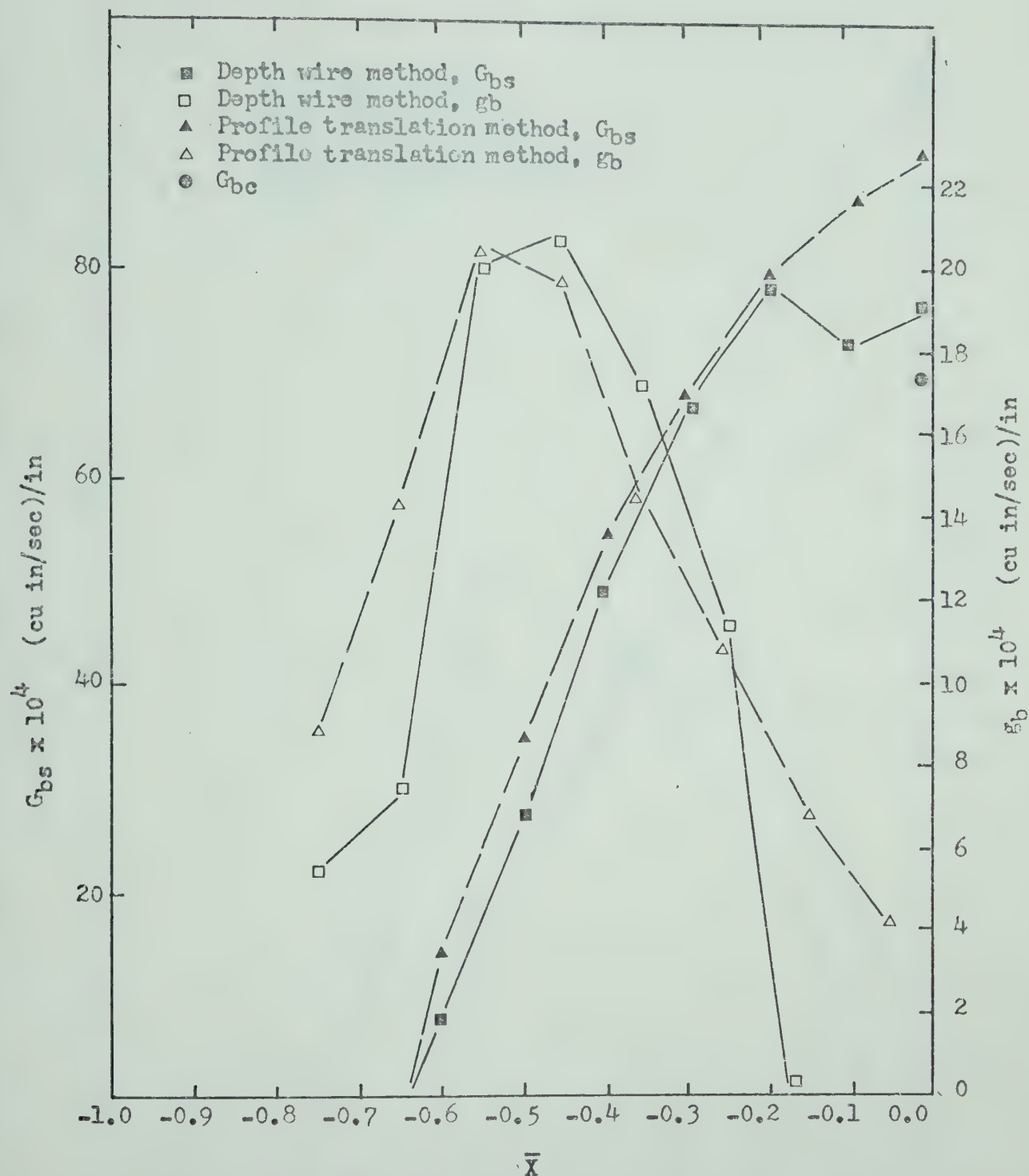


Figure 6.9(d). Distribution of Particle Entrainment and Transport Rates, Test 17, Range 3.

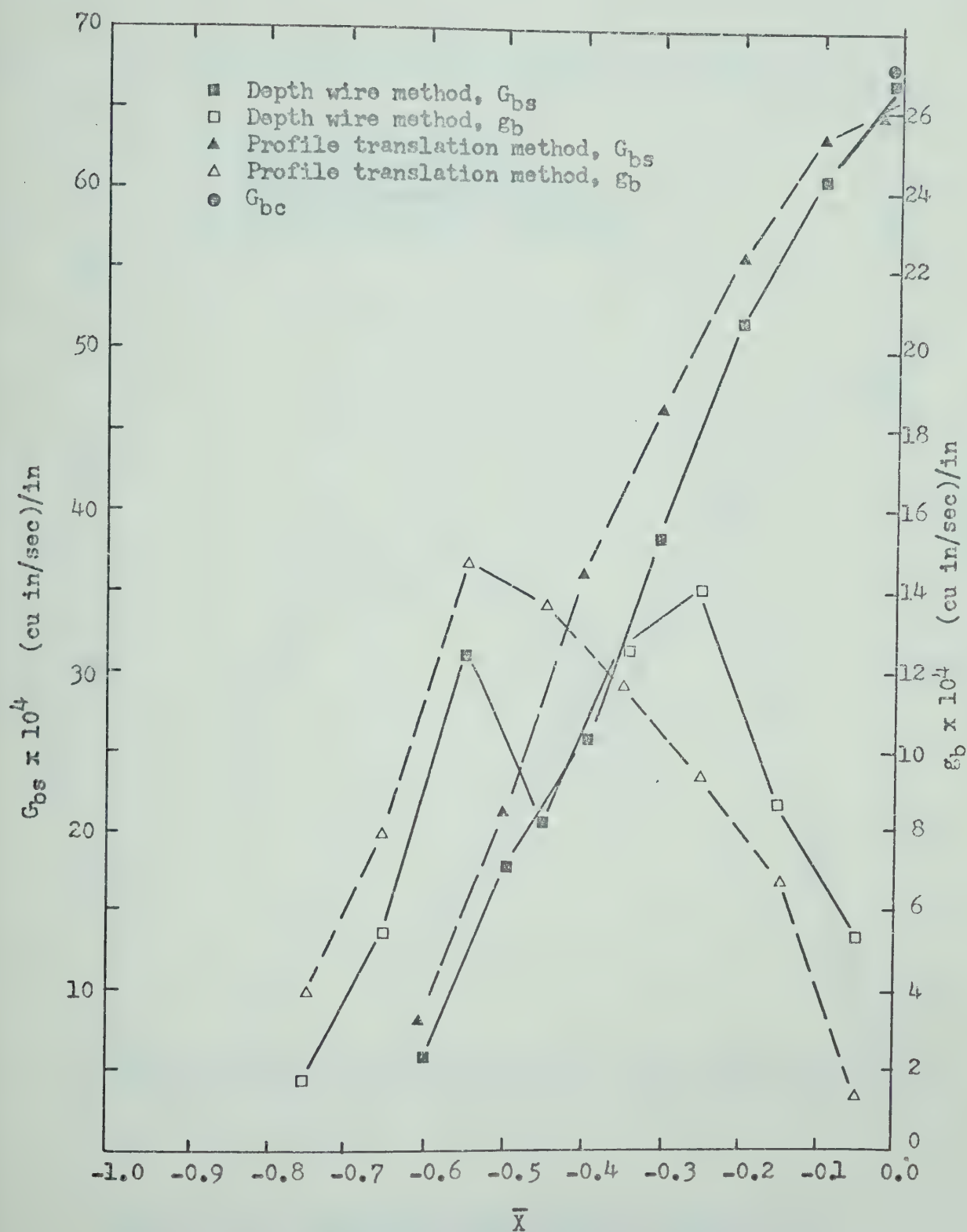


Figure 6.9(e). Distribution of Particle Entrainment and Transport Rates, Test 20, Range 2.

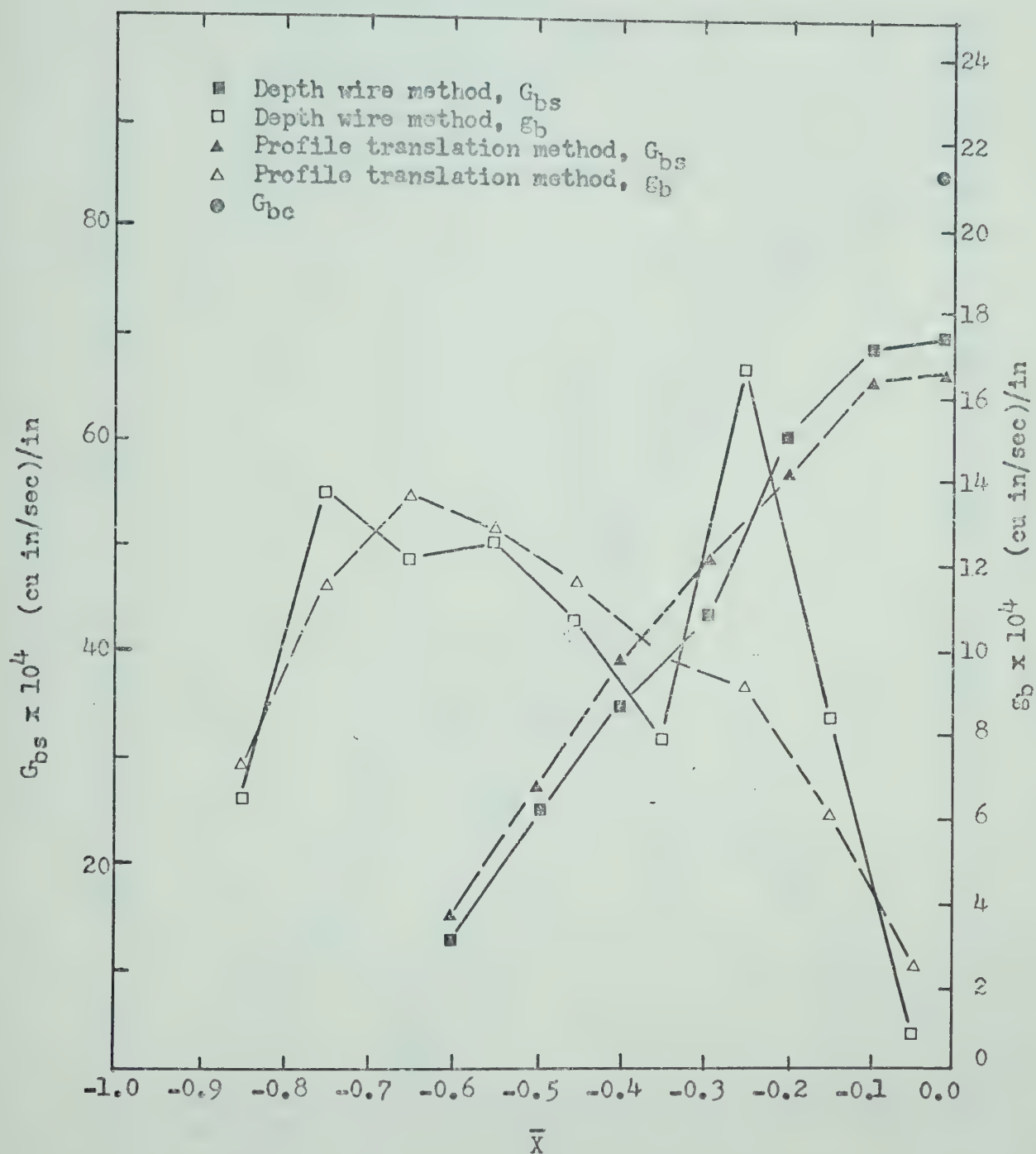


Figure 6.9(f). Distribution of Particle Entrainment and Transport Rates, Test 20, Range 3.

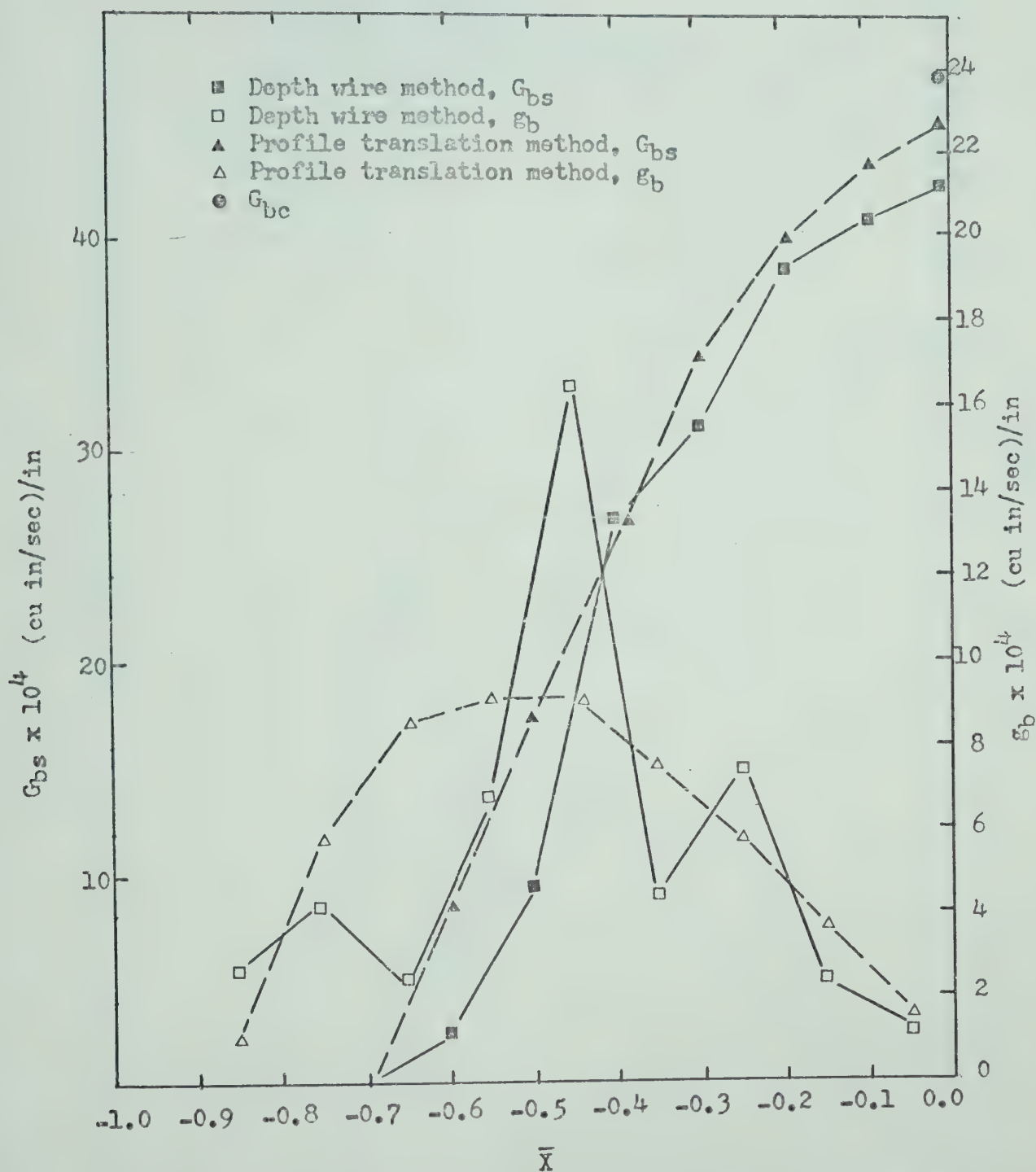


Figure 6.9(g). Distribution of Particle Entrainment and Transport Rates, Test 21, Range 2.

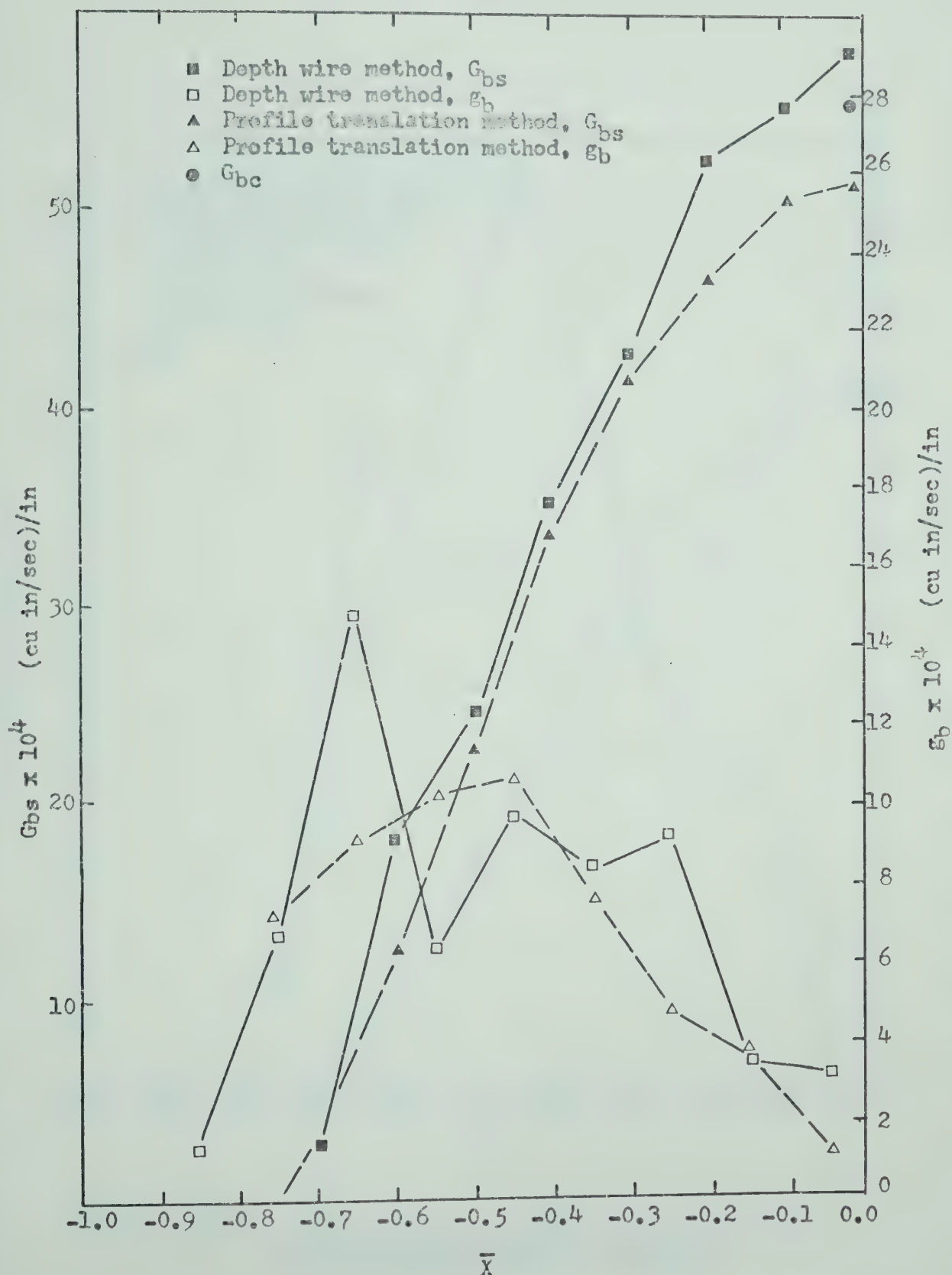


Figure 6.9(h). Distribution of Particle Entrainment and Transport Rates, Test 21, Range 3.

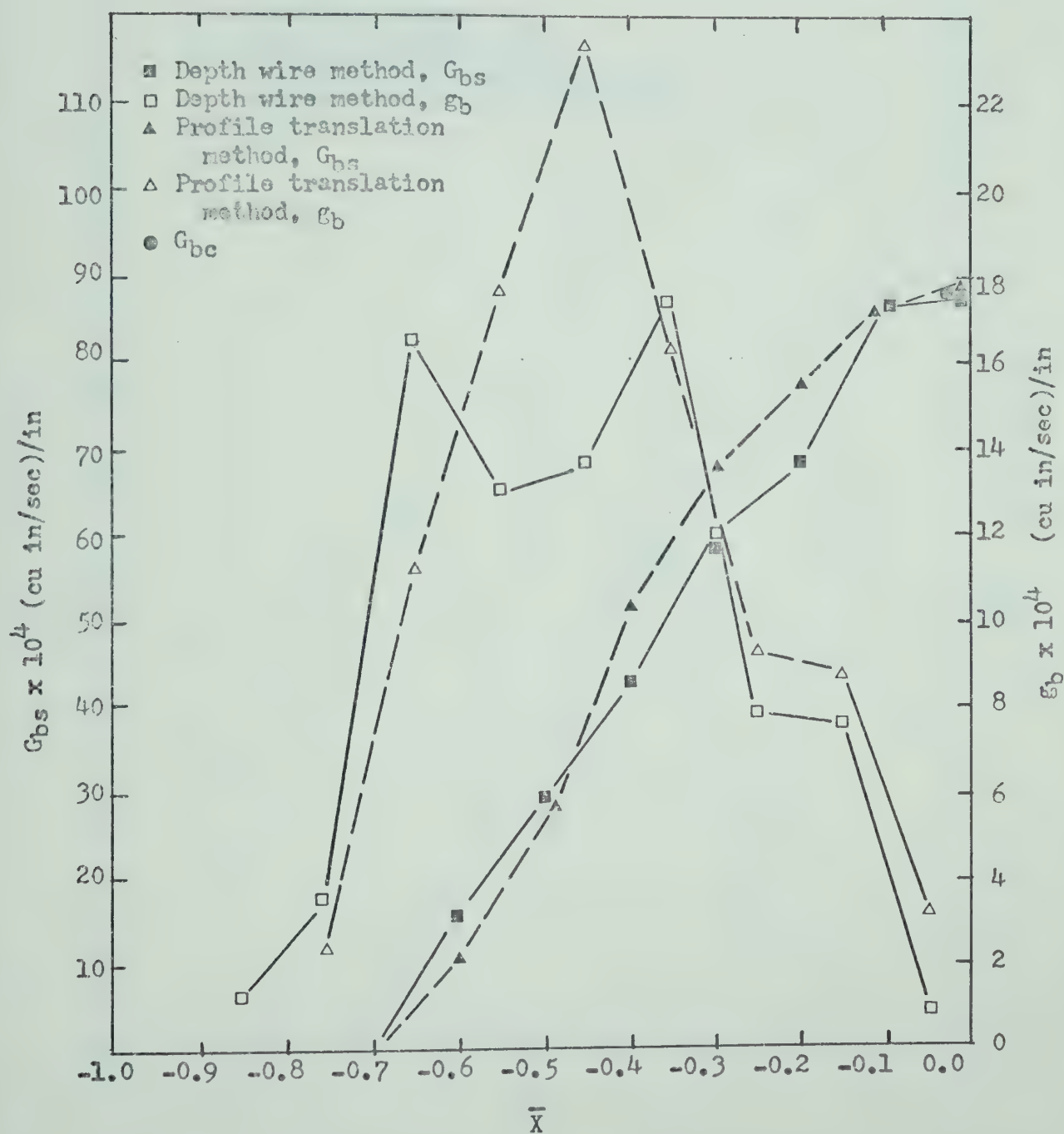


Figure 6.9(1). Distribution of Particle Entrainment and Transport Rates, Test 22, Range 2.

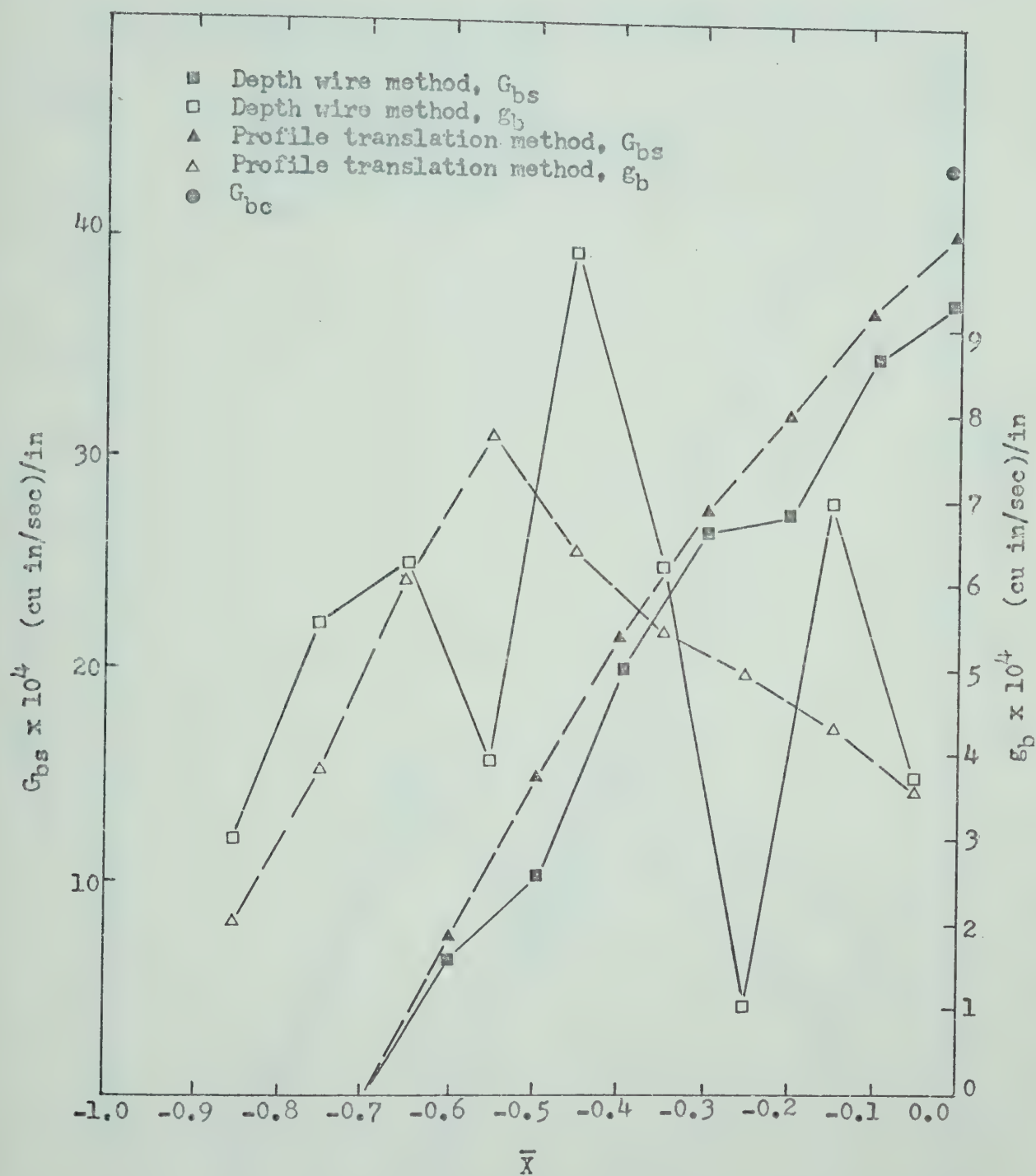


Figure 6.9(j). Distribution of Particle Entrainment and Transport Rates, Test 24, Range 2.

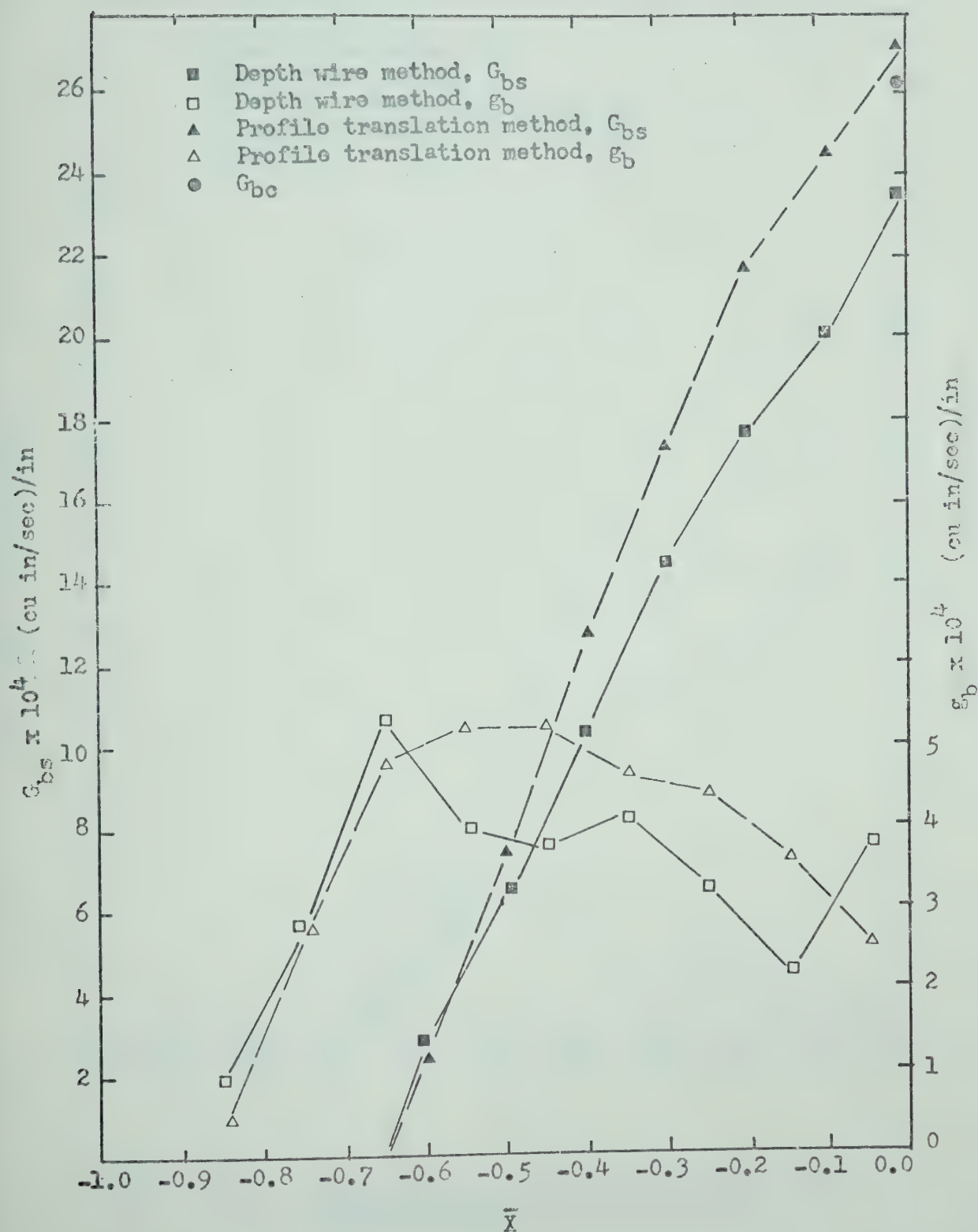


Figure 6.9(k). Distribution of Particle Entrainment and Transport Rates, Test 24, Range 4.

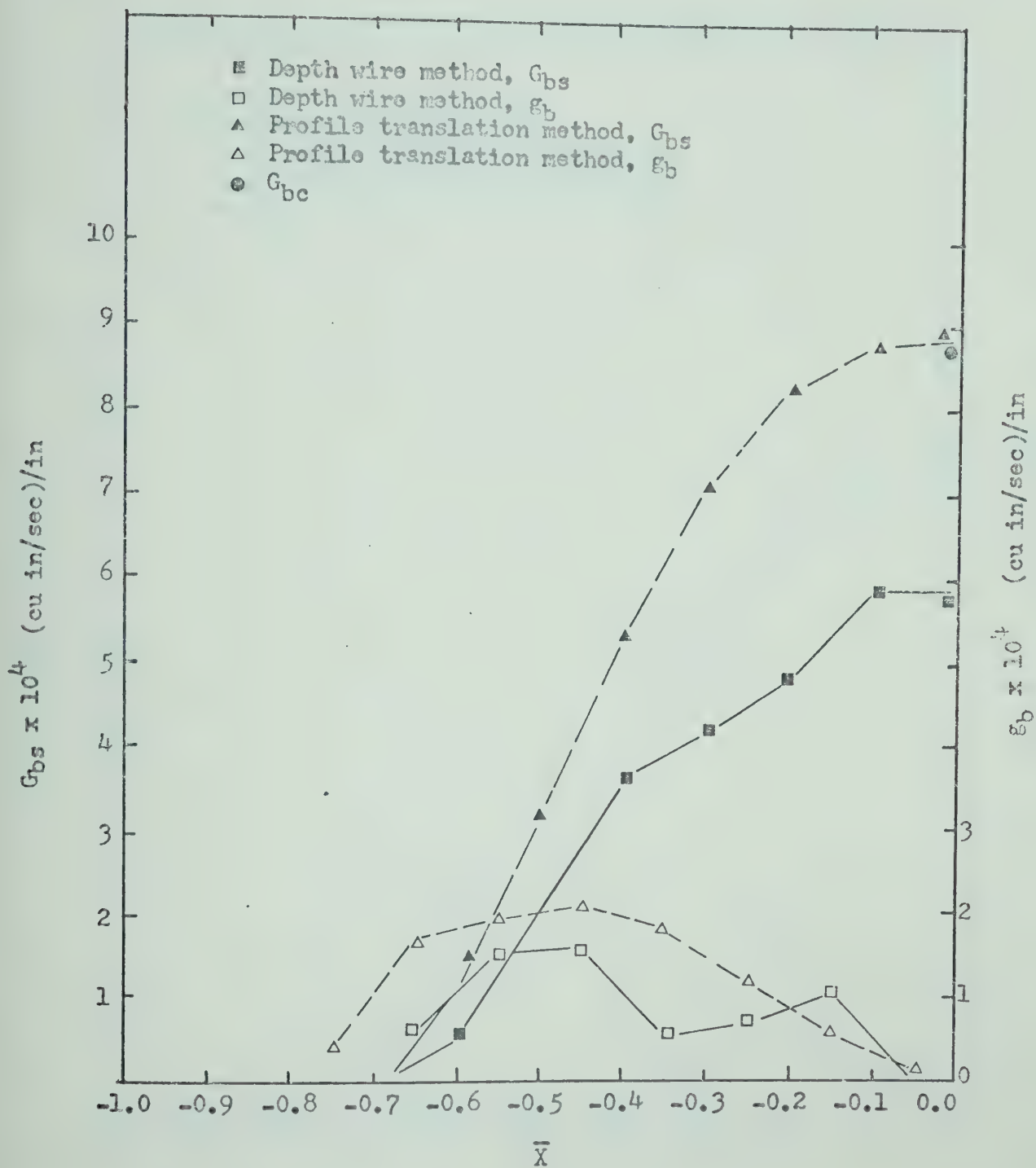


Figure 6.9(1). Distribution of Particle Entrainment and Transport Rates, Test 26, Range 2.

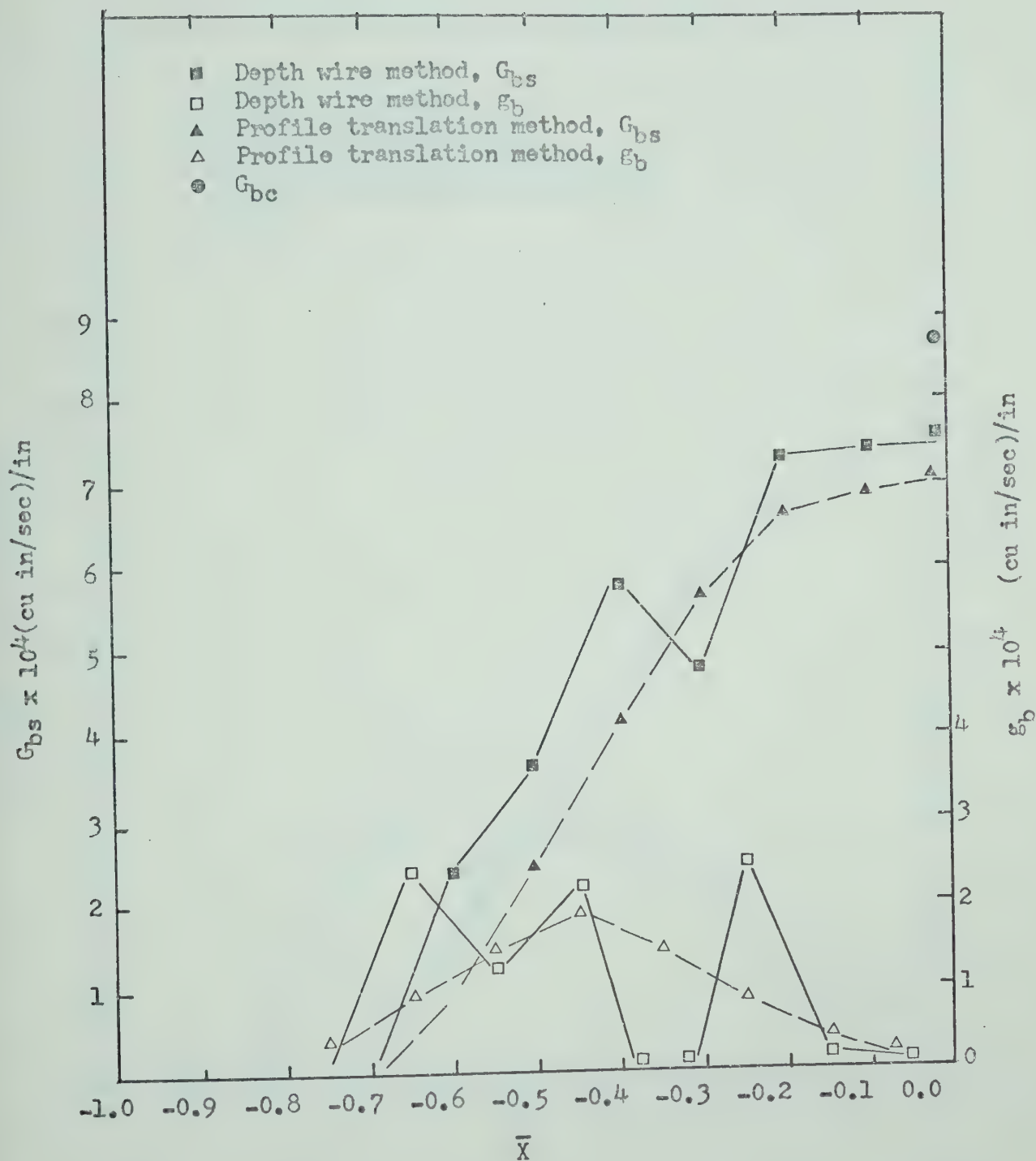


Figure 6.9(m). Distribution of Particle Entrainment and Transport Rates, Test 26, Range 3.

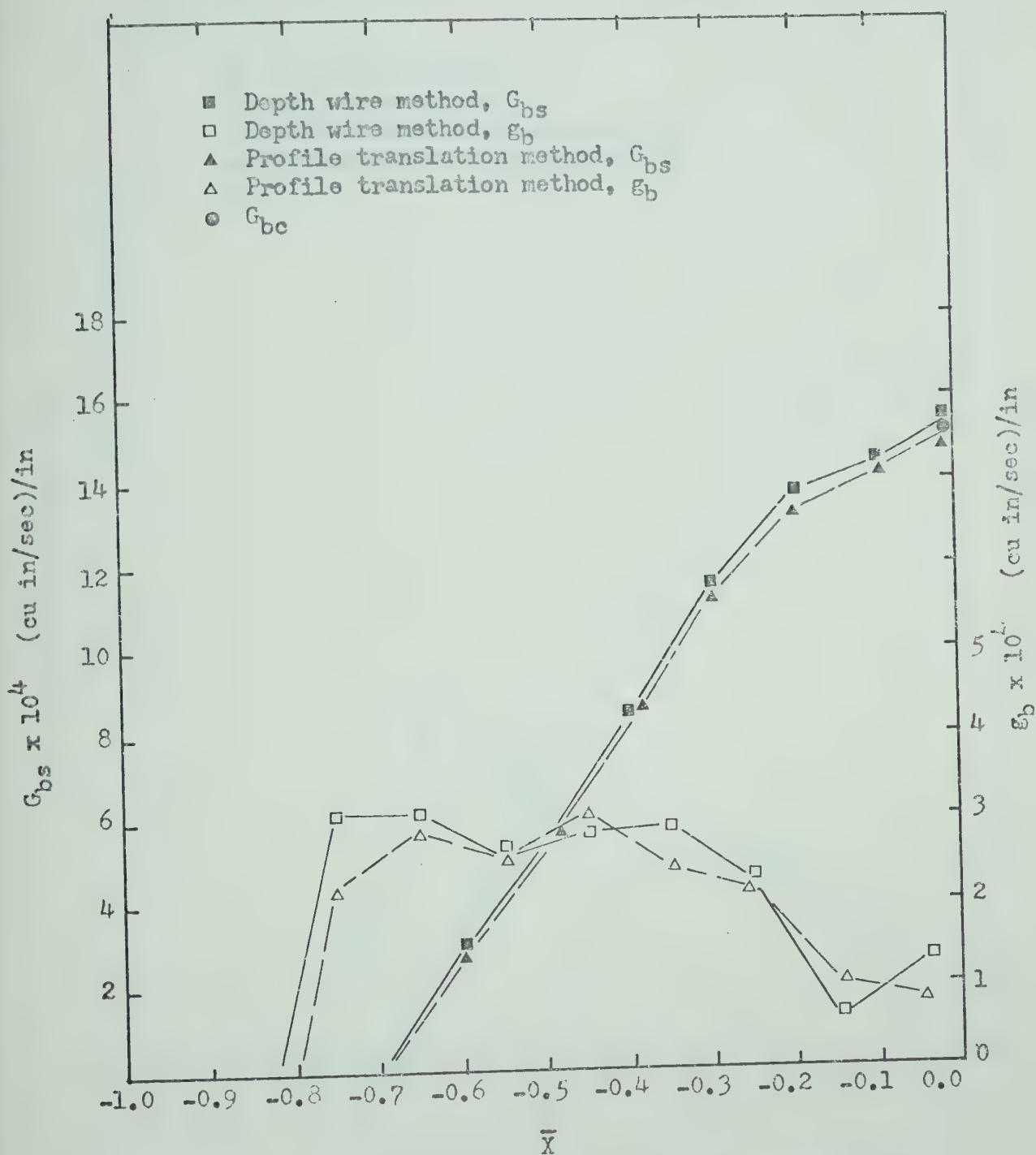


Figure 6.9(n). Distribution of Particle Entrainment and Transport Rates, Test 28, Range 2.

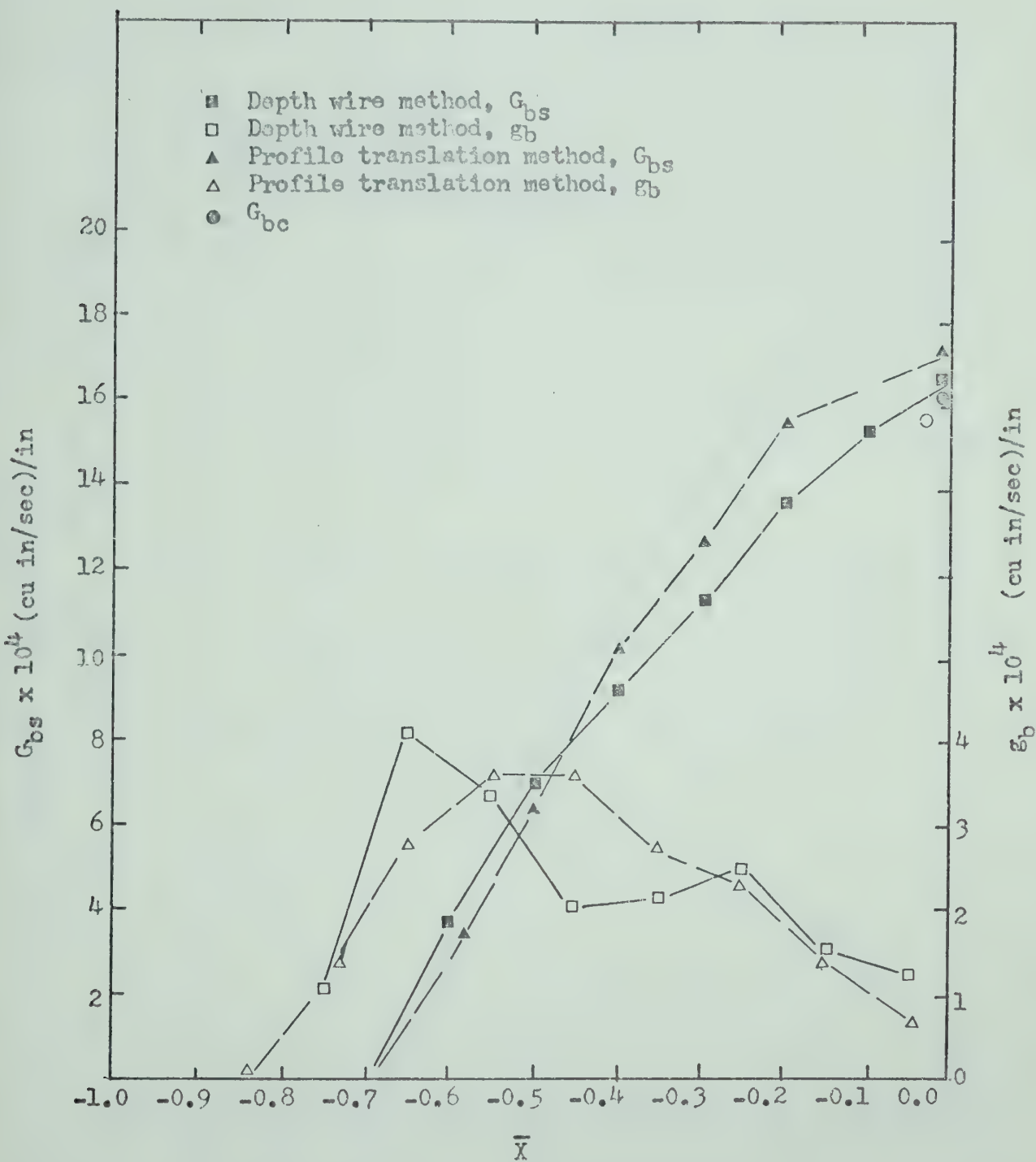


Figure 6.9(o). Distribution of Particle Entrainment and Transport Rates, Test 28, Range 3.

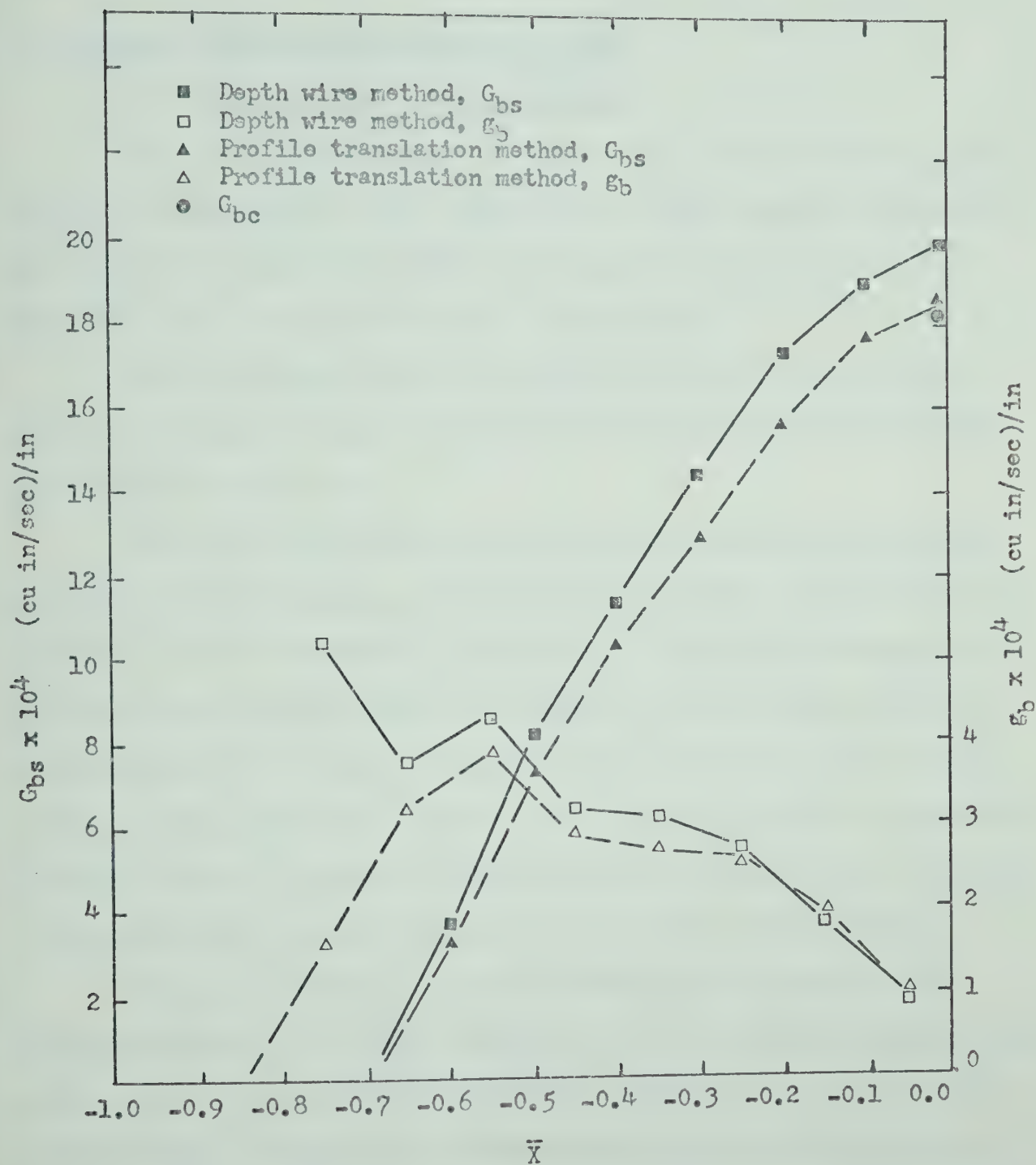


Figure 6.9(p). Distribution of Particle Entrainment and Transport Rates, Test 28, Range 4.

The sediment flux distribution on individual bed-forms is shown also in Figures 6.9(a) to (q).

6.6 Hydrogen Bubble Velocity Measurement Data

6.6.1 Instantaneous Velocity Profiles

The term "instantaneous" as used in this context denotes a point velocity or a velocity profile determined from the separation distance of two rows of hydrogen bubbles which were separately introduced into the flow at a short, usually 0.1 second, time interval.

The instantaneous velocity profiles parallel to the surface of flow were established from point velocities measured at different depths in the flow above the bed.

The number and spacing of depths at which point velocities were determined varied depending upon the uniformity of the separation distance of the two rows of bubbles on a photograph. If the spacing between the rows was uniform bubble separation distances were determined only at the extreme limits of the uniform separation zone. However, where velocity gradients were pronounced, such as near the sediment boundary, separation distances between the rows were determined at additional depths to provide sufficient number of points to properly define the velocity profile.

Although an attempt was made to determine the spacing of the hydrogen bubbles at the top of particles, the reflection of light from the white coloured sediment obscured the rows of bubbles in the near vicinity of the boundary. Hence, the transcribed data from this region cannot be considered as accurate. In some photographs, however, because of more favorable viewing angle or shadows developed by slight lateral slopes of the bed, the bubble rows were discerned at the top of boundary particles and the estimated flow velocities parallel to the bed were found to range

from zero to various finite values. The point velocity of flow at any depth below the surface was calculated by

$$u_y = \frac{(a_1 - a_2)r_s}{n_p \cdot T} \quad (6.15)$$

where u_y is the estimated point velocity at a distance y above the bed, a_1 and a_2 are the distances from the hydrogen bubble wire to the first (downstream) and second (upstream) row of bubbles respectively, n_p is the number of full pulse cycles between the rows of bubbles used in computation, T represents period of one pulse cycle, and r_s is the scale of the photograph.

The instantaneous velocity profiles were determined from point velocities measured at different depths of the flow. The horizontal position of a profile was assumed to be at the mid-point between two rows of bubbles used in surface velocity calculation. Since the time of the observation was known, the horizontal coordinate of the moving reference frame x_0 was determined either by interpolating the position of the controlling crest between two subsequent bed-form profile observations or from regression line of the crest position, and the coordinate of the instantaneous velocity profile in relation to the geometry of the bed-form, \bar{x}_v , was calculated in the dimensionless coordinate system by

$$\bar{x}_v = \frac{x_v - x_0}{\bar{L}} \quad (6.15)$$

where x_v is the position of the velocity profile in the fixed reference frame.

6.6.2 Flow Discharge Comparison

The hydrogen bubble method of velocity measurement was verified

against gross errors by comparing flow discharge measured by the flow meter with average discharge determined from all hydrogen bubble profiles in a test. The mean instantaneous flow velocity U_m was computed assuming linear velocity variation between adjacent point velocities on the instantaneous profile and using the local depth at the pulsing wire. The results of the comparison based on discharges per unit width of the flume are presented in Figure 6.10. Generally, the discrepancies between the observed and the metered discharges do not exceed ten per cent. They were attributed to two causes: (1) insufficient number of instantaneous velocity profiles in some tests to define accurately the average discharge, and (2) the retardation of flow near the side walls of the flume which reduced the true discharge value along the centre of the flume.

6.6.3 Dimensionless Velocity Profiles

Preliminary examination of instantaneous velocity profiles taken at short intervals of time and at the same relative positions to the bed-form showed, however, that large scale velocity fluctuations existed throughout the depth of flow. To develop average velocity profile characteristics corresponding to the actual flow above an individual bed-form by statistical means, a much larger number of instantaneous velocity profiles was therefore required than was available.

General considerations discussed previously in Section 4.3.4 indicated, however, that the bed-forms were exclusively in the dune phase. Assuming that the flow characteristics above dunes were similar, average velocity profiles were developed by combining all available velocity measurement information.

All instantaneous velocity profiles were non-dimensionalized into two sets. In the first set, dimensionless velocities were obtained by dividing the point velocity at any depth of flow by the instantaneous mean

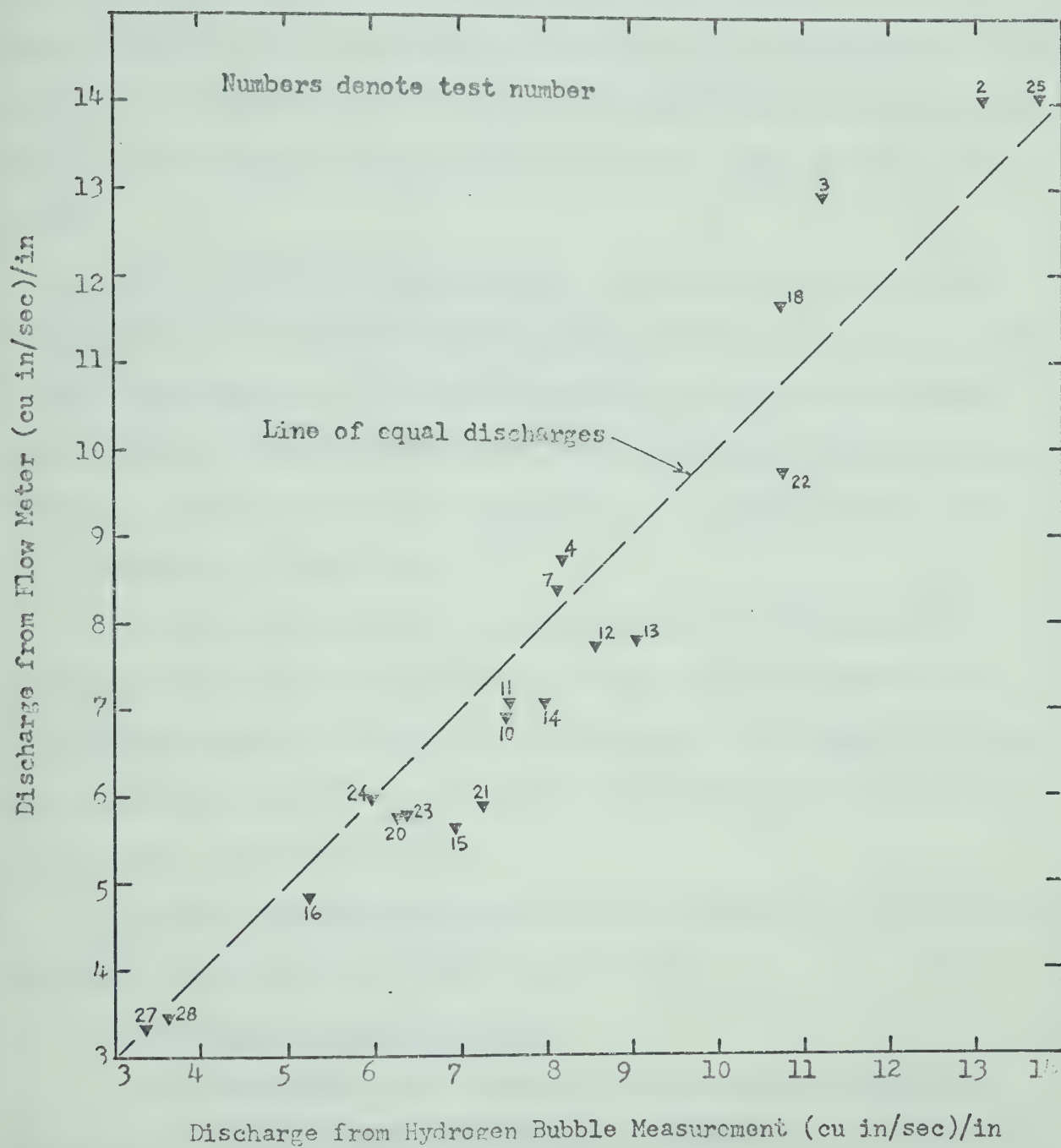


Figure 6.10. Comparison of Discharge Measurement.

velocity determined from the instantaneous profile. In the second set, the observed velocities at different depths were divided by the instantaneous velocity at the free surface of the flow. The dimensionless depth in both sets was calculated by dividing the vertical distance from the sediment bed to the point velocity depth by the total depth of flow at the wire.

All instantaneous dimensionless velocity profiles were grouped by position of observation relative to the crest into ten $0.1 \bar{L}$ segments along a dimensionless bed-form as previously was done with bed profile data. A group of instantaneous dimensionless profiles based on the instantaneous mean velocity and belonging to the segment $-0.3 < \bar{X} < -0.2$ is illustrated in Figure 6.11.

The mean dimensionless velocity profile in each segment was determined by averaging the instantaneous u/U_m or u/U_s velocities at ten dimensionless depths. Starting at the surface of the sediment particles, the instantaneous profiles at $0.0625 \frac{Y}{d}$, $0.125 \frac{Y}{d}$ and every other $0.125 \frac{Y}{d}$ level to the surface of the flow.

The two sets of dimensionless velocity profiles of flow above the bed-forms are presented in Figures 6.12 and 6.13.

6.6.4 Equal Mean Velocity Lines

The dimensionless mean velocity profiles given in Figure 6.12 illustrate local flow features at different locations above a bed-form. However, they cannot be used to demonstrate relative velocity characteristics along the length of a bed-form because each profile is referenced to the local depth of flow which varies along the bed-form.

The mean flow characteristics as represented by equal velocity lines along a bed-form are illustrated in Figure 6.14. The bed-form profile was developed from dimensionless mean profile coordinates given in

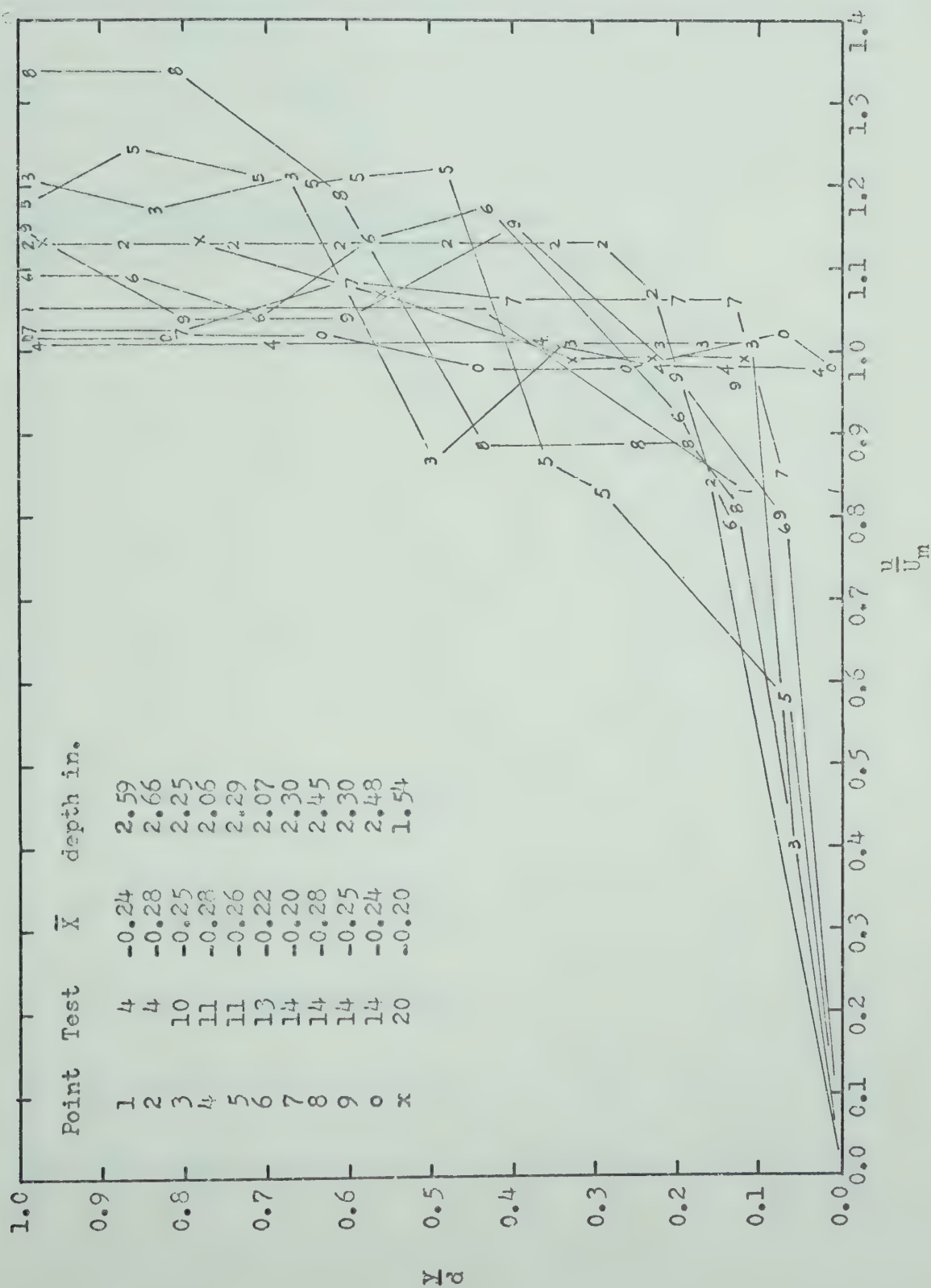


Figure 6.11. Instantaneous Hydrogen Bubble Profiles, $-0.3 < \bar{X} < -0.2$.

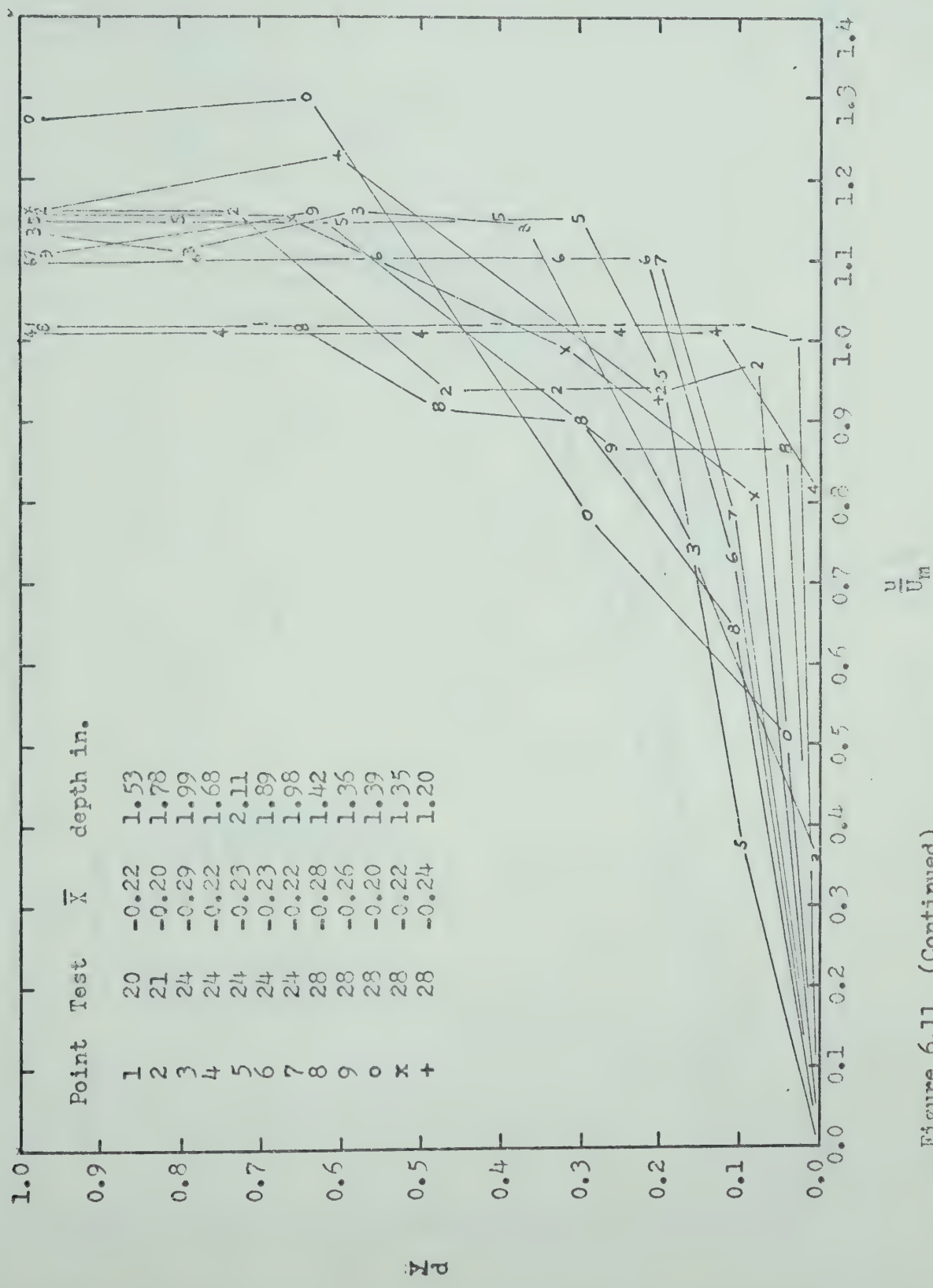


Figure 6.11 (Continued)

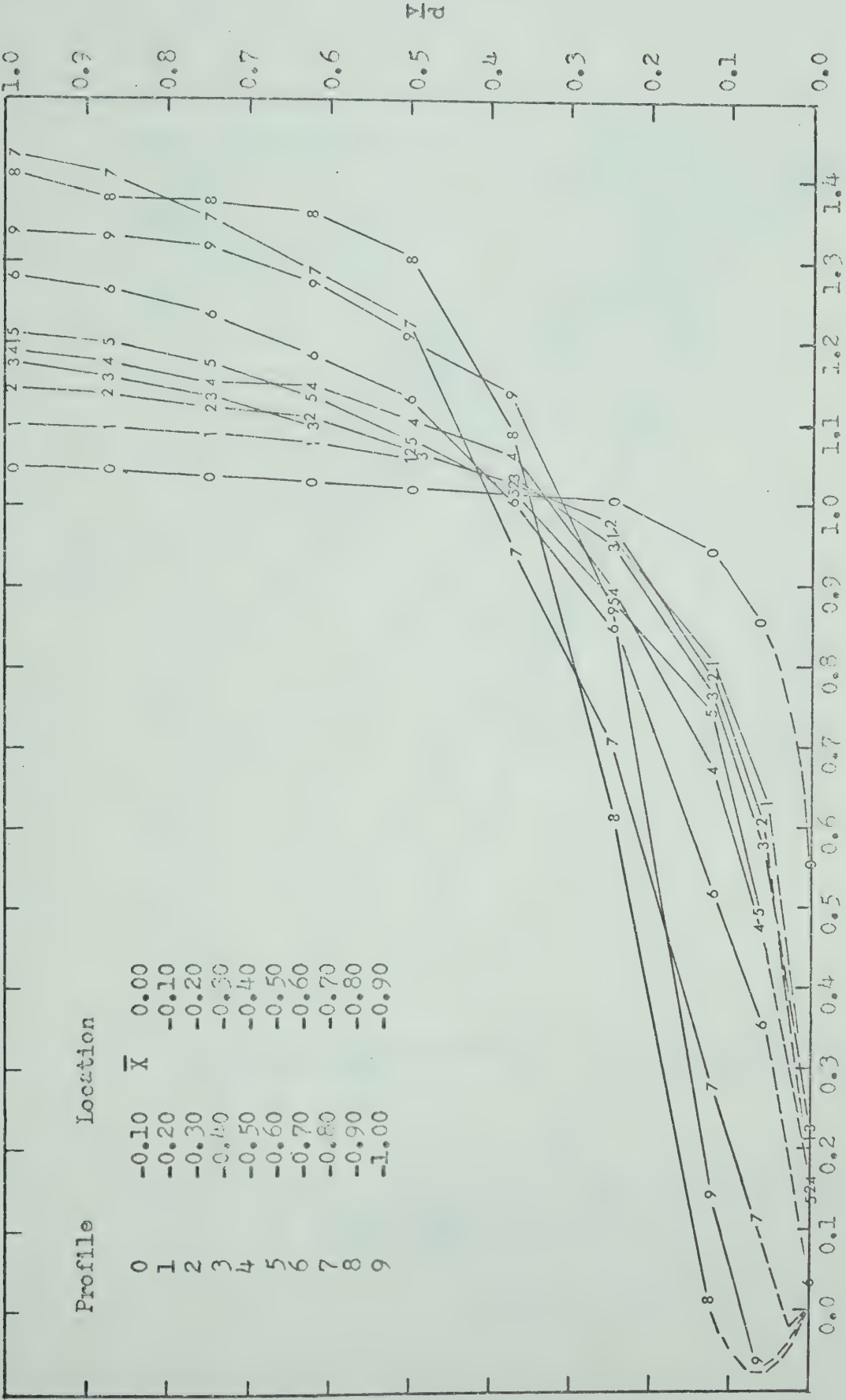


Figure 6.12. Mean Dimensionless Velocity Profiles $\left(\frac{u}{u_m}\right)^{1/n}$.

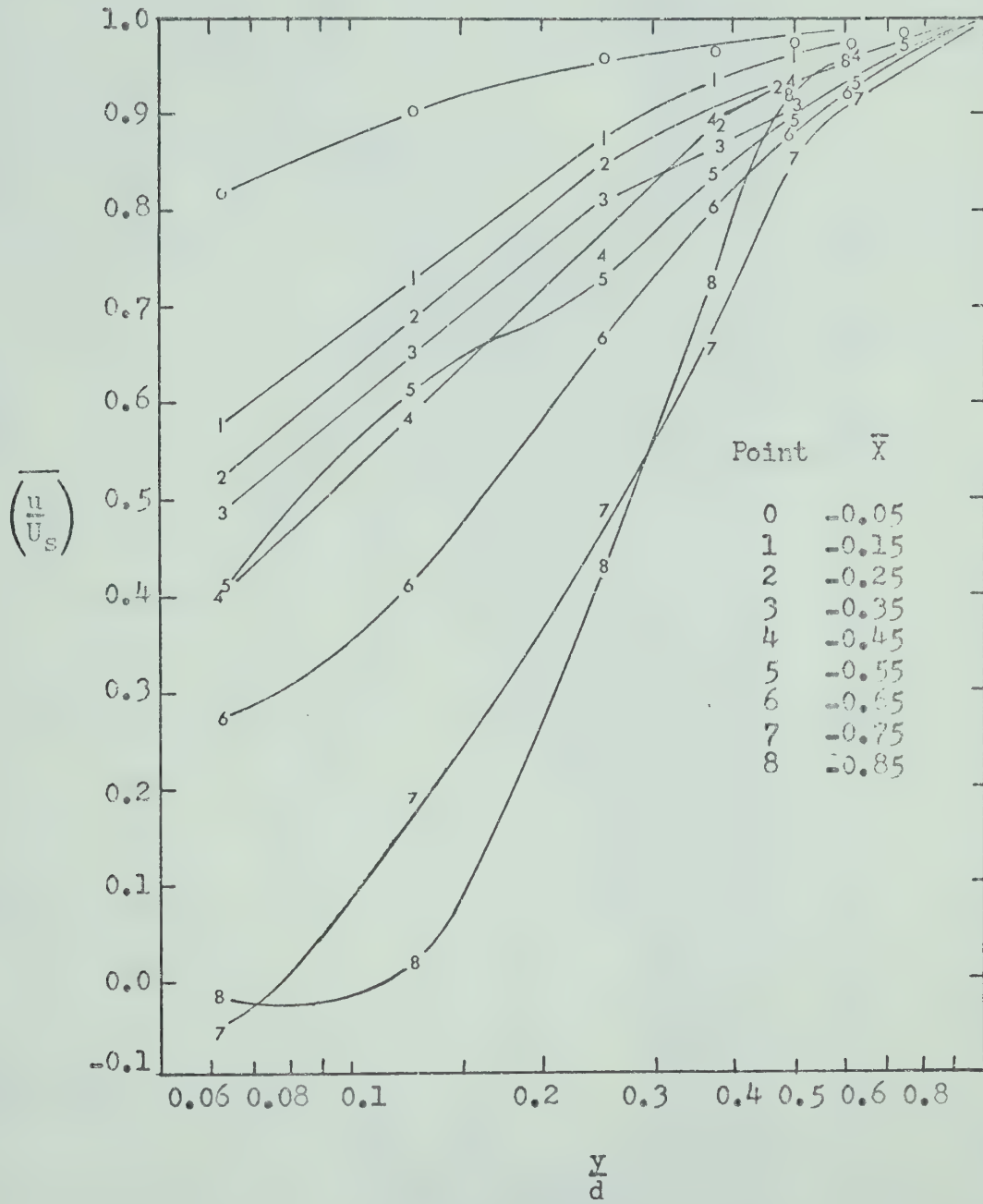


Figure 6.13. Mean Dimensionless Semi-logarithmic Velocity Profiles $\overline{\left(\frac{u}{U_s}\right)}$.

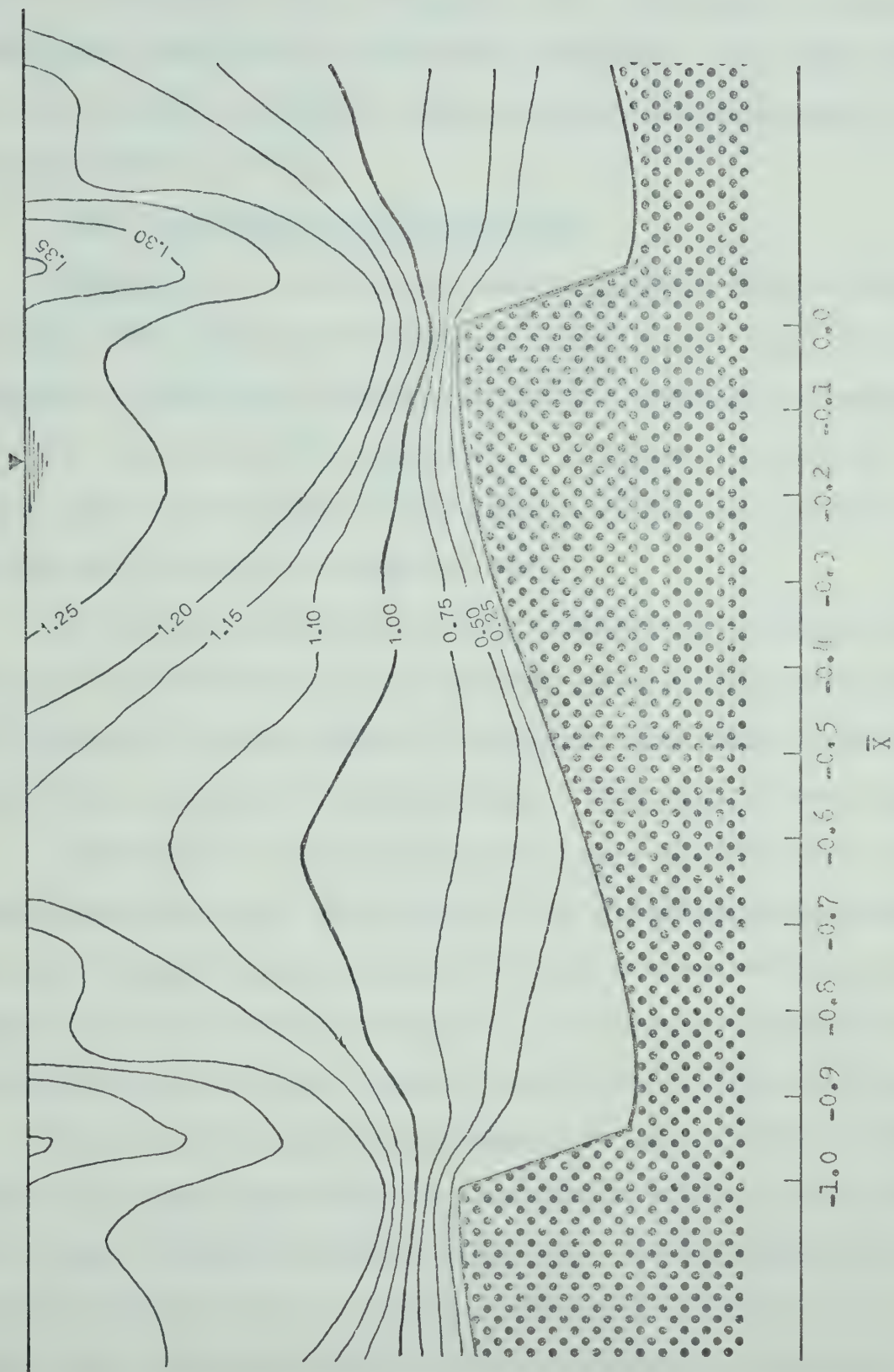


Figure 6.14. Equal Velocity Lines, $\frac{\bar{L}}{\bar{H}_r} = 10$, $\frac{dci}{\bar{H}_r} = 2.5$.

Figure 6.3 using \bar{L}/\bar{H}_r of 10, and \bar{d}_{cl}/\bar{H}_r of 2.5 which were in the range of bed-forms investigated in the present experiments. The equal velocities were calculated relative to the mean velocity at mean depth of flow above the average bed-form.

6.6.5 Flow Turbulence Characteristics

Examination of instantaneous velocity profiles clearly indicated that large scale turbulence fluctuations existed in the flow. Five instantaneous dimensionless velocity profiles all obtained from segment $-0.3 < \bar{X} < -0.2$ in test 28 and illustrated in Figure 6.15 show, for example, that the velocities in the direction of flow at $Y = 0.0625$ varied from the mean by as much as sixty per cent.

To determine horizontal velocity turbulence distribution in the flow above the bed-forms from the available hydrogen bubble information it was assumed that characteristics of turbulence, like those of the mean velocity of flow, were similar for flows above a given phase of bed-forms.

Dimensionless turbulence intensities were determined from the standard deviation of the fluctuations of the dimensionless velocities u/U_m about the mean in each segment of the bed-form and at the same dimensionless depth levels as were employed in the average velocity calculations. The dimensionless turbulence intensity results are presented in Figure 6.16.

For the reasons discussed previously in Section 6.6.4 the dimensionless turbulence intensities σ presented in Figure 6.16 are indicative of local turbulence characteristics only. The turbulence intensity variation in the flow above a bed-form is therefore illustrated in Figure 6.17. The dimensionless turbulence intensity is referenced to the mean velocity at mean depth \bar{U}_m and the bed-form and flow parameters

\bar{L}/\bar{H}_r and $\frac{\bar{d}_{cl}}{\bar{H}_r}$ are 10 and 2.5 respectively.

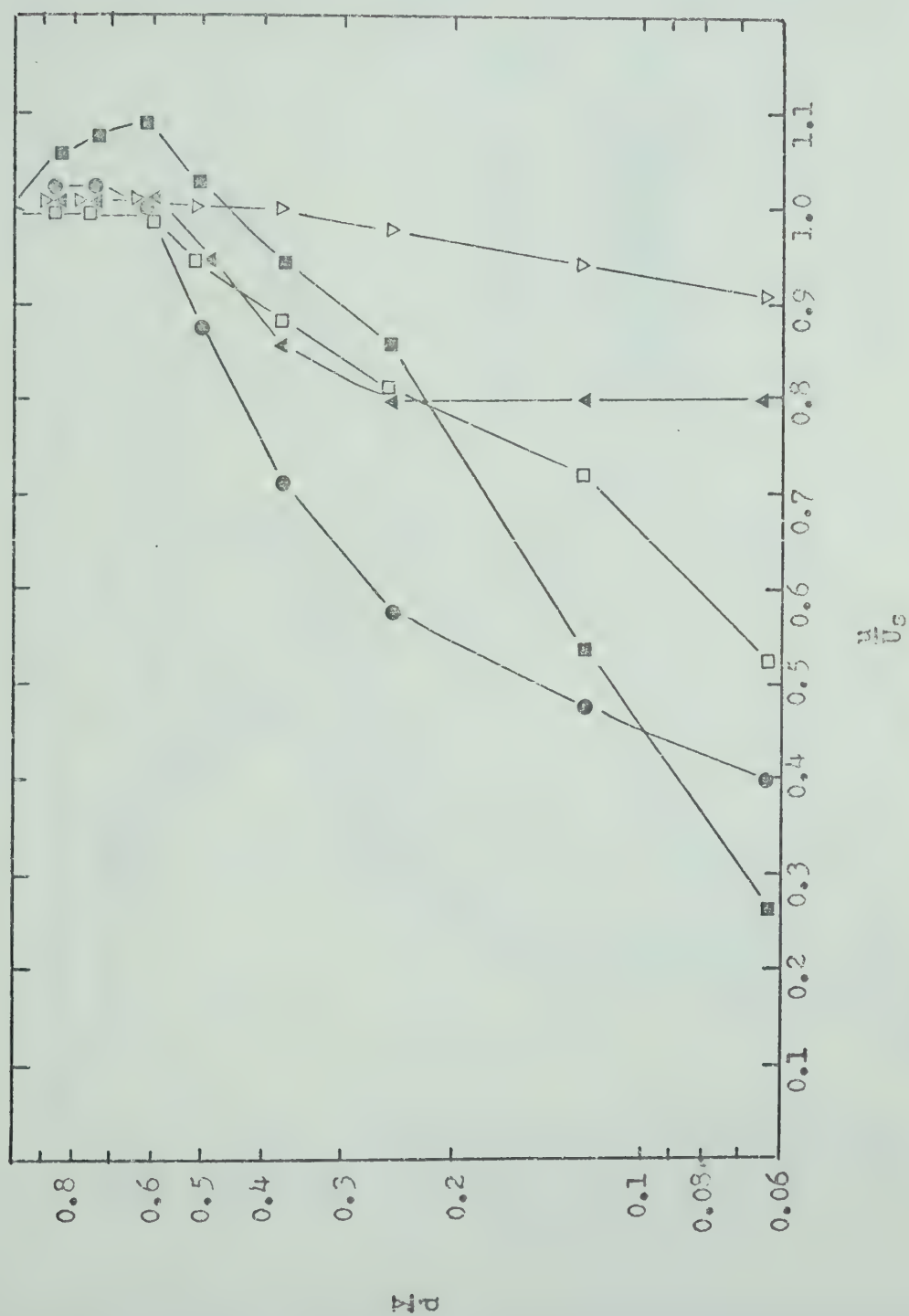


Figure 6.15. Illustration of Instantaneous Velocity Profiles, Test 28,
Segment $-0.3 < \bar{X} < -0.2$.

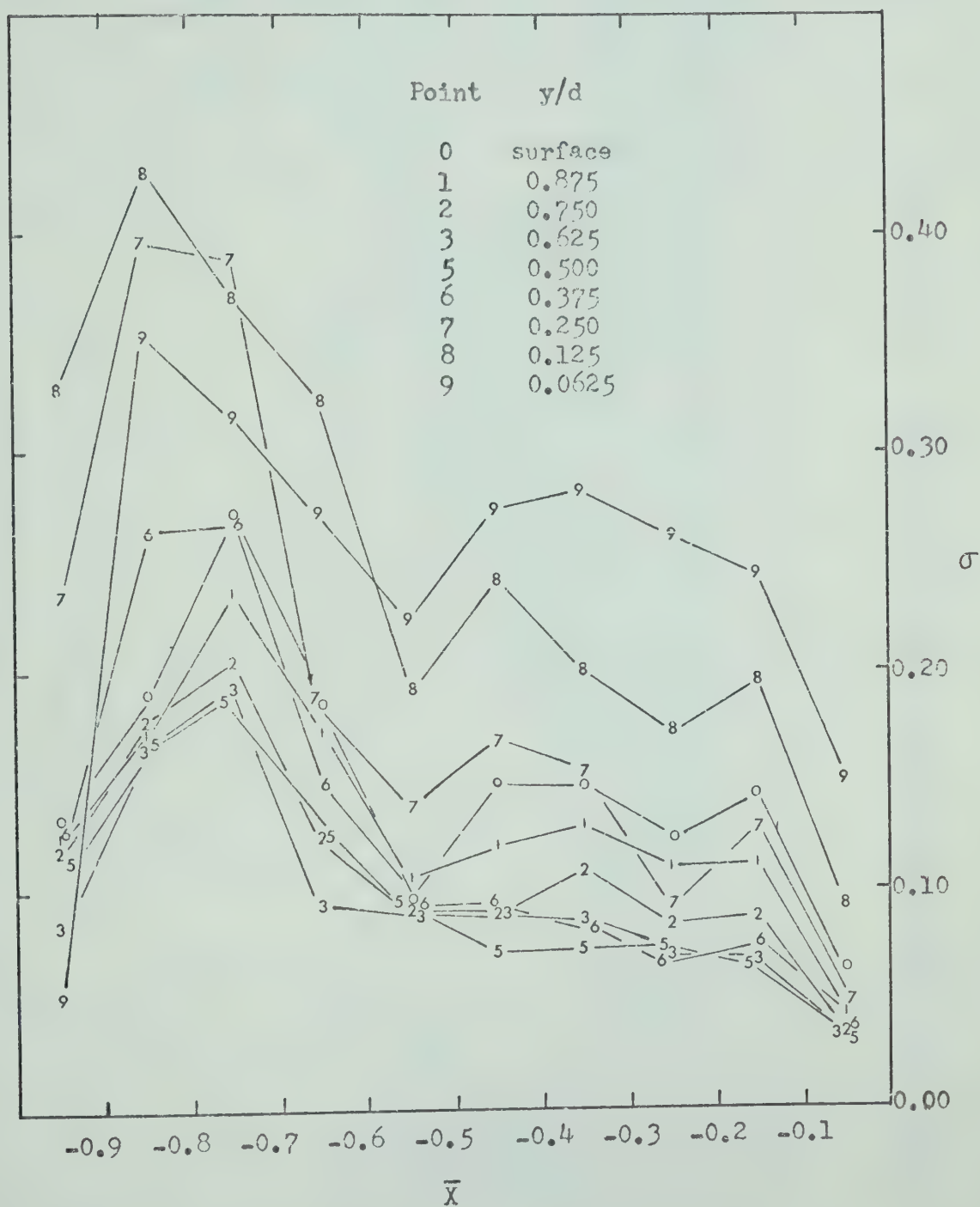


Figure 6.16. Distribution of Standard Deviation of Dimensionless Velocity $\frac{u}{U_m}$ Fluctuations.



Figure 6.17. Equal Turbulence Intensity Lines, $\frac{\bar{L}}{H_T} = 10$, $\frac{d\sigma_i}{H_T} = 2.5$, $(\sigma \times 10^3)$

6.7 Pressure Measurement

6.7.1 Pressure Data Evaluation

All pressure measurements were made at sensor positions stationary in the fixed reference system. To establish pressure distribution characteristics over individual moving bed-forms, the horizontal coordinates of each sensor in the dimensionless moving reference system were computed by equation (6.16)

$$\bar{x}_p = \frac{x_p - x_0}{\bar{L}} \quad (6.16)$$

where x_p is the position of a sensor in the stationary reference frame, and x_0 represents the horizontal coordinate position of the origin of the moving reference frame at the instant of a pressure observation.

Typical pressure measurement results obtained by the continuous monitoring method and the intermittent sampling procedure are illustrated in Figures 6.18 and 6.19 respectively. The recorded pressures represent pressure differences measured between the probe in the flume and the constant level reference source. Different pressure probes are represented by distinct symbols.

The results given in Figure 6.18 show a general scatter of pressure data points in the order of ± 0.001 inches of water. Two points identified in the plot, however, bear special mention. Both points appear below the general trend of pressure distribution values at their respective locations in the bed. The time of observation of these two pressure points, however, was found to be the same indicating that the recorded drop in pressure of 0.002 inches of water resulted from an external effect such as a long period surge in the flume.

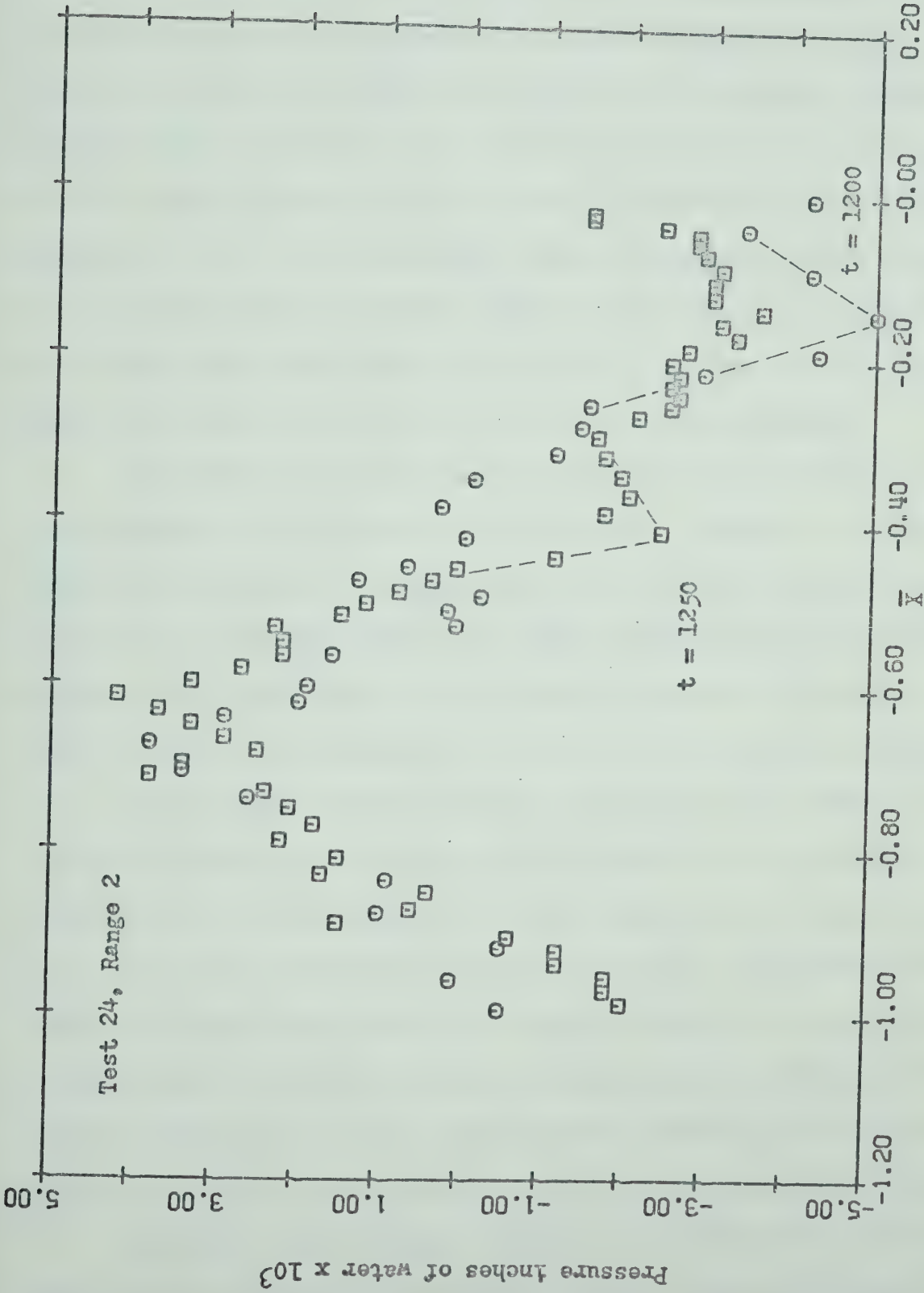


Figure 6.18. Example of Continuous Pressure Sampling Results

Because similar long period pressure fluctuations were observed in pressure observation plots in other tests, all selected test data were reviewed to isolate the external effects upon the normal pressure variations. To identify externally caused pressure fluctuations, recorded pressure traces from two or more sensors were compared noting discrepancies from the normal trends at identical times of observation and different positions relative to the bed-form. When an external pressure pattern was identified, its approximate amplitude and duration were estimated from two or more independent sensor output traces. A correction was then applied to restore the pressure record to the natural pattern.

Typical results of pressure measurement by the intermittent sampling technique are illustrated in Figure 6.19. Although considerable data scatter is indicated, a thorough analysis of the data disclosed that the scatter was due partially from externally produced pressure fluctuations, partially from small losses of water from the system, and possibly from small variations in the roughness of the bed in the approach channel.

To determine and, if possible, to eliminate the effects of pressure data scatter due to various external causes, and to establish pressure variation characteristics due to flow above bed-forms only, a standard pressure data evaluation procedure was evolved. The procedure was based on the fact that pressure at a fixed position in an equilibrium bed-form remains invariant. Hence, pressure variation along the bed-form and at a fixed distance below some reference elevation must retain individual and constant characteristics as the bed-form translates downstream.

To evaluate the external pressure effects all sensor probes were classified into three groups according to low, medium or high elevations of their ports in the flume. All available pressure data from individual

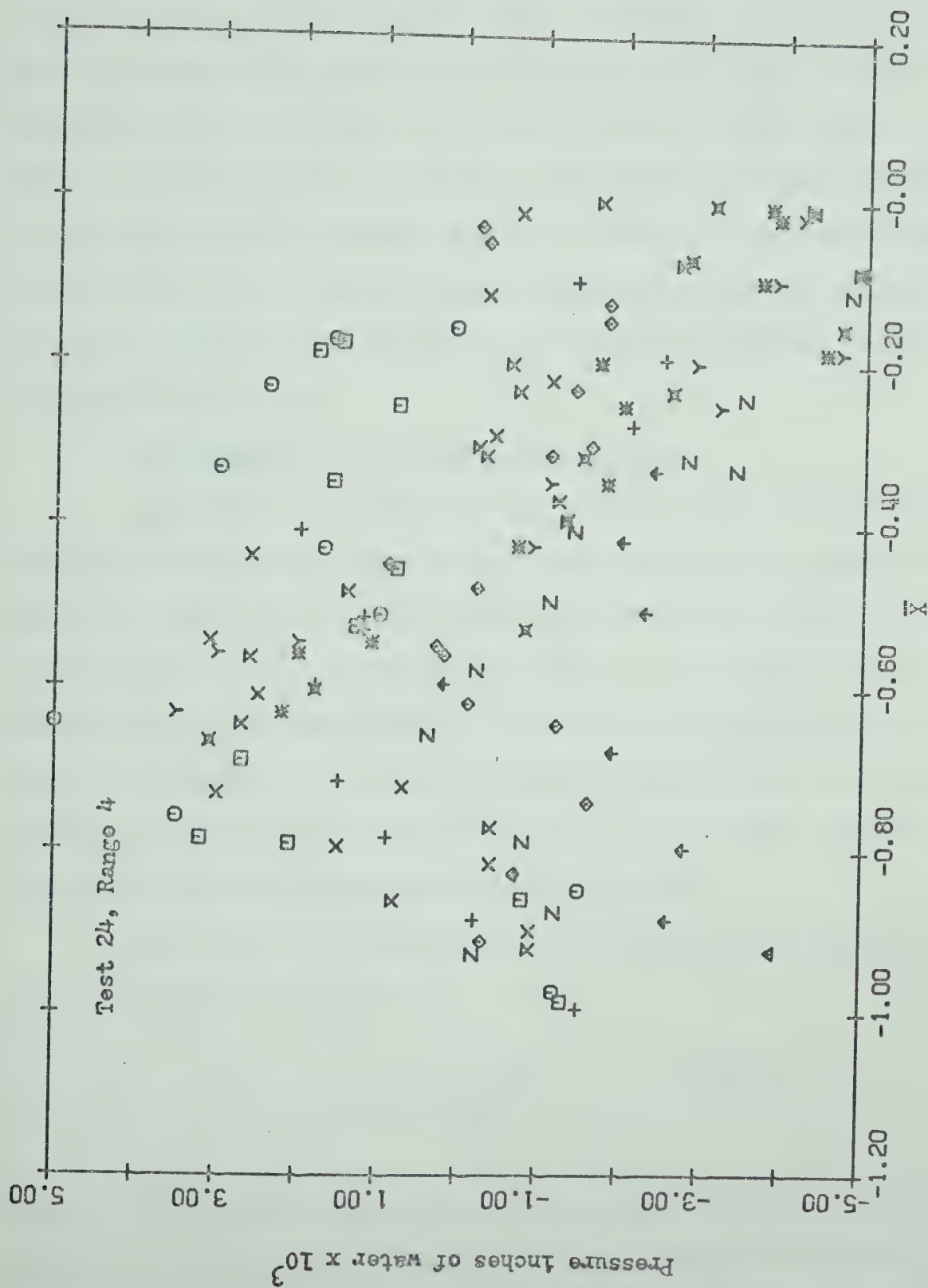


Figure 6.19. Example of Intermittent Pressure Sampling Results

sensors belonging to each group were replotted and compared. Because of probe spacing along the flume, pressure observations at a point by different sensors were time delayed and differences between the pressures recorded at a point along the bed by different sensors were indicative of external factors influencing the pressure. Time dependent trends of external pressure factors could then be established separately in all groups and verified by comparison between groups. If these trends were consistent in time and magnitude, mean pressure distribution characteristics were established by superposition of individual pressure sensor output data in each group.

6.7.2 Pressure Distribution Characteristics

The results showed that, except for the general scatter of data which could not be eliminated by time trend analysis, the pressure distribution characteristics established at different levels within the sediment bed along a bed-form were identical. Hence, within the precision of measurements the mean pressure distribution data indicated no vertical pressure gradients in the bed, and all data from different levels were therefore employed to establish mean pressure distribution characteristics along each bed-form as illustrated in Figure 6.20.

The results of pressure measurement were non-dimensionalized in accordance with equation (6.17)

$$\bar{P} = \frac{P - P_{c1}}{V_{c2}^2 / 2g} \quad (6.17)$$

where p_{c1} is the reference pressure at the origin of the moving reference frame, p is the mean observed pressure at any position in the bed, \bar{V}_{c2} is the mean velocity of flow at the crest of the upstream bed-form, and g

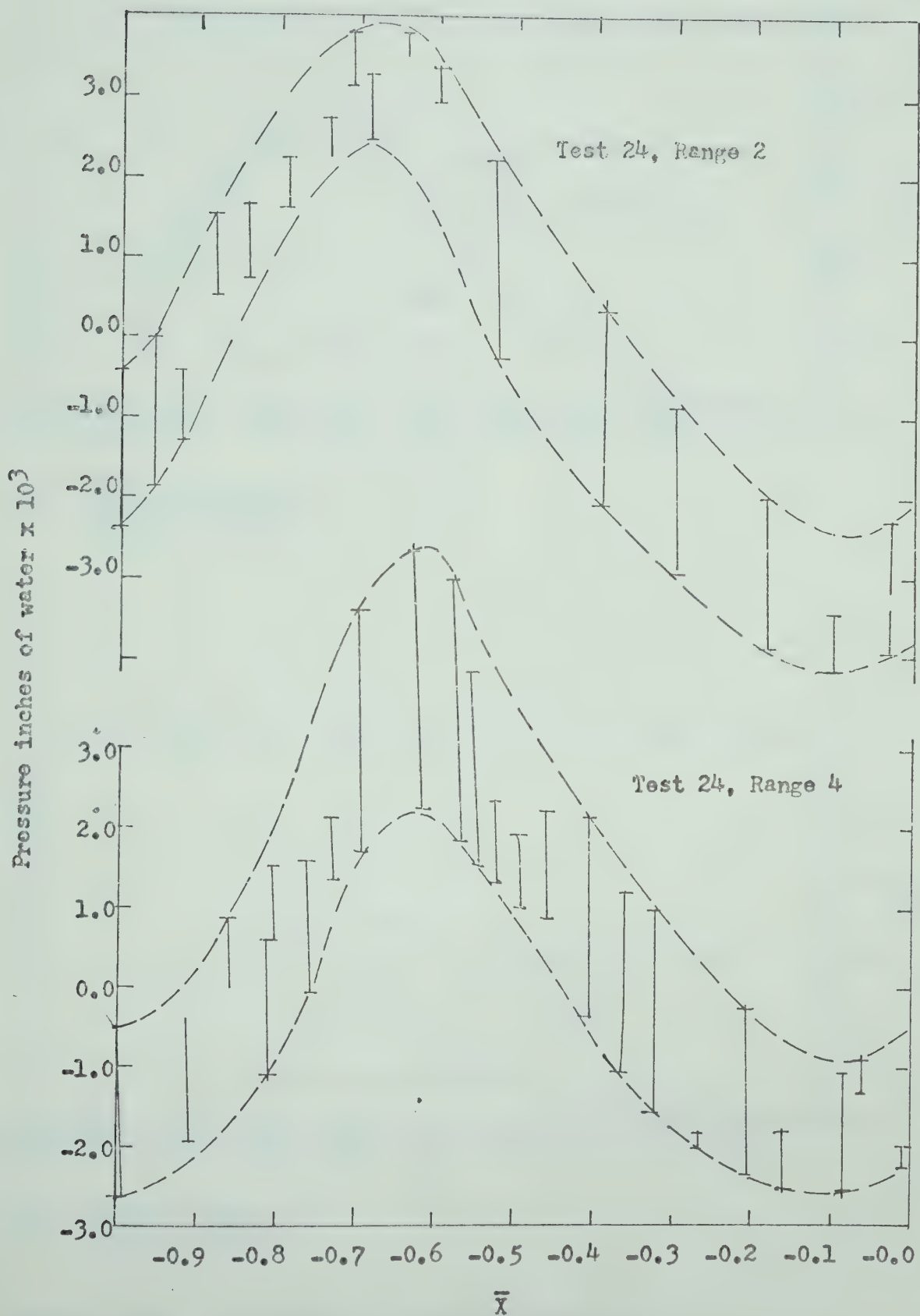


Figure 6.20. Typical Pressure Distribution Band

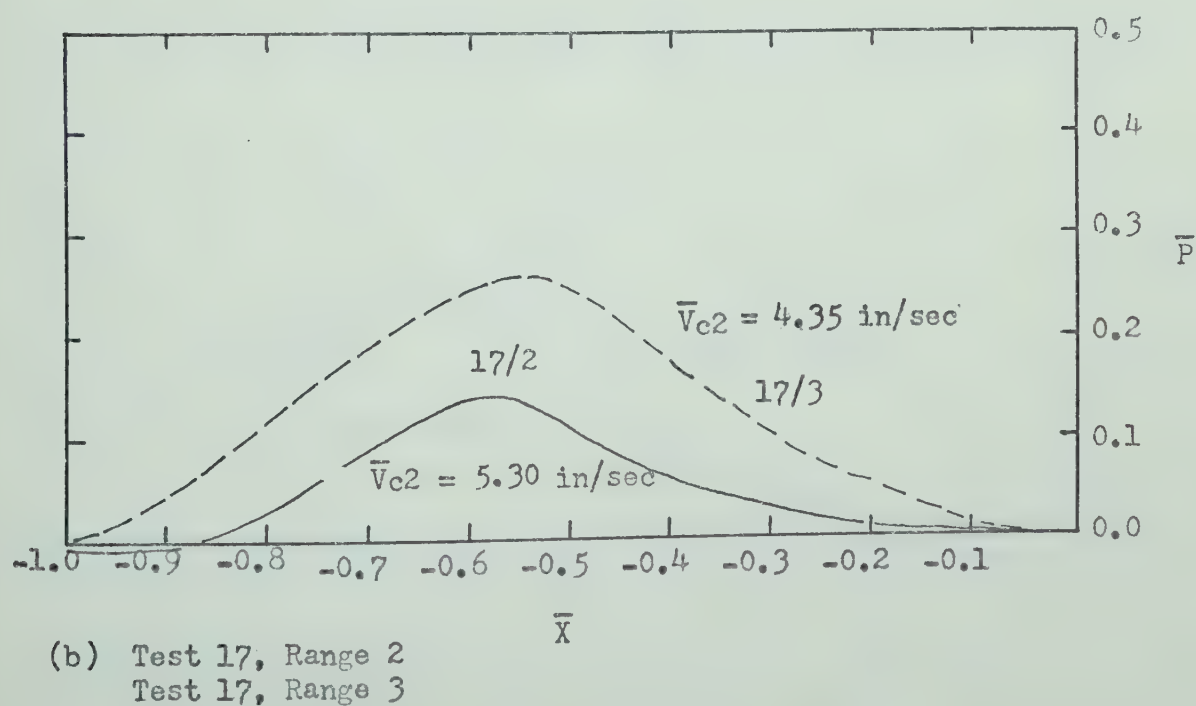
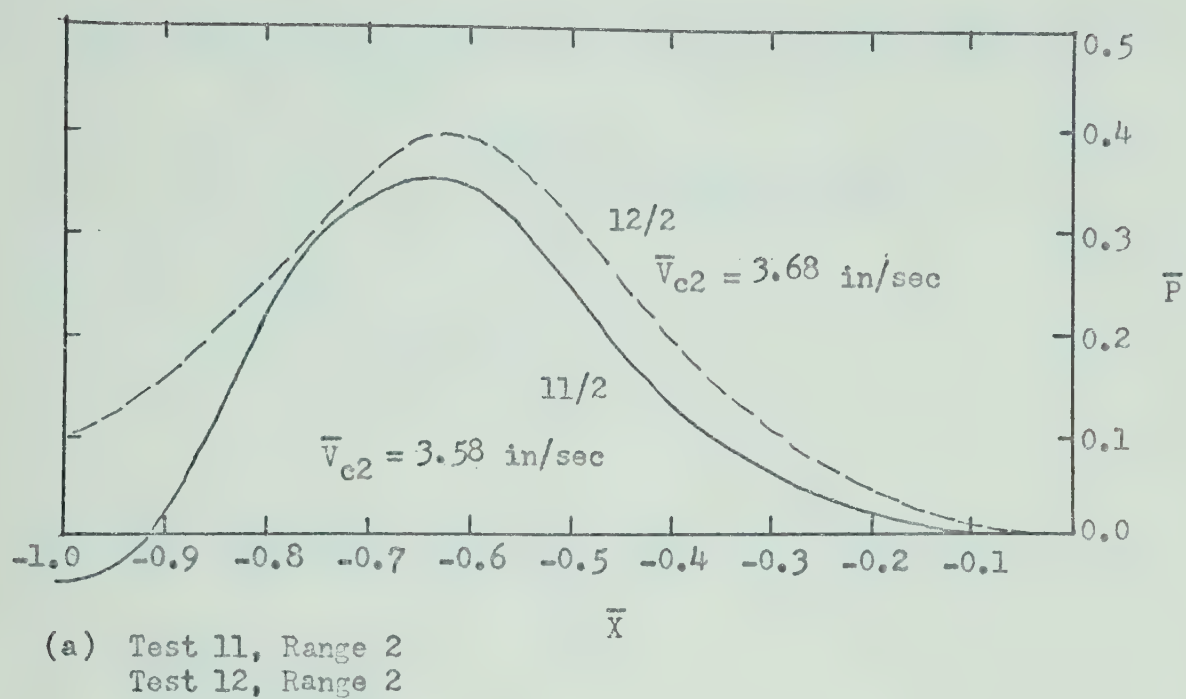
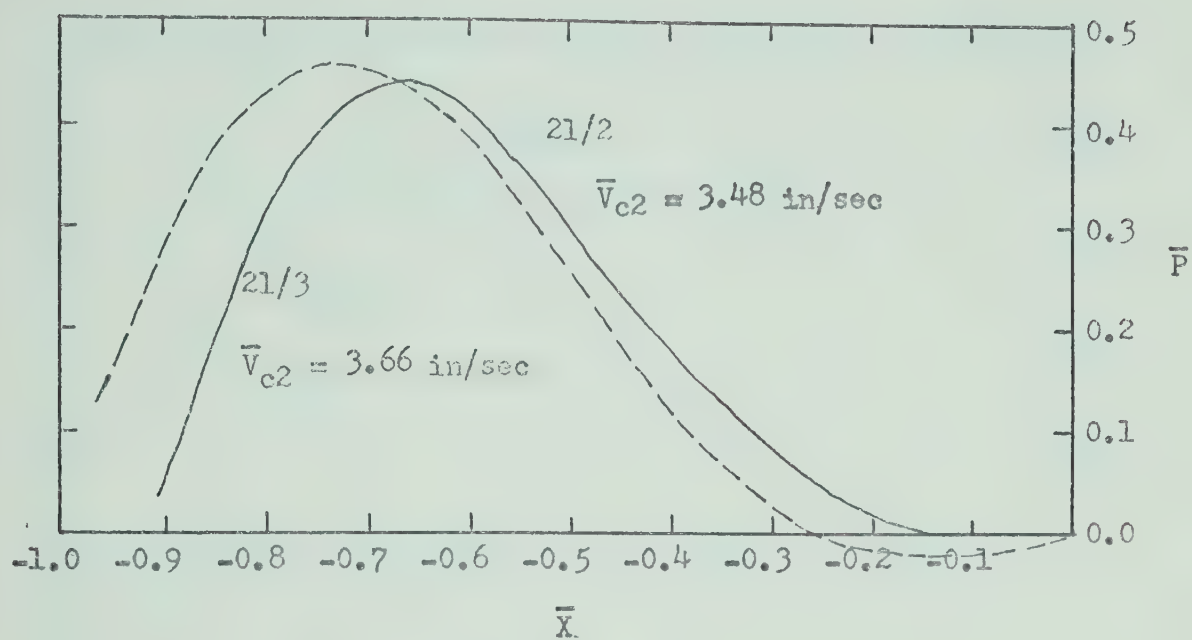
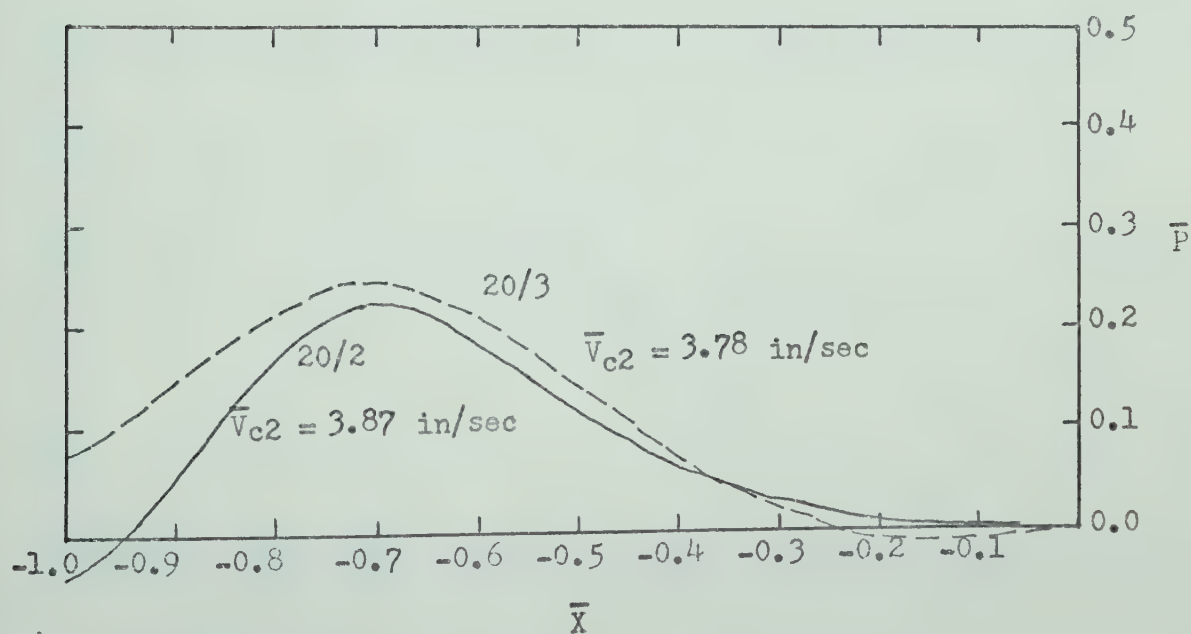


Figure 6.21. Dimensionless Pressure Distribution.

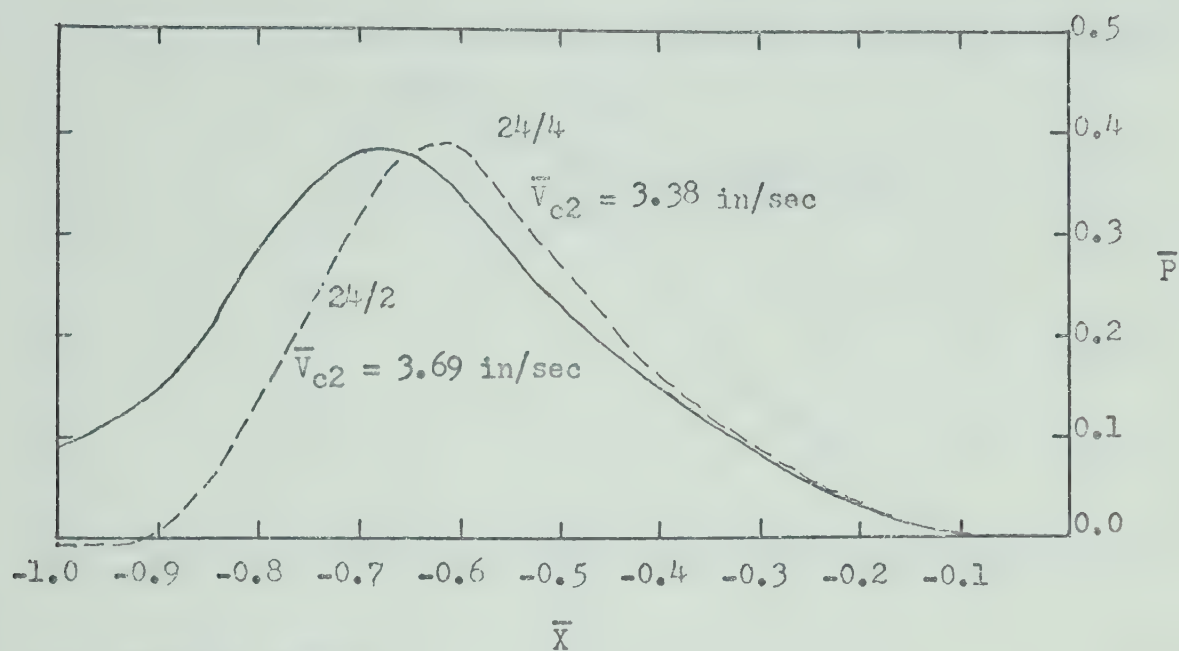


(c) Test 21, Range 2
Test 21, Range 3

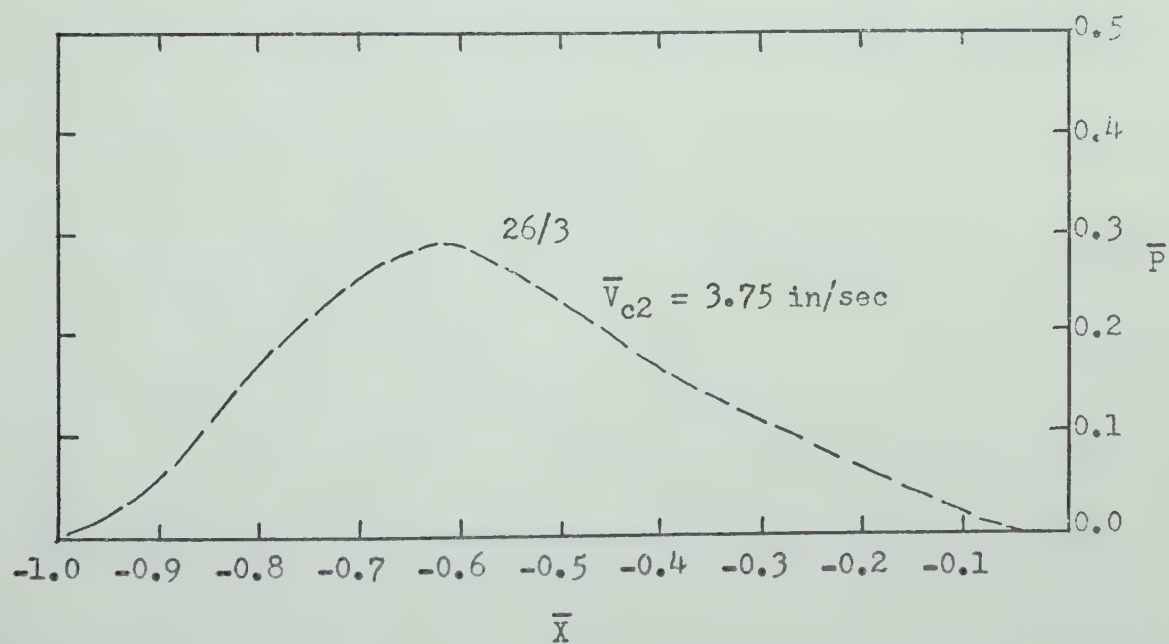


(d) Test 20, Range 2
Test 20, Range 3

Figure 6.21. (Continued)

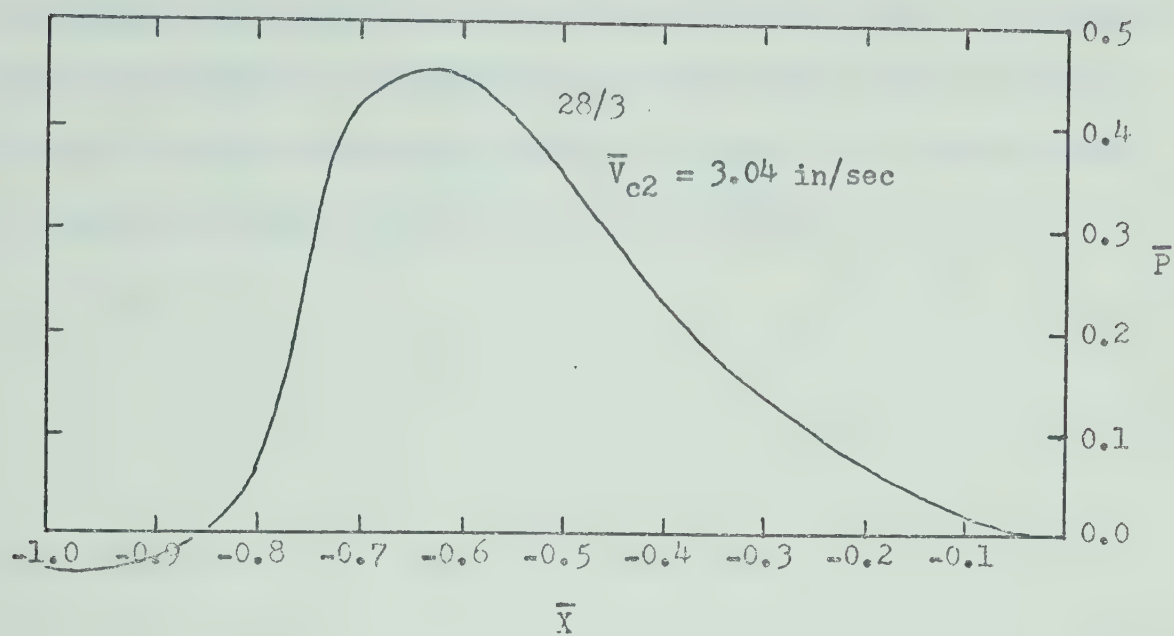


(e) Test 24, Range 2
Test 24, Range 4

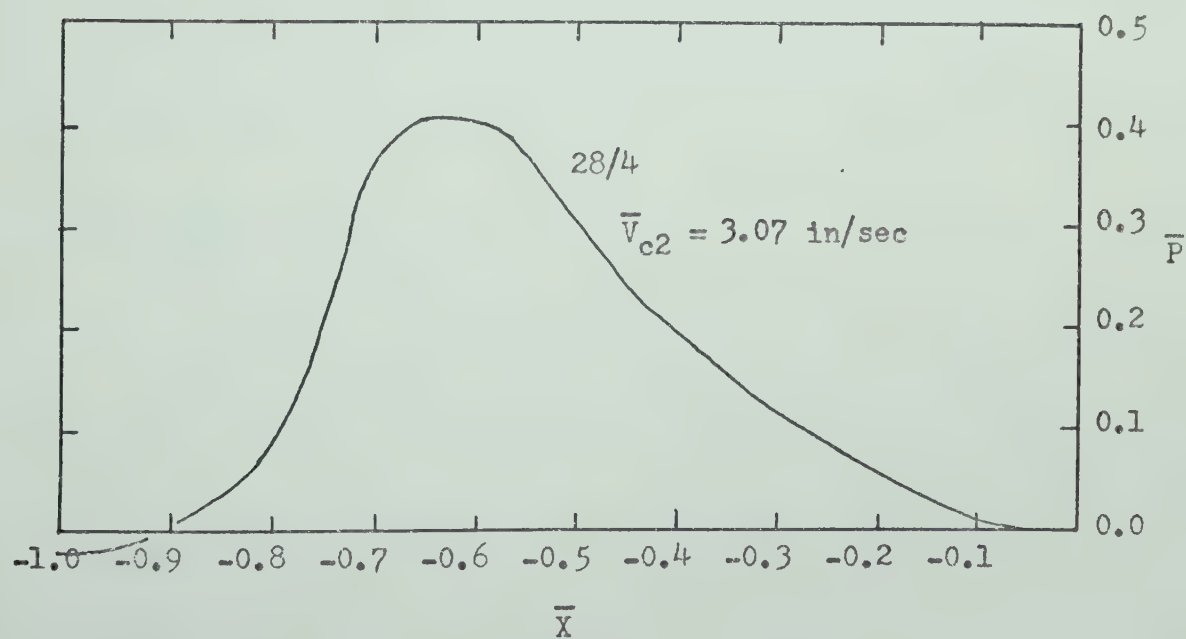


(f) Test 26, Range 3

Figure 6.21. (Continued)



(g) Test 28, Range 3



(h) Test 28, Range 4

Figure 6.21. (Continued)

represents the gravitational acceleration. The dimensionless pressure distribution characteristics are presented in Figure 6.21. No pressure measurement results are reported for test 22 ranges 2 and 3, and test 26 range 2 either because only partially complete data were obtained or external pressure effects could not be resolved.

CHAPTER VII

ANALYSIS AND DISCUSSION

7.1 Outline

The experimental findings are analyzed with a specific objective to establish the relative contributions of different forces in detaching particles from the surface of active bed-forms.

First, the observations and measurement results are analyzed and the characteristics of bed-forms and flow, pertinent to the objectives of the investigation, are identified from the experimental data. Then, force requirements to entrain particles from different locations along the surface of bed-forms are determined, and forces available for particle entrainment are estimated from the experimental results. Finally, relative contributions of flow shear and pressure gradient forces for particle entrainment are established.

7.2 Analysis of Observations

7.2.1 Bed-Form Geometry

Observations and profile measurements show that a typical bed-form may be divided into two regions distinguished by either predominant scour or deposition of surface particles. The region from which particles are scoured extends from the deepest location of the trough downstream to the crest of the bed-form. It corresponds to the region where the bed-form surface curve slope is positive. The region in which deposition of particles takes place extends downstream from a crest to the deepest position

in the trough of the bed-form. Throughout this region the surface slope is negative.

Each of the two regions may be further subdivided into zones of distinct bed-form surface geometry characteristics. In the region immediately downstream from the trough the bed-form surface profile is concave upward. However, the surface curvature becomes concave downward at a point of inflection, which from the various bed-form profiles was found to occur in the region $-0.60 < \bar{X} < -0.45$. In the majority of profiles, the surface curve approached the crest smoothly. However, surface profiles of five bed-forms (12/2, 17/2, 17/3, 24/2, and 24/4) showed discontinuities in the segment upstream of the crests. This result confirmed visual observations that a single particle often rested slightly above the adjacent particles at the apex of the crest.

The region of particle deposition, downstream from the crest to the trough, was also found to have two distinct zones: (1) the lee side of the bed-form upon which all particles arriving from upstream were deposited, and (2) the zone downstream from the toe to the deepest location in the trough.

Observations showed that on the lee side all particles were deposited near the crest. This increased the slope of the lee side of the bed-form and when the critical intergranular shear stresses were exceeded the particles on the slope avalanched downward. Immediately after the slope failure the lee side slope was less steep than the critical. But as the process of particle deposition near the crest was not interrupted, avalanching occurred again each time the slope increased to some critical value. A statistical analysis of 324 individual lee slope angle observations disclosed that the average slope of the lee side was 34.4° , rang-

ing from a minimum of 26° to a maximum of 45° . The average angle was higher than the angle of initial yield, $\phi_1 = 31^\circ$. However, the angle of the slope after avalanching was found to be equal to the angle of repose, $\phi_r = 26^\circ$. Especially significant is the observation that the lee side could reach a maximum slope of 45° . A possible explanation is that there was inflow into the lee side of the bed-form increasing the effective stresses between particles and helping to resist sliding at steeper slope angles.

For deposition in the toe to trough zone, particles were supplied partially by the transport in the upstream direction from the trough region, and partially by some loose particles during the avalanching of the lee side of the bed-form.

The distribution of the mean entrainment rates of particles from an equilibrium bed-form depends upon the local slope of the bed surface. The entrainment rate was zero at the deepest position of the trough where the bed surface slope was zero, and was maximum at the inflection point on the upstream slope of the bed-form where the surface slope was maximum. The entrainment rate, therefore, increased from the trough to a position at approximately $\bar{X} = -0.55$, and then decreased toward the crest.

The local flux of particles along the surface of the bed-forms was computed from the local entrainment results assuming zero net transport at the separation streamline reattachment position. The flux of particles, therefore, increased in the downstream direction and was maximum at the crest.

Since in these experiments all particles arriving at a crest were trapped in its lee, the flux of particles moving past the crest had to equal to the rate of particle deposition in the lee of crest. The flux at the crest, determined from entrainment information, was therefore compared with

the particle transport estimated by the crest velocity and height. Generally the results were found to be in good agreement, and since the variations between the two results showed no consistent trends, the discrepancies were attributed to experimental nature, especially in establishing the true position of zero net transport.

However, the reattachment position in all bed-forms was located in a zone of finite positive surface slope and entrainment of particles occurred between the trough and the reattachment point. The total rate of particle entrainment was therefore in excess of the transport at the crest, as the particles upstream of the reattachment point were not included in the transport calculation. Small part of these particles were transported upstream and were deposited on the bed downstream from the toe. In the trough area, however, the bed appeared to be very loose. And it is possible that, because of the method of measurement, the volume of particles entrained from this area, when measured in terms of volume occupied when deposited in the lee of a crest, was much less than predicted.

7.2.2 Velocity and Turbulence

The results of the mean velocity measurements have been presented in two forms: (1) by the mean local dimensionless velocity profiles \bar{U}_m and \bar{U}_s v.s. \bar{Y} given in Figures 6.12 and 6.13 respectively, and (2) by the equal velocity lines representation of a particular bed-form geometry--depth of flow condition given in Figure 6.14.

Each of the mean dimensionless velocity profiles \bar{U}_m v.s. \bar{Y} summarize the local flow conditions at different positions relative to the geometry of a typical bed-form. The results show that the flow between two adjacent crests may be divided into regions upstream and downstream from the separation streamline reattachment position located in the segment

$-0.7 < \bar{X} < -0.6$. Upstream from the reattachment position, in the region $-0.9 < \bar{X} < -0.7$, a shear flow zone, characterized by large velocity gradients, was found to exist at depth levels $0.1 < \bar{Y} < 0.5$. Near the sediment bed, at depth levels $0.0 < \bar{Y} < 0.1$, the mean flow was found to be in the upstream direction toward the adjacent toe. In the flow above $\bar{Y} = 0.5$ the dimensionless velocity gradients ($d\bar{U}_m/d\bar{Y}$) increased in the downstream direction and simultaneously extended toward the free surface of the flow. The maximum velocity gradients near the free surface in the flow occurred at $\bar{X} = -0.7$.

In the region downstream from the reattachment point the local velocity profiles became fuller in the downstream direction indicating development of boundary layer. The velocity gradients in the upper flow zones gradually decreased and the flow velocities became more uniform. Simultaneously the velocity gradients became more pronounced and were concentrated in gradually narrowing depth zones close to the sediment surface. The profiles showed that the mean local flow, represented by $\bar{U}_m = 1.00$ occurred in the depth zone $0.3 < \bar{Y} < 0.4$ at all positions along the bed-form except immediately upstream of the crest where the mean flow velocity occurred at $\bar{Y} = 0.24$. The results also show that the velocity profile at this position filled out suddenly from $\bar{X} = -0.15$ and that the flow above $\bar{Y} = 0.24$ became nearly uniform, as the velocity at the free surface exceeded the mean local velocity by only four per cent.

Equal velocity lines, based on the average flow velocity at mean depth of flow above a bed-form and shown in Figure 6.14 for a bed-form with $H/\bar{L} = 0.1$ and $d_c/\bar{H}_r = 2.5$, illustrate flow characteristics along the bed-form. It was found that the depth position of the mean velocity \bar{U}_M varies considerably above the bed, being at $\bar{Y} = 0.1$ immediately upstream

of the crest and at $\bar{Y} = 0.4$ and $\bar{X} = -0.62$. Furthermore, a cell of relatively high flow velocity was found to exist immediately downstream of the crest. As a result, in the given example, the free surface flow velocities ranged from a maximum of approximately $1.35 \bar{U}_M$ at $\bar{X} = -0.95$ to a minimum of $1.12 \bar{U}_M$ at $\bar{X} = -0.6$, where \bar{U}_M is the mean velocity at mean depth.

The basic turbulence characteristics, represented by the standard deviation of the fluctuations of the dimensionless velocities u/\bar{U}_M and summarized in Figure 6.16, show that in terms of local mean velocity \bar{U}_M the maximum intensity occurred in the trough region of the bed-form at $\bar{X} = -0.85$ and at the depth level $\bar{Y} = 0.125$ above the bed, and decreased toward the bed and toward the surface of the flow. Upstream from this position near the bed the turbulence intensity decreased rapidly, and in the vicinity of a toe at $\bar{Y} = 0.0625$ the intensity was found to be 0.01 indicating relatively negligible turbulence. Similarly, turbulence intensities decreased in the downstream direction. However, from approximately $\bar{X} = -0.60$ the intensity at $\bar{Y} = 0.0625$ was found to be larger than in the flow further from the bed. It decreased toward the central core of the flow and appeared to be minimum at $\bar{Y} = 0.50$, but increased again toward the free surface.

The distribution of turbulence intensities above a specific bed-form as represented by equal intensity lines are shown in Figure 6.17. The maximum intensity occurred in the core region of the roller downstream from a crest at approximately $\bar{X} = -0.85$. A low intensity region was found to exist throughout a central depth zone downstream from $\bar{X} = -0.70$ to beyond the crest of the bed-form. A zone of relatively high turbulence was found to exist throughout the full depth of flow above the trough

region which apparently limited the extent of the central, low-intensity turbulence region. In general, the turbulence intensity characteristics in the flow near the bed in these experiments agree qualitatively with the findings of Raudkivi (1966) on stabilized bed-forms, and Rifai and Smith (1971) on triangular elements. However, neither of these investigators found increasing turbulence intensities toward the free surface of the flow, or detected the zone of relatively high turbulence intensity penetrating to the surface from the trough region below.

The results also show that downstream from $\bar{X} = -0.55$ and near the bed, the distance of equal turbulence intensity lines oscillated from the boundary. Turbulence intensity appeared to be suppressed at $\bar{X} = -0.55$, however it increased in the downstream direction and reached a maximum at $\bar{X} = -0.35$. The position of the turbulence suppression point corresponds to the location of the maximum pressure gradient and with the maximum positive surface slope of the bed-form. It is possible, therefore, that inflow of fluid into the bed occurred in this region which, according to a summary presented by Watters and Rao (1971), would have tended to decrease the turbulence level in the flow field above. The increase in turbulence intensity from $\bar{X} = -0.65$ to $\bar{X} = -0.35$ appears to be due to turbulence generated in the developing boundary layer.

The velocity and turbulence measurement results show that the flow effects due to bed-forms penetrated to the free surface of the flow. The high velocity flow cell and the relatively high turbulence intensities in a region above the trough correspond approximately to the position on the surface of natural canals with dune beds at which upwelling of flow is often observed. This further confirms the conclusions of Section 4.3.4 indicating that the bed-forms under investigation were in the dune phase.

7.2.3 Pressure Distribution

The pressure distribution curves were found to be bell-shaped with skewness induced by assymetrical positioning of the maximum and minimum pressures in relation to the bed-form geometry. The results of pressure distribution measurements showed that maximum pressures occurred in the region $-0.75 < \bar{X} < -0.55$. This corresponds to the mean position of the stagnation point established from velocity measurements. The minimum pressures were found to occur in the region slightly upstream of the crest, $-0.15 < \bar{X} < 0.0$. This is in general agreement with the findings of Raudkivi (1963) who measured pressure distribution over a stabilized ripple, but contradicts the results of Vanoni and Hwang (1967) who also measured pressures over stabilized bed-forms and found that the minimum pressure occurred at or slightly downstream of the crest.

Downstream from the peak pressure position, the distribution curves had inflection points and became concave upward in the region $-0.60 < \bar{X} < -0.40$. Histograms showing the distribution of locations of the maximum and minimum pressures, the maximum pressure gradient, and the maximum bed-form surface slope are presented in Figure 7.1. It shows that maximum particle entrainment occurs at the location of the maximum pressure gradient.

7.3 Force Requirements for Particle Detachment

7.3.1 Statics of Surface Particles

The mechanics of sediment grain detachment from the surface of a bed of similar grains may be investigated by considering the static equilibrium of either a discrete grain or an assembly of particles in a surface layer. Both approaches were found to be useful in the present

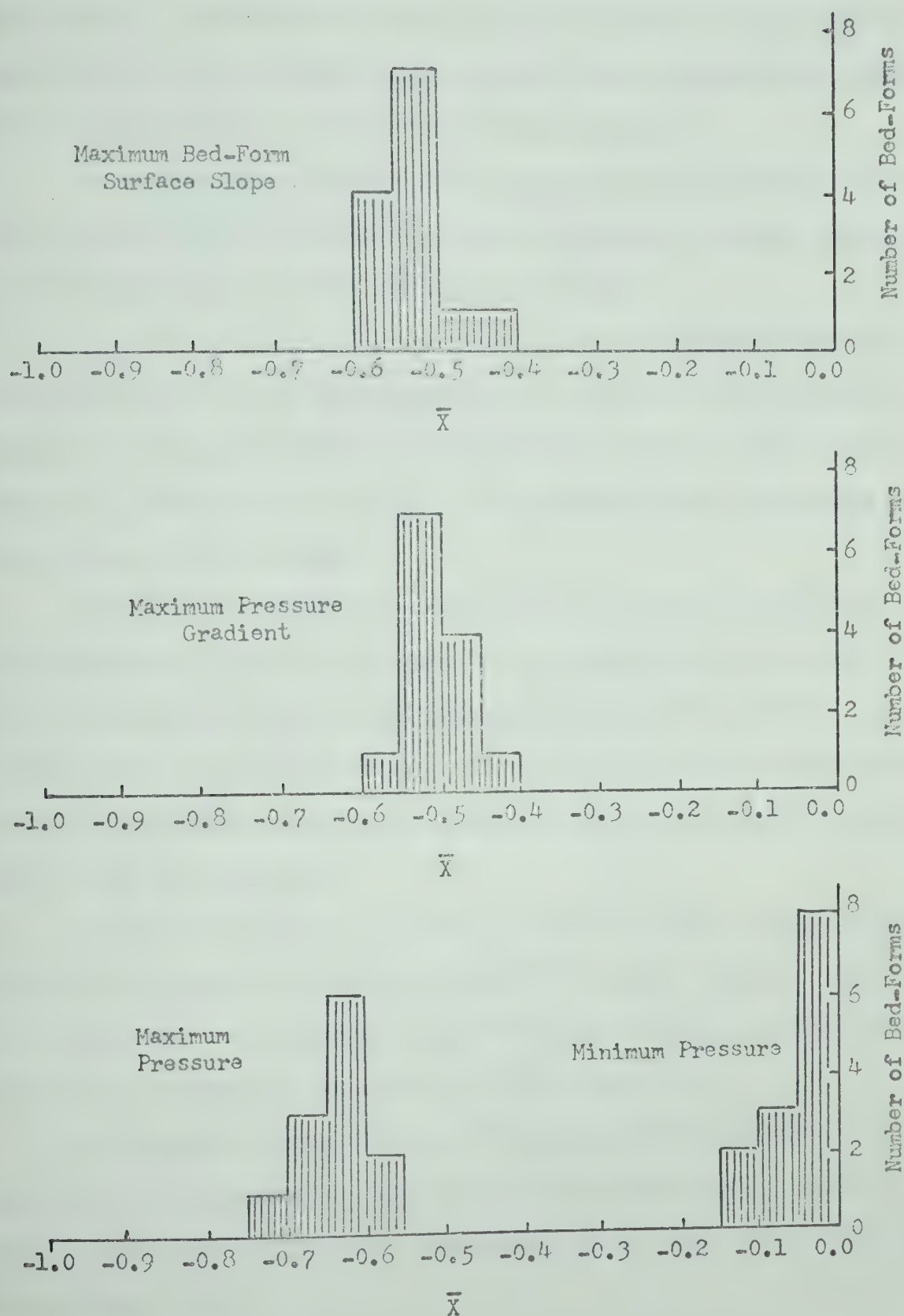


Figure 7.1. Histograms of Location of Maximum Bed-Form Surface Slope, Pressure Gradient, Pressure, and Minimum Pressure.

investigation. The discrete particle approach provided insight into the basic nature of the incipient motion problem. For practical work, however, the continuum approach was found to be more convenient.

In the following paragraphs both approaches are reviewed, compared, and an equation for determination of forces required to entrain particles from the back faces of active bed-forms is derived.

In a recent analysis of statics of discrete sediment particles, Yalin (1972) showed that the magnitude of an external force required to dislodge a stationary particle depends not only upon the weight of the particle W_p , but also upon its shape, the geometry of its environment and the condition of its surface.

A typical arrangement of equal diameter spherical grains in a two-dimensional situation is illustrated in Figure 7.2(a). Particle "A" rests in the hopper formed by two abutting particles "B" and "C". The centres of the supporting particles "B" and "C" are assumed to lie on a common line parallel to the local surface of the bed-form which makes an angle β with the horizontal.

If the angle between the mean local surface slope of the bed-form and the line tangent to particles "A" and "C" at their contact point "l" is Ψ' , the normal to the contact point "l" makes an angle of $\Psi' + \beta$ to the vertical. For spherical particles of equal size $\Psi' = 30^\circ$.

The relation between forces at the incipient motion stage for particle "A" is shown by the force-polygons in Figures 7.2(b) and (c). The body force due to gravity is represented by W_p , which can be estimated from equation (7.1):

$$W_p = (4/3)\pi r^3 g(\rho_s - \rho) \quad (7.1)$$

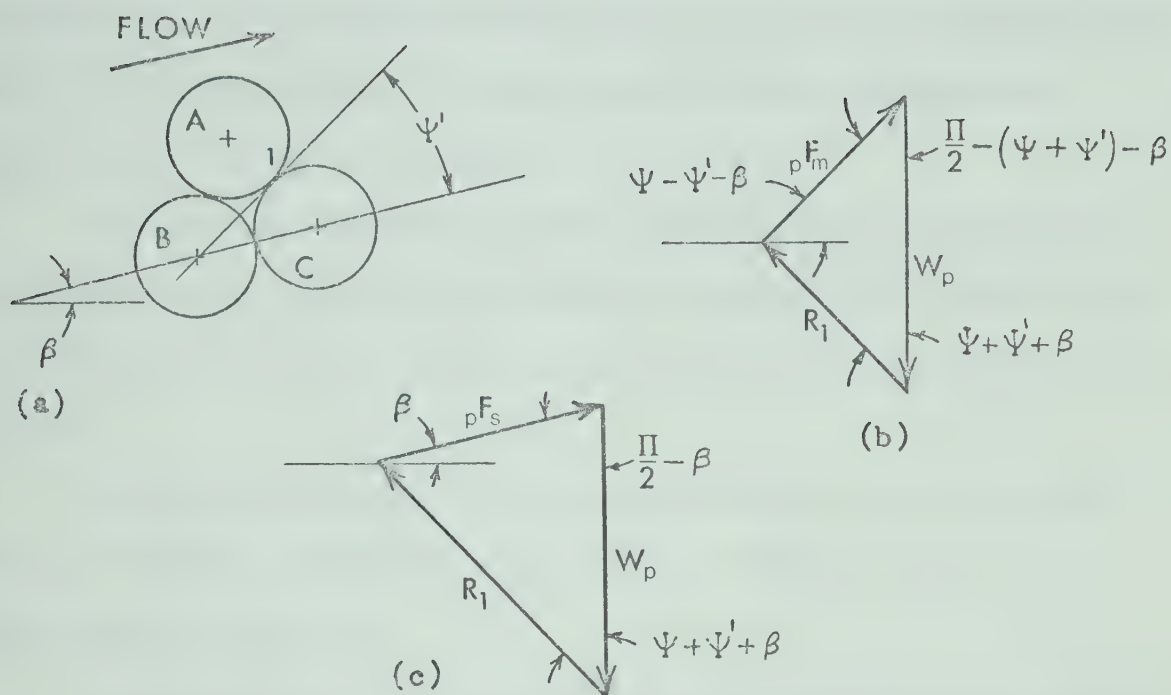


Figure 7.2. Statics of Individual Surface Particle.

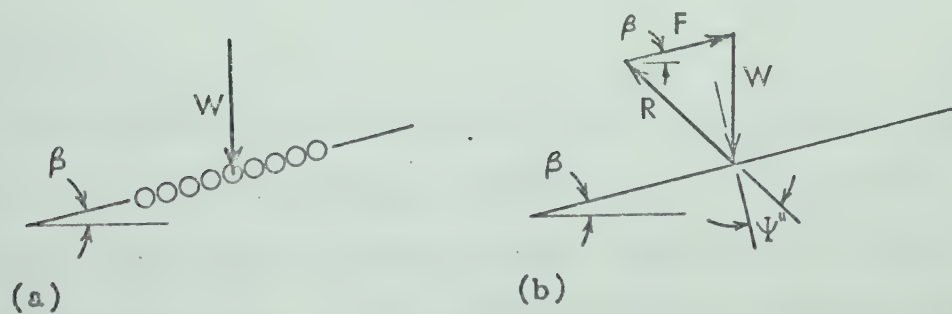


Figure 7.3. Statics of Surface Particle Layer.

where r represents the radius of the particle, g is the acceleration due to gravity, ρ_s is the density of the particle, and ρ is the density of the fluid. R_1 is the reaction at contact point "1" and Ψ represents the friction angle between the grains.

For a constant W_p the vector of a minimum force pF_m required to disturb the particle equilibrium is shown in Figure 7.2(b), while pF_s , in Figure 7.2(c), gives the minimum force vector parallel to the slope of the bed-form.

Clearly, the detachment of the particle may be caused by a wide variety of magnitude--direction combinations of the resultant of the external impelling forces.

The application of the sine law to the two minimum force conditions yields

$$pF_m = W_p \sin(a + \beta) \quad (7.2)$$

$$pF_s = W_p \tan a \cos \beta + W_p \sin \beta \quad (7.3)$$

where $a = \Psi + \Psi'$.

The equivalent body force diagram and force polygon at threshold conditions for a layer of particles resting on a surface inclined degrees to the horizontal is shown in Figure 7.3(a) and (b). W is the body force due to gravity of all particles contained in a volume one particle diameter thick and one unit in area, and Ψ represents the friction angle between the adjacent layers of particles.

The body force W is given by equation (7.4):

$$W = V_t C g (\rho_s - \rho) = D C \gamma (s - 1) \quad (7.4)$$

where C is the fractional volume concentration of particles equal to the

ratio of the volume of solids to the total volume V_t , D is the diameter of the particles, g represents the acceleration due to gravity, ρ_s is the density of the particles, ρ is the density of water, γ is the specific weight of water and s is the specific gravity of particles.

From the force polygon, the external impelling unit force parallel to the surface slope at particle threshold, F , is given by equations (7.5) or (7.6):

$$F = W \tan \Psi'' \cos \beta + W \sin \beta \quad (7.5)$$

$$F = D C \gamma (s - 1)(\tan \Psi'' \cos \beta + \sin \beta) \quad (7.6)$$

It is seen from equations (7.3) and (7.5) that the discrete particle and surface layer approaches are equivalent provided that Ψ'' is the friction angle which combines the individual particle environmental geometry (Ψ') and surface friction (Ψ) effects.

7.3.2 Concentration and Friction

Equation (7.6) for the minimum force required to entrain the particles has two terms which indicate that forces which resist the detachment arise because of interparticle friction and the direction of displacement in relation to the gravity field. Both components depend upon the thickness D and the concentration of the particles C in the layer immediately before entrainment. In addition the friction factor depends upon the instantaneous angle of friction between the layers Ψ'' . Both components depend also upon the local surface slope β which was the only parameter measured in the experiments.

To determine applicable values of C and Ψ'' an extensive review of literature was carried out, and considerable information related to granular particles in bulk volumes was found. However, little has been written

about these conditions at the surface of particle beds. Consequently, the analysis adopted a limit approach; probable maximum and minimum values of C and Ψ'' were estimated from bulk volume considerations and were used to determine the limiting bounds for minimum force requirement to entrain the particles.

Theoretical considerations by Graton and Frazer (1935) have shown that the volume concentration of equal size spherical particles depends upon the packing arrangement of the particles. Maximum and minimum concentrations of $C = 0.741$ and $C = 0.524$ are obtained when the spheres are in the ideal rhombohedral and cubical arrays respectively.

Although in the present experiments spherical particles of nearly uniform size distribution were used, their arrangement in the bed-forms was haphazard as they were deposited by sliding down the lee slope of the bed-forms.

This type of deposition produces relatively loosely packed granular beds, because as the granular solids shear, the mass of particles experiences an increase in bulk volume without change in the volume of solids. This well-known phenomenon, termed dilatancy, has been observed in the field by Imbris and Buchanan (1965). They confirmed that avalanched deposits, such as occur on the lee face of fluvial dunes were loosely packed in relation to sheet deposits.

These observations indicated that the expected concentration of particles in the bed-forms of the present investigation should be in the lower range of the theoretically possible concentration values.

The limits of volume concentration of haphazardly packed equal spheres were investigated by Scott (1960). In a theoretical study supported by experimental observations he determined that the maximum possible con-

centration was 0.637 and the minimum possible concentration was 0.601.

Later, in an experimental study of the effects of various material properties upon the packing of spherical particles, McRae and Gray (1961) found that 3.08 millimetre diameter spherical particles yielded volume concentration of 0.602 when deposited by cascading in air.

These results were found to correspond closely with the results of the average volume concentration of 0.598 of the polystyrene particles used in this study as determined from packing of particles for the permeability tests described previously in Section 3.3.4.

From the above observations it was concluded that a value of 0.601 for the volume concentration of particles in the bed-form could be reasonably assumed.

For the present experiments, in the absence of better information, it was assumed that the angle of friction between layers of particles on the surface of the bed-forms, Ψ' , can be represented by the angle of initial yield ϕ_1 .

Although in the present problem C and Ψ'' appear as independent parameters, past investigations of bulk volume behaviour of granular particles have indicated that they are closely interrelated. The relationships between C and ϕ_1 have been extensively reviewed by Allen (1969, 1970a, 1970b) who concluded, from theoretical considerations, that the angle of initial yield ϕ_1 is dependent upon the manner of packing and upon the orientation of particles relative to the direction of yield.

As numerous ways of particle packing are possible which yield different concentrations, Allen (1970a) proposed a semi-theoretical relationship between C and ϕ_1 :

$$\tan \phi_1 = 3.596C - 1.884 + A \quad (7.7)$$

where A is a dimensionless coefficient to account for real effects such as surface friction between particles. This relationship implies correctly that when $A = 0$ and C is the minimum possible concentration 0.524, ϕ_i equals zero. For haphazardly packed equal spheres with $A = 0$, application of equation (7.7) with maximum and minimum possible concentrations of 0.637 and 0.601 determined by Scott (1960) yields $\phi_i = 22.1^\circ$ and $\phi_i = 15.5^\circ$ respectively. Experimental results, in which 0.59 to 0.84 millimetre size range glass heads were employed (Allen, 1970a), showed that A was 0.220 only when C was greater than approximately 0.610. For C values less than 0.610, the experimental data indicated a very rapid decrease in the ϕ_i value with reduction in C , and at $C = 0.601$ ϕ_i was considerably less than 26° predicted by equation (7.7). It is obvious that this relationship was not applicable in the present situation, where C was established to be 0.601.

The value of ϕ_i , which represents the angle Ψ' , was therefore estimated from experimental considerations.

The tilting tests described in Section 3.3.5 showed that depending upon the mode of initial deposition the angle of initial yield ϕ_i was either 29° or 31° . The smaller angle of 29° was obtained when avalanched deposits of particles were tilted in the opposite direction. And since this condition of deposition approximated the conditions of particles in a bed-form, $\phi_i = 29^\circ$ was assumed to represent Ψ'' in the subsequent calculations.

The C and Ψ'' values of 0.601 and 29° respectively were assumed to represent the upper bound of conditions on the surface of the bed-forms.

For the lower limit, the following observations were considered. The concentration C of particles in the surface layer may be substantially lower than the particle concentration in the bed-forms because surface

layers are subject to dilatation effects arising as a result of shearing action by the flow and the impact by other particles. Visual observations such as particle oscillation prior to entrainment and the loose appearance of the bed surface confirm the tendency toward a lower C value. Furthermore, Bagnold (1955) has indicated that to allow grain movement to take place at all C must be approximately 0.5, which is the lower limit of the theoretical minimum concentration of spherical particles.

As discussed previously, the concentration of particles is related to the angle of initial yield ϕ_i . To achieve a lower volume concentration of particles in the surface layer while maintaining a constant areal concentration of equal number of particles per unit area, the effective thickness of the surface layer must be increased by increasing the distance of separation between the two upper layers of particles. It would appear therefore that a finite amount of energy must be expended to produce dilatation and a slight uplift or rearrangement of surface particles into a cubical array. This condition corresponds to an unstable particle arrangement and the angle of initial yield ϕ_i becomes zero. Therefore for the lower limit, the concentration of particles in the surface layer was assumed to be 0.524 equal to the theoretical minimum for equal spheres with $\Psi' = 0$.

7.3.3 Minimum Force Requirements for Detachment

To compute minimum force requirements to detach particles from various locations along the surface of the bed-forms using equation (7.6), γ was assumed to be 62.4 pounds per cubic foot, and the specific gravity of particles s was adjusted in each test for temperature effects. The local value of the angle was determined from the bed-form geometry measurements assuming linear profile between limits of individual segments 0.1 \bar{L} long each.

In all calculations $D = D_{50}$ of 1.4 millimetres was used. This may be questioned on the grounds that sliding on the lee face of the bed-forms produced sorting of the particles in the bed-form. As shown by Bagnold (1954), coarser particles accumulate near the bottom of the bed-forms. Hence, upon re-exposure on the upstream face of the bed-form the mean diameter of particles D_{50} in the zone upstream of $\bar{X} = -0.50$ was likely to be larger than in the region $-0.50 < \bar{X} < 0.0$. In accordance with equation (7.6), the minimum unit force required to entrain the particles from the upper half of the bed-forms should have been less than from the lower half. However, as in these experiments the particle gradation was very uniform, the errors introduced by neglecting the sorting effect upon local D values, would have been of relatively small magnitude in comparison with errors in estimating such factors as concentration or friction.

7.4 Particle Entrainment Forces

7.4.1 Boundary Shear Stresses

No reliable methods for determining boundary shear stresses on the surface of active bed-forms have been established to-date. The problem is exceedingly difficult because the combined effects of pressure gradients, movement of solid particles, curved boundaries, and inflow and outflow from the porous bed must be considered simultaneously in establishing the proper relationships. In the absence of a better approach, the shear stress distributions on the upstream face of the bed-forms in the present investigation were estimated using plane rigid boundary techniques.

The application of rigid boundary techniques to determine skin resistance to flow over alluvial bed-forms has been attempted by Einstein and Barbarossa (1952), Simons and Richardson (1966), Vanoni and Hwang (1967), and others. Generally these investigators assumed that the local shear

stresses can be estimated from some type of an universal logarithmic velocity relation.

The mean dimensionless velocity profiles $\frac{\bar{u}}{\bar{U}_s}$ presented in Figure 6.13 disclosed that between $\bar{X} = -0.50$ and $\bar{X} = -0.10$ and near the sediment boundary the velocities were logarithmically distributed. Therefore, to determine skin friction distribution characteristics the law of the wall relationships was employed. Preliminary considerations showed that at $y/d = 0.15$ the shear velocity (u_*) Reynold's numbers u_*y/ν in the region downstream from the reattachment point were in the order of 100. The thickness of the viscous sublayer δ' calculated from $11.6 \nu/u_*$, was found to be approximately 0.003 feet. Hence the ratio D_{50}/δ' of the characteristic particle size to the thickness of the viscous sublayer was estimated to be about 1.5. This represents conditions of flow over a hydrodynamically smooth surface in which the surface roughness elements are just beginning to have effect. Therefore, for surface shear stress determination the smooth boundary law of the wall relation given by equation (7.8) was employed:

$$\frac{u}{u_*} = \frac{1}{\kappa} \ln \frac{yu_*}{\nu} + B \quad (7.8)$$

where u is the mean velocity of flow at depth y , ν is the kinematic viscosity, B is an experimentally determined constant, and κ represents the von Karman's constant. According to Goma and Gelhar (1968), the value of $\kappa = 0.40$ was consistent with observations of flow in pipes with porous walls. It was therefore assumed to be applicable also in the present experiments.

The relationship to determine boundary shear stresses was obtained by rearranging equation 7.8 into

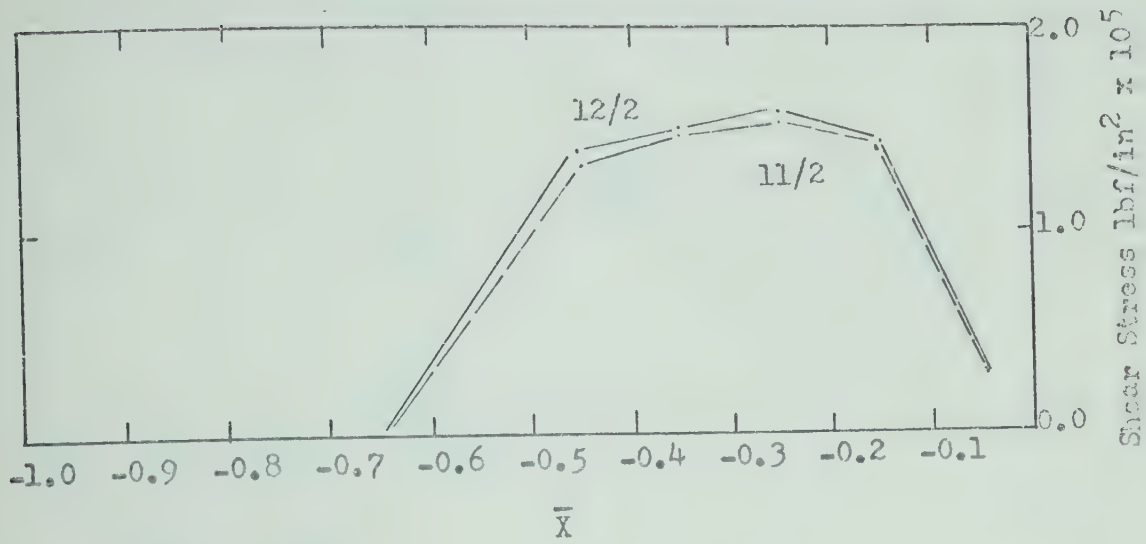
$$u = (5.75u_*)\log y + C' \quad (7.9)$$

where C' is a constant term not containing either u or y . Therefore $(5.75u_*)$ represents the slope of the velocity profile in a u v.s. $\log y$ plot. The method is constrained, however, to logarithmic velocity distributions at depths $\frac{y}{d} < 0.15$.

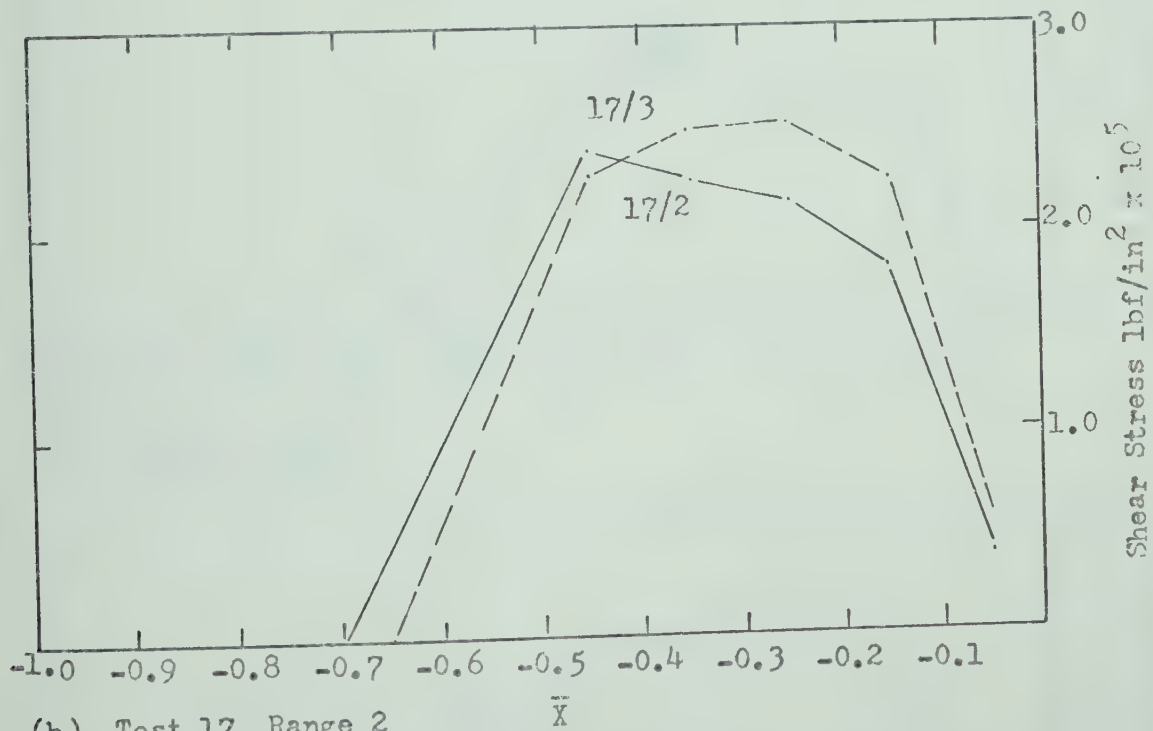
The information required to establish velocity distribution slope for each shear stress evaluation was obtained from experimentally determined data. The mean dimensionless velocity profiles $\frac{\bar{u}}{U_s}$ v.s. $\frac{y}{d}$, together with mean depth information given by the individual bed-form geometry data and the measured flow discharge in the flume were used to reconstruct the local u vs. $\log y$ profile. From this the slope of the velocity profile $du/d(\log y)$ between $y/d = 0.0625$ and 0.125 could be determined. The local shear was then computed from equation (7.10)

$$u_* = \sqrt{\frac{\tau_v}{\rho}} = \frac{1}{5.75} \frac{du}{d(\log y)} \quad (7.10)$$

The results of shear stress evaluation in all segments downstream from $\bar{X} = -0.50$ above all selected bed-forms are presented in Figure 7.4. From physical considerations, and as indicated by the results of Laursen et al. (1962) and Raudkivi (1963), the shear stress at the reattachment position, considered from velocity profile data to be at $\bar{X} = -0.65$, was assumed to be zero. At $\bar{X} = -0.55$ shear stresses were not calculated because the measured velocity profile as shown in Figure 6.13 did not appear to be logarithmic. The reason for this anomaly at $\bar{X} = -0.55$ is not clear. However, this location corresponds generally with the location of the maximum pressure gradient, the maximum bed-form surface slope, and the local suppression of turbulence as discussed in Section 7.2.2.



(a) Test 11, Range 2
Test 12, Range 2



(b) Test 17, Range 2
Test 17, Range 3

Figure 7.4. Boundary Shear Distribution.

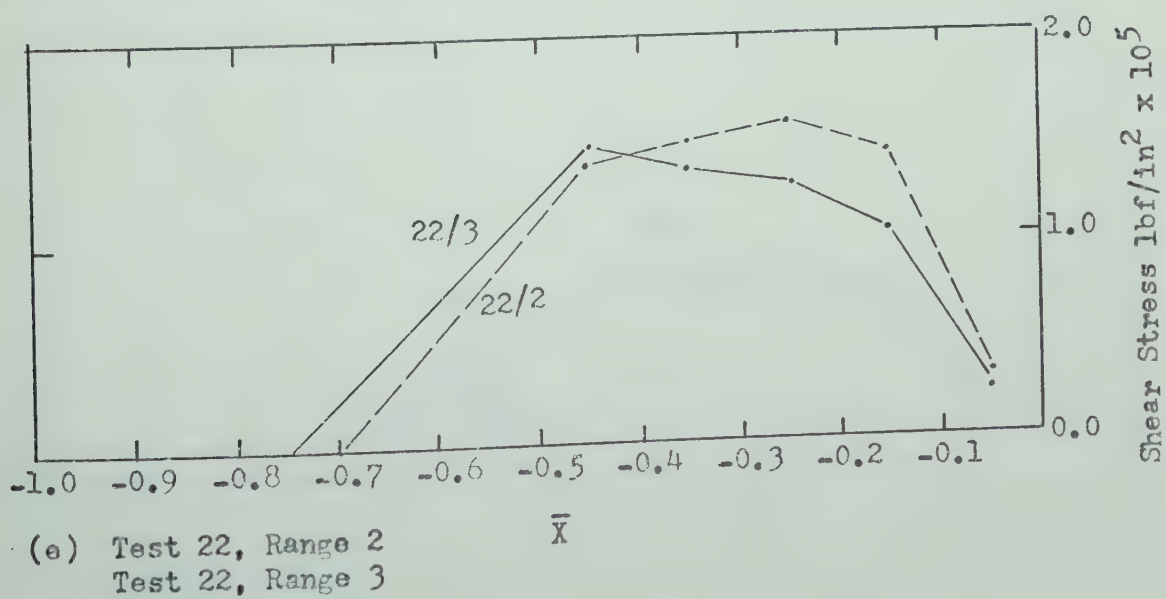
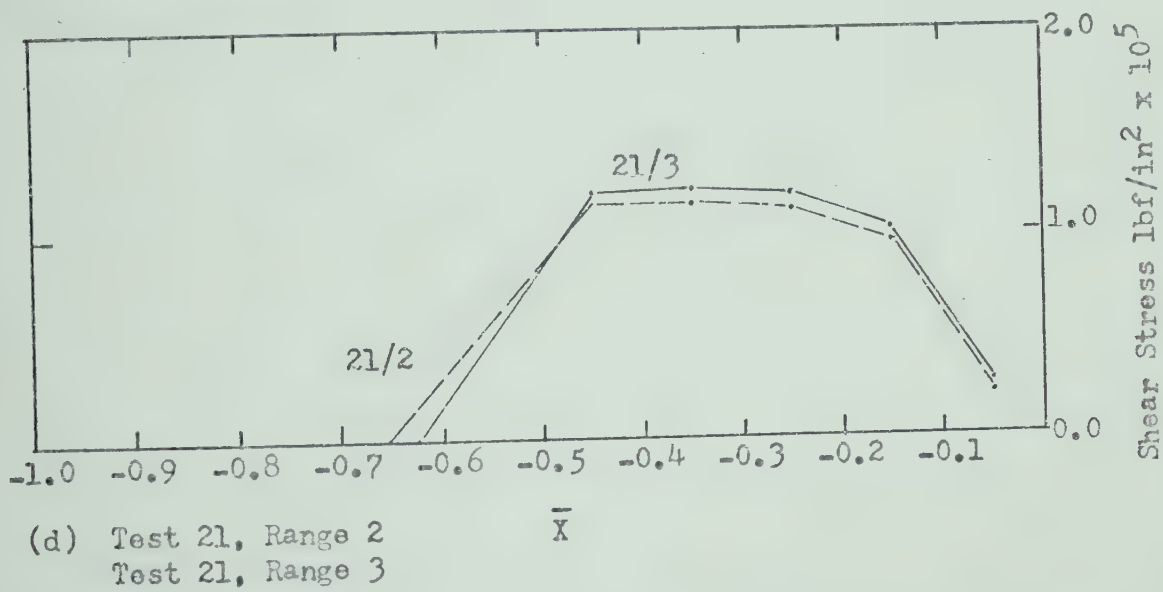
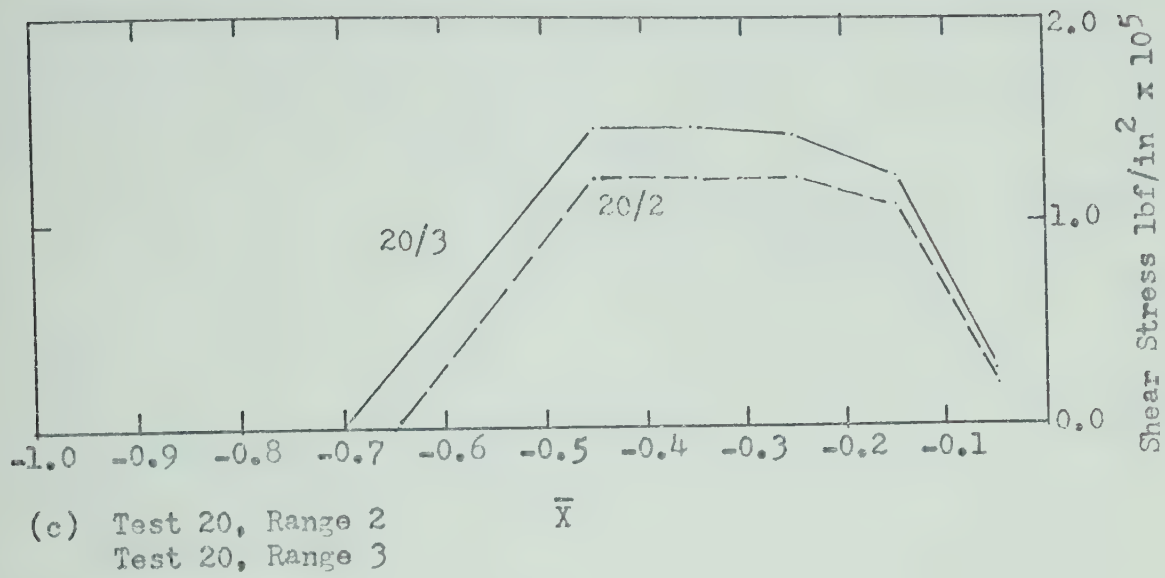


Figure 7.4. (Continued)

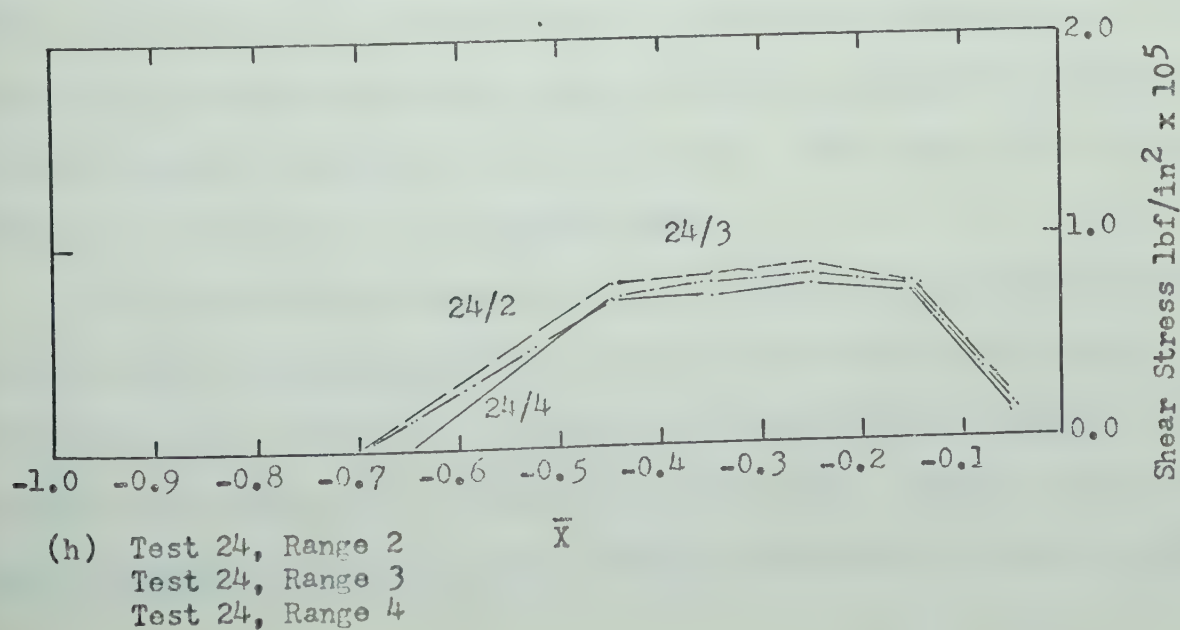
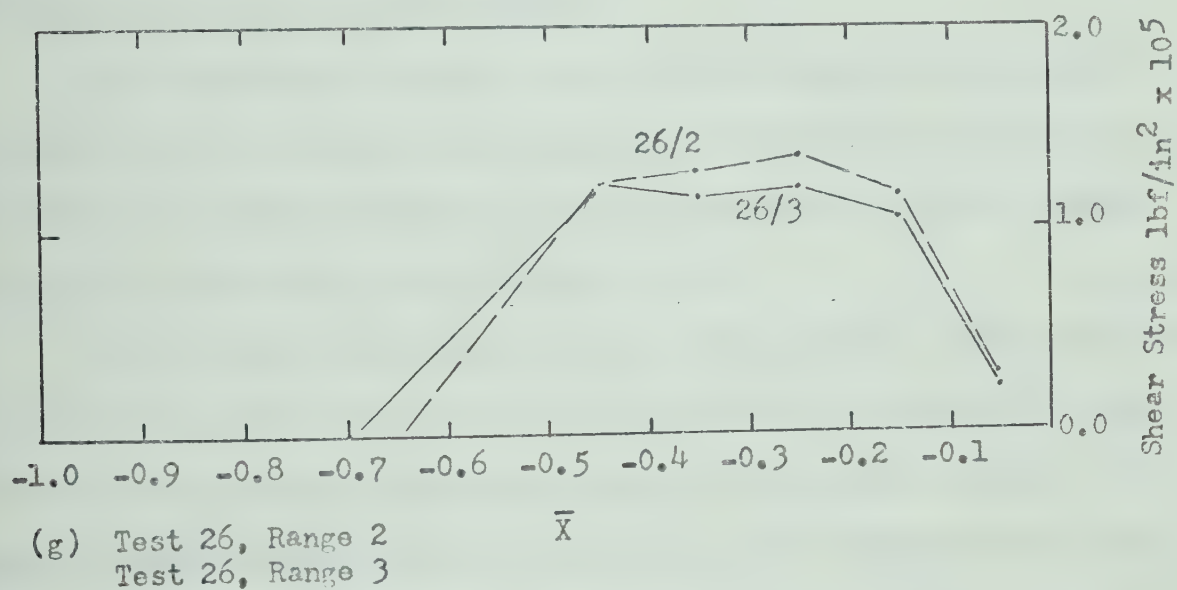
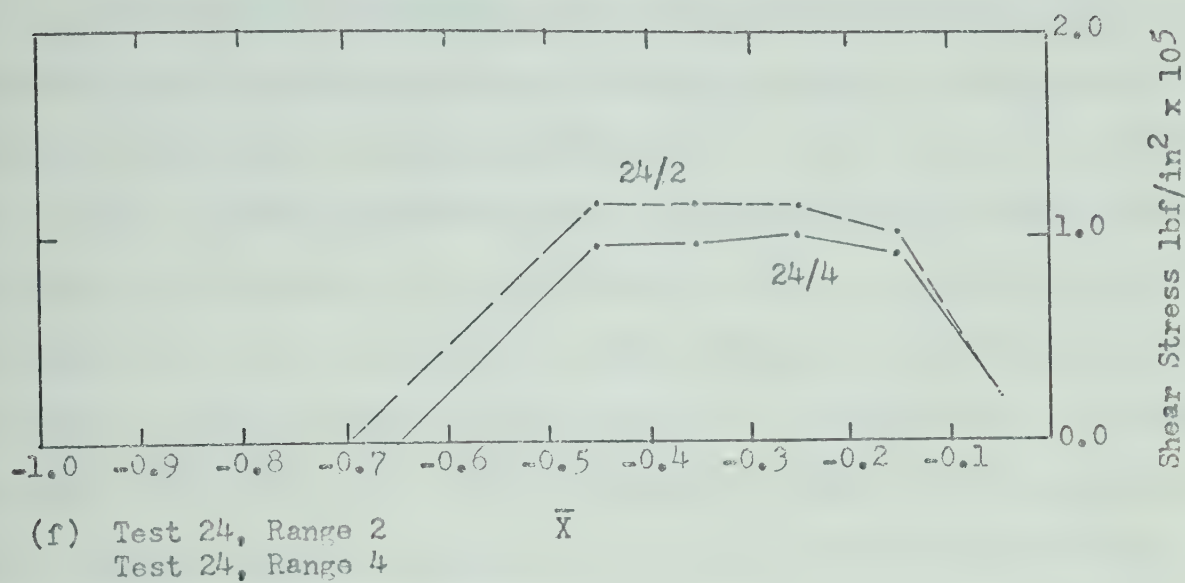


Figure 7.4. (Continued)

The results of the average shear stress distributions on the boundary of the bed-forms show that the shear stresses increase rapidly from the reattachment position downstream to $\bar{X} = -0.45$, and remain constant to $\bar{X} = -0.15$. However, downstream from $\bar{X} = -0.15$ the shear stresses diminish rapidly as indicated by the relatively low value of shear at $\bar{X} = -0.05$ and appear to be zero at the crest. These results are clearly not in agreement with the boundary shear stress distributions established on stabilized bed-forms by Laursen et al. (1962) and Raudkivi (1963) who found that the shear stresses increased continuously from the reattachment point downstream to the crest of the bed-forms.

The discrepancies between the present findings and the results obtained from measurements on rigid boundary bed-forms were attributed to the effects of particle movement along the bed and the possible outflow from the bed immediately upstream from a crest.

In the present experiments boundary shear stresses were established from velocity profile data which assumed boundary of the bed at the upper surface of the sediment particles. Because of bed particle movement the assumed boundary, as indicated in Figure 6.12, had a finite average velocity, and furthermore was located above the stationary particles. It appears that the velocity of the fluid in the layer adjacent to the particles was increased because of particle movement. This reduced the velocity gradient and, therefore, the estimated shear.

On rigid boundary bed-forms, the shear was found to increase because as the boundary layer developed in the downstream direction from the reattachment point, the velocity gradients near the boundary increased. Boundary layer developed on a granular boundary also. However, it is possible that the movement of the entrained particles, increasing in velocity in the

downstream direction, increased sufficiently the local velocity of fluid above the particles and effectively counteracted the increasing velocity gradients due to boundary layer development.

Experimental evidence suggested that small amounts of outflow from the bed into the flow occurred in the region upstream of the crest. Although pressure measurements did not disclose any vertical gradients, horizontal pressure distribution measurements showed that minimum pressures occurred immediately upstream of the crest. Therefore, pressure gradients would have produced seepage toward the low pressure zone from both sides. Evidence to support this observation was provided by the direction of particle movement near the crest on the lee side of the bed-form immediately prior to deposition, as discussed in Section 6.5.1, and also by the extremely steep lee-side slopes of the bed-forms as discussed in Section 7.2.1. As the flume bottom was impermeable, to maintain continuity, the outflow must have occurred through the interface of the bed-form upstream of the crest.

A summary of qualitative effects of fluid injection into the flow upon channel boundary layer has been presented by Watters and Rao (1971). According to this summary injection would have reduced the friction drag upon the boundary as was confirmed by the reduction of shear estimated from the experimental evidence.

Although the shear measurement results are subject to the limitations imposed by the measurement and evaluation technique, they nevertheless point out some possible misleading interpretation of results obtained from measurements on simulated bed-forms. Especially significant is the present observation that shear does not increase but decreases near the crests of the bed-forms. This seems to be reasonable because no

or very little particle entrainment near the crest takes place. If the shear were to increase continuously toward the crest, as indicated by Raudkivi (1963), more particles would have been entrained from the crest position, and the bed-form would have not retained its shape.

7.4.2 Forces Due to Pressure Gradients

The results of pressure measurements, presented in Figures 6.21 (a) to (h), have shown that pressure gradients were established throughout the mass of granular particles in the bed-forms. The characteristics of these pressure distributions were found to agree qualitatively with pressure distributions established on the surfaces of stabilized bed-forms as reported by Laursen et al. (1962) and Raudkivi (1963). On this basis it was assumed that the measured pressure characteristics were representative of conditions in the layer of stationary particles on the surface of the bed-forms in the present experiments.

When pressure gradient exists in the fluid of the pores of granular materials, a dynamic force in the direction of decreasing pressure, is exerted upon the stationary particles (Taylor, 1948). In the layer of stationary particles resting on the surface of the bed-forms the distribution of unit force, or stress, τ_p per unit area due to pressure gradients was estimated by equation (7.11):

$$\tau_p = h_w \gamma D_{50} \cos \beta \quad (7.11)$$

where h_w represents the local hydraulic pressure gradient in inches of water per inch length of bed-form, γ is the specific weight of water, D_{50} is the characteristic particle diameter, and β represents the local slope of the bed-form surface. The pressure gradient was determined from the mean pressure distribution characteristics by estimating the slope of the

pressure distribution curve at the mid-point of each $0.1 \bar{L}$ segment. The surface slope angle β was determined assuming linear profile between the limits of each segment. For all calculations D_{50} was assumed to be 1.4 millimetres.

The distribution of the pressure shear stress τ_p upon the particles in a surface layer of the bed-forms downstream from the reattachment point are presented in Figure 7.5.

In the majority of bed-forms investigated, the maximum surface slope angle β was less than 10° . The reduction in the local value of τ_p due to bed surface inclination was therefore less than two per cent.

7.5 Relative Force Contribution

7.5.1 Results

The relative contributions of the average boundary shear stresses due to fluid flow τ_v and pressure gradients τ_p on the particles in the surface layers of the bed-forms downstream from the reattachment point were determined for the two extreme conditions of particle concentration and friction assumed in Section 7.3.2.

The percentage contribution of each of the two stresses to particle entrainment and their distribution on each bed-form were computed by dividing the local values of τ_v or τ_p in each segment by the total force requirement F determined by equation 7.6.

The results for the upper limit condition with $C = 0.601$ and $\Psi'' = 29^\circ$ are presented in Figure 7.6 and show that the force contribution to the entrainment of particles by flow shear increases rapidly in the downstream direction from zero at the reattachment point to approximately $\bar{X} = -0.45$, gradually thereafter to a maximum at $\bar{X} = -0.25$ and decreases

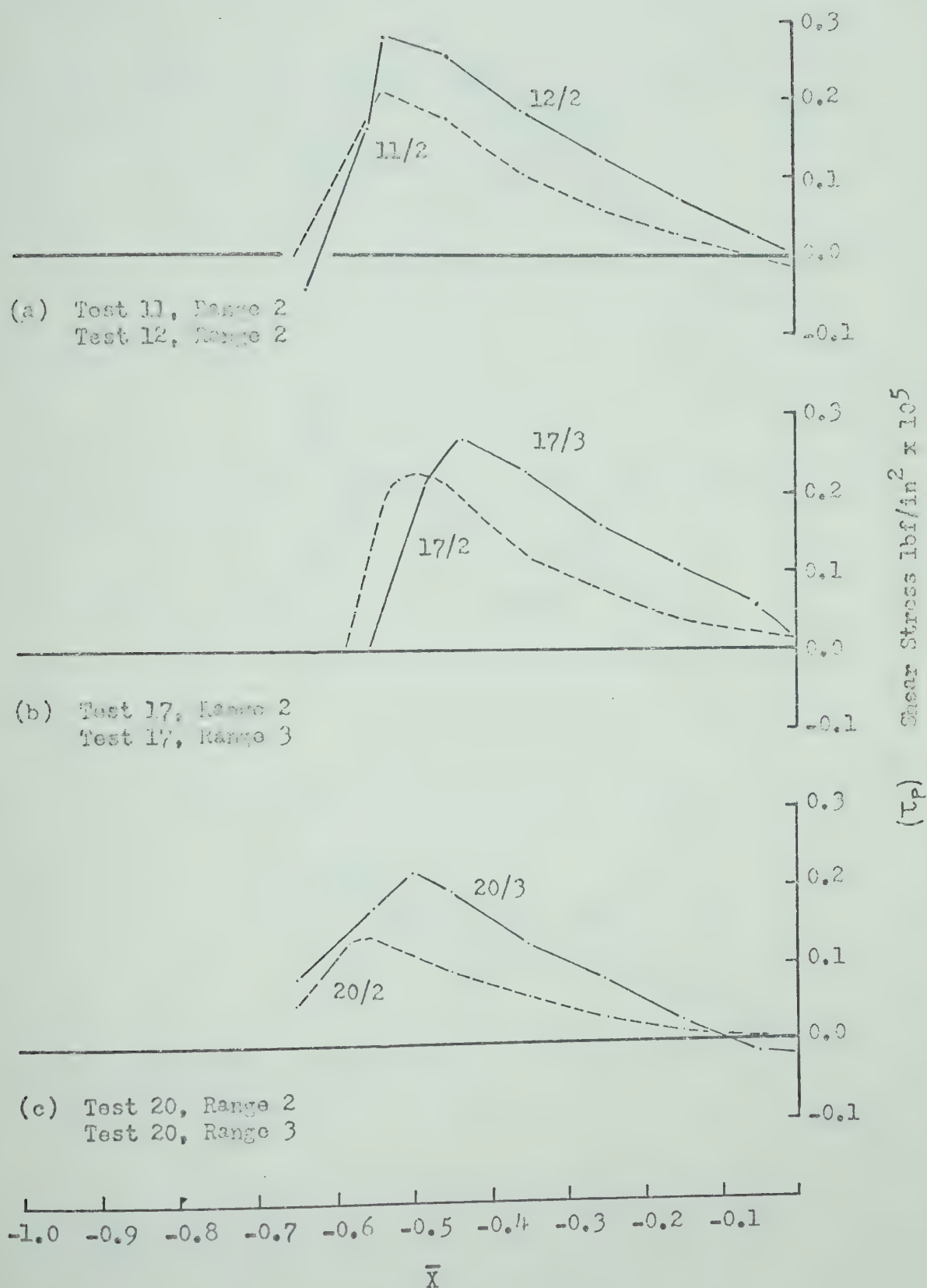


Figure 7.5. Distribution of Shear Stress Due to Pressure Gradients.

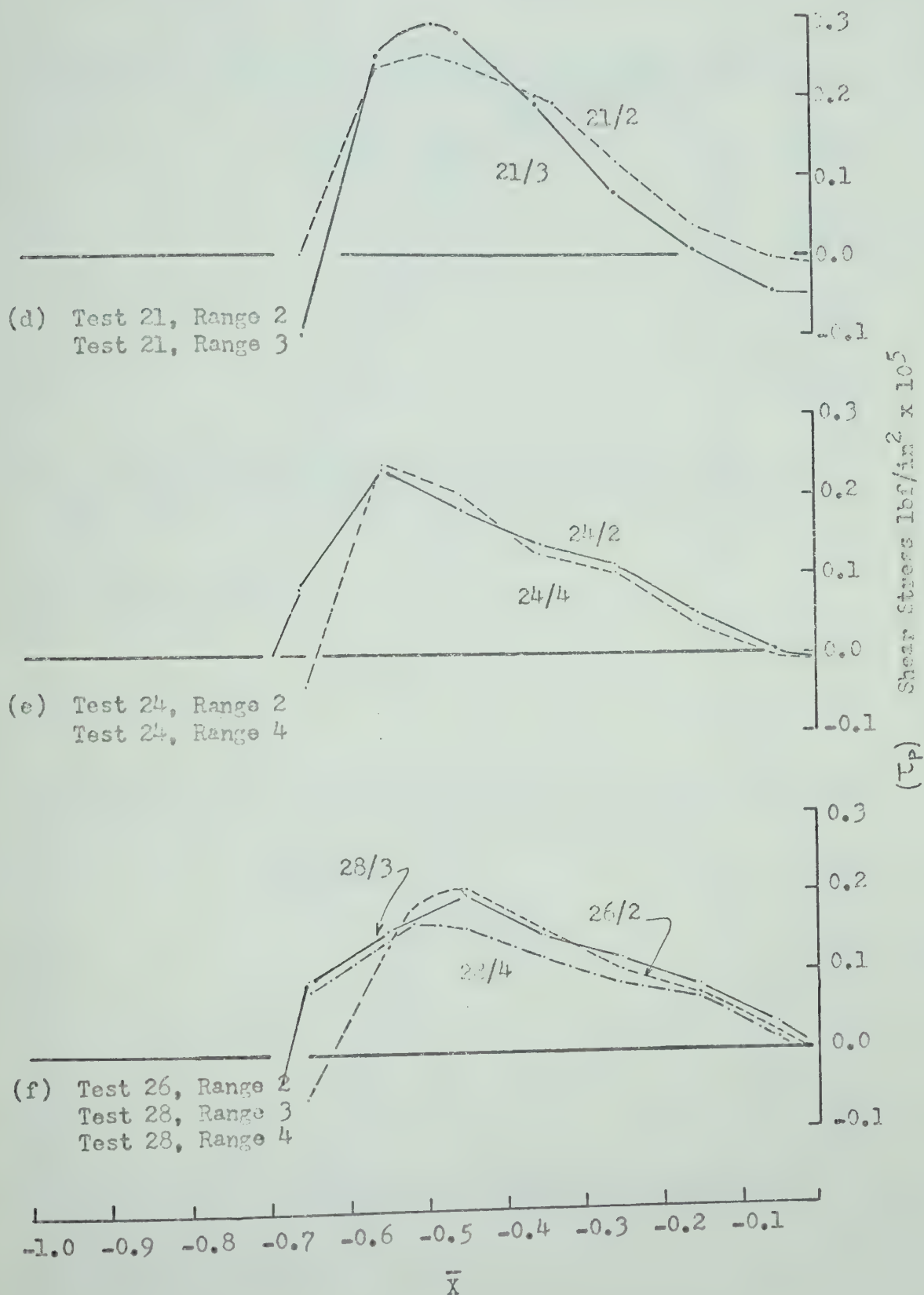
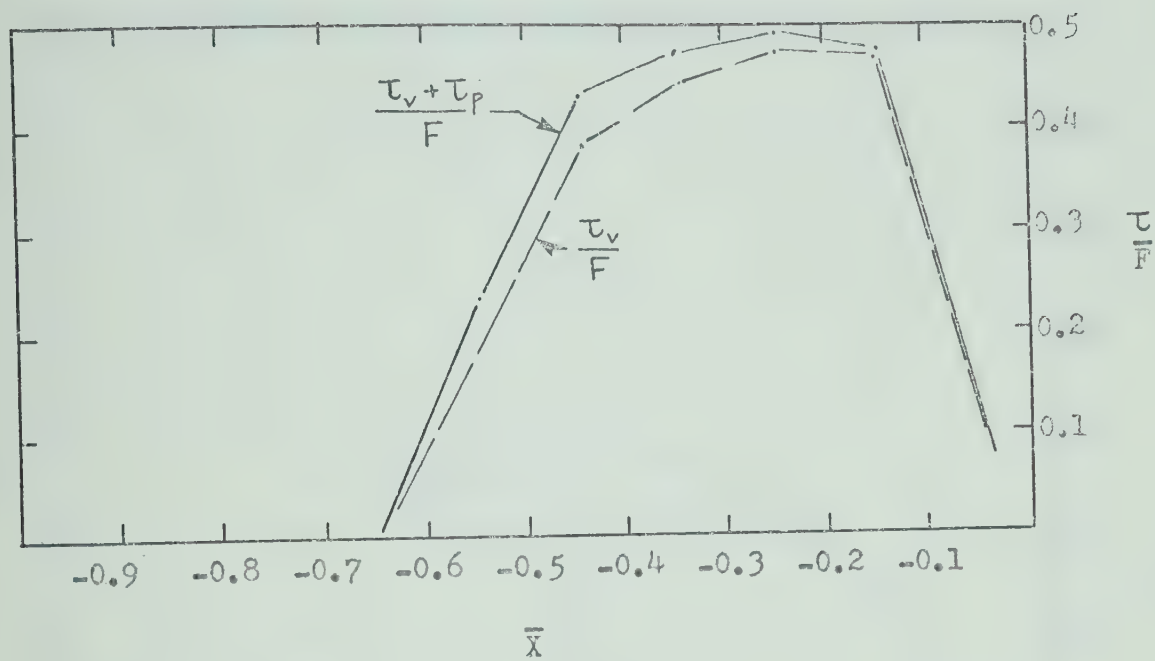
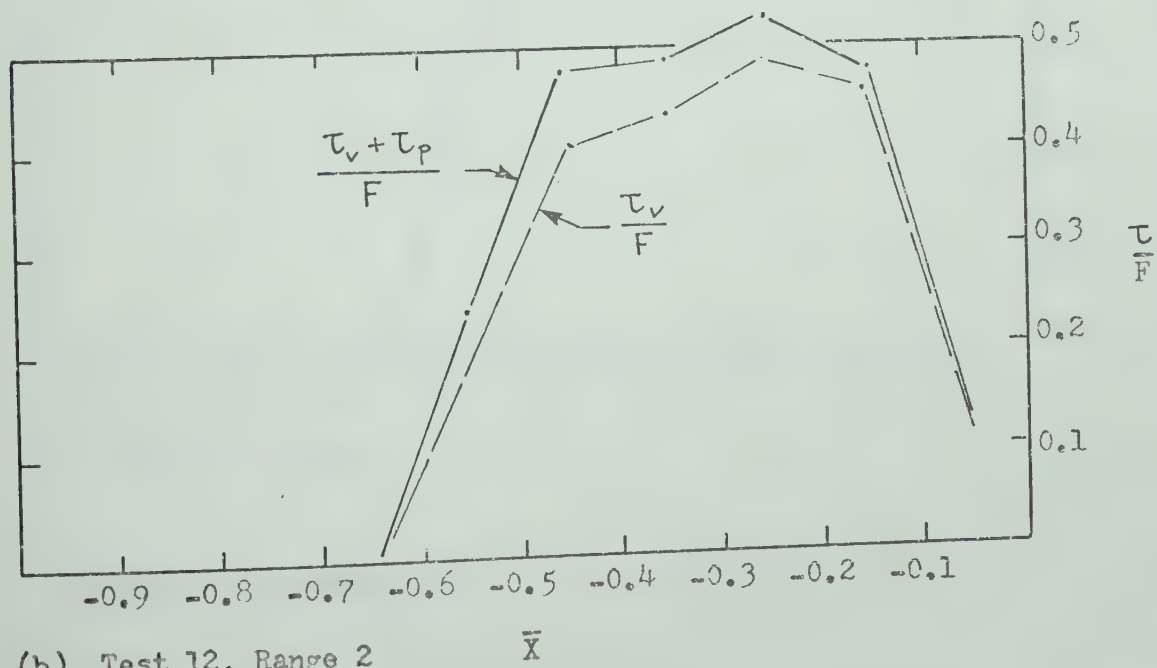


Figure 7.5. (Continued)



(a) Test 11, Range 2



(b) Test 12, Range 2

Figure 7.6. Relative Stress Contribution

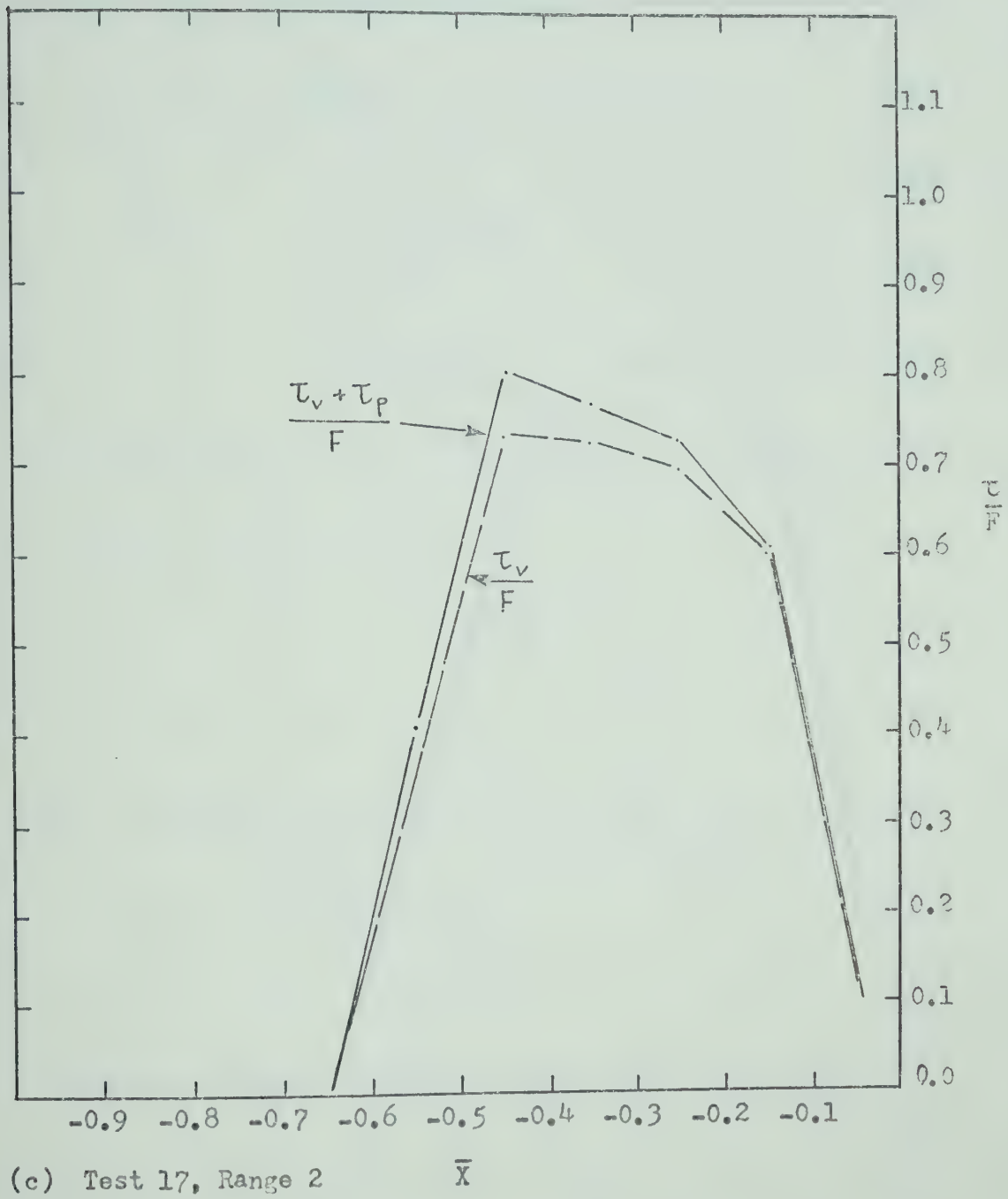
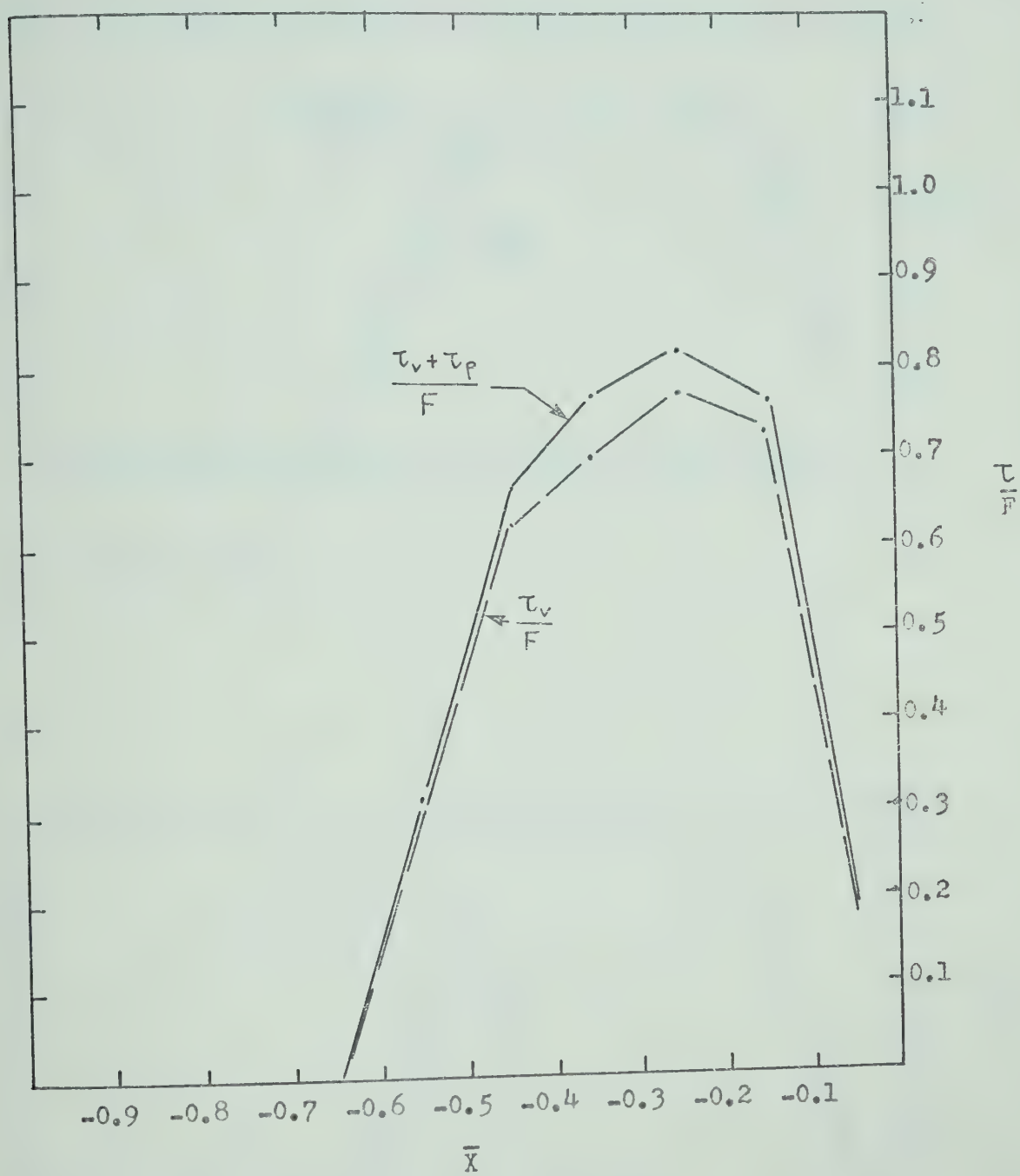
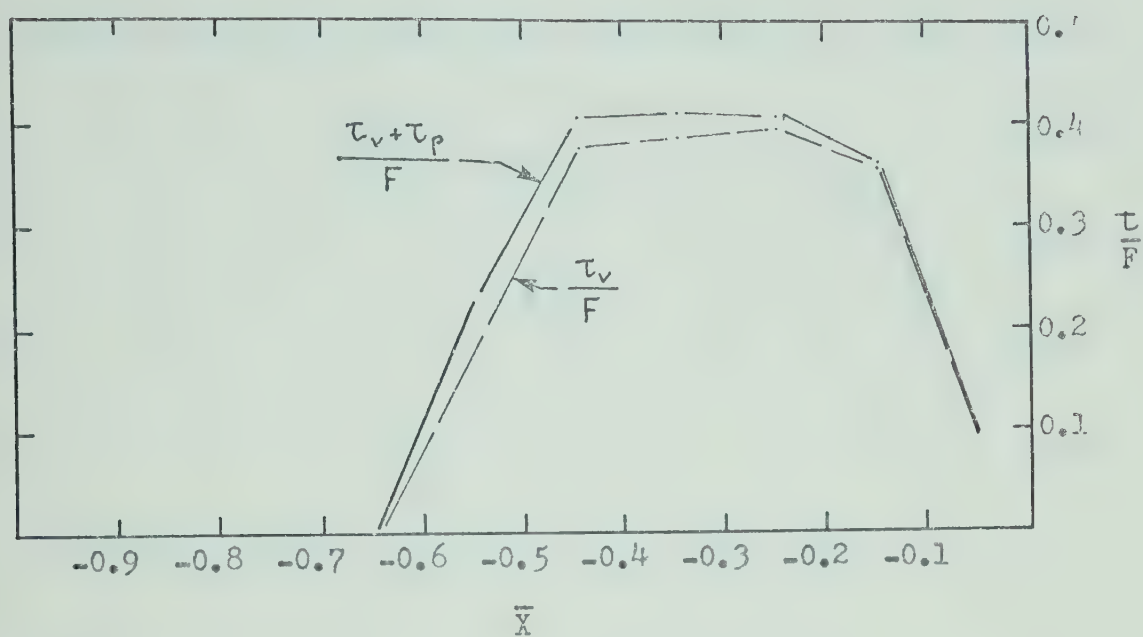


Figure 7.6. (Continued)

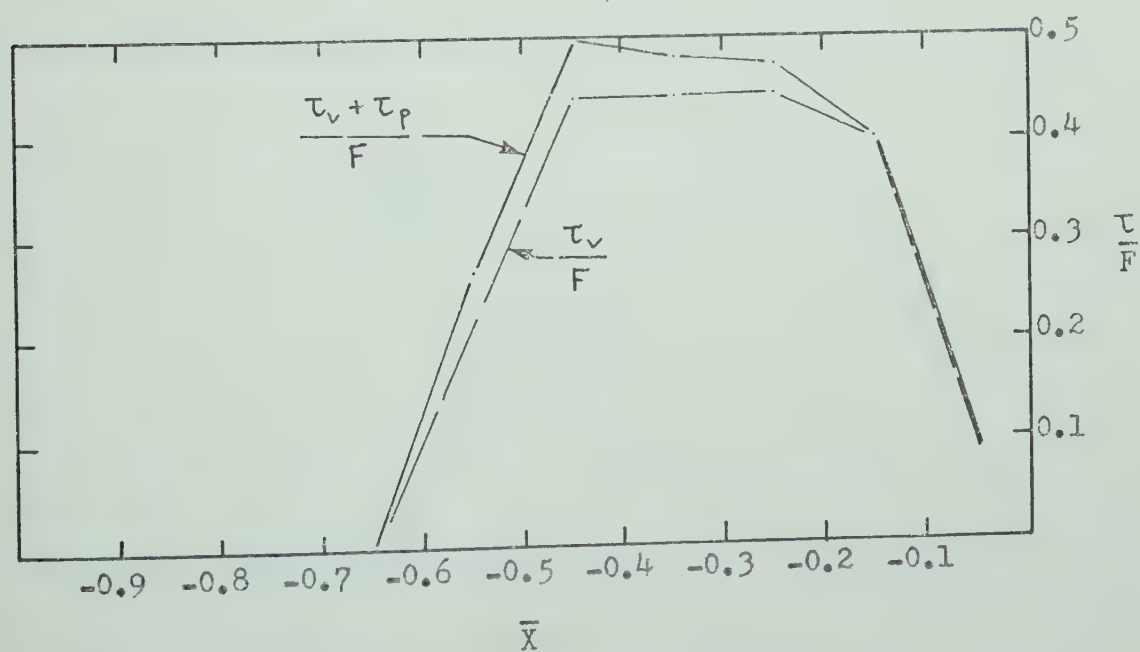


(d) Test 17, Range 3

Figure 7.6. (Continued)

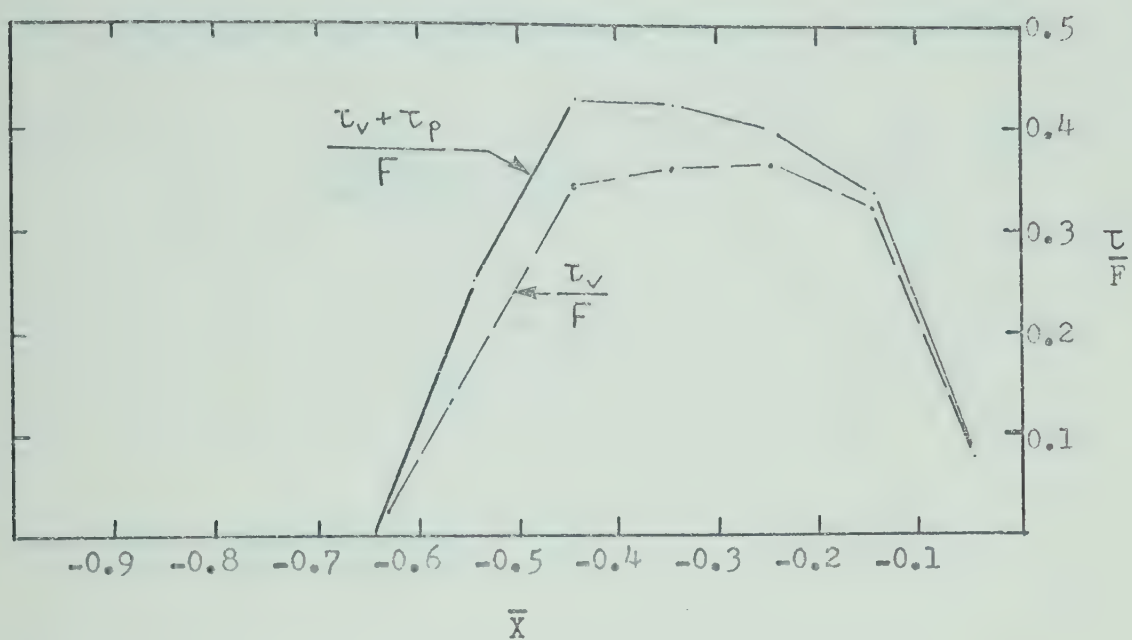


(e) Test 20, Range 2

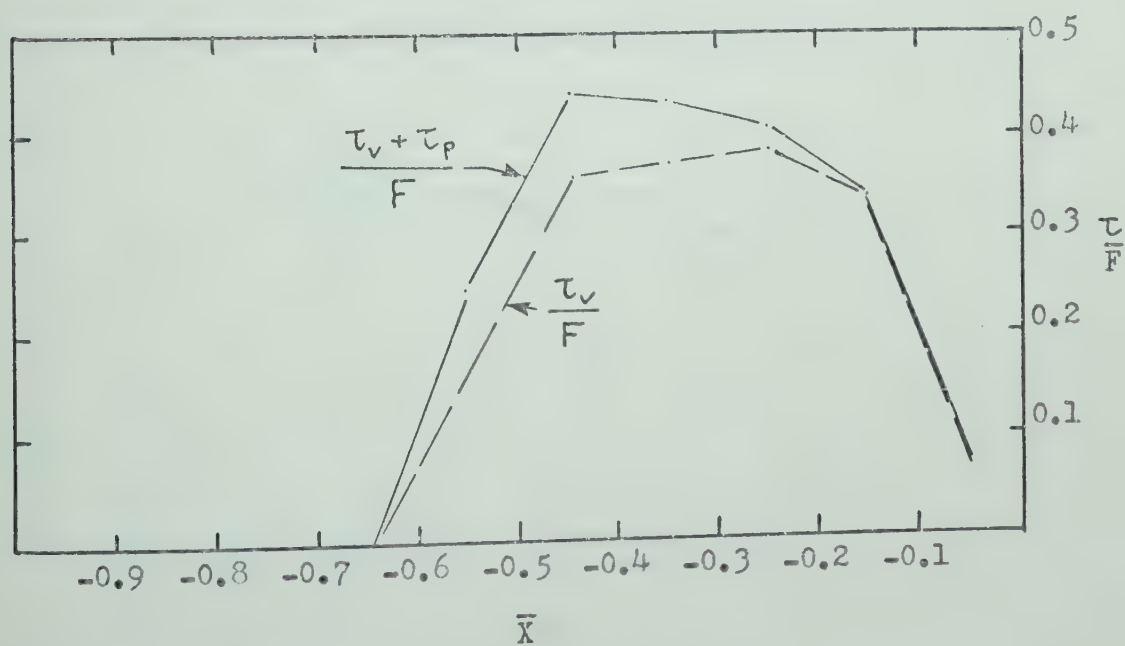


(f) Test 20, Range 3

Figure 7.6. (Continued)

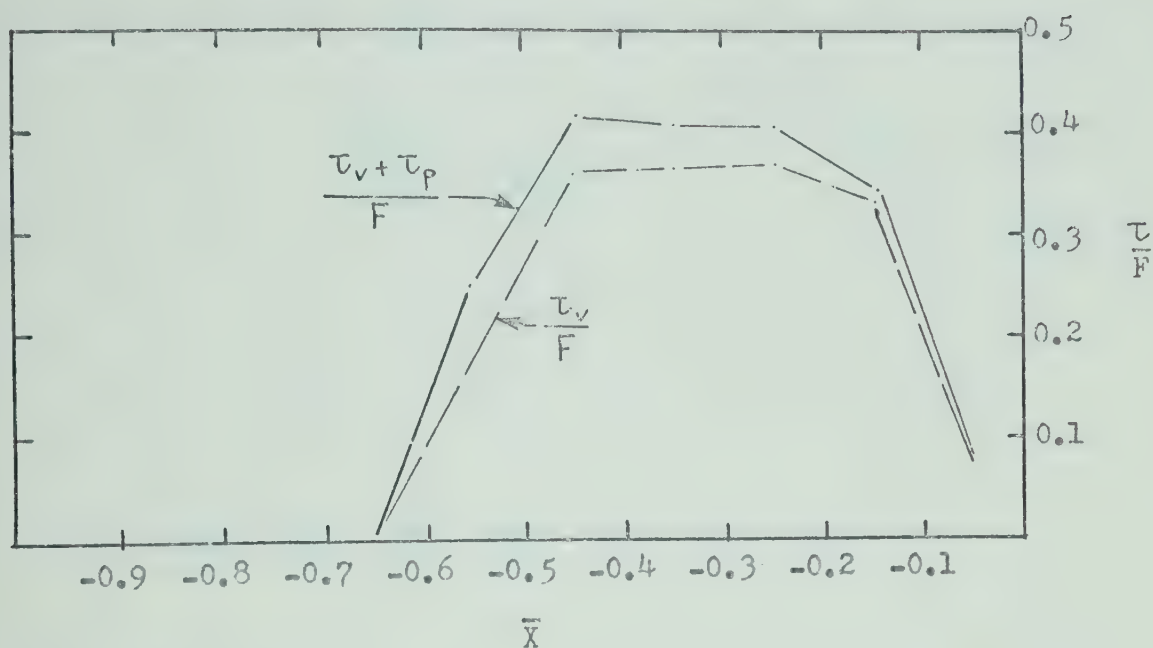


(g) Test 21, Range 2

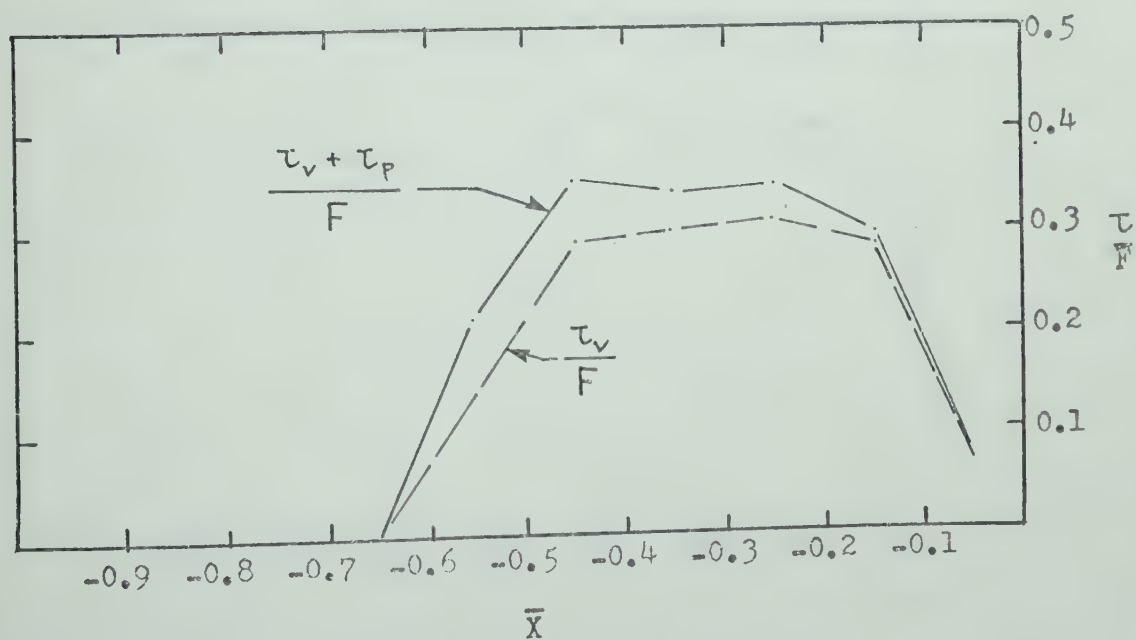


(h) Test 21, Range 3

Figure 7.6. (Continued)

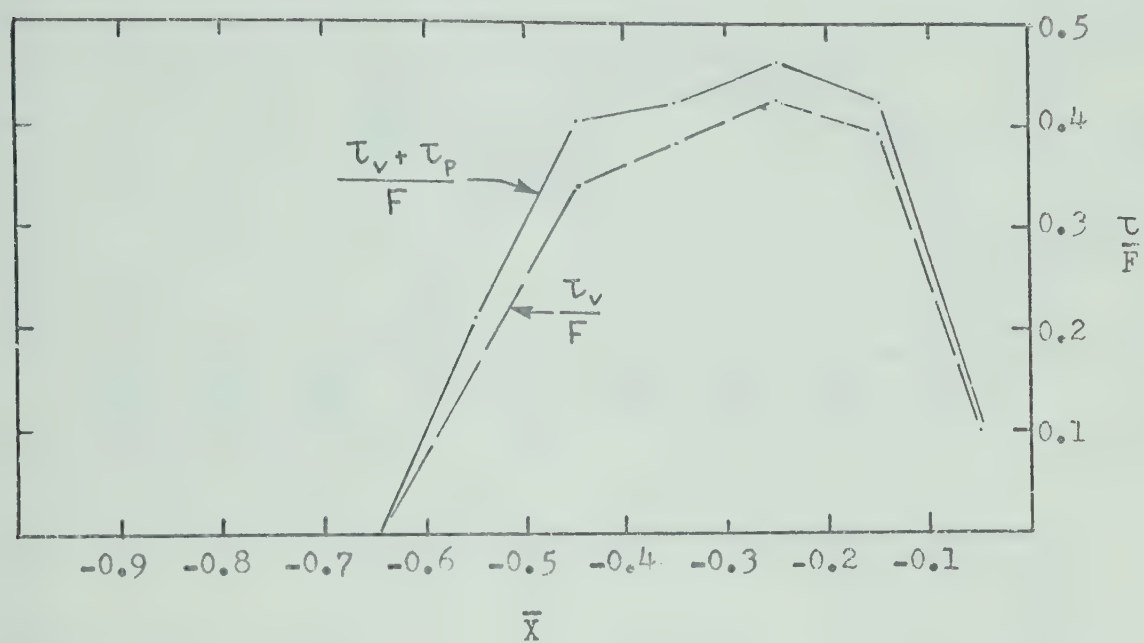


(i) Test 24, Range 2

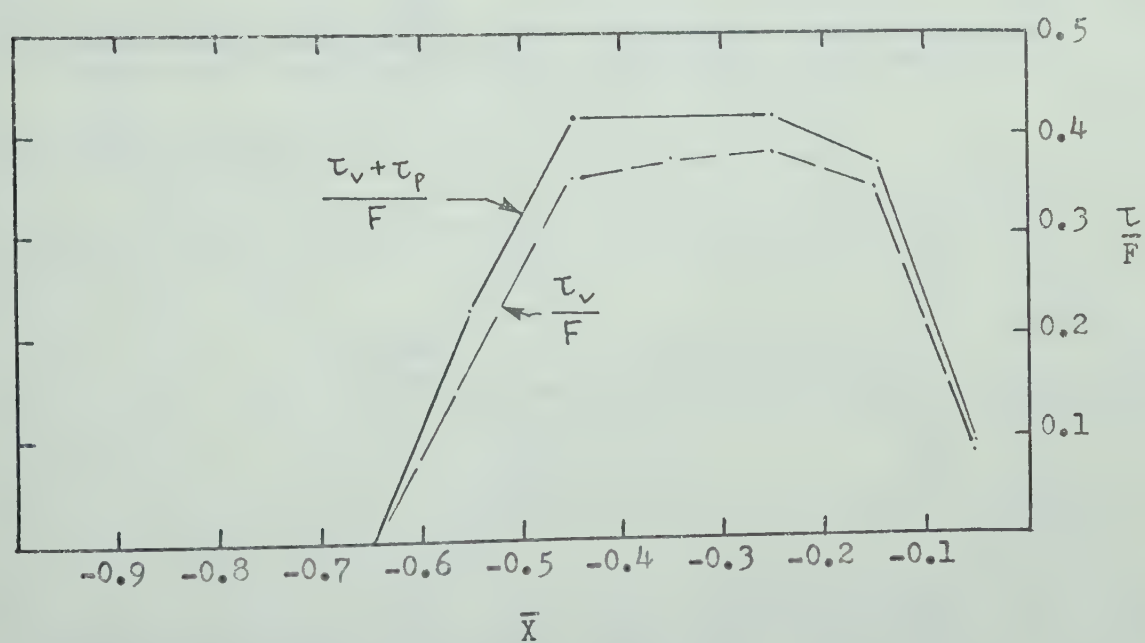


(j) Test 24, Range 4

Figure 7.6. (Continued)



(k) Test 26, Range 2



(l) Test 26, Range 3

Figure 7.6. (Continued)

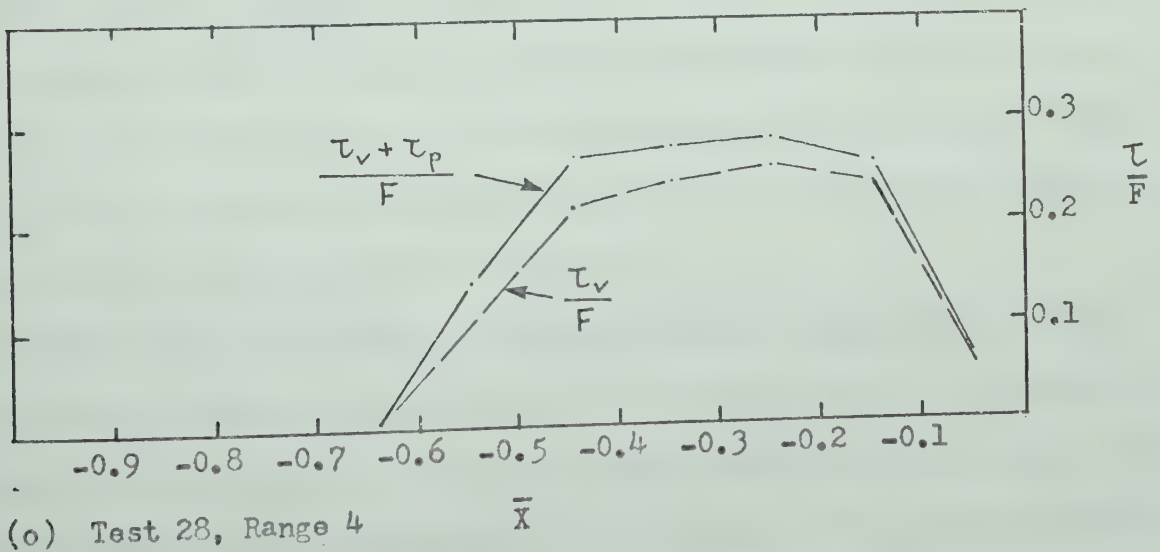
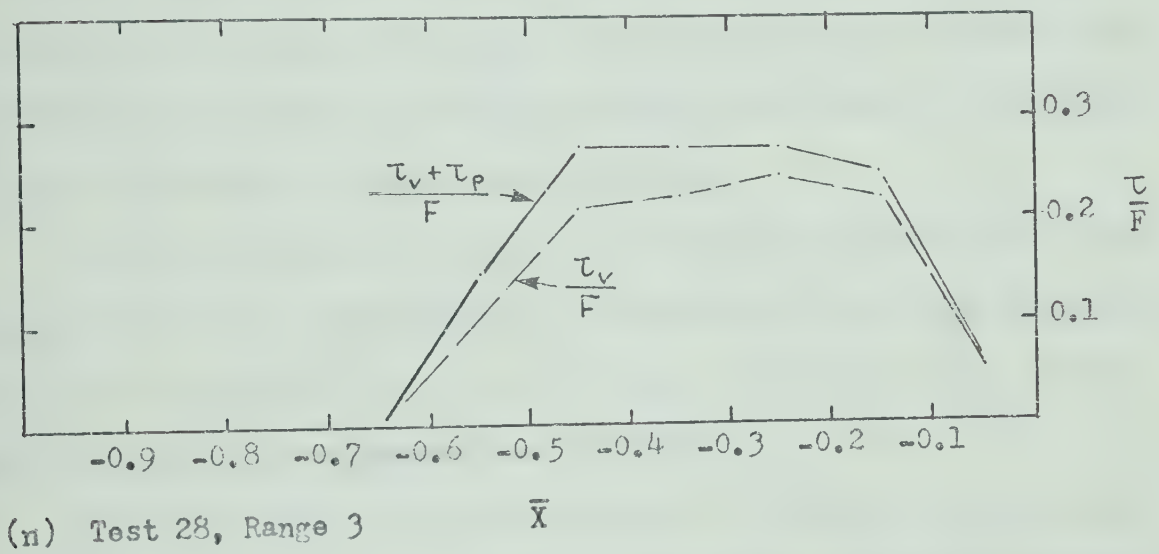
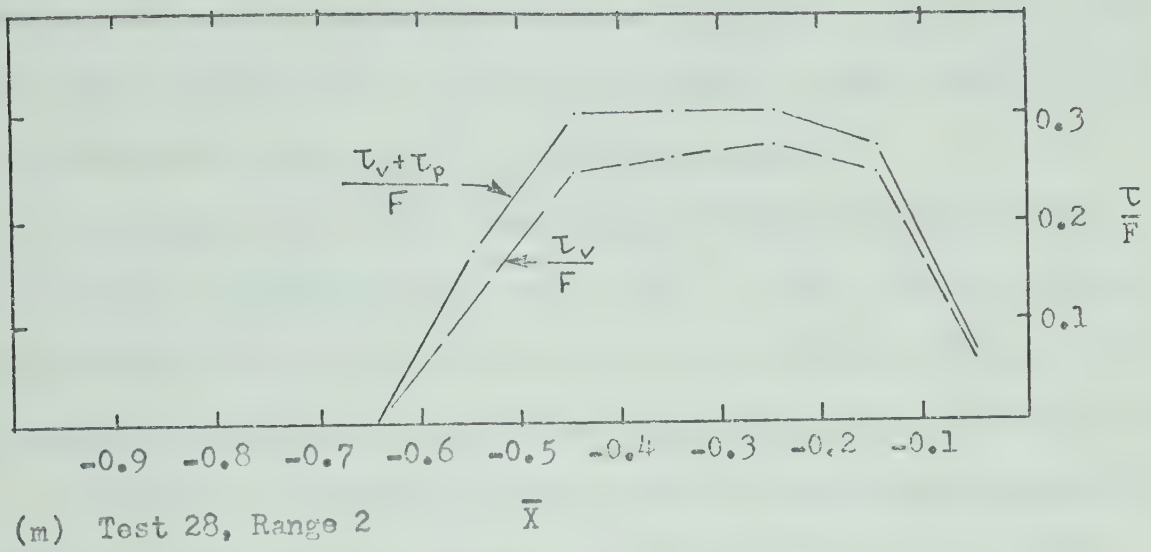


Figure 7.6. (Continued)

to zero at the crest. The maximum relative unit force contribution due to flow shear occurred at $\bar{X} = -0.25$ and was found to range from 27 to 78 per cent depending mainly upon the mean flow velocity.

The maximum unit force contribution by the pressure gradients occurred in the region between $\bar{X} = -0.60$ and $\bar{X} = -0.45$, and was found to be approximately six per cent in nine out of the thirteen bed-forms. In the remaining four bed-forms this value ranged from four to eight per cent.

Obviously, the maximum pressure gradient contribution occurred in the region of increasing flow shear. This tended to equalize the distribution of the combined flow shear and pressure gradient stresses and in a number of bed-forms the combined contribution between $\bar{X} = -0.50$ and $\bar{X} = -0.20$ was found to be relatively constant.

As shown in Figure 7.6, the sum of the mean flow shear and pressure gradient stress contributions on the upstream face of the bed-forms between $\bar{X} = -0.50$ and $\bar{X} = -0.15$ provided from 30 to 80 per cent of the total required stress to entrain the particles.

Under the lower limit conditions of $C = 0.524$ and $\Psi'' = 0$, which in effect assumed no friction between the particles, the total resisting force throughout most of the bed-form face downstream from the reattachment point was found to be less than the estimated flow shear τ_v . Therefore, only the relative unit force contribution by the pressure gradients were estimated and summarized in Figure 7.7.

The results show that the maximum relative contribution by the mean pressure gradient occurred also in the region between $\bar{X} = -0.60$ and $\bar{X} = -0.45$, and in different bed-forms ranged from 30 to 80 per cent. This range corresponds in magnitude with the sum total of the relative contributions by flow shear and pressure gradient stresses under the assumed

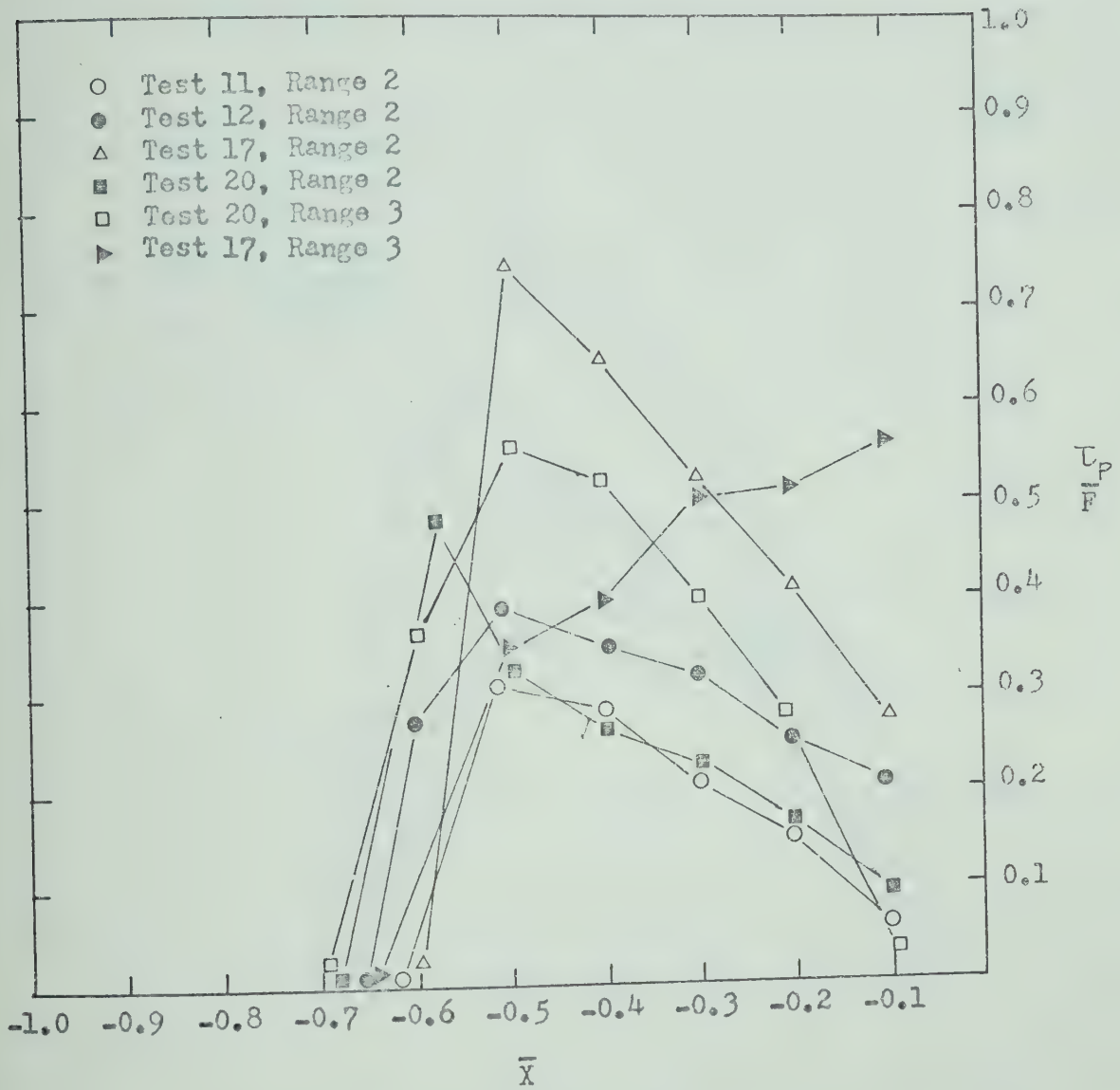


Figure 7.7. Relative Contribution of Pressure Gradient Shear Stress with Frictionless Surface Layer Conditions.

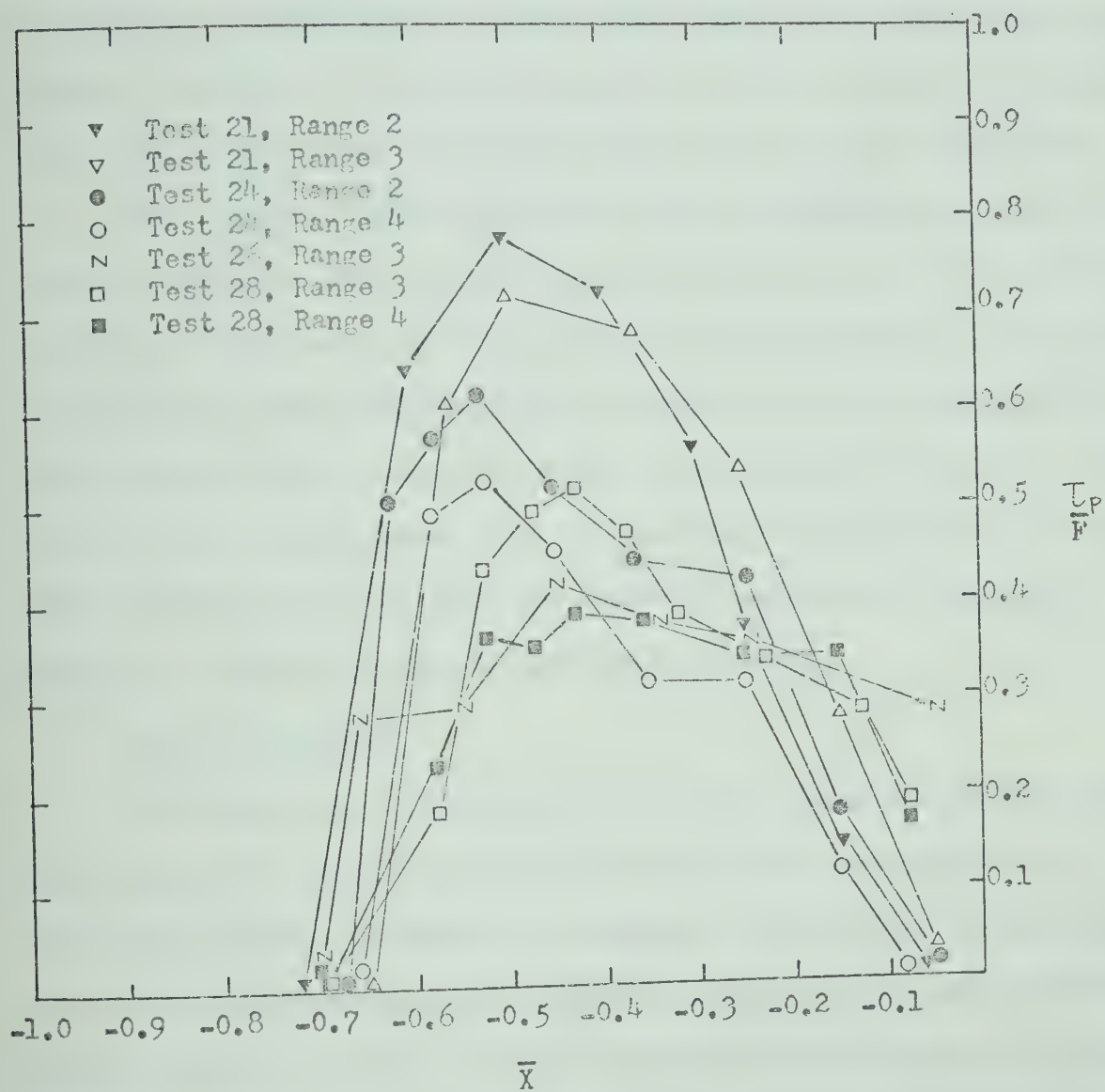


Figure 7.7. (Continued)

upper limit conditions. However, possibly because of considerable data scatter, no direct correspondence between the sum total of flow shear and pressure gradient stress contributions under the maximum concentration and friction and the pressure gradient stress under the frictionless conditions on individual bed-forms could be conclusively established.

The maximum relative pressure gradient contribution under frictionless conditions and the corresponding maximum estimated local rate of particle entrainment for twelve bed-forms were compared in Figure 7.8. The comparison shows that on eight bed-forms the rate of particle entrainment increased with increased relative contribution due to pressure gradient stresses. Data points from the remaining four bed-forms did not follow the same trend and from the available information it was not possible to explain the reasons for the discrepancy.

7.5.2 Discussion

Although every attempt was made to obtain accurate experimental data, the results presented in the previous section are generally of qualitative nature. A number of assumptions were employed in computing the relative contributions of the mean flow shear and the mean pressure gradient stresses for the detachment of sediment particles from the surface of active bed-forms. Rigid boundary techniques were used for the determination of boundary shear stresses from mean velocity profiles which themselves were developed on the assumption of similarity at corresponding positions relative to the geometry of the bed-forms. Secondly, with the exception of the local slope of the bed-form surface, actual conditions in the surface layer of particles, necessary for the determination of forces resisting particle entrainment, were not experi-

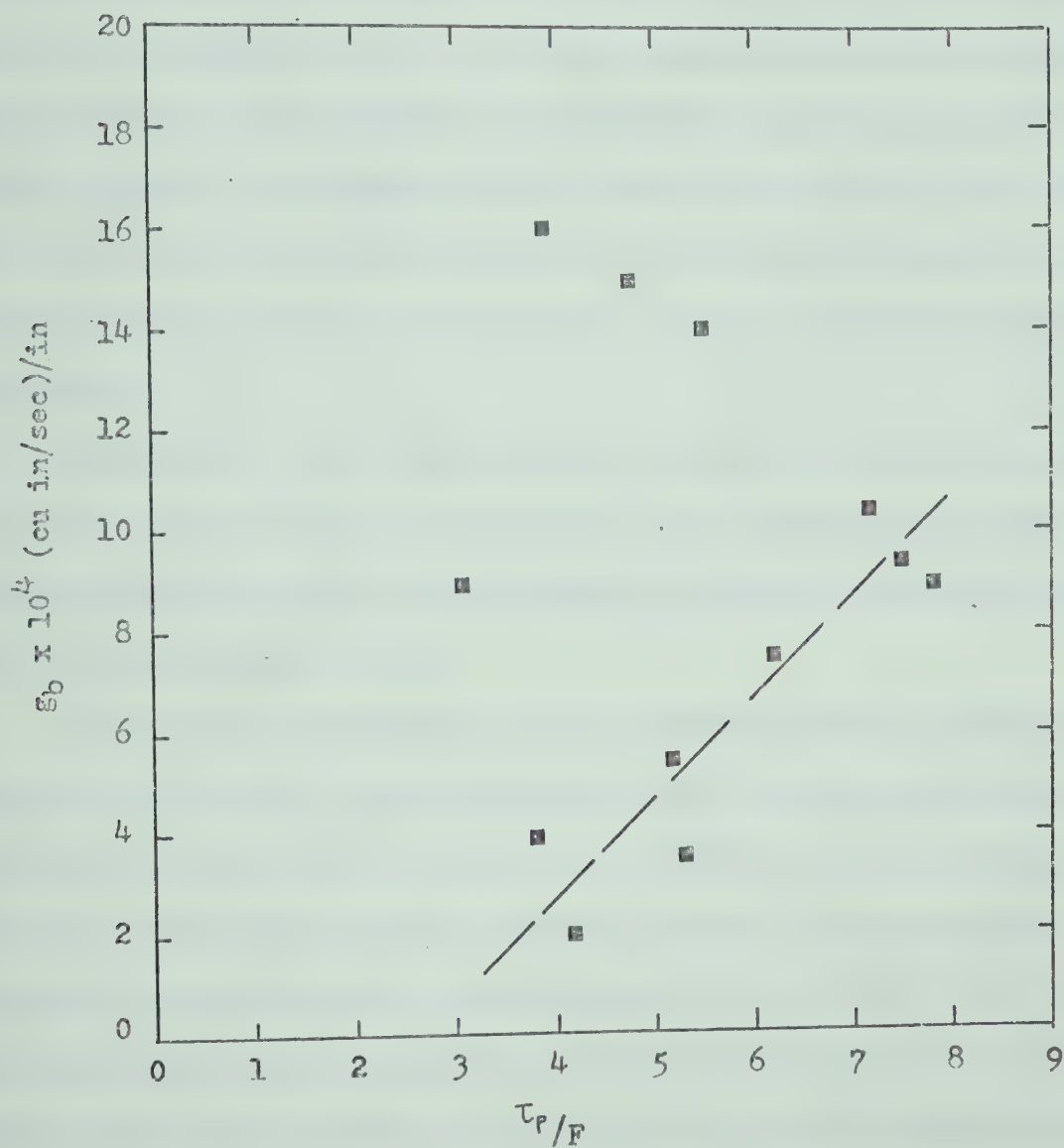


Figure 7.8. Comparison of Maximum τ_p/F v.s. Maximum Entrainment Rate.

mentally obtainable. Hence, the mean measured stresses could not be compared with the measured resisting forces, but were compared with the calculated unit forces based upon two extreme surface layer conditions immediately prior to particle detachment: (1) maximum concentration and friction corresponding to assumed conditions in the bulk of particles deep within the bed-form, and (2) minimum concentration and no friction between particles corresponding to theoretically unstable arrangement of equal spheres. The comparisons were made also considering local drag forces parallel to the surface of the bed-forms because the nature of experimental data provided no information from which lift forces could be evaluated.

Nevertheless, even under the above assumptive restrictions, the qualitative results of this investigation show a number of previously not established facts about the entrainment of sediment particles on the backs of the bed-forms.

The relative contribution results obtained under the maximum concentration and friction conditions show that the combined drag by the local mean flow shear and the mean pressure gradient stresses was not adequate to entrain the particles from the surface of the bed-forms. Furthermore, the distribution characteristics of the relative unit forces showed that entrainment of particles was occurring from positive bed-form surface slope locations where the mean flow shear and pressure gradient stresses were calculated to be zero.

These observations suggested, first, that other force systems were acting upon the particles on the surface of the bed-forms. Among these may be the hydrodynamic lift as considered by Einstein and El-Samni (1949) and the effects of turbulence fluctuations. However, lift by

itself cannot entrain the particles because translation of the bed-forms requires that the particles be displaced in the direction of flow. Therefore, drag forces must be present. The experimental results similarly suggested that turbulent velocity fluctuations were not directly responsible for the entrainment. The maximum turbulence intensity of the horizontal velocity component was observed to occur in the trough region of the bed-form which is the region of zero particle entrainment.

In addition to other force systems, the calculated local relative contributions by the mean flow shear and mean pressure gradient stresses may also have been influenced by the concentration and friction values used in the calculations. Equation 7.6 shows that the minimum drag required for particle layer entrainment has to overcome the friction between the particles and the gravity force component which depends upon the local bed-form surface slope. The mass of particles in the surface layer is governed by the concentration.

In evaluating the unit force requirements to detach the particles, the friction angle Ψ and concentration C in the surface layer above a bed-form were assumed to be constant. This may not be true as visual observations and physical considerations suggested that both values may have been affected by the action of the flow, turbulence or particle impact even before the entrainment. Generally the mass of particles on the surface of the bed-forms was loose indicating that the assumed concentration of 0.601 was too high. In some regions of the bed-form, especially in the vicinity of the reattachment point, particles were observed to oscillate above their supporting particles suggesting that at least the static friction between particles had been overcome. In regions of transport, the impact of moving particles upon the stationary particles

exerted an equivalent shearing action which dilated the stationary mass of particles and reduced the concentration. These observations suggested that the conditions in the stationary surface layer of particles may be substantially altered prior to actual particle entrainment.

In relation to these observations, it is significant that qualitatively the pressure gradient distribution characteristics were found to correspond more closely with the particle entrainment distribution curves than other parameters. The maximum entrainment rates were found to occur at the location of maximum pressure gradients. Zero or very small entrainment occurred immediately upstream of the crest of the bed-forms, where the pressure gradient was zero but where the shearing action by particle impact was likely to be most intensive and dilation most complete. Near the reattachment point, although the mean pressure gradient was zero, the finite entrainment could be attributed to pressure fluctuations.

These observations suggest that pressures and their gradients may be the basic variables governing the entrainment of particles from the surface of the bed-forms. This is in agreement with the comments of Einstein and El-Samni (1949) regarding statistical description of turbulence in the vicinity of a wall and Luque's (1967) theory of stability of erosive soils. However, if pressure gradients and pressure fluctuations actually are the basic variables, then boundary shear and velocity fluctuations are relegated to other functions--perhaps to the dilation of the surface layer particles.

CHAPTER VIII

SUMMARY, CONCLUSIONS, AND RECOMMENDATIONS

8.1 Summary

The present experimental investigation was undertaken to obtain a better insight into the mechanics of bed-forms in alluvial channels.

A distinctly new experimental approach was adopted for the study. The measurements of various flow and bed-form parameters were made using actively translating bed-forms with bed-load mode of sediment transport. This differed fundamentally from similar studies carried out by other investigators in the past who employed simulated, non-translating bed-form shapes.

The development of experimental techniques for use in active sediment transport and bed-form translation environment formed a significant part of the investigation. All experiments were made in a laboratory flume with spherical, light weight (polystyrene) particles of nearly uniform size gradation. Measurements were made of the pressure distribution characteristics within the mass of granular particles in the bed-forms, of the velocity profiles in the flow above the bed-forms, and of the bed-form geometry.

All instrumentation probes were stationary in the flume and all instantaneous observations of the various parameters were related to the geometry of the bed-forms. Also, all probes were of sufficiently small size and disturbed neither the local flow field nor the sediment boundary.

Pressure distribution characteristics were established using differential pressure gages. Difficulties were experienced in the measurement of pressures because of very small pressure variation above light weight sediment bed-forms, pressure fluctuations due to surface wave activity and turbulence, changing roughness in the flume due to natural development of bed-forms, and the loss of water from the recirculating system of the flume. Special techniques were developed and successfully employed to minimize these effects.

Flow velocity measurements were made using hydrogen bubble technique. This technique was found to be satisfactory because the inclusion of the small diameter bubble generating wires had absolutely no effects upon the flow or the sediment bed. It provided the information for establishment of instantaneous velocity profiles throughout the full depth of flow, and resolved flow in upstream and downstream directions. The major disadvantages of the hydrogen bubble method were the large number of instantaneous observations necessary to establish mean velocity profiles, the extremely time consuming processes of data reduction, and difficulties in data interpretation near the sediment bed.

Measurement of bed-form profile characteristics were made using a series of small diameter wire scales installed vertically along the centreline of the flume.

Bed-forms were naturally formed, two-dimensional and in the dune phase. Because of secondary circulation effects which tended to distort the bed-forms into irregular features, two-dimensionality of the bed-forms was maintained by manually advancing the retarded crests of the bed-forms near the flume sidewalls.

Major difficulties were experienced in obtaining constant bed-

form heights and lengths during their passage through the observation area. Statistical techniques were used to select seventeen of the fifty-five bed-forms observed in the experiments.

8.2 Conclusions

The conclusions reached from the results of this investigation were as follows:

- (1) Pressure gradient induced seepage forces contribute a finite force upon the stationary bed particles in the surface layer of the bed-form.
- (2) The maximum pressure on the bed-forms occurs at the reattachment point, and the minimum at or slightly upstream of the crest.
- (3) The location of the maximum mean pressure gradient was approximately one tenth of the bed-form wavelength downstream from the reattachment point.
- (4) The location of the maximum mean pressure gradient corresponds with the position of the maximum bed-form surface slope and with the region of maximum particle entrainment.
- (5) The minimum pressure gradient occurs slightly upstream of the crest of the bed-forms and corresponds to the location of minimum particle entrainment from the upstream face of the bed-forms.
- (6) The mean boundary shear, estimated from mean velocity profiles by rigid boundary techniques was found to increase downstream from the reattachment point to a point approximately one quarter of the wavelength upstream of the crest and to decrease to zero at the crest.
- (7) The mean local velocity of flow occurs between 0.3 and 0.4 of the local depth above the bed-form surface.

(8) The maximum horizontal velocity turbulence intensity occurs in the trough region and approximately 0.10 above the surface of the bed-form.

(9) The horizontal velocity turbulence intensity appears to be suppressed in the vicinity of the maximum bed-form surface slope.

(10) From the trough region, turbulence effects penetrate to the surface of the flow.

(11) The relative contributions of the mean flow shear and pressure gradient stresses upon the particles contribute only a part of the total required forces for particle entrainment.

(12) The mean pressure gradient distribution above bed-form surface downstream from the reattachment point corresponds with the particle entrainment distribution characteristics except between the reattachment and maximum entrainment locations.

8.3 Recommendations

Further studies are necessary to establish quantitatively the contributions of pressure gradients and pressure fluctuations, boundary shear stresses and turbulence upon the entrainment of particles from the surface of bed-forms. Specifically the following areas should be investigated:

(1) The determination of boundary shear stresses on porous boundaries with pressure gradients, surface curvature and movement of discrete particles.

(2) The effects of flow shear and turbulence upon entrainment and/or dilation of surface particles, including particle resonance to fluctuations and particle gradation effects.

(3) Pressure distribution, pressure fluctuation and seepage characteristics within and near the surface of bed-forms.

It is recommended that, because of difficulties in pressure measurement, heavier bed-materials be used in future studies. If hydrogen bubble technique is used for velocity measurement, the bed-materials should also be of dark colour and non-reflecting. All instrumentation should be automatized.

BIBLIOGRAPHY

- Allen, J. R. L., The maximum slope-angle attainable by surfaces underlain by bulked equal spheroids with variable dimensional ordering: Geol. Soc. America Bull., v. 80.
- Allen, J. R. L., 1970a, The angle of initial yield of haphazard assemblages of equal spheres in bulk: Geologie en Mijnbouw, v. 49, no. 1.
- Allen, J. R. L., 1970b, The systematic packing of prolate spheroids with reference to concentration and dilutancy: Geologie en Mijnbouw, v. 49, no. 3.
- Anderson, A. G., 1953, The characteristics of sediment waves formed by flow in open channels: Trans. Third Midwestern Conference in Fluid Mechanics, Minneapolis.
- Bagnold, R. A., 1954, Experiments on the gravity-free dispersion of large spheres in a Newtonian fluid under shear: Proc. Royal Soc. London, v. A225, no. 49.
- Bagnold, R. A., 1955, Some flume experiments on large grains but little denser than the transporting fluid and their implications: Proc. Inst. of Civil Engineers, pt. 3.
- Blench, T., 1969, Mobile-bed fluvicology: University of Alberta Press, 2nd Edition.
- Brownlee, K. A., 1960, Statistical theory and methodology in science and engineering: John Wiley and Sons, Inc.
- Clutter, D. W., Smith, A. M. O., and Brazier, J. G., 1961, Techniques of flow visualization using water as the working medium: Aerospace Engineering, v. 20.
- Darwin, G. H., 1883, On the formation of ripple-marks: Proc. Roy. Soc., London.
- Davidson, J. F., Pearson, J. R. A., and Vanoni, V. A., 1969, Report on the I.U.T.A.M. Symposium on the flow of fluid--solid mixtures: Journ. Fluid Mechanics, v. 39, pt. 2.
- Davis, W., and Fox, R. W., 1967, An evaluation of the hydrogen bubble technique for the quantitative determination of fluid velocities with clear tubes: Am. Soc. Mechanical Engineers, Journ. Basic Engineering, v. 87.
- Einstein, H. A., and El-Samni, E-S. A., 1949, Hydrodynamic forces on a rough well: Reviews of Modern Physics: v. 21, no. 3.
- Einstein, H. A., and Barbarossa, N. L., 1952, River channel roughness: Am. Soc. Civil Engineers Trans., v. 117.

- Engel, F. W. A., 1969, Discussion of "Rationalisation of Lacey's regime flow equations" by M. A. Gill: Am. Soc. Civil Engineers Journ., v. 95, no. HY-3.
- Exener, F. M., 1925, Über die Wechselwirkung zwischen Wasser und Geschiebe in Flüssen: Sitzungsberichte der Akademie der Wissenschaften, Wien, Hft 3-4.
- Goma, Munoz R. J., and Gelhar, L. W., 1968, Turbulent pipe flow with rough and porous walls: Hydrodynamics Laboratory Report no. 109, (Massachusetts Institute of Technology).
- Graton, L. C., and Fraser, H. J., 1935, Systematic packing of spheres with particular relation to porosity and permeability: Journ. Geology, v. 43.
- Ingrie, J., and Buchanan, H., 1965, Sedimentary structures in modern carbonate sands of the Bahamas: Primary sedimentary structures and their hydrodynamic interpretation, Soc. Economic Paleontologists and Mineralogists, Spec. Publication no. 12.
- Jumikis, A. R., 1962, Soil mechanics: D. Van Nostrand Co. Inc., Princeton, N. J.
- Keeping, E. S., 1962, Introduction to statistical inference: D. Van Nostrand Co. Inc., Princeton, N. J.
- Kennedy, J. F., 1963, The mechanics of dunes and anti-dunes in erodible-bed channels: Journ. Fluid Mechanics, v. 16, pt. 4.
- Kennedy, J. F., 1969, The formation of sediment ripples, dunes and anti-dunes: Annual review of fluid mechanics, v. 1, Annual Reviews Inc., Palo Alto, Calif.
- Khanna, S. D., 1970, Experimental investigation of form and bed-roughness: Am. Soc. Civil Engineers Journ., v. 96, no. HY-10.
- Kondratov, N. E., Lyapin, A. M., Popov, I. V., Pinkovski, S. I., Federov, N. N., and Yakunin, I. I., 1962, River flow and river channel formation: N.S.F. and V.S. Dept. of Interior, Washington, D. C.
- Laursen, E. M., 1952, Observations on the nature of scour: Proc. Fifth Hydraulics Conf., Bul. 34, State University of Iowa, Iowa City, Iowa.
- Laursen, E. M., Adams, J. R., Huang, Li-San, and Chen, Cheng-Ling, 1962, Pressure and shear distribution on schematic dunes: Technical Report no. 2., Michigan State University, East Lansing, Michigan.
- Luque, R. F., 1967, Stability of sand deposits under erosive flow: Research Report no. 1248, Shell Exploration and Production Laboratory, Rijswijk, The Netherlands.
- MacRae, J. C., and Gray, W. A., 1961, Significance of the properties of materials in the packing of real spherical particles: British Journ. of Applied Physics, v. 12.

- Martin, C. S., and Aral, M. M., 1971, Seepage force on interfacial bed particles: Am. Soc. Civil Engineers, Journ., v. 97, no. HY-7.
- Mercer, A. G., 1971, Analysis of alluvial bed-forms: chapter 10 in River Mechanics v. 1, edited by H. W. Shen, Fort Collins, Colorado.
- Posey, C. J., 1963, Scour at bridge piers, 2. Protection of threatened piers: Civil Engineering, v. 33.
- Raudkivi, A. J., 1963, Study of sediment ripple formation: Am. Soc. Civil Engineers Journ., v. 89, no. HY-6.
- Raudkivi, A. J., 1964, Bed-forms in alluvial channels: Journ. Fluid Mechanics, v. 26, pt. 3.
- Rifai, M. F., and Smith, K. V. H., 1971, Flow over triangular elements simulating dunes: Am. Soc. Civil Engineers, Journ. v. 97, no. HY-7.
- Rouse, H., 1940, Criteria for similarity in the transportation of sediment: Proc. First Hydraulics Conf., Bul. 20, State University of Iowa, Iowa City, Iowa.
- Schraub, F. A., Kline, S. J., Henry, J., Runstadler, P. W. Jr., and Littell, A., 1965, Use of hydrogen bubbles for quantitative determination of time dependent velocity fields in low-speed water flows: Am. Soc. Mechanical Engineers, Journ. Basic Engineering, v. 85.
- Scott, G. D., 1960, Packing of spheres, Nature, v. 188.
- Shields, A., 1936, Anwendung der Ähnlichkeits-Mechanik und der Turbulenzforschung auf die Geschiebebewegung: Preussische Versuchsanstalt für Wasserbau und Schiffbau, Berlin.
- Simons, D. B., Richardson, E. V., and Haushild, W. L., 1962, Depth-discharge relations in alluvial channels: Am. Soc. Civil Engineers, Journ. v. 88, no. HY-5.
- Simons, D. B., and Richardson, E. V., 1966, Resistance to flow in alluvial channels: U.S. Geol. Survey Prof. Paper 422-J.
- Sutherland, A. J., 1967, Proposed mechanism for sediment entrainment by turbulent flows: Journ. Geophysical Research, v. 72, no. 24.
- Taylor, D. W., 1948, Fundamentals of soil mechanics: John Wiley and Sons, Inc., New York, N. Y.
- Vanoni, V. A., and Hwang, Li-San, 1967, Relation between bed forms and friction in streams: Am. Soc. Civil Engineers, Journ. v. 93, no. HY-3.
- Watters, G. Z., and Rao, M. V. P., 1971, Hydrodynamic effects of seepage on bed particles: Am. Soc. Civil Engineers, Journ. v. 97, no. HY-3.

Williams, P. E., and Kemp, P. H., 1971, Initiation of ripples on flat sediment beds: Am. Soc. Civil Engineers, Journ. v. 97, no. HY-4.

Yalin, M. S., 1972, Mechanics of sediment transport, Pergamon Press, Inc.

A P P E N D I X A

BED-MATERIAL TEST PROCEDURES
AND TEST SUMMARIES

TABLE A.1
SEDIMENT PARTICLE SPECIFIC GRAVITY

Test	Temperature °C	Specific Gravity
1	25.6	1.0427
2	25.6	1.0366
3	24.5	1.0430
4	24.5	1.0425
5	25.7	1.0383
6	25.7	1.0415

TABLE A.2
SEDIMENT PARTICLE SPECIFIC GRAVITY DISTRIBUTION

Range of Specific Gravity	Per Cent by Weight				Average
	Test #1	Test #2	Test #3	Test #4	
1.020 - 1.025	0	0	0	1	0.25
1.025 - 1.030	1	0	2	0	0.75
1.030 - 1.035	6	11	8	8	8.25
1.035 - 1.040	7	19	27	23	19.00
1.040 - 1.045	67	58	57	64	61.50
1.045 - 1.050	18	9	1	0	7.00
1.050 - 1.055	1	3	5	3	3.00
1.055 - 1.060	0	0	0	1	0.25

TABLE A.3
SUMMARY OF GRAIN SIZE DISTRIBUTION TESTS

Size of Opening Millimetres	Per Cent Finer by Weight		
	Test #1	Test #2	Test #3
4.760	100.00	100.00	100.00
2.000	98.45	98.94	98.50
0.840	5.57	0.87	0.92
0.591	0.25	0.39	0.23
0.420	0.06	0.07	0.10
0.149	0.00	0.00	0.00

TABLE A.4
PERMEABILITY AND VOLUME CONCENTRATION DATA

Sample	Coefficient of Permeability* cm/sec	Porosity	Volume Concentration
A	1.16×10^{-1}	0.377	0.620
B	1.09×10^{-1}	0.377	0.620
C	1.19×10^{-1}	0.459	0.540
D	1.32×10^{-1}	0.399	0.604
E	1.30×10^{-1}	0.399	0.604
Average	1.21×10^{-1}	0.402	0.598

*At 20°C.

PROCEDURE A.1
METHOD TO DETERMINE DISTRIBUTION OF SPECIFIC
GRAVITIES OF SEDIMENT MATERIAL

- (1) Place 50 grams of dry particles into distilled water for 24 hours to eliminate air bubbles adhering to the surface of the particles.
- (2) In flasks used for soils hydrometer analysis prepare eight one litre solutions of different specific gravities by dissolving different amounts of sodium phosphate detergent (Calgon) in water.
- (3) Remove the sample from the distilled water and place in the sodium phosphate solution with the highest specific gravity. Stir the mixture vigorously for one minute, and remove particles which rise to the surface with a special mesh spoon. Allow the particles to drain and place them in a cylinder containing solution with the highest specific gravity. Repeat the process to the last solution with the lowest specific gravity.
- (4) Using a hydrometer determine the specific gravity of the solutions with the remaining sediment particles in each cylindrical flask. Simultaneously measure the temperature of the solution.
- (5) Remove the sediment particles remaining in each sedimentation cylinder, rinse with distilled water, dry at 30°C temperature, and weigh.

A P P E N D I X B

LIST OF EQUIPMENT FOR HYDROGEN BUBBLE PRODUCTION,
CONTROL, AND PHOTOGRAPHY

1. Electrical Equipment

(1) Power Supply:

Regulated Power Supply Unit, Lambda Corp., Model C-1581M.

(2) Control Equipment:

(a) Pulse generator; Hewlett-Packard, Model 214A

(b) Frequency oscillator; Krohn-Hite Corp., Model 400-C

(c) Relay, mercury wetted type; Potter and Brunfield Co.,
Model JM 311531

2. Photographic Equipment

(1) Camera:

Nikon F with f 3.5/55 mm macro-lens.

(2) Film:

Kodak 2475 Recording Type rated at 1000 ASA.

A P P E N D I X C

BED-FORM PROFILE

DATA

TABLE C.1

SUMMARY OF STATISTICAL BED-FORM STABILITY
TEST RESULTS

Test	Range	Bed- Form	d _{c1}	H ₁	d _{c2}	H ₂	\bar{L}	Test	Range	Bed- Form	d _{c1}	H ₁	d _{c2}	H ₂	\bar{L}
1A	2	1	0	x	0	0	0	18	2	1	x	a	x	x	x
	3	2	0	0	0	0	x		3	2	x	x	0	x	x
	4	3	0	0	0	0	x		4	3	0	x	a	b	0
1B	2	1	x	0	x	x	x	19	2	1	a	b	0	x	x
	3	2	x	x	x	a	x		3	2	0	x	0	0	0
	4	3	x	a	0	0	x								
2	2	1	x	0	x	0	0	20	*2	1	c	0	0	0	0
	3	2	x	0	0	0	x		*3	2	0	0	0	0	b
									4	3	0	0	0	0	x
3	2	1	0	x	0	x	x	21	*2	1	0	0	0	0	0
	3	2	0	x	0	a	0		*3	2	0	0	a	0	a
4	2	1	x	b	x	x	0	22	*2	1	0	a	0	0	0
	3	2	x	x	0	0	b		*3	2	0	0	0	0	a
									4	3	0	0	x	0	x
7	2	1	0	0	0	0	x	23	2	1	x	c	x	x	x
10	2	1	x	0	x	0	x		3	2	x	x	0	x	x
									4	3	0	x	0	0	x
11	*2	1	0	0	0	0	0	24	*2	1	0	0	c	0	0
12	*2	1	0	0	0	b	0		3	2	c	0	b	0	x
									*4	3	b	0	0	0	0
13	2	1	0	0	0	0	x	25	2	1	0	a	0	x	x
	3	2	0	0	x	0	x		3	2	0	x	0	x	x
14	2	1	x	0	x	0	x	26	*2	1	0	0	0	a	0
	3	2	x	0	0	0	x		*3	2	0	a	0	a	a
15	2	1	x	0	0	x	x	27	2	1	0	0	0	0	x
16	2	1	0	0	0	x	0	28	*2	1	0	c	0	0	0
	3	2	0	x	0	0	0		*3	2	0	0	0	0	0
17	*2	1	0	0	0	a	a		*4	3	0	0	0	0	0
	*3	2	0	a	0	0	0								

*Bed-Form data accepted for analysis

Code:

0 not significant at 0.05 level

a not significant at 0.02 level

b not significant at 0.01 level

c not significant at 0.005 level

x significant at 0.005 level

TABLE C.2
DIMENSIONLESS BED-FORM COORDINATE DATA

Test and Range	\bar{H}_r	Profile Coordinate Points														
		\bar{X}	\bar{H}	-0.067	-0.154	-0.249	-0.343	-0.441	-0.544	-0.650	-0.748	-0.844	-0.936			
Test 11 Range 2	1.408	\bar{X}	\bar{H}	0.976	0.951	0.923	0.741	0.609	0.425	0.212	0.070	-0.013	0.000			
Test 12 Range 2	1.314	\bar{X}	\bar{H}	-0.048	-0.154	-0.272	-0.378	-0.460	-0.542	-0.657	-0.744	-0.853	-0.929			
		\bar{X}	\bar{H}	0.905	0.848	0.774	0.594	0.457	0.315	0.163	-0.004	-0.012	0.000			
Test 17 Range 2	0.657	\bar{X}	\bar{H}	-0.059	-0.150	-0.262	-0.352	-0.443	-0.545	-0.650	-0.745	-0.849	-0.930			
		\bar{X}	\bar{H}	0.875	0.804	0.708	0.651	0.601	0.534	0.451	0.106	0.100	0.000			
Test 17 Range 3	1.159	\bar{X}	\bar{H}	-0.062	-0.158	-0.270	-0.370	-0.427	-0.526	-0.657	-0.770	-0.842	-0.915			
		\bar{X}	\bar{H}	0.923	0.907	0.853	0.621	0.500	0.304	0.017	-0.069	-0.112	0.000			
Test 20 Range 2	0.578	\bar{X}	\bar{H}	-0.068	-0.153	-0.247	-0.350	-0.450	-0.554	-0.644	-0.737	-0.844	-0.922			
		\bar{X}	\bar{H}	1.013	0.945	0.788	0.645	0.555	0.450	0.069	0.035	-0.015	0.000			
Test 20 Range 3	0.689	\bar{X}	\bar{H}	-0.062	-0.171	-0.253	-0.331	-0.456	-0.544	-0.663	-0.743	-0.841	-0.930			
		\bar{X}	\bar{H}	1.044	0.931	0.745	0.701	0.653	0.435	0.435	0.116	0.103	0.000			
Test 21 Range 2	0.666	\bar{X}	\bar{H}	-0.053	-0.124	-0.252	-0.377	-0.429	-0.521	-0.642	-0.749	-0.859	-0.930			
		\bar{X}	\bar{H}	1.000	0.950	0.808	0.700	0.625	0.425	0.312	0.036	0.048	0.000			
Test 21 Range 3	0.732	\bar{X}	\bar{H}	-0.060	-0.146	-0.255	-0.358	-0.455	-0.560	-0.620	-0.747	-0.854	-0.939			
		\bar{X}	\bar{H}	0.929	1.093	0.870	0.778	0.581	0.387	0.392	0.123	0.058	0.000			
Test 22 Range 2	1.383	\bar{X}	\bar{H}	-0.068	-0.173	-0.246	-0.359	-0.440	-0.594	-0.664	-0.769	-0.834	-0.935			
		\bar{X}	\bar{H}	0.985	0.899	0.826	0.718	0.464	0.284	0.055	0.009	0.031	0.000			

TABLE C.2 (Continued)

Test and Range		\bar{H}_r	Profile Coordinate Points													
Test 22 Range 3		0.321	\bar{X} \bar{H}	= 1.000	0.000	-0.083	-0.182	-0.275	-0.373	-0.441	-0.545	-0.641	-0.746	-0.840	-0.930	
					0.934	0.934	0.934	0.685	0.583	0.467	0.467	0.155	-0.311	-0.093	0.000	
Test 24 Range 2		0.813	\bar{X} \bar{H}	= 1.000	0.000	-0.031	-0.134	-0.243	-0.354	-0.463	-0.546	-0.642	-0.732	-0.849	-0.935	
					0.935	0.935	0.880	0.712	0.616	0.581	0.391	0.160	0.151	0.107	0.000	
Test 24 Range 4		0.903	\bar{X} \bar{H}	= 1.000	0.000	-0.049	-0.150	-0.248	-0.350	-0.447	-0.547	-0.651	-0.752	-0.836	-0.932	
					0.946	0.946	0.830	0.760	0.595	0.474	0.254	0.152	-0.019	-0.059	0.000	
Test 26 Range 2		0.720	\bar{X} \bar{H}	= 1.000	0.000	-0.062	-0.170	-0.250	-0.350	-0.441	-0.547	-0.650	-0.758	-0.838	-0.932	
					1.000	1.000	0.958	0.809	0.703	0.508	0.305	0.097	-0.028	0.042	0.000	
Test 26 Range 3		0.637	\bar{X} \bar{H}	= 1.000	0.000	-0.067	-0.146	-0.276	-0.349	-0.444	-0.544	-0.657	-0.753	-0.856	-0.930	
					1.000	1.015	0.914	0.662	0.662	0.505	0.348	0.054	-0.044	-0.044	0.000	
Test 28 Range 2		0.655	\bar{X} \bar{H}	= 1.000	0.000	-0.061	-0.161	-0.242	-0.330	-0.438	-0.542	-0.636	-0.744	-0.836	-0.932	
					0.960	0.960	0.913	0.837	0.702	0.554	0.341	0.224	0.004	0.066	0.000	
Test 28 Range 3		0.690	\bar{X} \bar{H}	= 1.000	0.000	-0.067	-0.153	-0.247	-0.339	-0.445	-0.555	-0.650	-0.741	-0.846	-0.928	
					0.975	0.975	0.875	0.723	0.644	0.504	0.384	0.168	-0.003	-0.004	0.000	
Test 28 Range 4		0.742	\bar{X} \bar{H}	= 1.000	0.000	-0.042	-0.141	-0.232	-0.318	-0.460	-0.553	-0.634	-0.734	-0.871	-0.948	
					0.977	0.977	0.920	0.798	0.674	0.525	0.393	0.168	-0.027	-0.030	0.000	

A P P E N D I X D

HYDROGEN BUBBLE MEAN DIMENSIONLESS VELOCITY
AND TURBULENCE DATA

TABLE D.1
MEAN DIMENSIONLESS VELOCITY $\frac{u}{U_m}$ PROFILE DATA

Y	X	-0.932 TOE	-0.848	-0.739	-0.646	-0.535	-0.442	-0.349	-0.239	-0.149	-0.036
1.000*		1.334	1.404	1.431	1.282	1.209	1.185	1.173	1.142	1.097	1.047
0.875		1.322	1.376	1.401	1.268	1.198	1.174	1.155	1.137	1.092	1.043
0.750		1.316	1.364	1.352	1.235	1.177	1.154	1.133	1.120	1.085	1.032
0.625		1.271	1.358	1.283	1.182	1.135	1.143	1.101	1.104	1.072	1.027
0.500		1.201	1.309	1.227	1.130	1.079	1.110	1.069	1.067	1.058	1.020
0.375		1.135	1.088	0.945	1.032	1.016	1.064	1.021	1.023	1.031	1.015
0.250		0.875	0.610	0.708	0.857	0.883	0.890	0.957	0.971	0.964	1.007
0.125		0.148	0.012	0.282	0.528	0.745	0.674	0.769	0.798	0.802	0.943
0.063		-0.069	0.009	0.118	0.352	0.497	0.481	0.575	0.603	0.636	0.859
0.000**			-0.011	-0.019	0.060	0.144	0.044	0.231	0.145	0.212	0.555

*Free Surface
**Bed Surface

TABLE D.2
MEAN DIMENSIONLESS TURBULENCE INTENSITY DATA

Y	X	-0.932 TOE	-0.843	-0.739	-0.646	-0.535	-0.442	-0.349	-0.239	-0.149	-0.035
1.000*	0.1345	0.1902	0.2754	0.1863	0.0995	0.1500	0.1491	0.1218	0.1433	0.0652	
0.875	0.1234	0.1766	0.2380	0.1742	0.1065	0.1200	0.1300	0.1053	0.1104	0.0413	
0.750	0.1210	0.1788	0.2052	0.1284	0.0935	0.0905	0.1065	0.0835	0.0862	0.0356	
0.625	0.0831	0.1635	0.1946	0.0942	0.0873	0.0900	0.0852	0.0683	0.0680	0.0340	
0.500	0.1149	0.1633	0.1886	0.1247	0.0922	0.0731	0.0728	0.0716	0.0653	0.0327	
0.375	0.1236	0.2620	0.2713	0.1495	0.0912	0.0902	0.0823	0.0696	0.0755	0.0383	
0.250	0.2306	0.3952	0.3895	0.1854	0.1394	0.1699	0.1530	0.0904	0.1244	0.0547	
0.125	0.3273	0.4275	0.3781	0.3216	0.1949	0.2419	0.2020	0.1749	0.1982	0.0942	
0.063	0.0558	0.3540	0.2993	0.2767	0.2225	0.2737	0.2828	0.2636	0.2435	0.1506	
0.000**		0.2212	0.1229	0.1233	0.2563	0.1675	0.3128	0.3201	0.3601	0.3262	

*Free Surface

**Bed Surface

TABLE D.3
MEAN DIMENSIONLESS VELOCITY $\frac{U}{U_s}$ PROFILE DATA

Y	X	-0.932 TOE	-0.848	-0.739	-0.646	-0.535	-0.442	-0.349	-0.239	-0.149	-0.036
1.000*	1.000	1.000	1.000	1.000	1.000	1.000	1.000	1.000	1.000	1.000	1.000
0.875	0.991	0.980	0.979	0.979	0.989	0.991	0.990	0.984	0.996	0.995	0.996
0.750	0.986	0.971	0.945	0.945	0.963	0.973	0.973	0.966	0.981	0.989	0.986
0.625	0.952	0.967	0.900	0.923	0.923	0.934	0.964	0.939	0.967	0.977	0.981
0.500	0.900	0.932	0.857	0.881	0.881	0.892	0.937	0.911	0.934	0.964	0.974
0.375	0.850	0.775	0.660	0.805	0.805	0.840	0.898	0.870	0.896	0.940	0.969
0.250	0.656	0.434	0.495	0.668	0.668	0.730	0.751	0.816	0.850	0.879	0.962
0.125	0.111	0.008	0.197	0.412	0.412	0.616	0.569	0.655	0.699	0.731	0.901
0.063	-0.052	0.006	0.082	0.274	0.274	0.411	0.406	0.490	0.528	0.580	0.820
0.000**		-0.007	-0.013	0.046	0.046	0.119	0.037	0.197	0.126	0.193	0.530

*Free Surface

**Bed Surface

A P P E N D I X E

PRESSURE MEASUREMENT

DATA

TABLE E.1

DIMENSIONLESS MEAN PRESSURE DISTRIBUTION

$$\bar{p} = \frac{p - p_r}{\bar{v}_{c2}^2/2g}$$

Test/ Range	11/2	12/2	17/2	17/3	20/2	20/3	21/2	21/3	24/2	24/4	26/3	28/3	28/4
\bar{v}_{c2} in/sec	3.58	3.68	5.30	4.35	3.87	3.78	3.48	3.66	3.69	3.38	3.75	3.04	3.07
\bar{x}													
0.00	0.000	0.000	0.000	0.000	0.000	0.000	0.000	0.000	0.000	0.000	0.000	0.000	0.000
-0.05							-0.001					-0.007	-0.004
-0.10	0.003	0.014	0.004	0.016	0.004	-0.004	0.000	-0.023	0.002	0.000	0.011	0.012	0.011
-0.15							0.005					0.042	0.033
-0.20	0.019	0.048	0.013	0.049	0.011	-0.002	0.019	-0.017	0.025	0.020	0.066	0.067	0.057
-0.25	0.036	0.071	0.019	0.073	0.019	0.008	0.045	0.023	0.078	0.078	0.110	0.096	0.084
-0.30	0.057	0.107	0.030	0.099	0.032	0.028	0.077	0.023	0.078	0.078	0.110	0.131	0.115
-0.35	0.084	0.145	0.042	0.135	0.047	0.053	0.127	0.023	0.078	0.078	0.110	0.171	0.151
-0.40	0.123	0.194	0.058	0.169	0.067	0.077	0.178	0.121	0.142	0.148	0.159	0.226	0.197
-0.45	0.178	0.251	0.079	0.212	0.090	0.110	0.240	0.260	0.224	0.258	0.228	0.288	0.245
-0.50	0.235	0.314	0.105	0.247	0.116	0.153	0.300	0.260	0.280	0.313	0.228	0.357	0.303
-0.55	0.300	0.366	0.132	0.258	0.149	0.185	0.360	0.382	0.334	0.375	0.280	0.418	0.365
-0.60	0.337	0.389	0.134	0.245	0.188	0.216	0.420	0.382	0.375	0.375	0.280	0.443	0.401
-0.65	0.338	0.383	0.114	0.220	0.215	0.238	0.420	0.450	0.375	0.365	0.247	0.409	0.399
-0.70	0.319	0.346	0.085	0.187	0.221	0.247	0.420	0.450	0.375	0.320	0.247	0.409	0.344
-0.75	0.271	0.299	0.058	0.157	0.201	0.238	0.300	0.421	0.282	0.172	0.187	0.033	0.197
-0.80	0.189	0.241	0.030	0.120	0.164	0.211	0.300	0.421	0.282	0.172	0.187	0.033	0.074
-0.85													
-0.90	-0.030	0.147	0.002	0.049	0.049	0.151	0.038	0.279	0.150		0.055	0.015	0.016
-0.95	-0.048	0.098	-0.009	0.004	-0.041								
-1.00	-0.048	0.147	-0.009	0.004	-0.041	0.076			0.098		0.005		0.025

APPENDIX F

SAMPLE OF RAW EXPERIMENTAL DATA

EXPERIMENTAL DATA

TEST NO= 28

JULY 3 1970

BED-WAVE DEPTH WIRE READINGS (YY-DATA), INCHES

TIME/XX=	0.0	4.00	8.00	12.00	14.00	16.00	18.00	20.00	22.00
30	3.00	2.90	3.20	3.45	3.50	2.80	3.00	3.10	3.20
275	3.50	2.80	3.15	3.45	3.45	2.85	2.90	3.00	3.10
665	3.40	2.75	3.00	3.35	3.40	3.25	2.90	3.00	3.10
1265	3.35	2.80	2.95	3.25	3.40	3.50	3.05	2.90	3.00
1820	3.25	3.35	2.90	3.20	3.25	3.40	3.50	3.00	2.90
2320	3.20	3.45	2.75	3.05	3.20	3.40	3.50	3.50	3.00
3520	2.95	3.25	3.45	2.90	3.00	3.20	3.40	3.45	3.50
4220	2.80	3.15	3.35	2.80	2.95	3.00	3.25	3.40	3.50
4710	2.75	3.10	3.25	2.85	2.75	2.95	3.20	3.25	3.40
5030	2.70	3.00	3.20	3.45	2.80	2.90	3.10	3.20	3.35
5425	2.80	2.95	3.20	3.40	2.80	2.80	3.00	3.10	3.25
5810	3.20	2.80	3.05	3.40	3.45	2.80	2.90	3.15	3.25
6200	3.40	2.70	3.00	3.40	3.45	2.80	2.80	3.00	3.10
66750	3.40	2.75	2.90	3.25	3.35	3.50	2.80	2.90	3.00
7070	3.40	2.80	2.80	3.15	3.25	3.40	3.10	2.90	3.00
7385	3.30	3.30	2.70	3.10	3.20	3.40	3.50	2.90	2.80
7810	3.25	3.50	2.75	3.00	3.10	3.30	3.50	3.20	2.80
8250	3.25	3.45	2.75	2.90	3.10	3.25	3.45	3.45	2.90
8900	3.20	3.40	2.70	2.80	3.00	3.20	3.40	3.45	3.50
9210	3.15	3.40	3.00	2.80	2.95	3.15	3.30	3.40	3.50
9740	3.00	3.25	3.50	2.80	2.85	3.10	3.25	3.40	3.45
9960	2.90	3.20	3.40	2.80	2.80	3.05	3.25	3.35	3.45
10265	2.85	3.10	3.40	2.85	2.95	3.00	3.20	3.30	3.40
10680	2.75	3.05	3.20	3.30	2.80	2.90	3.20	3.25	3.35
11150	2.60	3.00	3.25	3.50	2.80	2.80	3.05	3.20	3.35
11730	2.50	2.90	3.25	3.40	3.40	2.80	2.80	3.00	3.25
12255	2.60	2.80	3.10	3.50	3.50	3.50	2.70	2.80	3.00
12590	3.50	2.70	3.00	3.40	3.50	3.55	2.80	2.80	2.90
13270	3.50	2.80	2.80	3.20	3.25	3.40	3.50	3.20	2.90

TEST NO= 28

EXPERIMENTAL DATA (CONT'D)

BED-WAVE PROFILE CREST AND TOE DATA

TIME	BED-WAVE 1				BED-WAVE 2				BED-WAVE 3			
	XCR	YCR	XTOE	YTOE	XCR	YCR	XTOE	YTOE	XCR	YCR	XTOE	YTOE
30	14.0	3.50	15.1	2.80	-1.0	3.50	0.2	2.80				
275	14.7	3.50	15.7	2.85	0.0	3.50	1.0	2.80				
665	15.9	3.50	16.8	2.90	1.0	3.45	2.0	2.80				
1265	17.0	3.50	18.2	2.90	2.2	3.45	3.2	2.80				
1820	19.0	3.55	20.0	3.00	3.9	3.45	4.9	2.85				
2320	20.0	3.50	21.0	3.00	5.2	3.50	6.0	2.80				
3520	23.0	3.50	24.0	3.00	8.0	3.45	8.8	3.00				
4220					9.5	3.50	10.5	2.90				
4710					11.0	3.45	12.0	2.85				
5030					12.0	3.45	12.8	2.90				
5425					13.0	3.45	14.0	2.80				
5810					14.0	3.45	15.0	2.90				
6200					15.0	3.50	16.0	2.80	-0.2	3.50	0.8	2.80
6750					16.8	3.50	17.5	2.80	0.7	3.45	1.6	2.75
7070					17.2	3.50	18.4	3.00	2.0	3.50	3.0	2.75
7385					18.4	3.50	19.4	2.90	2.9	3.50	4.0	2.80
7810					19.4	3.50	20.4	2.80	3.9	3.45	4.9	2.75
8250					21.0	3.50	22.0	2.90	4.2	3.50	5.5	2.75
8900					22.0	3.50	23.0	2.80	5.2	3.50	6.4	2.75
9210									7.0	3.45	8.0	2.70
9740									7.5	3.45	8.5	2.80
9960									9.0	3.55	10.2	2.80
10265									9.8	3.50	11.0	2.80
10680									10.4	3.50	11.6	2.85
11150									11.6	3.45	12.8	2.80
11730									13.0	3.50	14.0	2.80
12255									14.5	3.40	15.5	2.80
12590									16.0	3.50	17.0	2.80
13270									16.8	3.55	18.0	2.80
									19.8	3.60	21.0	2.90

BED-WAVE 4

	XCR	YCR	XTOE	YTOE
	0.0	3.50	1.0	2.70
	3.0	3.50	4.0	2.80

HYDROGEN BUBBLE VELOCITY PROFILE DATA TEST 28 JULY 3 1970

TIME	150	RANGE	2	HB	WIRE	NO 1	NON-DIM DIST	FROM REF	CREST	-0.82	
DEPTH		INCHES			0.0	-0.26	-0.52	-1.04	-1.30	-1.56	-2.08
VELOCITY		IN/SEC			2.86	2.86	2.60	2.34	1.30	0.0	0.0
TIME	150	RANGE	2	HB	WIRE	NO 3	NON-DIM DIST	FROM REF	CREST	-0.28	
DEPTH		INCHES			0.0	-0.25	-0.50	-0.75			
VELOCITY		IN/SEC			2.77	2.77	2.77	2.52			
TIME	835	RANGE	2	HB	WIRE	NO 1	NON-DIM DIST	FROM REF	CREST	-0.89	
DEPTH		INCHES			0.0	-0.25	-0.51	-0.76	-1.01	-1.27	-1.39
VELOCITY		IN/SEC			3.29	3.29	3.29	3.10	2.85	0.0	-1.65
											-0.51
											0.0
TIME	835	RANGE	2	HB	WIRE	NO 3	NON-DIM DIST	FROM REF	CREST	-0.38	
DEPTH		INCHES			0.0	-0.25	-0.50	-0.75	-0.99	-1.24	-1.49
VELOCITY		IN/SEC			2.61	2.48	2.36	2.36	2.24	2.24	1.99
TIME	1130	RANGE	2	HB	WIRE	NO 1	NON-DIM DIST	FROM REF	CREST	-0.97	
DEPTH		INCHES			0.0	-0.46	-0.92	-1.01	-1.29		
VELOCITY		IN/SEC			3.22	3.22	3.22	3.22	0.0		
TIME	1130	RANGE	2	HB	WIRE	NO 2	NON-DIM DIST	FROM REF	CREST	-0.70	
DEPTH		INCHES			0.0	-0.46	-0.92	-1.38	-1.34		
VELOCITY		IN/SEC			2.53	2.76	2.85	2.85	0.0		
TIME	3715	RANGE	3	HB	WIRE	NO 1	NON-DIM DIST	FROM REF	CREST	-0.42	
DEPTH		INCHES			0.0	-0.46	-0.93	-1.39	-1.62		
VELOCITY		IN/SEC			3.43	3.62	3.71	2.18	0.0		

TIME 3715	RANGE 3	HB	WIRE NO 2	NON-DIM DIST FROM REF CREST	-0.14
DEPTH	INCHES		0.0	-0.46	-0.91 -1.18 -1.28
VELOCITY	IN/SEC		3.19	3.14	1.96 2.73 0.0

TIME 3715	RANGE 2	HB	WIRE NO 3	NON-DIM DIST FROM RFF CREST	-0.88
DEPTH	INCHES		0.0	-0.46	-0.91 -1.37 -1.46
VELOCITY	IN/SEC		2.96	3.28	2.82 0.68 0.0

TIME 4400	RANGE 3	HB	WIRE NO 1	NON-DIM DIST FROM RFF CREST	-0.54
DEPTH	INCHES		0.0	-0.51	-1.02 -1.52 -1.73
VELOCITY	IN/SEC		3.05	2.79	2.39 2.44 0.0

TIME 4400	RANGE 3	HB	WIRE NO 2	NON-DIM DIST FROM REF CREST	-0.26
DEPTH	INCHES		0.0	-0.50	-1.01 -1.31 -1.36
VELOCITY	IN/SEC		2.42	2.52	1.92 1.92 0.0

TIME 4400	RANGE 2	HB	WIRE NO 3	NON-DIM DIST FROM REF CREST	-0.98
DEPTH	INCHES		0.0	-0.50	-1.01 -1.26
VELOCITY	IN/SEC		3.08	2.77	2.52 0.0

TIME 6730	RANGE 3	HB	WIRE NO 1	NON-DIM DIST FROM REF CREST	-0.97
DEPTH	INCHES		0.0	-0.50	-0.99 -1.49
VELOCITY	IN/SEC		3.23	3.23	0.0

TIME 6730	RANGE 3	HB	WIRE NO 2	NON-DIM DIST FROM REF CREST	-0.70
DEPTH	INCHES		0.0	-0.49	-0.99 -1.48 -1.92
VELOCITY	IN/SEC		2.96	2.22	2.17 0.99 0.0

TIME 6730	RANGE 3	HB	WIPE NO 3	NON-DIM DIST	FROM REF CREST	-0.44
DEPTH	INCHES		0.0	-0.49	-0.99 -1.38 -1.53	
VELOCITY	IN/SEC		2.22	2.22	1.72 0.0	

TIME 7150	RANGE 4	HB	WIPE NO 1	NON-DIM DIST	FROM REF CREST	-0.05
DEPTH	INCHES		0.0	-0.53	-0.79 -1.06 -1.19 -1.32 -1.38	
VELOCITY	IN/SEC		3.44	3.44	1.85 1.06 0.0	

TIME 7150	RANGE 3	HB	WIPE NO 2	NON-DIM DIST	FROM REF CREST	-0.77
DEPTH	INCHES		0.0	-0.49	-0.99 -1.48 -1.58 -1.67	
VELOCITY	IN/SEC		2.96	2.66	3.20 0.0 0.0	

TIME 7150	RANGE 3	HB	WIPE NO 3	NON-DIM DIST	FROM REF CREST	-0.49
DEPTH	INCHES		0.0	-0.49	-0.99 -1.48 -1.65	
VELOCITY	IN/SEC		2.96	2.61	2.71 0.74 0.0	

TIME 8490	RANGE 4	HB	WIPE NO 1	NON-DIM DIST	FROM REF CREST	-0.20
DEPTH	INCHES		0.0	-0.50	-1.00 -1.34 -1.39	
VELOCITY	IN/SEC		3.74	3.84	2.29 1.49 0.0	

TIME 8490	RANGE 3	HB	WIPE NO 2	NON-DIM DIST	FROM REF CREST	-0.97
DEPTH	INCHES		0.0	-0.49	-0.99 -1.33	
VELOCITY	IN/SEC		2.96	3.00	3.05 0.0	

TIME 8490	RANGE 3	HB	WIPE NO 3	NON-DIM DIST	FROM REF CREST	-0.71
DEPTH	INCHES		0.0	-0.49	-0.99 -1.28 -1.97	
VELOCITY	IN/SEC		2.96	2.96	0.0 0.0	

TIME 10075	RANGE 4	HB	WIRE NO 1	NON-DIM	DIST FROM REF CREST	-0.46
DEPTH	INCHES	0.0	-0.46	-0.92	-1.38 -1.52	-1.57
VELOCITY	IN/SEC	3.55	3.55	3.23	3.00 2.97	0.0

TIME 10075	RANGE 4	HB	WIRE NO 2	NON-DIM	DIST FROM REF CREST	-0.22
DEPTH	INCHES	0.0	-0.46	-0.92	-1.24 -1.35	
VELOCITY	IN/SEC	3.12	3.12	2.71	2.20 0.0	

TIME 10075	RANGE 3	HB	WIRE NO 3	NON-DIM	DIST FROM REF CREST	-0.99
DEPTH	INCHES	0.0	-0.46	-0.92	-1.06 -1.10	-1.15
VELOCITY	IN/SEC	3.21	2.75	2.75	2.29 1.15	0.0

TIME 13020	RANGE 4	HB	WIRE NO 1	NON-DIM	DIST FROM REF CREST	-0.98
DEPTH	INCHES	0.0	-0.46	-0.92	-1.20 -1.29	
VELOCITY	IN/SEC	2.62	2.90	2.99	2.76 0.0	

TIME 13020	RANGE 4	HB	WIRE NO 2	NON-DIM	DIST FROM REF CREST	-0.74
DEPTH	INCHES	0.0	-0.47	-0.94	-1.41 -1.88	
VELOCITY	IN/SEC	2.54	1.97	2.35	0.70 0.23	

TIME 13020	RANGE 4	HB	WIRE NO 3	NON-DIM	DIST FROM REF CREST	-0.50
DEPTH	INCHES	0.0	-0.47	-0.95	-1.42 -1.51	
VELOCITY	IN/SEC	2.84	2.84	2.89	2.79 0.0	

TIME 11640	RANGE 4	HB	WIRE NO 3	NON-DIM	DIST FROM REF CREST	-0.24
DEPTH	INCHES	0.0	-0.48	-0.96	-1.20	
VELOCITY	IN/SEC	2.73	2.97	2.25	0.0	

EXPERIMENTAL DATA (CONT'D) TEST NO= 28 JULY 3 1970

DIFFERENTIAL PRESSURE TRANSDUCER OUTPUT DATA, IN INCHES OF WATER X1000

TIME PRESSURE TIME PRESSURE TIME PRESSURE TIME PRESSURE TIME PRESSURE

PIEZOMETER C1 X= 4.00 PORT ELEV= 1.00
NUMBER OF PRESSURE DATA POINTS IS 12

3160	1.0	10500	0.3	11410	1.9	12590	0.1
9600	-0.2	10815	1.6	11780	1.6	12940	0.2
10280	0.4	11090	1.3	12280	1.2	13230	-0.1

PIEZOMETER C2 X= 4.00 PORT ELEV= 2.00
NUMBER OF PRESSURE DATA POINTS IS 12

3530	2.0	10430	1.9	11330	2.2	12540	-0.3
9570	1.3	10770	1.8	11750	2.1	12850	-1.3
10120	1.4	11050	1.9	12230	1.4	13210	-1.4

PIEZOMETER C3 X= 4.00 PORT ELEV= 3.00
NUMBER OF PRESSURE DATA POINTS IS 38

2915	1.7	7500	0.5	8300	0.6	9100	1.5	11200	3.4
2950	1.8	7600	0.2	8400	0.5	9200	1.8	11600	4.3
3330	1.8	7700	0.2	8500	0.8	9300	2.2	11950	2.7
3370	1.9	7800	0.5	8600	1.7	9400	2.8	12430	3.0
7200	0.4	7900	0.1	8700	0.7	9500	3.5	12750	0.6
7250	0.6	8000	1.1	8800	1.8	10060	4.0	13100	0.8
7300	0.7	8100	0.8	8900	1.9	10680	4.1		
7400	0.7	8200	0.7	9000	2.3	10950	3.7		

PIEZOMETER G2 X=12.00 PORT ELEV= 2.25
NUMBER OF PRESSURE DATA POINTS IS 16

2840	2.2	9500	2.4	10860	-2.4	12330	-2.7
3615	0.7	9700	0.7	11130	-2.3	12650	-1.8
3840	0.7	10230	-0.8	11460	-2.2	13000	-1.2
4050	0.6	10540	-1.6	11840	-2.1	13280	-0.1

PIEZOMETER G3 X=12.00 PORT ELEV= 1.75
NUMBER OF PRESSURE DATA POINTS IS 11

3300	1.4	10600	-2.1	11530	-1.9	12700	-0.3
9750	0.3	10900	-2.4	11900	-3.5	13080	0.9
10370	-1.4	11150	-2.0	12380	-2.9		

PIEZOMETER I1 X=16.00 PORT ELEV= 1.25
NUMBER OF PRESSURE DATA POINTS IS 63

1600	-2.6	2900	-1.4	4600	-0.3	5900	-1.1	7180	-1.1
1700	-2.4	3400	-1.2	4700	-0.6	6000	-1.3	10050	1.1
1800	-2.8	3500	-1.3	4800	-0.6	6100	-1.0	10180	1.3
1900	-2.5	3600	-1.0	4900	-0.7	6200	-1.0	10739	0.8
2000	-2.2	3700	-1.3	5000	-0.7	6300	-0.9	11000	-0.4
2100	-2.4	3820	-1.1	5100	-0.6	6400	-1.1	11250	-0.4
2200	-2.5	3900	-0.9	5200	-0.9	6500	-1.3	11700	-3.3
2300	-2.0	4000	-0.6	5300	-0.7	6600	-1.2	12000	-2.8
2400	-1.3	4100	-0.8	5400	-0.6	6700	-1.1	12500	-4.1
2500	-1.4	4200	-0.8	5500	-0.5	6800	-1.0	12800	-3.7
2600	-1.6	4300	-0.7	5600	-0.6	6900	-0.9	13150	-3.0
2700	-1.8	4400	-0.8	5700	-0.7	7000	-0.4		
2800	-1.5	4500	-0.8	5800	-0.9	7100	-0.7		

PIEZOMETER E1 X= 8.00 PORT ELEV= 1.50
NUMBER OF PRESSURE DATA POINTS IS 12

3070	0.0	10430	-0.9	11330	-1.0	12540	0.0
9570	-1.7	10770	-0.5	11750	-0.7	12850	0.9
10220	-1.1	11050	0.8	12230	-0.1	13190	2.5

PIEZOMETER E2 X= 8.00 PORT ELEV= 2.50
NUMBER OF PRESSURE DATA POINTS IS 13

2780	0.6	10170	-1.2	11090	-0.9	12280	-0.4	13220	1.8
3580	-0.7	10480	-1.3	11420	-0.7	12590	-0.2		
9600	-2.7	10820	-1.5	11800	-0.7	12940	1.0		

PIEZOMETER E3 X= 8.00 PORT ELEV= 0.50
NUMBER OF PRESSURE DATA POINTS IS 13

3230	0.3	10320	0.0	11130	1.0	12330	1.4	13280	2.3
9700	-1.1	10530	-0.1	11450	1.1	12650	2.0		
10130	-0.3	10860	1.0	11850	1.4	13000	2.2		

PIEZOMETER G1 X=12.00 PORT ELEV= 2.75
NUMBER OF PRESSURE DATA POINTS IS 54

2710	3.1	5000	-1.5	6100	1.3	8500	3.7	9970	-1.8
3950	1.1	5100	-1.3	6200	1.6	8600	4.5	10330	-2.4
4100	0.3	5200	-1.1	7660	3.4	8700	4.2	10680	-2.1
4200	0.5	5300	-1.0	7700	3.1	8800	4.5	10960	-2.5
4300	0.1	5400	-1.3	7800	3.8	8900	4.4	11200	-2.3
4400	-0.6	5500	-1.1	7900	3.2	9000	4.1	11600	-2.8
4500	-1.3	5600	-0.9	8000	3.9	9100	4.4	11950	-3.1
4600	-1.2	5700	-0.6	8100	3.8	9200	4.3	12430	-3.2
4700	-2.0	5800	-0.1	8200	3.8	9300	4.2	12750	-3.0
4800	-1.8	5900	0.2	8300	3.8	9400	3.6	13100	-1.5
4900	-1.8	6000	0.5	8400	3.4	9450	3.3		

PIEZOMETER I2 X=16.00 PORT ELEV= 0.75
NUMBER OF PRESSURE DATA POINTS IS 14

3850	0.0	9770	1.2	10600	-0.8	11500	-1.7	12700	-4.0
3900	0.1	10255	-0.3	10900	-1.4	11900	-3.2	13070	-3.3
9730	1.1	10290	0.1	11170	-1.7	12380	-4.6		

PIEZOMETER I3 X=16.00 PORT ELEV= 3.25
NUMBER OF PRESSURE DATA POINTS IS 48

1500	-0.8	2500	0.8	3450	0.2	7000	0.1	10730	0.2
1600	0.0	2600	0.9	6250	0.2	7100	0.2	11000	-1.8
1700	0.4	2650	0.8	6300	0.2	7200	0.4	11260	-2.0
1800	-0.2	2865	0.1	6400	0.0	7300	0.4	11700	-2.7
1900	-0.1	2950	0.2	6500	-0.1	7400	0.3	12000	-3.1
2000	-0.4	3000	0.5	6600	0.0	7500	-0.2	12490	-4.1
2100	-0.2	3100	0.9	6700	0.1	7570	-0.5	12800	-3.7
2200	0.1	3200	0.6	6770	-0.1	7630	-0.1	13150	-2.2
2300	0.4	3300	0.3	6870	-0.6	10050	0.6		
2400	0.6	3400	0.3	6900	0.0	10370	0.5		

B30054